VRIJE
UNIVERSITEIT
BRUSSEL

Faculty of Engineering
Department of Mechanical Engineering

Development and Validation of Innovative Structural Health Monitoring Methodology

Thesis submitted in fulfilment of the requirements
of the degree of Doctor of Engineering Sciences

Michaël Hinderdael

Supervisor:	Prof. Dr. Ir. P. Guillaume
Jury:	Prof. Dr. Ir. L. Pyl (Chair, VUB)
	Prof. Dr. R. Vounckx (Vice-chair, VUB)
	Dr. Ir. W. Devesse (Secretary, VUB)
	Prof. Dr. Ir. M. Van Overmeire (VUB)
	Prof. Dr. Ir. D. Aggelis (VUB)
	Dr. H. Pfeiffer (KU Leuven)
	Prof. Dr. Victor Giurgiutiu (USC)

May 2018

Printed by
Crazy Copy Center Productions
Vrije Universiteit Brussel
Pleinlaan 2, 1050 Brussels, Belgium
Tel./Fax. +32 (0)2 629 33 44
E-mail: crazycopy@vub.ac.be
www.crazycopy.be

ISBN 978 94 9231 275 4
NUR 950

The more you know, the more you know you don't know.

— Aristotle

Acknowledgements

First of all, I would like to acknowledge the Agency For Innovation By Science And Technology (IWT) for granting me a PhD fellowship. This fellowship allowed me to conduct the presented research over the past years in an enjoyable work environment which Vrije Univesiteit Brussel has always been to me. It furthermore allowed me to publish the research results and present those at internationally renowned conferences.

Next, I would like to thank my promoter, prof. Patrick Guillaume, for having given me the opportunity to perform this PhD. Thank you for having entrusted me with a high level of independence and for having been always available for a discussion. Thank you for the guidance throughout the years.

I would like to thank all members of the jury for their time to evaluate this doctoral thesis. Thank you for sharing with me your knowledge. Your constructive feedback is highly appreciated.

I would like to express special words of thank to Dieter De Baere. Dieter, thank you very much for sharing with me your ever lasting enthusiasm, your vision and sometimes crazy ideas. I have always liked the many discussions we had on the train which have certainly had a big impact on the quality of this work. Many thanks for your immediate assistance whenever I was in need.

I had the privilege to conduct this research in a very friendly atmosphere. I have always liked coming to work. Thank you Wim Devesse, Galid Aroud, Julien Ertveldt, Marc Moonens, Margot Lison and Zoé Jardon for creating this enjoyable working environment. Many thanks for the meetings we had in which we exchanged ideas to reach our end-goal. Also many thanks to my colleagues of the MECH and MeMC department for the chats we had at the coffee machine, during receptions and barbecues, during the train rides, and more.

Thank you Maria Strantza for having helped me out with my first steps with the Scanning Electron Microscope and your guidance throughout the exploration of the world of materials research and fracture analysis. I would also like to express words of thank to Reza Vafadari (U Gent) for the insights gained through the numerical simulations he performed and to Bey Vrancken (KU Leuven) for the assistance in the production of test specimens.

This thesis is written on the basis of a vast amount of practical tests on experimental setups build for the sole purpose of this thesis. These practical tests would not have been possible without the technical assistance of Marc Luypaert, Marnix De Boom, Jean-Paul Schepens and Geoffrey Warniez of the workshop of MECH, Gabriël Van den Nest, Daniel Debondt and Rene Heremans of the workshop of MeMC. I owe special thanks to Frans Boulpaep for his continuous support during the many test hours at the MeMC department. Thank you for always asking me if I join for having a drink together. Thank you Birgit Buys and Jenny D'haes for the administrative support for the purchases which were required for the production of the test specimens and test setups. I would also like to express my gratitude to Priya Laha, Marc Raes and Bart Lippens for the support when manipulating the Scanning Electron Microscope, the hardness measurements and for lending me your equipment.

Above all, a very big thank you to my parents, sister, family and friends who have always supported me throughout the last years. I was lucky to have met my girlfriend at the start of this PhD journey. Thank you for creating those relaxing moments and always being my listening ear whenever I came up with a new finding and immediately started to make some drawings. Thank you for your patience and understanding, especially when writing this book.

Thank you all,

Michaël Hinderdael
Brussels, May 2018

Abstract

Additive Manufacturing (AM) is an emerging manufacturing technology, able to create three dimensional components in a layerwise manner. The free-form design freedom and the ability to integrate functions have paved the way for the creation of lightweight smart materials. Such materials have gained the interest of many industries and in particular aerospace, with the first AM components already flying around. However, the unrepeatable material behaviour and lack of proper AM process control still form major challenges for AM to become widely adopted in aeronautical applications. Structural Health Monitoring (SHM) is used to provide information about the structural integrity of components. The so-called effective Structural Health Monitoring (eSHM) system, a dedicated SHM strategy for AM components, was developed at the Vrije Universiteit Brussel to inspect the AM material for fatigue cracks. Capillaries are integrated during the production of the component. The capillaries are located in the zones where fatigue cracks are expected to grow. Initially being pressurized, the capillary pressure becomes very sensitive to leaks created by the fatigue cracks beaching the capillary.

The purpose of this thesis is to understand the pressure variations inside the capillary of the eSHM system to derive information about the presence of a crack, its size and location. Four-point bending fatigue tests were conducted on test specimens with an integrated eSHM system. The integration of a capillary inside AM materials is challenging, both from a production as well as from a structural integrity point of view. The influence of the integrated capillary on the structural performance of the test specimen will be analysed and the influence of surface roughness on a capillary produced by the laser based directed energy deposition process will be determined. The pressure measurements of the four-point bending fatigue tests will be analysed and the crack size will be estimated on the basis thereof. Also, Negative Pressure Waves (NPWs) contain important information about the crack size. A new, theoretical, model will be presented capable of deriving the crack size on the basis of the amplitude of the NPWs, valid under all possible configurations for the eSHM system. A test set-up was built to generate NPW in a controlled way to verify the model under various parameter sets. The difference in time-of-arrival of propagating NPWs allows locating the leak with high accuracy.

The embedded capillary of the eSHM can furthermore be used to measure the loads acting on the structure. As a structure deforms under the loads acting upon them, so does the integrated capillary, leading to measurable pressure fluctuations inside the capillary. A last chapter of this thesis explores the possible use of the integrated eSHM as a load monitoring technique.

Contents

List of Figures

List of Tables

Nomenclature

Acronyms

2D	two dimensional
3D	three dimensional
AB	as-built
ABS	acrylonitrile butadiene styrene
AE	acoustic emission
AISI	American Iron and Steel Institute
AM	additive manufacturing
ASTM	American Society for Testing and Materials
AU	acousto ultrasonics
AVG	average
bara	1 bar absolute pressure
barg	1 bar gauge pressure
CA	constant amplitude
CAD	computed aided design
CBM	condition based maintenance
CVM	comparative vacuum monitoring
DED	directed energy deposition
DLP	digital light processing
EC	eddy current
EDM	electron discharge machining

EMI	electromechanical impedance
eSHM	effective structural health monitoring
FBG	Fibre Bragg Grating
FDM	fused deposition modelling
FEM	finite element modelling
FFT	Fast Fourier Transform
GE	General Electric
GCF	giga cycle fatigue
HCF	high cycle fatigue
HIP	hot isostatic pressing
HUMS	Health and Usage Monitoring Systems
HV	Hardness Vickers
IWT	Agency For Innovation By Science And Technology
LCF	low cycle fatigue
LED	light-emitting diode
LEFM	linear elastic fracture mechanics
LENS	laser engineered net shaping
LMD	laser metal deposition
LP	liquid penetrant
MFCR	microwave frequency cavity resonator
NDT	non destructive testing
NLR	Netherlands Aerospace Centre
NPW	negative pressure wave
PBF	powder bed fusion
PLA	polyactic acid
PoD	probability of detection
rpm	round per minutes
RUL	remaining useful lifetime
SEM	scanning electron microscope
SHM	structural health monitoring

SLA	stereolithography
SLM	selective laser melting
SR	stress relieved
SS	stainless steel
STD	standard deviation
STL	surface tensellation language
TBPM	time based preventive maintenance
TIR	third industrial revolution
TLC	total life cycle
TO	topology optimization
TOA	time-of-arrival
TRL	technology readiness level
UM	usage monitoring
UV	ultraviolet
VA	variable amplitude
VHCF	very high cycle fatigue

Latin symbols

a	smallest distance from the capillary surface to the outher specimen surface
A	cross sectional area of the capillary before tensile deformation
A_{cap}	cross sectional area of the capillary
A_{load}	cross sectional area of the capillary after tensile deformation
$A_{l,max}$	maximal cross sectional area of the leak
A_l	cross sectional area of the leak
a	crack size
C_{PL}	linear Paris Law constant
C_D	discharge coefficient
c	speed of sound

Δc	error on the measured speed of sound
D_{cap}	capillary diameter
D_l	leak diameter
D_p	pipeline diameter
D_{tube}	tube diameter
D_{sensor}	sensor diameter
F	alternating load during fatigue test
F_{close}	Maximum load level at which the fatigue crack is closed
F_{max}	Maximum load during fatigue cycle
F_{open}	Minimal load level required to open the fatigue crack
f	frequency
f_s	sampling frequency
H	stress history
$H(\omega)$	Transfer function
h_l	enthalpy at the leak location
K	bulk modulus
K^*	bulk modulus factor
K_S	adiabatic bulk modulus
K_T	isothermal bulk modulus
K_{H2O}	bulk modulus of water
k	heat capacity ratio
k_0	wave number
K_{min}	minimal stress intensity
K_{max}	maximal stress intensity
ΔK	stress intensity range
L	length of capillary/tube
ΔL	error on the measured length
L_{load}	length after tensile deformation
m_{PL}	exponential Paris Law constant
M_l	Mach number in the leak

m	mass
m_{cap}	fluid mass in capillary
Δm	mass increment
$\dot{m}_l$	leakage mass flow rate through the fatigue crack
Δh_l	infinitesimal enthalpy change at the leak location
l_t	scan length during roughness measurement
N	number of fatigue cycles
N_i	crack initiation life
N_f	fatigue life
N_p	crack propagation life
N_{RO}	number of fatigue cycles considered run out
N_{max}	maximum fatigue test cycles
$P(\omega)$	Fourier transform of the pressure measurement
P_0	initial pressure inside the capillary
P_{amb}	ambient pressure
$P_{t,amb}$	total ambient pressure
P_{cap}	Pressure inside the capillary
P_{def}	pressure fluctuation inside the capillary due to deformation
P_l	pressure in the leak
$P_{t,l}$	total pressure in the leak
P_p	static pipeline pressure
ΔP	Negative Pressure Wave amplitude
ΔP_0	initial amplitude of Negative Pressure Waves
ΔP_n	amplitude of Negative Pressure Waves after n reflections
$\left(\frac{P_{amb}}{P_{cap}}\right)^*$	critical pressure ratio resulting in choked flow conditions
$Q(\omega)$	Fourier transform of the leakage mass flow rate
R_{air}	individual gas constant of air
R_a	arithmetical mean height of the roughness profile
R_{cap}	capillary radius
R_i	stress intensity ratio

R_t	total height of the roughness profile
$r1$	ellipse radius along minor axis
$r2$	ellipse radius along major axis
S1	name of sensor located closest to the leak
S2	name of sensor located furthest away from the leak
$S-N$	Stress-Cycle
s_l	entropy at the leak location
Δs_l	infinitesimal entropy change at the leak location
T_{amb}	ambient temperature
$T_{t,amb}$	total ambient temperature
T_{cap}	temperature in capillary
T_l	temperature in the leak
$T_{t,l}$	total temperature in the leak
t	time
Δt	time step
ΔT_s	sampling interval
t_1	time of arrival of the first Negative Pressure Wave
t_2	time of arrival of the second Negative Pressure Wave
V	volume
V_0	initial volume
ΔV	volumetric change
V_{cap}	capillary volume
v_l	leak flow speed
Δv	instantaneous flow speed change in the leak
v	speed of travelling wavefront
x_1	distance between the leak location and sensor S1
$x_{1,real}$	actual distance between the leak location and sensor S1
$x_{1,est}$	estimated distance between the leak location and sensor S1
Δx	theoretical uncertainty on the determination of the crack location

Greek symbols

α	sensitivity of capillary pressure to structural deformation caused by load
α_L	linear thermal expansion coefficient
α_V	volumetric thermal expansion coefficient
β	attenuation coefficient
γ	relative sensitivity of capillary pressure to thermal expansion versus longitudinal strain
ϵ_{xx}	longitudinal strain x direction
ϵ_{yy}	transversal strain y direction
ϵ_{zz}	transversal strain z direction
ν_{air}	kinematic viscosity of air
ν	Poisson coefficient
ρ_{amb}	ambient density
$\rho_{t,amb}$	total ambient density
ρ_l	fluid density in the leak
$\rho_{t,l}$	total density in the leak
σ	standard deviation
σ_{max}	maximum stress level
σ_{max}	minimum stress level
σ_{mean}	mean stress level
$\Delta\sigma$	applied cyclic stress range
τ	thermal relaxation time
τ_1	response delay of sensor S1 to the input signal
τ_2	response delay of sensor S2 to the input signal
ω	pulsation

List of publications

Journal publications

[1] M. Hinderdael, D. De Baere, and P. Guillaume, “Proof of concept of crack localization using negative pressure waves in closed tubes for later application in effective SHM system for additive manufactured components,” *Applied Sciences*, vol. 6(2), pp. 1–12, jan 2016.

[2] W. Devesse, D. De Baere, M. Hinderdael, and P. Guillaume, “Hardware-in-the-loop control of additive manufacturing processes using temperature feedback,” *Journal of Laser Applications*, vol. 28(2), pp. 1–8, may 2016.

[3] M. Hinderdael, M. Strantza, D. De Baere, W. Devesse, I. D. Graeve, H. Terryn, and P. Guillaume, “Fatigue performance of ti-6al-4v additively manufactured specimens with integrated capillaries of an embedded structural health monitoring system,” *Materials*, vol. 10(9), pp. 1–19, aug 2017.

[4] M. Hinderdael, Z. Jardon, M. Lison, D. De Baere, W. Devesse, M. Strantza, and P. Guillaume, “Proof of concept of integrated load measurement in 3d printed structures,” *Sensors*, vol. 17(2), pp. 1–12, feb 2017.

[5] W. Devesse, D. De Baere, M. Hinderdael, and P. Guillaume, “Model-based temperature feedback control of laser cladding using

high-resolution hyperspectral imaging," *IEEE/ASME Transactions on Mechatronics*, vol. 22, pp. 2714–2722, dec 2017.

Conference publications

[1] D. De Baere, M. Strantza, M. Hinderdael, W. Devesse, and P. Guillaume, "Effective structural health monitoring with additive manufacturing," in *Proceedings of the 7th European Workshop on Structural Health Monitoring* (V. L. Cam, L. Mevel, and F. Schoefs, eds.), pp. 2314–2321, July 2014.

[2] M. F. Hinderdael, D. De Baere, W. Devesse, M. Strantza, and P. Guillaume, "Negative pressure waves analysis for crack localization and crack size estimation for 3d printed SHM system," in *Proceedings of the ASME 2015 Conference on Smart Materials, Adaptive Structures and Intelligent Systems*, no. SMASIS2015-8845, pp. 1–9, ASME, sep 2015.

[3] M. Strantza, R. Vafadari, D. De Baere, M. Rombouts, I. Vandendael, H. Terryn, M. Hinderdael, A. Rezaei, W. V. Paepegem, P. Guillaume, and D. V. Hemelrijck, "Evaluation of different topologies of integrated capillaries in effective structural health monitoring system produced by 3d printing," in *Proceedings of the 10th International Workshop on Structural Health Monitoring (IWSHM)*, pp. 153–160, Sept. 2015.

[4] W. Devesse, D. De Baere, M. Hinderdael, and P. Guillaume, "Hardware-in-the-loop control of additive manufacturing processes using temperature feedback," in *Proceedings of the 34th international congress on applications of lasers & electro-optics*, no. 1602, pp. 753–744, Oct. 2015.

[5] M. Hinderdael, D. De Baere, M. Strantza, R. Vafadari, and P. Guillaume, "Effective structural health monitoring system for 3d printed components," in *Proceedings of the 34th Conference and the 28th Symposium of the International Committee on Aeronautical Fatigue and Structural Integrity*, pp. 136–142, June 2015.

[6] M. Strantza, M. Hinderdael, D. De Baere, I. Vandendael, H. Terryn, D. V. Hemelrijck, and P. Guillaume, "Additive manufacturing for novel structural health monitoring systems," in *Conference proceedings of*

the 8th European Workshop on Structural Health Monitoring, pp. 1–9, 2016.

[7] D. De Baere, W. Devesse, B. De Pauw, M. Hinderdael, and P. Guillaume, "Evaluation of the diffuse reflectivity behaviour of the melt pool during the laser metal deposition process," in *Proceedings of the 35th international congress on applications of lasers & electro-optics*, no. 506, pp. 1–7, Oct. 2016.

[8] W. Devesse, D. De Baere, M. Hinderdael, and P. Guillaume, "Temperature feedback control of laser cladding using high resolution hyperspectral imaging," in *Proceedings of the 35th international congress on applications of lasers & electro-optics*, Oct. 2016.

[9] W. Devesse, D. De Baere, M. Hinderdael, and P. Guillaume, "High resolution temperature estimation during laser cladding of stainless steel," in *Physics Procedia*, no. 83, pp. 1253–1260, 2016.

[10] M. Hinderdael, D. De Baere, M. Moonens, R. Vafadari, and P. Guillaume, "Effect of surface roughness on fatigue crack initiation in additive manufactured components with integrated capillary for shm application," in *Proceedings of the 35th Conference and the 29th Symposium of the International Committee on Aeronautical Fatigue and Structural Integrity*, pp. 1–9, June 2017.

[11] M. Hinderdael, Z. Jardon, D. De Baere, and P. Guillaume, "Effective structural health monitoring through the monitoring of pressurized capillaries in additive manufactured materials," in *Proceedings of the 9th European Workshop on Structural Health Monitoring (EWSHM)*, 2018.

With the exception of [5, 10], all these publications have been subjected to an international peer review.

Awards

[1] ASME SMASIS 2015 Best Student Paper Award. At *ASME 2015 Conference on Smart Materials, Adaptive Structures and Intelligent Systems (SMASIS 2015)*, 23 Sept 2015, Colorado Springs, CO, USA.

Chapter 1

Introduction

Additive manufacturing is an emerging manufacturing technology, which is more widely known under the popular term of 3D printing. Gaining momentum as a production technology for metallic functional parts, those parts' structural integrity must be ensured over the entire usage life. An integrated structural health monitoring system can continuously monitor the health of the component in service. A new integrated eSHM system was invented by the fruitful combination of the design freedom offered by additive manufacturing and the improved safety by integrating a structural health monitoring system. This thesis explores the opportunities the eSHM system offers as a monitoring system for additive manufacturing components. This chapter gives a short introduction to the subject of additive manufacturing and structural health monitoring. The research topic will be defined and the objectives of this thesis will be formulated. The chapter will be concluded with an outline of the thesis.

1.1 Research context

On April 21st, 2012, The Economist called Additive Manufacturing (AM) to be the “Third Industrial Revolution” (TIR). The digitisation of manufacturing will transform the way goods are made, they claimed [1]. Only one month earlier, The Huffington Post said that the TIR will allow everyone to become their own manufacturer. The process is called 3-D printing and although it sounds like science fiction, it is already coming online, and promises to change the entire way we think of industrial production [2]. AM is a hype. And as with all hypes, AM is believed to be very promising, but many challenges remain to be tackled before mass adoption will be achieved. The Gartner Hype Cycle for AM in 2014 (see Figure 1.1 taken from [3]) indicated that at the beginning of this PhD thesis, 3D printing was mostly adopted as a prototyping methodology. Industrial 3D (metal) printing was very promising but not yet adopted. During the course of this PhD work, the use of AM has exploded and by the end of 2017, many applications of AM are actively used in the industry (see Figure 1.2 taken from [4]). However, the use of AM in very demanding industries such as Aerospace and Defense has shown to go through the “Trough of Disillusionment”. The current lack of process knowledge and the lack of a proper closed-loop process control system currently results in material imperfections that are unacceptable for use in safety critical applications. Especially the fatigue properties of additively manufactured metals are inferior to conventionally produced metals. Inspection intervals must then be shortened, increasing inspection costs and system unavailability, which inevitably induce large economic losses. The promisingness of metal AM enabling weight gains through topology optimization and allowing function integration, has made place for the disillusion that the technology still has to mature.

Within the context of this disillusion of the metal AM process for functional part production, our research group at the Vrije Universiteit Brussel realized that the AM community would benefit from an online inspection principle for metal AM components in service. Fatigue cracks will be detected by the integrated system before failure of the component. The embedded monitoring system continuously inspects the structural integrity of the component and serves as an on-board inspection system. Such a system is generally called a structural health monitoring system, commonly abbreviated as a SHM system. In the particular case for the application of the monitoring of AM components, the system developed by the Vrije Universiteit Brussel was named “effective Structural Health Monitoring system”,

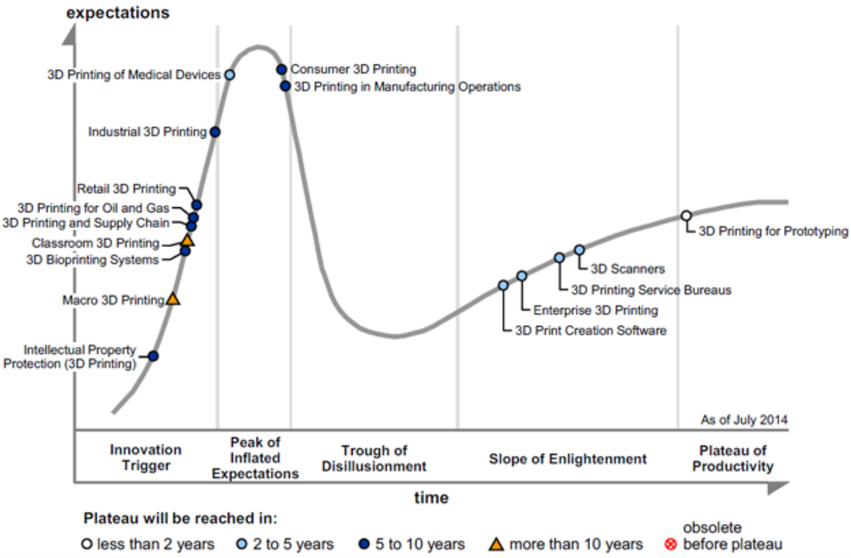

Figure 1.1: *Gartner Hype Cycle for 3D printing as of July 2014.*

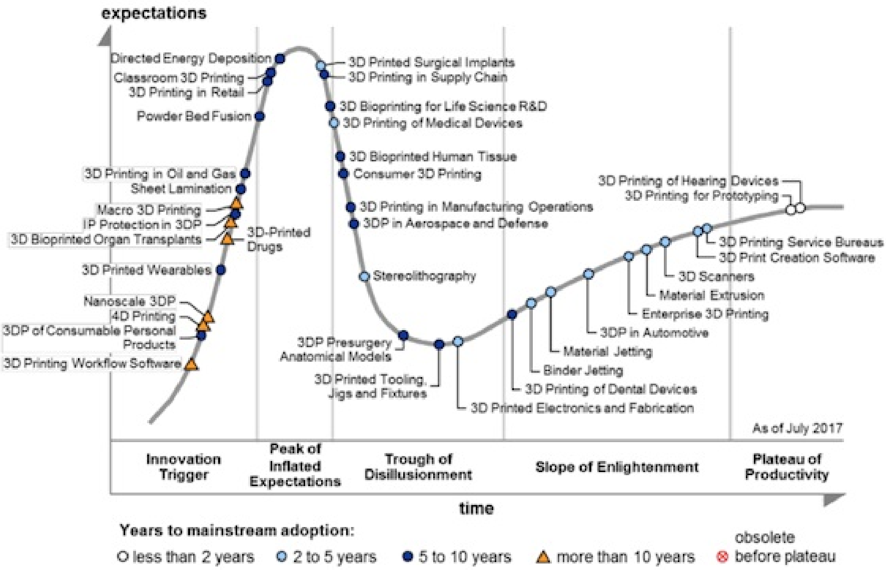

Figure 1.2: *Gartner Hype Cycle for 3D printing as of July 2017.*

shortly abbreviated as the "eSHM system". Small subsurface capillaries are embedded in the structure by means of AM techniques, close to the region where fatigue cracks are expected to initiate. A cogwheel equipped with the eSHM system is presented in Figure 1.3. The embedded capillaries are highlighted in red. A pressure sensor is externally installed to the capillary end. The capillaries are then pressurized (vacuum or overpressure) and the capillary pressure is continuously monitored during the operation of the component. A crack, that initiated at the surface of the component, propagates through the material till it breaches the capillary. The resulting leak alters the internal capillary pressure which is detected by the pressure sensor. The fatigue crack is detected when the capillary pressure bypasses a preset detection limit (indicated by the dashed red line in Figure 1.3 (right)).

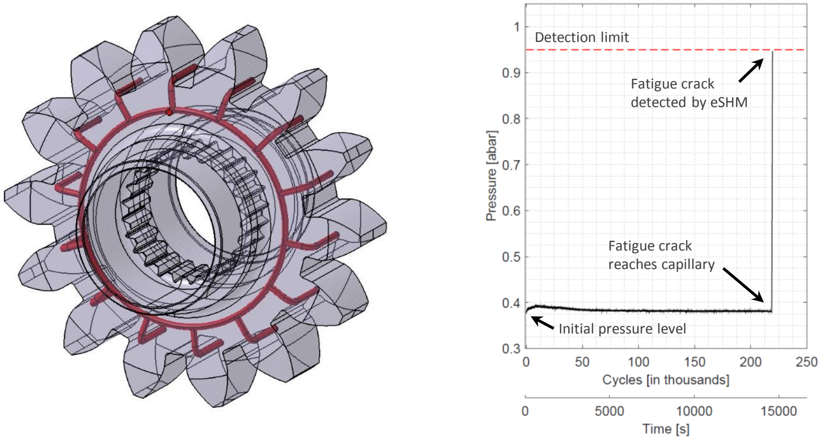

Figure 1.3: Embedded capillaries (in red) of the effective Structural Health Monitoring System (eSHM) integrated in an AM cogwheel and an actual measurement of the eSHM system.

AM is undoubtedly capable of generating smart materials with integrated functionality that allow continuous monitoring of the component. The embedded capillaries of the eSHM not only allow the monitoring of fatigue cracks, but also allow deriving the loads acting on the component. When adequately positioned, the integrated capillaries deform under the loads acting on the component. The deformation of the capillary, in turn, alters the pressure inside the capillary. Using this principle, the eSHM system can be used to measure the loads throughout the operational lifetime of the component and derive the expected damage thereof. This principle is called Usage Monitoring (UM) and can be seen as an indirect way of evaluating the potential damage a structure may have accumulated.

The embedded eSHM system can be used both for fatigue crack detection (SHM) as well as for the continuous evaluation of the loads acting on the structure (UM). It is the main research topic of this thesis to further explore and develop the opportunities the eSHM system offers.

1.2 Techniques and technologies

1.2.1 Additive Manufacturing

According to the ASTM standard [5], AM is defined as the process of joining materials to make objects from 3D model data, usually layer upon layer, as opposed to subtractive manufacturing methodologies. Conventional subtractive manufacturing technologies, such as drilling, milling, grinding, etc. start from an initial block of raw material from which, after multiple operations, material is removed to obtain the required shape corresponding to the proposed design. Those operations require that a tool can reach the spot that has to be shaped, which is not always possible. The production cost increases when the design is more complex and more operations are required to obtain the desired shape. With AM, the process of creating objects is inverted. Usually starting from a base plate, material is added according to the design presented in the 3D model data. Layer after layer, material is deposited where it is required. This different approach of creating objects results in many advantages. The design freedom is one of the most important ones. AM allows creating complex shapes at almost no additional cost which would otherwise be impossible or extremely expensive to produce. The cost is related to the amount of printed material, not to the complexity of the design. As the tendency exists to produce components at the lowest possible cost, there even exists a stimulus to reduce the weight of 3D printed components, which is a clear benefit in several sectors such as aerospace. Using AM technology, General Electric (GE) optimized the fuel injector of the Leap jet engine (Figure 1.4 taken from [6]) which is 25% lighter, 5 times more durable and consists of only a single piece instead of an assembbly of 20 different parts (see Figure 1.4 a)). This design freedom furthermore enables topology optimization (TO), a mathematical method that optimizes material layout within a given design space, for a given set of loads, boundary conditions and constraints

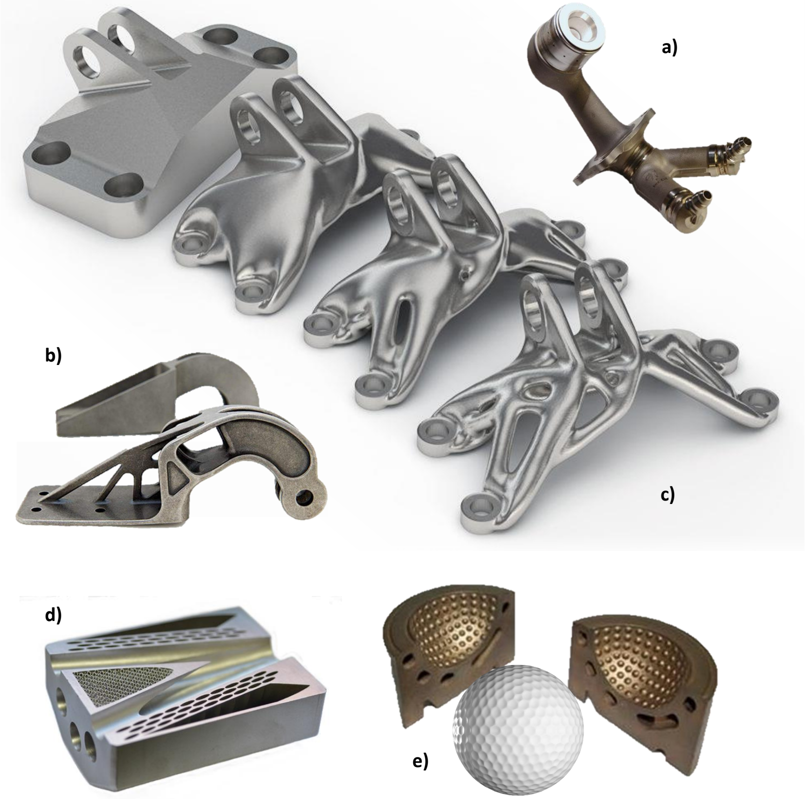

Figure 1.4: Additive Manufactured parts. a) Fuel injector of GE's LEAP jet engine, b) Nacelle hinge bracket of the Airbus A320, c) Different stages of a topology optimization study, d) Nozzle with internal cooling channels and e) Golf ball mould with integrated conformal cooling channels.

with the goal of maximizing the performance of the system. One such a maximization of performance is often weight reduction. The nacelle hinge bracket of the Airbus A320, depicted in Figure 1.4 (Figure taken from [7]) b), was topology optimized and produced using metal AM technologies. As opposed to conventional subtractive manufacturing technologies, such a persevering weight optimization does not increase production costs, but even reduces them since less material is to be deposited (see Figure 1.4 c) taken from [8]). Function integration is another benefit of using AM. Due to its layerwise addition of material, additional functions can be integrated on the inside of the component. One such example is the direct integration of cooling channels inside a fuel nozzle (see Figure 1.4 d) taken from [9]) and conformal cooling channels in moulds and mould inserts (see Figure 1.4 e) taken from [10]) in a more efficient way.

AM process chain

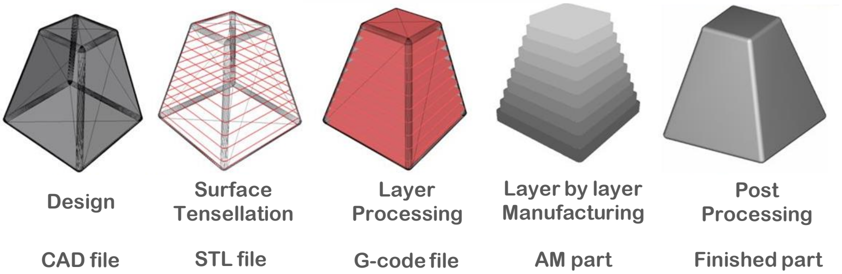

Figure 1.5: AM process chain

The general AM process chain is outlined in Figure 1.5. The 3D model data, usually in the form of a Computer Aided Design (CAD) file, is virtually created by the designer and is the end product of the 3D modelling process. The CAD file is a volumetric representation of the part to be manufactured. Although some metal AM printing companies have developed a solution to skip the generation of a Surface Tessellation Language (STL) file, generally the CAD is converted to an STL file format. An STL file describes only the surface geometry of a three-dimensional object without any representation of color, texture or other common CAD model attributes. The STL file is then sliced, the process of dividing the part into multiple layers one upon the other. Each such layer represents the two dimensional outline of a cross section of the component at a particular height. The AM software then processes the geometry of each layer and defines the path the AM tool will follow to create the desired shape. The outcome of this process is the G-code, the machine code, that will be sent to the AM machine. Starting from the bottom layer, the AM tool will follow the path defined in the G-code and deposit material along its way across the layer. After completion of the first layer, the build platform is lowered by one layer thickness. The AM tool now scans the path defined in the second layer. The platform is again lowered and the same procedure is repeated till the build is completed. A 3D object is created according to the design defined in the CAD file. Post processing is often required in order to improve the mechanical or surface properties of the additively manufactured part. The exact process of the addition of material depends on the actual AM technology that is considered and the type of material that has to be deposited. The following section will detail the most common AM technologies that exist nowadays. The discussions on the technologies that were used in this thesis are elaborated afterwards.

AM Technologies

Back in the 1980s, Stereolithography (SLA) was developed as the first AM technology. Since then, numerous AM processes have been developed and different material types can now be additively manufactured. A complete list of commercially available AM technologies is given on the following pages.

Vat photopolymerization AM techniques are based on the solidification of a resin in a basin on the basis of the exposure to light coming from a laser, a projector or a Light-Emitting Diode (LED). Vat photopolymerization is used to create polymer parts. **Material extrusion**, also known as Fused Deposition Modelling (FDM), is the most widely adopted AM technology nowadays. Currently being the most affordable AM technology, many hobbyists can afford one for AM prototyping in polymers. The material that is to be deposited is a thermoplast that is extruded through a heated nozzle. Also 3D printed composite material can be created by integrating fibre material inside the deposited tracks (the matrix). **Material jetting** is a 3D printing process based on the solidification of ink droplets by an inkjet print head, very similar to the well known 2D paper printing. The solidification of the ink droplets is based on ultraviolet (UV) light or heat and can create parts in both polymer, metal and wax material. **Binder jet** is an AM technique in which a liquid binding agent is selectively deposited to join powder particles of a powder bed. Similarly, yet different, **Powder Bed Fusion** (PBF) technologies use a bonding agent or an energy source (such as a laser or electron beam) to fuse the powder particles of the powder. As opposed to binder jetting, the powder particles are fused instead of joined. **Direct Energy Deposition** (DED) locally heats the substrate material to create a melt pool in which metal (powder or wire) is added. A last category of AM technologies consist in the layerwise addition of material already in sheet form, named **Sheet lamination**. Depending on the material type, a gluing agent (paper and composites) or the heat of ultrasonic friction is used to join the stacked sheets.

Many AM technologies were used throughout this thesis work. Fused Deposition Modelling (FDM) and Stereolithography (SLA) were mainly used as a prototyping technology for the production of low-cost tensile test specimens with integrated capillaries. During a tensile test, the pressure change resulting from the capillary deformation is evaluated, proving the concept of UM on the basis of the eSHM system. These polymer test specimens were thus mainly used for the proof-of-concept studies of the UM principle on basis of the eSHM system. The availability of multiple Ultimaker 2+ and a Stratasys Dimension 768 FDM 3D printers at the Department of Mechanical Engineering (MECH) of the Vrije Universiteit Brussel made it the most affordable and fastest way of testing initial concepts. As the principle of the eSHM is based on the pressure build up inside embedded capillaries, air- and watertightness of the 3D printed parts was crucial for the well functioning of the prototype. Fused Deposition Modelling (FDM) generally does not create air-and watertight parts. Small air gaps remain present in between the tracks and layers. A cumbersome post process involving acetone vapour was required to blend together adjacent tracks and layers. Stereolithography (SLA) immediately creates air- and watertight parts and was therefore considered as a second technology for the creation of functional polymer prototypes.

ADDITIVE MANUFACTURING TECHNOLOGIES

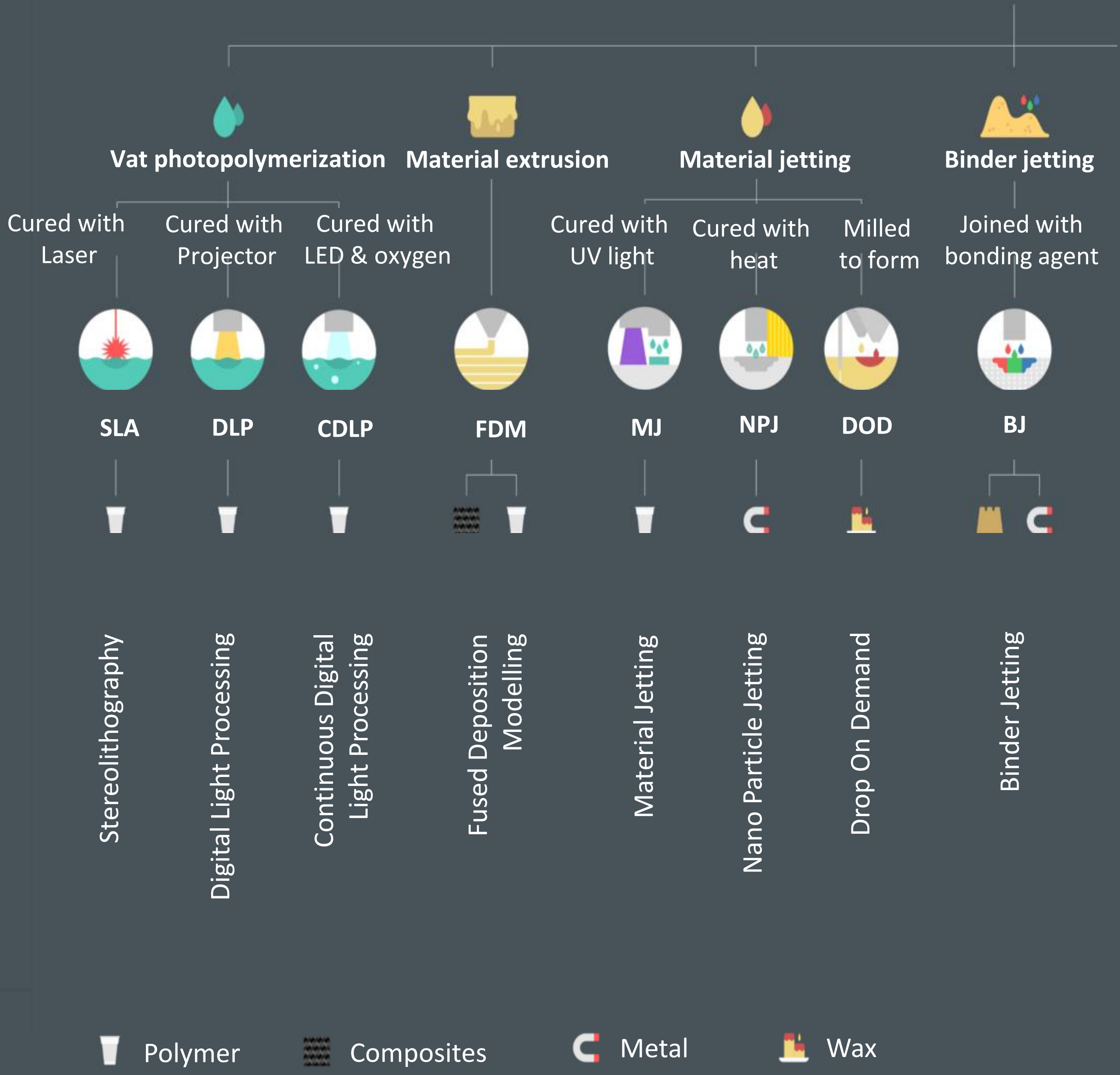

Vat photopolymerization

Cured with Laser

Cured with Projector

Cured with LED & oxygen

Material extrusion

Material jetting

Cured with UV light

Cured with heat

Milled to form

Binder jetting

Joined with bonding agent

SLA **DLP** **CDLP** **FDM** **MJ** **NPJ** **DOD** **BJ**

Stereolithography

Digital Light Processing

Continuous Digital Light Processing

Fused Deposition Modelling

Material Jetting

Nano Particle Jetting

Drop On Demand

Binder Jetting

Polymer

Composites

Metal

Wax

3D HUBS

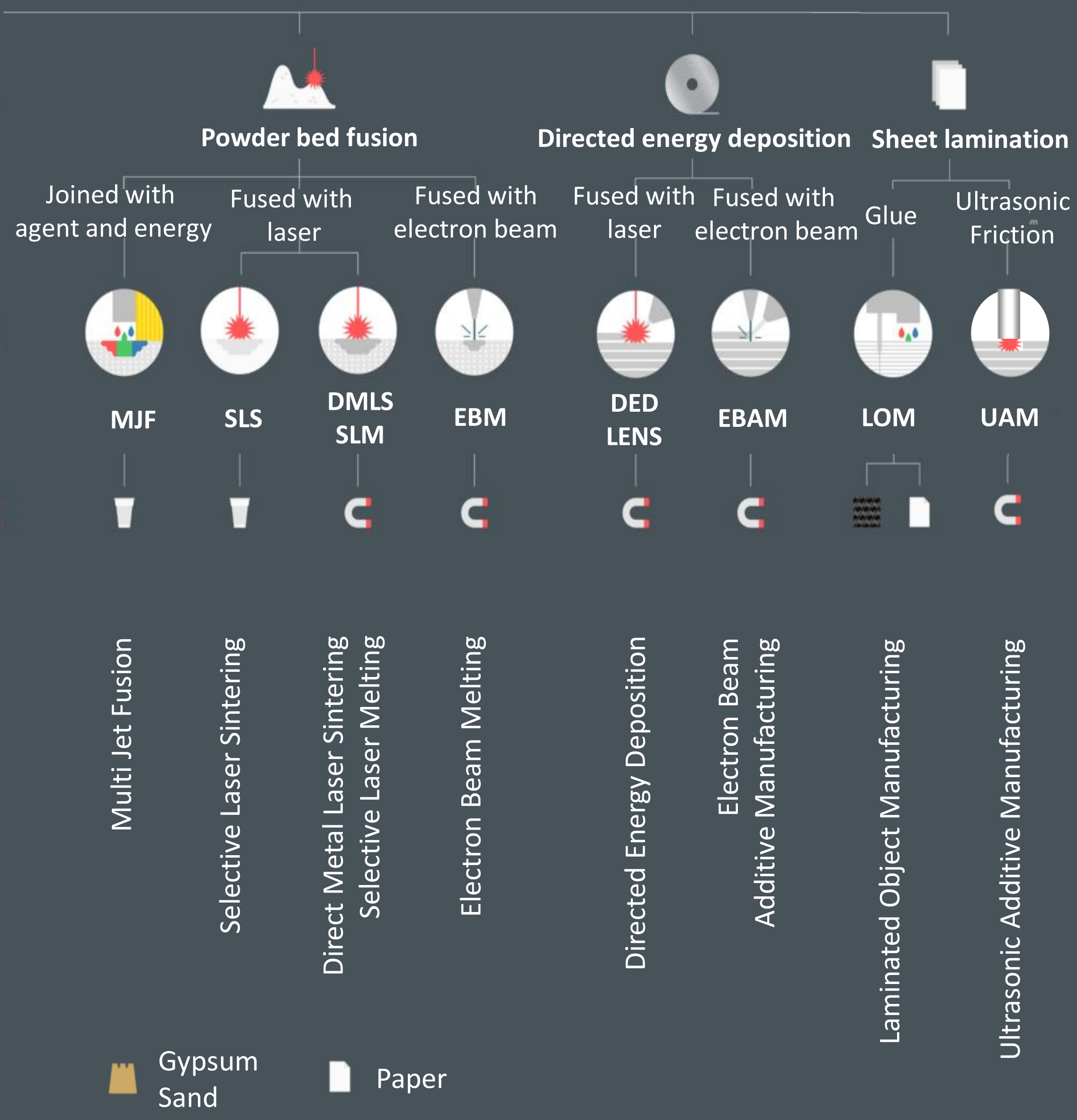
Powder bed fusion
Directed energy deposition
Sheet lamination
Joined with agent and energy
Fused with laser
Fused with electron beam
Fused with laser
Fused with electron beam
Glue
Ultrasonic Friction
MJF
SLS
DMLS SLM
EBM
DED LENS
EBAM
LOM
UAM
Multi Jet Fusion
Selective Laser Sintering
Direct Metal Laser Sintering
Selective Laser Melting
Electron Beam Melting
Directed Energy Deposition
Electron Beam Additive Manufacturing
Laminated Object Manufacturing
Ultrasonic Additive Manufacturing
Gypsum Sand
Paper

Both laser based Powder Bed Fusion (PBF) and laser based Directed Energy Deposition (DED) were used throughout this thesis for the creation of solid metallic components. Because of their different nature, both technologies were used for the production of test specimens in different test campaigns. Powder Bed Fusion (PBF) is the geometrically more accurate technology, capable of creating smaller capillaries but leaving higher amounts of material imperfections and thermal stresses inside the material. For those metallic functional prototypes that were not used for fatigue tests, laser based PBF was considered since it is geometrically more accurate, widely available in the industry and a thermal treatment solves the issue of residual stresses. Laser based DED on the other hand creates better quality material with less imperfections and a smaller heat affected zone, but is dimensionnaly less accurate. Being the principal focus of our research group, laser based DED was used for the production of four point bending fatigue test specimens with integrated capillaries. These test specimens were produced to proof the concept of detecting fatigue cracks by the eSHM system. A more detailed discussion on the state-of-the art of the technologies used throughout this work will be provided in Chapter 2.

1.2.2 Structural Health and Usage Monitoring

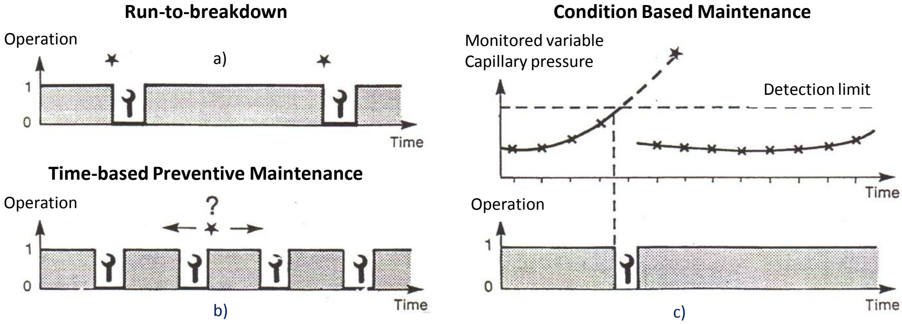

Figure 1.6: SHM is a form of Condition Based Maintenance. The star indicates a component failure. a) Run-to-breakdown: no inspections are performed and structure is operated till failure. b) Time-based Preventive Maintenance: Inspections are performed on the basis of operational time without actual necessity for inspection/repair. c) Condition Based Maintenance: A selected variable informs maintenance personnel that an inspection/repair is necessary to avoid breakdown.

Maintenance inspections keep a system running and enhance the safety of people and that of the machine. Three main maintenance philosophies exist, i.e. Run-to-breakdown, Time-based Preventive Maintenance and Condition Based Maintenance (CBM). When adopting a Run-to-breakdown approach, systems are operated till failure, without the adoption of any preventive inspection or repair (see Figure 1.6 a)). Although the system is operated uninterrupted, the damage caused by the failure may end up more costly since joint systems may also suffer damage from such an unexpected failure. Major damage and economic losses due to an unscheduled breakdown, as well as safety issues arise from this methodology. Time-based preventive maintenance is therefore adopted by a majority of the industries. Based on experience gained, periodic inspections are carried out to ensure the system can safely operate till the next scheduled inspection (see Figure 1.6 b)). If damage is observed which may lead to a premature failure of the component, the component is replaced. Although this methodology enhances safety and largely omits unexpected failures, it leaves the maintenance personnel with a lot of unnecessary inspections and system occupancy which induce production losses. Although such a methodology reduces the risk of a failure below a predetermined level, it does not guarantee that failures will not occur. This is mainly a consequence of the generalization of the system and its usage. A system may unexpectedly be overloaded, components may show unusual weaknesses, loads may not be according to the design, etc. which still leads to failures within an inspection interval.

The ultimate solution would be an inspection methodology that is based on the actual response of the system. By means of online, continuous inspections on the system, information is gained about the current status of the system. Repairs are postponed until the system approaches its end-of-life. Such a methodology is called Condition Based Maintenance (CBM) (see Figure 1.6 c)). Besides the general benefit of enhanced safety and plant availability, the adoption of a CBM methodology furthermore plays a major role for inspections in hazardous, potentially dangerous situations such as in nuclear reactors. Continuous inspections can be carried out without the direct involvement of maintenance personnel. In applications such as aviation and aerospace, the implementation of a CBM methodology furthermore enables weight gains for components at inaccessible places that cannot frequently be inspected and would otherwise be largely overdimensioned as a risk mitigation solution (see SHM of the second generation according to Airbus in Figure 2.8 [11]).

The adoption of a CBM philosophy requires the determination of at least one variable which is to be followed throughout the system's operational lifetime. This variable can be a global parameter (e.g. vibration levels of rotary machinery) or a local parameter (e.g. fatigue crack detection at a fatigue hot-spot). Depending on the type of variable that is selected and the information that is extracted thereof, the CBM methodologies are divided into three main categories: Vibration-based Condition Monitoring, Usage Monitoring and Structural Health Monitoring.

Condition Monitoring

Within the group of the CBM methodologies, the Condition Monitoring is the most widely adopted. Vibration-based Condition Monitoring interrogates the global response of the system, typically applied as a vibration or noise measurement on rotary machinery [12]. Under comparable operating conditions, the component can be expected to behave comparable and vibration levels are expected to remain unchanged. However, in the case damage grows or boundary condition alter (e.g. a defect bearing), vibration levels will change and damage can be identified on the basis of the vibration signature. Oil systems are furthermore inspected using a filtering system, capable of deriving extensive wear down.

Usage Monitoring

Usage Monitoring (UM) is based on the monitoring of the loads acting on the component under investigation. Rather than the direct monitoring of damage, this philosophy is based on the belief that the damage can be estimated on the basis of the load history on the component. It is one way to tackle the issue that damage is a local phenomenon while a monitoring strategy rather monitors a system as a whole. If the region where the damage is expected is not a priori known, it is difficult to catch the local phenomena of a growing crack without distributing enormous amounts of sensors all across the component. Components are furthermore designed according to assumed design loads, but the loads may be different in practice. The principle of Usage Monitoring allows comparing the actual loads with the assumed design loads and allows the re-estimation of the remaining useful lifetime (RUL).

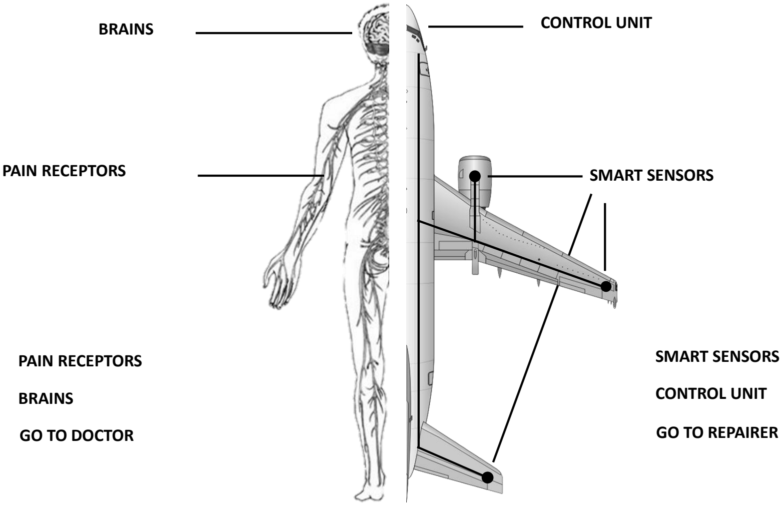

Figure 1.7: SHM resembles the human nervous system. Smart sensors record damaging conditions of a structure and report to the control unit, just as the pain receptors sent pain signals to the human brain.

Structural Health Monitoring

SHM is defined as the integration of sensing and possibly also actuation devices to allow the damaging conditions of a structure to be recorded, analyzed, localized and predicted in a way that non-destructive testing (NDT) becomes an integral part of the structure [13]. In other words and similarly to our human nervous system, SHM is used to detect local damage. SHM is a network of smart sensors distributed across a structure or machine, each providing insight about the presence of local damage to that part of the structure or machine, just as pain receptors all across our body detect damage/pain and inform our brain thereof. SHM resembles to the human nervous network as is clear from Figure 1.7. Likewise the human brain, the control unit of the SHM system receives all signals and coordinates the actions to be taken. The system alarms when a damaging condition is detected and further, more in-depth, investigations are required. The ultimate outcome of the automated SHM system is, besides the detection of the damage, the evaluation of the severity of the damage, the retrieval of the location of the damage and a prediction of the remaining useful lifetime (RUL) of the component.

Many SHM systems are being developed and have proven to be successful in laboratory conditions, but practical implementations of SHM remain limited. Most of the SHM principles are not robust and fail because of environmental influences, dirt and grease, weak signals in a noisy environment, accidental damages, etc. To be successful, an SHM system must be robust and unaffected by the environment. It is especially therefore, and with the knowledge of weak fatigue properties of additively manufactured materials, that the Vrije Universiteit Brussel has developed an embedded SHM strategy for AM components. The effective SHM was developed to be a robust way of detecting fatigue cracks in additively manufactured components.

1.2.3 The effective Structural Health Monitoring system

To be successful in real applications, the SHM system must be robust and uninfluenced by environmental influences. Ultimately, the SHM must be incorporated into the component and cut off from the world. The design freedom offered by AM techniques allows smart designs with integrated functionalities. Integrating a SHM system inside additively manufactured components allows continuous inspection and enables safe operation of AM components, of which the operation is otherwise uncertain because of the fatigue issues related to AM material. As SHM benefits from the design freedom enabled by AM technologies, so does AM benefit from the continuous inspections performed by the integrated SHM system. This very strong interaction between AM and SHM led to the idea of developing an SHM methodology particularly suitable for AM components and which should, to the benefit of AM, help introducing AM easier into the market.

The idea of the eSHM system is based on the integration of small pressurized capillaries inside the AM component. The capillary is pressurized at a pressure different than that of the atmosphere and sealed by an externally mounted pressure sensor. The pressure remains at its initial level if no damage is present. However, when a (surface) fatigue crack reaches the capillary, a leak flow will originate and equalize the pressure inside the capillary with that of the outside atmosphere. The capillary pressure is continuously monitored and a pressure deviation is an indication of the presence of a fatigue crack. When the capillary pressure exceeds a preset limit, the SHM has detected a fatigue crack and a more elaborated inspection can be performed if required. In order to be effective, the capillaries of the eSHM system must be located close to the fatigue hot-spots, the regions where fatigue cracks are expected to initiate. This is a challenging design requirement, since the presence of the capillary may not influence the fatigue performance of the component. As part of this thesis work, four point bending fatigue tests are performed and the fracture surface was analysed in order to retrieve the fatigue initiation location to determine the effect of the capillary surface roughness on the fatigue performance.

Embedding the capillary in a way that it connects all locations prone to fatigue allows monitoring the critical areas without the need for multiple sensing devices. In the example of the cogwheel of Figure 1.3, only one pressure measurement is required to inspect all teeth. This largely facilitates the installation, data storage and post-processing of the data of the eSHM system. After detection of a fatigue crack, further analysis may be be performed on the critical area. It is therefore interesting to know, on the basis of the pressure measurement, where the cracked region is located (e.g. which tooth of the cogwheel suffers from a crack) and what size the crack has. A major part of this thesis is therefore devoted to the crack localization and crack size estimation of a crack inside the component. This was mainly modelled as a leak inside tubes/capillaries. A similar approach to pipeline leak detection techniques was used.

The initial pressure level remains unchanged as long as no fatigue crack is present. At least, the average pressure level remains intact and equal to the initial pressure level. Small pressure fluctuations inside the capillary are present as a consequence of the loads acting on the component. The deformation of the component and consequently the deformation of the integrated capillaries give rise to pressure fluctuations inside the capillary. This principle can be used to estimate the loads acting on the structure or component. A third facet of this thesis will be devoted to the exploration of the possibilities of eSHM in terms of usage monitoring, both for gaseous (compressible) and liquid (incompressible) media inside the capillary.

1.3 Objectives and outline of the thesis

The main goal of this thesis is the development of the eSHM and discovering the opportunities that it offers. According to Farrar and Lieven [14, 15], a SHM must be capable of (a) detecting the damage in a structure, (b) localizing the damage, (c) identifying the damage type, (d) quantifying the damage severity and (e) prognosing the remaining useful life (RUL) of the structure. These objectives were used as the guideline for the development of the eSHM system.

Back in April 2016, Maria Strantza defended her doctoral thesis called "Additive Manufacturing as a Tool for Structural Health Monitoring of Metallic Structures" [16]. She presented the initial proof-of-concept of the eSHM system capable of detecting fatigue cracks during four point bending fatigue testing. She furthermore investigated AM material properties and crack propagation. The research presented in this thesis can be seen as a continuation of the research presented by Strantza. The following four main research topics are extensively investigated within this thesis:

- Investigate the influence of the presence of a capillary on the fatigue performance of four point bending fatigue specimens. Special attention is paid to the importance of the capillary surface roughness and capillary location.
- Estimate the size of the crack on the basis of the pressure measurements of the eSHM system inside a leaking capillary.
- Localize the crack on the basis of the pressure measurements of the eSHM inside a leaking capillary.
- Utilize the eSHM system to determine the deformation of and the loads acting on a structure or component.

After this short introduction to the subjects of AM, SHM and the presentation of the eSHM principle, Chapter 2 will further introduce the reader to these subjects with a state-of-the-art on the basis of a literature review.

In Chapter 3, the fatigue performance of AM components with the integrated capillary of the eSHM system are analysed. Both conventional and AM specimens were tested using four point bending fatigue tests. The influence of the capillary surface roughness and capillary location on the fatigue initiation location and fatigue life are discussed.

Chapter 4 then presents two methods to determine the size of the crack. A first method is based on modelling the capillary pressure increase and thereby predicting the leak flow and leak size. A second, analytical model, was derived for the determination of the amplitude of Negative Pressure Waves. These pressure waves originate when a leak opens. Their amplitude is related to the size of the leak.

Chapter 5 presents a crack localization principle based on the difference in time-of-arrival of the Negative Pressure Waves at either end of the capillary. The feasibility to localize the leak with high accuracy will be demonstrated first on a larger scale test setup with tubes and secondly on a setup using capillaries. The effect of bends in the capillary will be analysed and a principle will be demonstrated allowing to locate the leak even with a single pressure sensor.

Chapter 6 present the proof-of-concept studies of the eSHM as a Usage Monitoring system. The capillary pressure change to externally applied tensile and compression strain will be analyzed for both polymer and steel tensile test specimens. By varying the Poisson coefficient of the material and the bulk modulus of the fluid inside the capillary, the sensitivity of the system can be changed. Also the thermal influence on the capillary pressure is investigated.

Chapter 2

Literature review

This chapter starts with an in-depth description of the fatigue phenomenon, the phenomenon that currently limits the use of AM components. A second part of this chapter will be devoted to the history and state-of-the-art of SHM and UM in the industry and recent developments of SHM combined with AM. The state-of-art of the eSHM at the start of this PhD will be presented. A third section will detail the AM processes used throughout this work and will present how the process parameters influence static and fatigue properties.

2.1 Fatigue

At least half of all mechanical failures are due to fatigue. No exact percentage is available, but many books and articles have suggested that 50 to 90 percent of all mechanical failures are fatigue failures; most of these failures are unexpected [17]. According to the ASTM E 1150 standard, fatigue is defined as the process of the progressive localized permanent structural damage occuring in a material subjected to conditions that produce fluctuating stresses and strains at some point or points and that may culminate in cracks or complete fracture after a sufficient number of fluctuations. Metal fatigue cracks initiate and propagate in regions where the strain is most severe. [18].

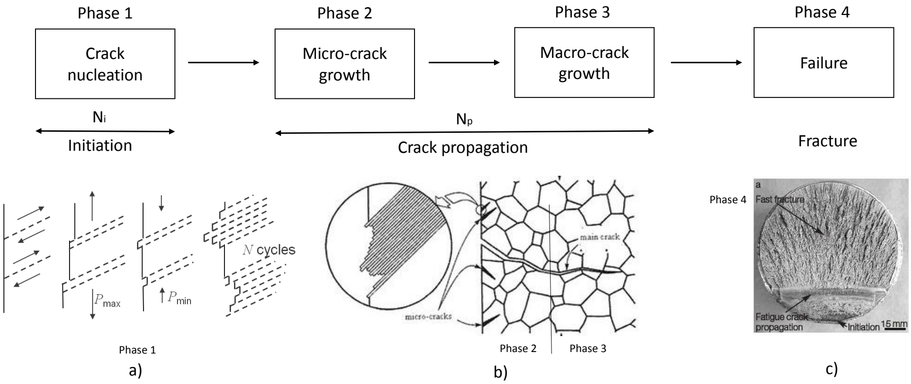

Figure 2.1: The process of fatigue consists of four main phases. a) Fatigue initiation involves the creation of persistent slip bands b) The crack propagation phases with micro crack propagation in line with the slip band and macro crack propagation across grains perpendicular to the load direction and c) Final rapid fracture.

The process of fatigue consists of four main phases: the crack initiation phase, the micro crack propagation, macro crack progagation phase and the final but sudden fracture of the remaining cross section. Fatigue initiation is a very complex phenomenon, yet not fully understood and still not predictable. The crack generally results from dislocation pile-ups and imperfections such as surface roughness, voids, scratches, etc. From a materials science perspective, the fatigue initiation process involves a dislocation movement in a slip band when the load is applied (Figure 2.1 a) taken from [19]). The alternation of the load direction may result in the return of the slip band, but this generally happens in an adjacent slip plane. It is believed that the exposed protruding part of the first slip movement immediately oxidices and the addition of oxygen counteracts the slip return in the same plane. Slip is forced in another, adjacent slip plane in the other direction. This leads to protrusions and intrusions on the surface, creating persistant slip planes and ultimately leading to the formation of a micro crack that propagates in the direction of the initial slip plane within one grain (see Figure 2.1 b) adapted from [20,21]). The micro crack then propagates very slowly in the direction of the slip band. The crack initiation and micro crack growth are shear driven. The macro crack phase starts when the crack has a substantial size and the propagation direction is no longer determined by the slip planes in individual grains, but propagation occurs perpendicular to the applied load. The macro-crack growth is tension driven. The crack propagation is now faster but well predictable by a power law:

$$\frac{da}{dN} = f(\Delta K, R_i, H) \tag{2.1}$$

with $\Delta K = K_{max} - K_{min}$ the stress intensity range, $R_i = {}^{K_{min}}/_{K_{max}}$ the stress intensity ratio and H the stress history. The Paris Law is usually used to predict the crack growth per stress cycle ${}^{da}/_{dN}$ as a function of the stress intensity range ΔK. The law is expressed as:

$$\frac{da}{dN} = C_{PL} \Delta K^{m_{PL}} \tag{2.2}$$

where C_{PL} and m_{PL} are material parameters. Each such Paris Law expression is thus material dependent and applicable for one stress ratio R_i and stress history H. With stress history it is meant previous loadings, internal residual stresses, etc. The region in which the Paris Law is valid is highlighted in Figure 2.2 a) (Figure adapted from [22]). Fatigue striations, the fracture surface markings indicating the crack growth in each stress cycle, are equidistant with a distance 'a'. With typical values of ${}^{da}/_{dN} = 10^{-3} - 10^{-6}$ ${}^{\text{mm}}/_{\text{cycle}}$, striations only become visible with a Scanning Electron Microscope (SEM) at magnifications beyond x1000, as shown in Figure 2.2 b) and Figure 2.6 d).

Integration of the Paris Law over the crack length yields the crack propagation life N_p of a structural component:

$$N_p = \int_{a_0}^{a} \frac{da}{C_{PL} \Delta K^{m_{PL}}} \tag{2.3}$$

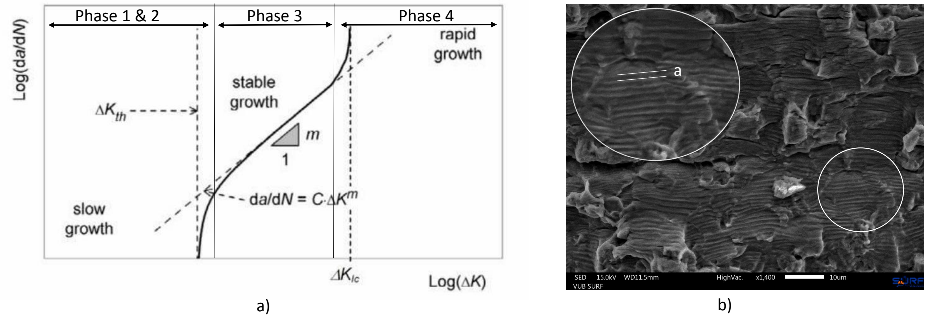

a) b)

Figure 2.2: The Paris Law predicts the crack propagation speed during the macro crack propagation phase. a) The Paris Law is only valid in Phase 3 of the fatigue process and b) Fatigue striations on the fracture surface of mill annealed Ti-6Al-4V.

To solve the integral, the evolution of ΔK in function of the crack length a must be known. In Linear Elastic Fracture Mechanics (LEFM), ΔK can be expressed as:

$$\Delta K = Y \Delta\sigma \sqrt{\pi a} \tag{2.4}$$

where Y is the product of various multipliers accounting for the geometry of the crack and the geometry of the cracked body, $\Delta\sigma$ for the applied cyclic stress range. The crack propagation life (N_p) is thus a function of the applied cyclic stress range $\Delta\sigma$.

S-N Curve

The total amount of cycles resisted by the material (N_f) equals the sum of the cycles in the crack initiation phase (N_i) and the cycles in the crack propagation phases (N_p) till final rupture:

$$N_f = N_i + N_p \tag{2.5}$$

The majority of the life of a fatigue specimen is spent in the initiation phase [23]. But since the amount of cycles till crack nucleation (N_i) is hard to predict, they are often omitted from the equation as an extra safety margin. The total amount of fatigue cycles resisted by the material is a function of the stress level applied. The higher the stress level, the lower

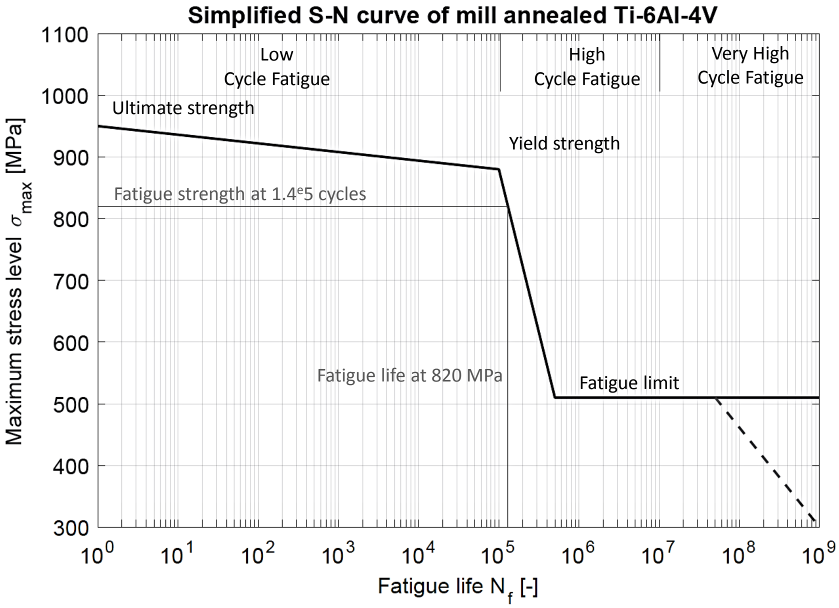

Figure 2.3: A simplified S-N curve for mill annealed Ti-6Al-4V for a stress ratio of R=0.1.

the fatigue life. This behaviour is generally described by a Stress-Cycle ($S-N$) curve and serves as the basis for fatigue design. Figure 2.3 shows a typical S-N curve applied to data of mill annealed Ti-6Al-4V. The x axis presents the fatigue life N_f. The y axis can be expressed in either the stress amplitude $\Delta\sigma$ or the maximum stress level σ_{max}.

The S-N curve presents the dynamic material properties. The left part of the S-N curve describes Low Cycle Fatigue (LCF) which involves macroplastic deformation in every cycle. The fatigue life in the LCF regime is generally limited to a few 10^4 cycles [24]. Starting from the left in Figure 2.3, the ultimate strength is the stress level at which the material fails, even when subjected to only one cycle. Therefore it is actually a static property. On the other side of the LCF regime, the High Cycle Regime (HCF) starts where maximum stress levels remain below the yield strength. The HCF regime presents the fatigue behaviour when no macro-plastic deformation occurs in a cycle. Fatigue lifes typically exceed 10^5 cycles up to 10^7 cycles [24]. The HCF is characterized by a power law (the linear decrease on a semilog plot in function of the fatigue life N_f, also called Wöhler line) followed by an asymptotic limit called the Fatigue Limit or Endurance Limit.

The Wohler line in the S-N curve is closely related to the power law describing crack propagation. For one stress ratio R_i, the higher the maximum stress, the higher the stress intensity range $\Delta K = f(\Delta\sigma)$ and the higher the crack propagation speed ${}^{da}\!/\!{}_{dN}$. The fatigue crack grows faster to its critical size and final fracture occurs sooner (lower N_f). The Fatigue Limit is the stress level below which no fatigue failure occurs. Microcracks may be initiated, but do not grow to macrocracks due to the barriers such as grain boundaries and therefore no fatigue failure will occur [24]. At least not within 10^7 cycles, which have long been the maximum fatigue lifes tested. With the development of newer test machines enabling fatigue testing at higher test frequencies, current research is focusing on the Very High Cycle Fatigue (VHCF) $10^7 > N_f > 10^9$ cycles [25–27] and even the Giga Cycle Fatigue (GCF) $N_f > 10^9$ cycles [28–30]. This research has shown that eventually fatigue still occurs, even below the Fatigue Limit, indicated as the dashed line in Figure 2.3.

Cumulative damage

Each point on the S-N curve indicates the fatigue life N_f of the material when loaded at one particular stress amplitude, a so-called constant amplitude (CA) test condition. Since most of the components in real-life applications are subjected to a variable amplitude (VA) load spectrum, it is still to be discussed how to evaluate the cumulated damage inside the material. Although its applicability is questioned [24], the most simple method for fatigue life predictions appears to be the Miner-rule: [24, 31].

$$\sum_{k=1}^{m} \frac{n_k}{N_k} < 1 \tag{2.6}$$

The stress amplitude range on the S-N curve is discretized and the load spectrum is analyzed to evaluate the amount of load cycles that have happened within each of these stress amplitude intervals. This discretisation is shown in Figure 2.4. In theory, the Miner rule then expresses that the sum of all relative lifes consumed remain below 1. However, many practical tests have shown large spreads from well below 1 to values significantly larger than 1 [24].

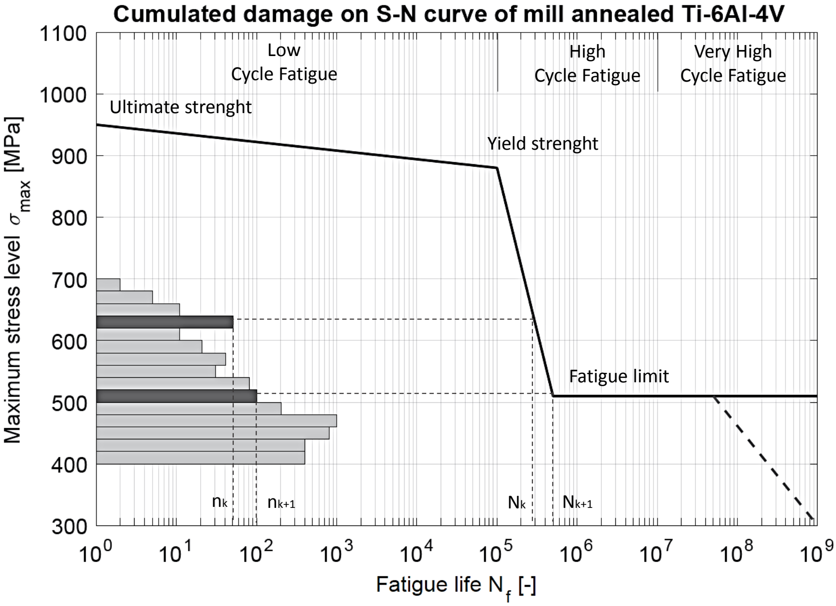

Figure 2.4: Cumulated damage on the simplified S-N curve of mill annealed Ti-6Al-4V

2.1.1 Fatigue testing

Fatigue performance of materials are compared using fatigue testing methods. Accelerated test methods, such as the staircase and step method, were developed to accelerate testing time. The standard fatigue test, the staircase method and step method are schematically represented on Figure 2.5.

Standard fatigue test The fatigue strength, and more specifically the determination of the fatigue limit of a material is determined on the basis of fatigue tests. The most straight-forward but most (time-)expensive form of a fatigue test is a constant amplitude (CA) test up to a maximum amount of cycles N_{max} which is limited by a maximum testing time and frequency. Each of the specimens is loaded at a different amplitude and the fatigue lifes of all samples are recorded and plotted on the S-N graph. Although this method requires many specimens and tests, it is a suitable method for the determination of the complete S-N curve. Specimens loaded beneath the fatigue limit will not provide any data except for the knowledge that the fatigue limit is higher. This method is therefore not optimized to find the fatigue limit of a certain material. Accelerated fatigue testing principles were developed in order to obtain an indication of the fatigue limit with very low amount of test samples to be tested.

Staircase method The staircase method starts with a stress level above or below the fatigue limit. The sample is subjected to a fixed amount of cycles N_{RO} that is expected to be large enough to fail the component, except if the stress level is below the fatigue limit (so-called Run Out). A first specimen is then tested and it either fails or survives the test. A second specimen is then tested at an increased stress level (in case the first sample survived) or a decreased stress level (in case the first sample failed). This method is repeated till the stress increase or decrease alters the fatigue test outcome, indicating that the fatigue limit must be in between the latter two stress levels. Further testing can be performed to lower the uncertainty interval.

Step method The step method is based on the same principle of repeated stress increments, but only one sample is required to obtain an indication of the fatigue limit. The sample is subjected to a fixed amount of cycles N_{RO} that is expected to be large enough to fail the component, except if the stress level is below the fatigue limit. The sample is loaded at an initial stress level, expected to be below the fatigue limit and failure may not occur. The stress amplitude is increased keeping the stress ratio constant and the same amount of cycles N_{RO} is again applied to the same test specimen. If failure does not occur, the same increment in the stress amplitude is applied and testing is continued till failure occurs in one of the steps. The stress level below which no fatigue failure occured is a good estimation of the fatigue limit of that specimen. This method has the advantage of accelerated testing and providing an indication of the fatigue limit of each specimen tested. The method also has drawbacks. The method is based on the idea that the cycles applied at lower stress levels, below the fatigue limit, do not influence the fatigue life. This is a dubious assumption. On the one hand, as it was pointed out earlier, microcracks may initiate at lower stress levels and fatigue response of the material may be different when previous cycles at lower stress levels were applied. The cumulated damage is expected to remain low as long as N_k in formula (2.6) remains high, possibly infinite in the presence of a fatigue limit. On the other hand, studies have indicated an improvement in high cycle fatigue

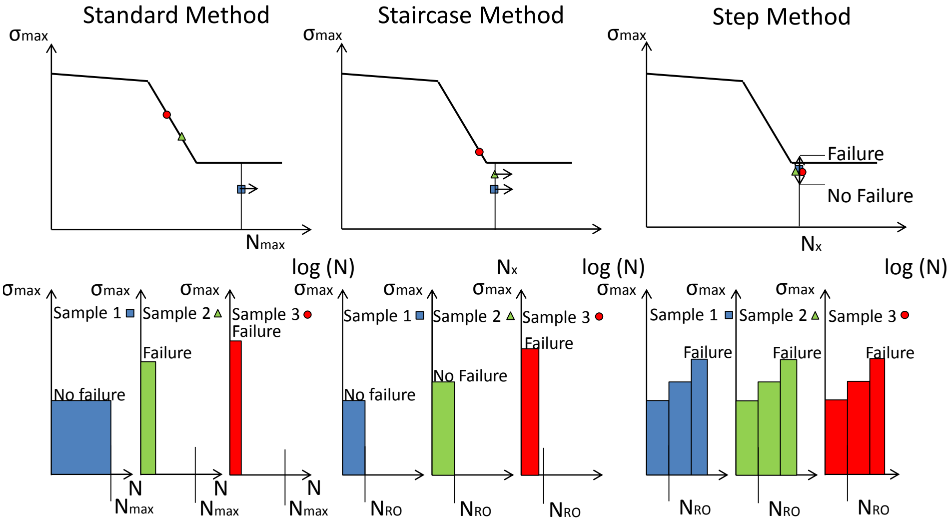

Figure 2.5: Cumulated damage on the simplified S-N curve of mill annealed Ti-6Al-4V

strength can be atributed to the gradually increased stress amplitude, usually starting below the fatigue limit. The latter phenomenon is called the coaxing effect [32–35]. However, the use of various stress amplitudes also has its advantages since practical applications are also subjected to various load conditions [36].

Generally, a sinusoidal load pattern is applied to the specimen with a stress amplitude related to the stress intensity range ΔK (see equation (2.4)):

$$\Delta\sigma = \frac{\sigma_{max} - \sigma_{min}}{2} \tag{2.7}$$

around a mean stress level σ_{mean}:

$$\sigma_{mean} = \frac{\sigma_{max} + \sigma_{min}}{2} \tag{2.8}$$

and with a stress ratio R_i equal to,

$$R_i = \frac{\sigma_{min}}{\sigma_{max}} = \frac{K_{min}}{K_{max}} \tag{2.9}$$

2.1.2 Fractographic analysis

Failures do happen. Even with regular inspections put in place and a specific design following the best design rules, unexpected failures do occur. The failure of a component is a valuable source of information since the fracture surface may tell the load history and failure origin. In materials science, fractographic analysis is the study of the fracture surface to determine the cause of a failure of an engineering structure. Such an analysis allows deriving whether the failure was caused by fatigue or a static overload, whether the failure originated from a material defect and more. A good understanding of the features on the fracture surface is critical for the determination of the failure cause and the localization of the fatigue crack initiation. Since for the puropose of this PhD only fatigue tests were performed, only the typical fatigue features will be discussed.

Faceted Surface Internal or subsurface cracks in titanium alloys, as a result of HCF loading, are found to initiate at facetted features, which can be seen on the fracture surface after failure. These facets are in fact fractured α grains, which have broken in a very planar manner [37]. Figure 2.6 b) presents facets on the fracture surface of a conventionally manufactured mill annealed Ti-6Al-4V specimen.

River markings The cleavage facets often show the presence of river marks. River marking is one of the main cleavage features and is usually observed within a grain. The branches of the river pattern join in the crack-propagation direction and can thus be used to find the fracture direction [38]. Although river markings are a microscopic feature, the river-marks can be observed with the naked eye as the white markings in the crack propagation direction. Figure 2.6 c) presents a subsurface defect in the same material as described before. The river marks are radially directing outward. The origin of the river marks points to the crack nucleation site.

Striations Striations are microscopic equidistant ridges on the fracture surface as depicted in Figure 2.6 d). The crack growth due to fatigue leaves clear fractographic evidence known as fatigue striations. Striations are formed during the crack propagation phase and are generally not seen during the fatigue initiation phase. Each fatigue striation has been shown

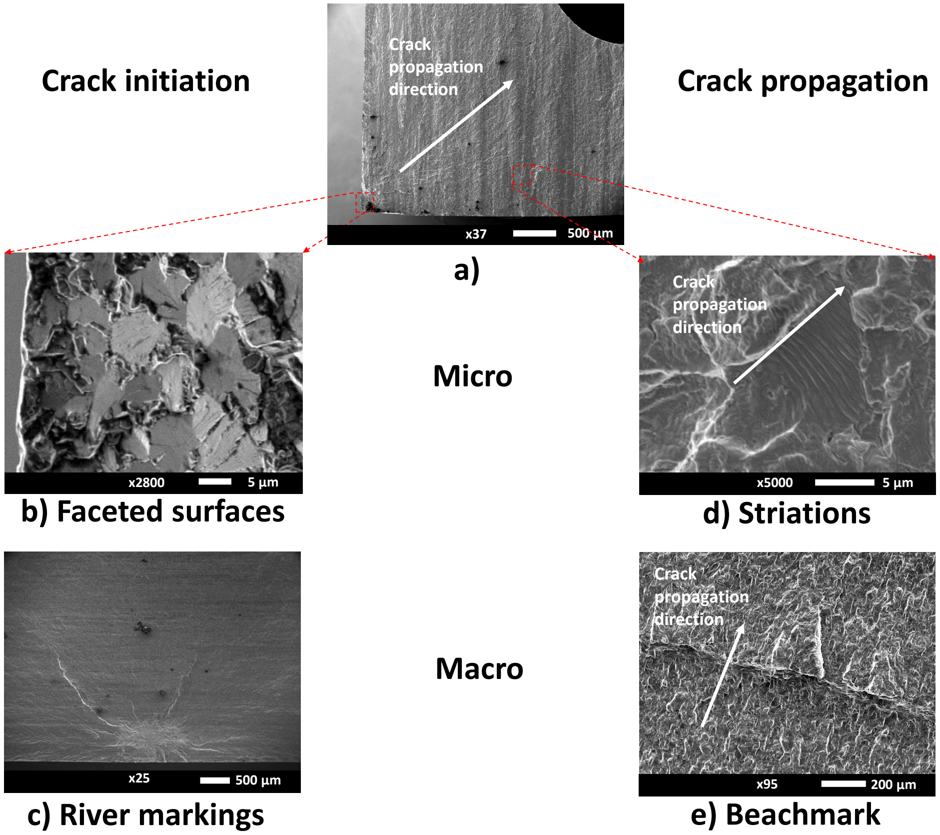

Figure 2.6: Typical fracture features observed on conventional mill anealed Ti-6Al-4V. a) A fracture surface with crack initiation from the bottom lef corner, b) Faceted surfaces, c) River marks, d) Striations and e) Beachmarks

to be the result of a single stress cycle. High-cycle fatigue generally has closely spaced, well-defined fatigue striations [38].

Beachmarks Beachmarks are a unique feature found in many fatigue fractures, and their presence is a positive means of identifying fatigue fractures. This term is used to describe macroscopically visible marks or ridges that are characteristic of interruptions in the propagation periods of fatigue fractures in relatively ductile metals. Beachmarks must not be confused with striations, although they frequently are present on the same fracture surface; there may be many thousands of microscopic striations between each pair of macroscopic beachmarks [39].

Rough surface and shear lips The last phase of the fatigue failure is the sudden fracture of the remaining section of the cross section. This area of the fracture surface is typically rough and shear lips are present. This area is of less interest for the fatigue analysis since fatigue initiation and propagation have happened in other areas of the fracture surface.

2.1.3 Fatigue design and inspections

Many structures are subjected to a cyclic loading and must be designed for fatigue. The design for fatigue is very closely related to the maintenance inspections that will be carried out on the component. There exist four main philosophies for fatigue design: infinite life, safe-life, fail-safe and damage tolerance.

Infinite-life design

This design criteria is the oldest design philosphy and requires all stresses to remain well below the fatigue limit. It is the most simple philosophy, yet the most requiring in terms of structural weight. This design philosphy is especially used for parts subjected to millions of cycles and inspections are therefore impossible or uneconomical to perform.

Safe-life design

According to the safe-life design, products have to be designed to survive a specific finite design life with a chosen reserve. The component is designed such that stress levels inside the component remain well below the fatigue limit of the material. The safe-life must include a safety margin for the scatter on fatigue results and for other, unknown, parameters. The component has to be replaced after the design life, even if the component is still functional. No inspections are carried out during the lifetime of the component. As an example, turbine blades of jet engines are designed according to a safe-life design. Jet engines of commercial airplanes have typical rotating speeds around 40000 rpm, completing 2.4 million cycles each flight hour. The safe-life design philosophy is required since inspections cannot be carried out frequently enough. Such a design criteria is often uneconomical or unpractical because of the excessive weight it entails. The safe-life design philosophy is therefore only used for those components that cannot be inspected for fatigue cracks and that the risk of a failure has catastrophic consequences.

Fail-safe

Fail-safe is a design philosophy in which the failure of a component is not impossible, nor improbable but that the design mitigates unsafe consequences of a failure. It is envisaged that if a component fails, the system does not fail. One example to accomplish this requirement is redundancy. Two components are in place, the first being operational and a second one waiting to take over the function of the first in case of a failure. Fail-safe recognizes the presence of fatigue cracks and infrequent inspections are put in place to repair failed components. Very often visual inspections are sufficient, but the integrated redundancy comes at a price: higher component cost and weight. One example of a fail-safe philosophy in an aircraft is the wing root fitting with the fuselage. Instead of using a small amount of big bolts, of which the failure of one would be detrimental for flight safety, wings are fixed to the fuselage using a multitude of smaller bolts such that the loss of one of them does not have a big impact on flight safety.

Damage Tolerance

The damage tolerance philosophy is a refinement of the fail-safe design criteria. It supposes the presence of damage inside the material, both from the production process and the usage, and it ensures that this damage will not grow large enough to produce failures within an inspection period. The better the inspection system and the smaller the cracks that can be detected during inspection, the longer the inspection intervals can be made. It is because of this very important relationship that NDT techniques are evaluated on basis of Probability of Detection (PoD). NDT reliability may be defined as the probability of detecting a crack in a given size group under inspection conditions and procedures specified [40]. In order to ensure the structural integrity of critical components it was becoming more evident that instead of asking the question *'What is the smallest flaw that can be detected by an NDT method?'*, it was more appropriate, from a fracture mechanics point of view, to ask *'What is the largest flaw that can be missed?'* [40]. This largest flaw size not to be missed then forms the basis of a crack propagation analysis. The remaining lifetime of the component, i.e. the amount of cycles required till this initial crack has grown till final rupture is calculated. Usually two inspections are scheduled within this lifespan. However, since a component is often part of a whole system, one inspection interval is fixed for the entire system and the component is then designed to survive at least two such inspection periods.

The most straightforward application of SHM lies in those design methodologies in which frequent inspections are involved and can be automated, notably in applications where a damage-tolerance design is selected. Since the continuous inspections of the SHM reduce the inspection interval, cracks may be larger at the moment of detection, just before the event of a failure and therefore optimally consuming the lifetime of the component. System downtimes are reduced since online inspections are performed in-situ and component repairs are limited to an absolute minimum. The implementation of a SHM system ultimately increases safety levels since continuous inspections will detect failures that might otherwise fall in between two inspection intervals and operation is continued without the knowledge of a defect. SHM may also be employed to alter the design methodology used for a component. Components in regions that cannot frequently enough be manually inspected using traditional NDT methods can now be inspected (more) frequently by the implementation of a SHM system. Weight gains then result from the adoption of a different design methodology which is made possible by the implementation of a SHM method.

2.2 Structural Health and Usage Monitoring

With a damage-tolerance philosophy put in place, the vast majority of maintenance inspections are scheduled with fixed time intervals based on the expected usage of the component and the time it takes for an undetectable crack to grow to a failure. Such a maintenance philosophy is called Time-based preventive maintenance (TBPM). Current research is focusing on the development of Structural Health and Usage Monitoring systems to enable Condition Based Maintenance (CBM). SHM enables maintenance inspections to be scheduled on the basis of the actual (rather than predicted) health status, while UM predicts the health status on basis of the actual cumulated usage (rather than the design usage) of the component.

The actual usage spectrum, e.g. of the US Navy AH-1W helicopter [41], may largely deviate from the design usage spectrum [42]. Although large economic benefits (reduced maintenance costs and improved system availability) may result from adopting these methodologies, especially the improved safety was the driving force for the development of SHM and UM. The need for SHM and UM actually resulted from various accidents in the past that could have been prevented using these technologies.

A little history on SHM and UM

It is impossible to identify the first form of Structural Health Monitoring (SHM), since SHM is a recent term that has evolved from activities formerly known as structural monitoring, structural integrity monitoring or just monitoring [43]. Back in 1997, the first International Workshop on Structural Health Monitoring (IWSHM) was held at Stanford University. Eleven editions later now, in 2017, this conference is the most respected in the field of SHM and has a European version (EWSHM). A summary of the topics presented at the conference in 1997 were published by the organizing chairman, Fu-Kuo Chang [44]. Back then, the applications envisaged for SHM were broad and ranging from aerospace structures, civil engineering structures and even military rockets. Especially the monitoring of civil engineering structures by means of SHM was considered cost-effective since these systems are generally the most expensive asset in any country and rarely replacable. Civil infrastructures are huge in size, have long service lifetimes and are exposed to harsh environments at all times and susceptibe to natural disasters. Any downtime has a serious economic impact on a country and human safety might be at risk. For critical structures, such as nuclear plants, pipelines, water treatment plants and major bridges, it is imperative that their health would be assessed immediately after a major catastrophic event. In january 1994, an earthquake weakened several structures in Northridge, California, but the damage remained undetected after the main shock but the structures eventually collapsed after a major after shock. The identification of critically damaged structures would have enabled timely evacuation of occupants [44].

A second field of interest pointed out during that first conference on SHM was aerospace. Aircraft SHM was considered as an essential element for continued safe operation of the existing aircraft fleet. Many aircrafts are operated beyond their design lifetime and the time for inspections and repairs on these aircrafts are rising. An example was given by Sampath [45], that for the EF-11A aircraft, on an average, the man-hours required for scheduled inspection and repair of each aircraft have increased from about 2200 hours in 1985 to about 8000 hours in 2000. Automated inspections could therefore be of great benefit to an aging aircraft fleet. In 1974, a Sikorsky S-61 Helicopter crashed into the North Sea with the loss of six lives. The Netherlands Aerospace Centre (NLR) investigated the failure and concluded one of the helicopter blades failed due to fatigue. The blades were equiped with a patented rotor blade inspection system [46]. The blades were pressurized with nitrogen and equiped with pressure indicators installed on each rotor blade. The pressure indicators could only be inspected on the ground when the rotor was not rotating. A fatigue crack present in one of the blades would result in the loss of pressure inside the blade, which would be detected prior to the flight. However, NLR showed that the fatigue design by Sikorsky was inadequate and that a fatigue crack could grow from an undetectable size to a failure in only 2.1-4.3 flight hours. The NLR concluded that the blade pressure indicators must be both installed on the rotor blade and inside the cockpit such that a pressure loss can be both detected on ground and during the flight. Speed reductions after detection of a pressure loss were put in place to retard fatigue crack growth such that the helicopter could safely reach a destination [47]. This will be one of the first examples of the adoption of SHM in an aerospace application. Similarly, also metal tubes of an airframe were inspected using pressure monitoring of the tubes [48]. Aloha Airlines accident flight 231, which occured on April 1988, triggered the issue of damage monitoring in aerospace applications. The riveted fuselage failed due to many small cracks on either side of the rivet holes. Till then, and for the determination of the inspection intervals, each crack around the rivet holes was considered as an individual crack. The damage was actually bigger since it ranged from the crack end on one side of the rivet till the crack end of the other side, including the rivet size. The effect of such damage is more important than the sum of the indivual crack lengths. Since then, airworthiness authorities required that ageing aircraft (usually those at the age of 15 years and beyond) have to become subject of an enhanced inspection effort. This is were SHM specifically comes into play. Sadly enough, the origin of SHM is a consequence of some serious accidents [49]. Within the aerospace industry, Health and Usage Monitoring Systems (HUMS) systems have been most widely adopted in helicopters. The vibrations and noise are continuously monitored in order to derive the status of the main drive train and gear boxes.

State-of-the-art of SHM and UM

Many developments in the field of SHM have taken place over the last decays, both in terms of technologies, materials and applications. Many SHM technologies have been proposed in the literature, often based on existing NDT techniques [50, 51]: Optical Fibre (FBG) sensing [52–61], strain gauges [60, 62, 63], accelerometers [57, 60, 64–66], acousto ultrasonics (AU) [67–70], ultrasonic guided lamb waves [71–75], eddy current foils [76–78], acoustic emmission [70] and Comparative Vacuum Monitoring (CVM) [79–82]. With a global market share of 34.8% [83], SHM has been mostly studied and applied for the monitoring of bridges and dams [53–56,84–86]. The second largest application domain is large buildings and stadiums [57,58,62, 64,83,87,88]. Wind turbines [59,60,63,65,89,90] and aerospace applications hold the third place [61, 66, 72, 75, 83].

With 90% of the Total Life Cycle (TLC) cost occuring after aircraft delivery, the US Navy is implementing SHM and UM to exploit the full fatigue life of their rotary wing aircraft while minimizing cost [42]. In 2002, the nine major US airlines spent 5.32 billion USD on maintenance alone [91,92]. Various of the large aircraft manufacturers are currently exploring which of the SHM technologies being proposed may have a chance to be implemented into real aircraft. Airbus works since 1990s with an increased effort on the subject of SHM for civil aircraft airframe design in cooperation with worldwide leading R&T institutes and other subcontractors. Airbus was the first civil aircraft manufacturer working on this topic to have it available for the whole product range. It has been identified that SHM is one of the key technologies to ensure the integrity of aircraft structure in future aircraft [93]. In 2015, Airbus announced that local SHM limited-area monitoring close to sensors has moved away from R&D and is now ready for qualification per specific aircraft application [81]. Confidence in local SHM applications for selected technologies - for example Comparative Vacuum Monitoring (CVM) - is no longer an issue [81]. CVM is suitable for the detection of surface fatigue cracks and rupture detection of structures. CVM relies on cracks in the structure breaching microscopic pressurized galleries in sensors attached to the surface [79,80]. The principle of CVM is depicted in Figure 2.7. From 2014 on, CVM sensors were flying on Delta Air Lines Boeing 737 aircrafts as part of a program aimed to approve SHM as an alternative inspection technique to manual disassembly and visual inspection for commercial aircraft by 2016 [81, 82]. In August 2017, Structural Monitoring Systems (SMS) announced that it has executed the worlds first

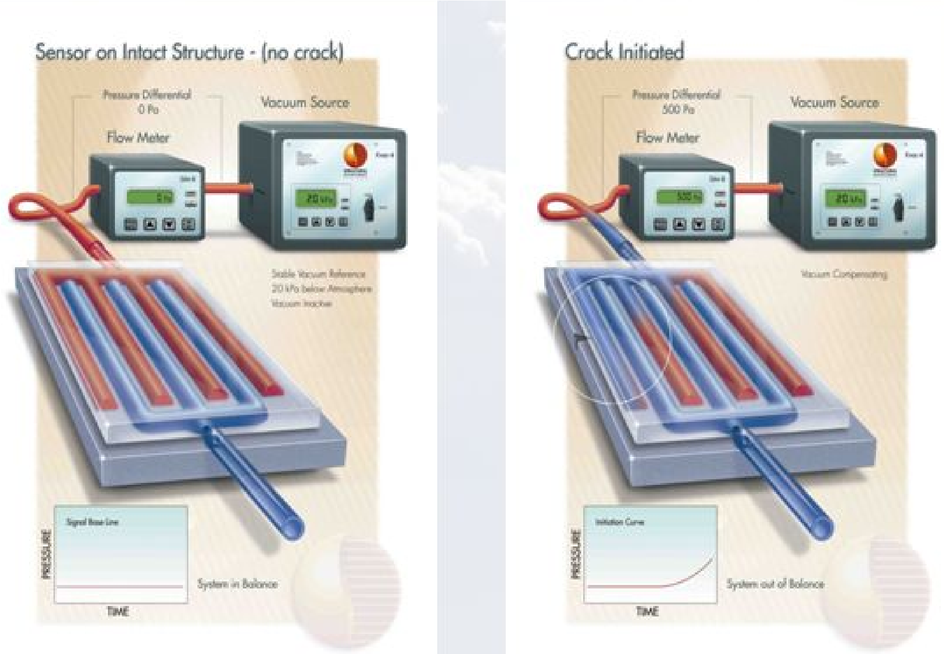

Figure 2.7: Working principle of Comparative Vacuum Monitoring (CVM). A patch, consisting of a double set of capillaries is attached to the surface of the structure to be monitored. Half of the capillaries is connected to a vacuum pump while the other half is at ambient pressure. A surface crack breaching the capillaries interconnects the two sets of capillaries, resulting in an air flow through the measurement equipment, thereby detecting a surface crack.

commercial agreement related to the supply and permitted use of a SHM technology with a commercial airline operator (Delta Airlines) [94]. CVM was the first SHM principle to reach TRL level 6 within Airbus.

Current research and future of SHM

SHM is a widely studied research topic with a lot of potential but difficult to beginners due to the multidisciplinary nature of the subject [50]. Especially applications in the aerospace sector are requiring and currently formulate the biggest challenges for the mass adoption of SHM. Airbus expects that the adoption of SHM in aerospace applications will happen in four major steps within the next years (see Figure 2.8 taken from [11]). Generation 0

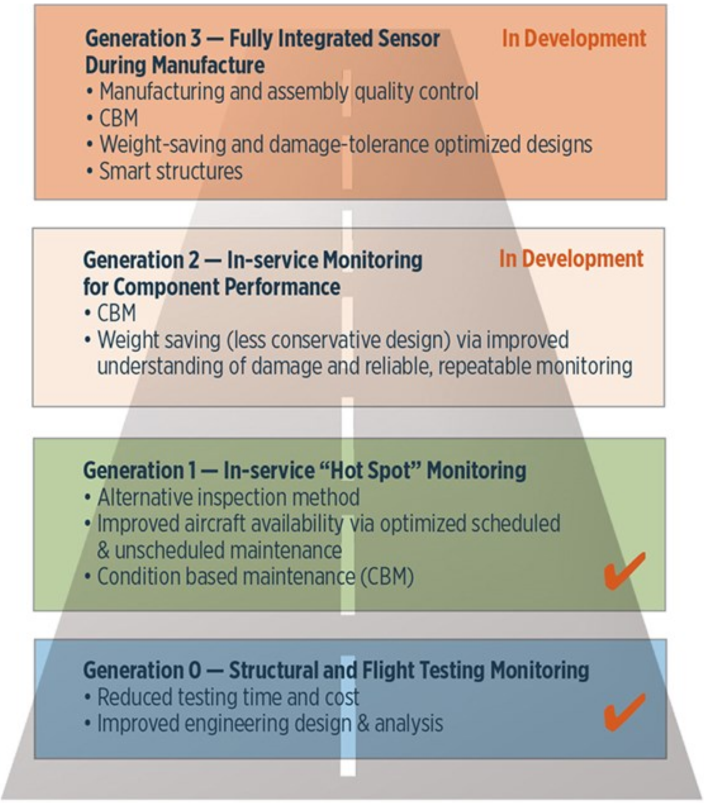

Figure 2.8: According to Airbus, the implementation of SHM will happen in four main steps.

of SHM systems will be used on Structural and Flight Testing to reduce testing time and costs. SHM generation 1 would be deployed on real aircraft for In-service Hot Spot Monitoring (i.e. local damage) as an alternative inspection method to enable CBM. The current deployment of CVM fits within Generation 1 of SHM. In a next step, the implementation of SHM will enable weight gains through a better understanding of the damage and frequent automated inspections. In a last phase, SHM generation 3 would consist of fully integrated SHM sensors during manufacturing, enabling weight savings and creating smart structures.

The work of Khan et al. [50] presents an extensive summary of the challenges that remain in the field of SHM for aerospace applications. From a technology point of view, the most important remaining challenges are the following:

- The foremost challenge is to develop and demonstrate SHM technologies that can be used to monitor structural integrity in service conditions with high reliability and durability [50].
- As in conventional NDT, a single SHM technology will not be suited for the entire range of applications based on different materials, component geometries and damage scenarios [50].
- Diagnosis must have high reliability over the aircraft lifetime, since unjustified maintenance actions are quite costly to the operator and spurious warnings degrades confidence in the system [50, 91].
- Accuracy and reliability may even be more stringent, since further optimization of structural design will rely on SHM with better knowledge of actual flight loads & condition [50].
- Another challenge is the robustness and reliability of installed sensors. There might be a need to monitor the sensors themselves if there is any chance of failure [50, 91].

Not only technical challenges remain for the deployment of SHM in the field of aeronautics. Especially the certification forms a major stumbling stone. Inspection procedures need to be certified and confidence in SHM need to be gained in order to base maintenance programs on SHM. The first deployment of SHM will therefore be as an assisting technology besides the NDT techniques currently in place. Current maintenance programs happen within fixed time intervals and detection of damage requires an immediate repair action. With SHM, continuous information about the health of the component is gathered and detection of damage may happen at any time. The certification authorities will nowadays require the airlines to immediately perform a repair action after detection of damage, leading to unscheduled repairs and increased downtimes. With that, a second non-technical challenge is to be tackled. The cost of SHM development and deployment should not exceed the benefits gained or not be too prohibitive so that mass adoption is slowed down or halts. [50]

Up to now, a large amount of small sensors of multiple types are necessary to deploy SHM systems over large areas and moving the technology beyond hot-spot monitoring [95]. In an attempt to reduce the amount of sensors used, to reduce their installation cost and reduce the environmental impact (noise, accidental damage, hazardous conditions, etc.) on the SHM system performance, integrated SHM systems are currently under investigation [95–97].

Smart Materials

The third generation of SHM will consist of SHM sensors directly integrated during the manufacturing process, capable of detecting the presence of damage inside the structure to be monitored. With the invent of new manufacturing techniques, such as composite structures, the capability of integrating sensors came along. The application of SHM sensors to the structure can be done as part of the component manufacturing and not as a secondary operation [91]. Similarly, the layerwise addition of material during the additive manufacturing process enables function integration such as an embedded SHM sensor.

Much research is ongoing to integrate electrical conductors inside AM polymers to generate built-in sensors. Liquid metal is being inserted in 3D printed microchannels [98–100]. Strain gauges have been printed in conductive ink on top of a structure [101] and inside highly stretchable elastomers [96]. Despite their successful operation, many drawbacks have been reported on the use of conductive ink. The curing must happen at an elevated temperature and for a significant amount of time, which might be incompatible with the polymers commonly used in 3D printing. The process is also too costly for large scale production. The conductive ink is approximately 100 times more expensive than ordinary copper, but its conductivity is commonly 30 times less. Therefore, researchers have begun to explore the use of solid metal conductors, such as copper wires, in 3D printing [101]. Scheyer and Anton employed the electromechanical impedance (EMI) method on piezoelectric transducers embedded inside AM parts to evaluate the feasibility of performing SHM on parts fabricated using additive manufacturing [102].

Saheb and Mekid provided a review of methods for the integration of optical fibres for sensing applications in metals with the inclusion of additive manufacturing [103]. Fiber-optic strain sensors are being embedded in metals by means of powder-bed based additive manufacturing [104, 105], shape deposition manufacturing [106, 107] and ultrasonic additive manufacturing [108]. The 'Sensor Embedding in Additive Manufacturing Team', abbreviated as

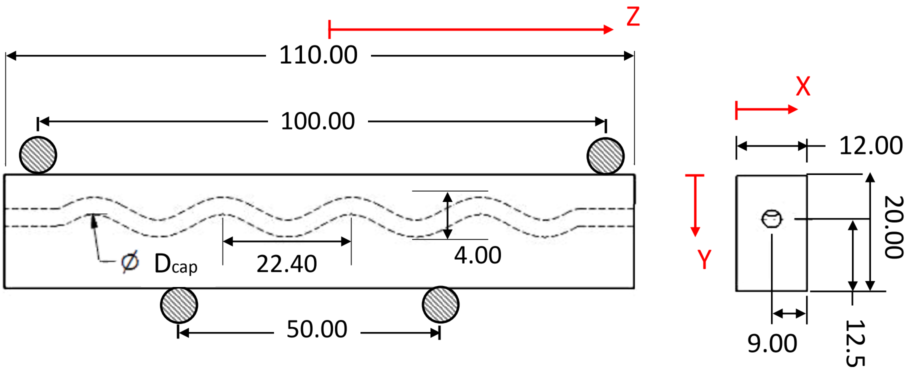

Figure 2.9: Four point bending fatigue test specimen with sinusoidally shaped capillary. Dimensions in millimeter.

the SEAM team developed an original sensor concept called a microwave frequency cavity resonator (MFCR). In this concept, a radio frequency wave was transmitted into the cavity. As the specimen changed length due to the applied forces, the change in cavity length correlated to the change in a resonant frequency, which was detected from the inside [109].

2.2.1 effective Structural Health Monitoring

At the Vrije Universiteit Brussel, a new SHM methodology was invented using additive manufacturing. The concept of effective Structural Health Monitoring (eSHM) was first presented by De Baere et al. [110]. During the design phase of a component, a capillary is integrated at the location were a fatigue crack is expected to grow. The designed component can then be manufactured using metal additive manufacturing. Before taking into service, the capillary is pressurized and sealed by a pressure sensor externally installed at the capillary end. The capillary is now very sensitive for leaks. A crack breaching through the capillary induces a leak flow and a pressure change inside the capillary that is detected by the pressure sensor.

Strantza et al. [111] presented the first proof of concept of the eSHM by succesfully integrating capillaries using AM technologies and detecting the fatigue crack in all four tested four point bending fatigue specimens. Both stainless steel AISI 316L specimens produced by laser based Directed Energy Deposition (DED) and titanium alloy Ti-6Al-4V specimens produced by laser based Powder Bed Fusion (PBF) were tested. The capillaries were

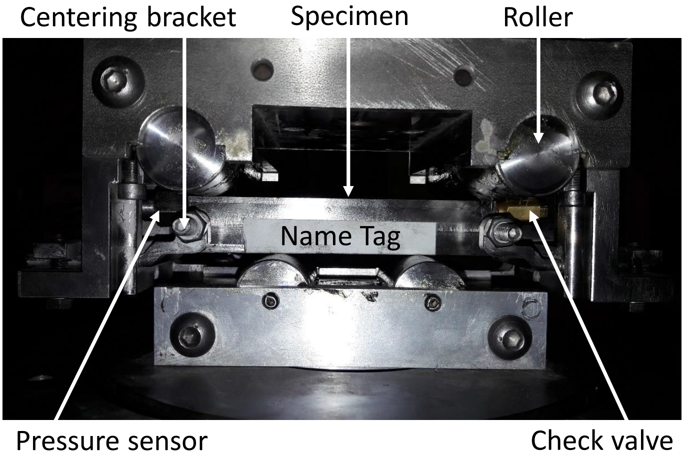

Figure 2.10: Four point bending fatigue test setup.

sinusoidally shaped along the length direction of the specimens in order to evaluate the intrusive character of the capillaries (see Figure 2.9 for the specimen design). If the presence of the capillary would deteriorate the structural integrity of the component, all cracks would initiate at those locations where the capillary is positioned closest to the specimen outer surface that is tensile stressed. Since cracks initiated at different locations in the specimen and the initiation occured at internal pores and traces of a different material, it was concluded that the integrated SHM system had no influence on the crack initiation location. With proven feasibility of both embedding the sinusoidally shaped capillaries and detecting the fatigue cracks, it was concluded that the eSHM reached TRL level 3 [111, 112].

Since then, all specimens were tested using the same method. Four point bending fatigue specimens with integrated capillaries of the eSHM system are produced and tested using the step method. The step method was chosen since the amount of specimens is limited due to the high production cost. The test setup, as also used throughout this work, is depicted in Figure 2.10.

Strantza et al. presented a more thorough discussion of Ti-6Al-4V specimens produced by PBF with an integrated SHM system consisting of a sinusoidally shaped capillary. Those specimens produced by laser based PBF had a significant lower fatigue strenght then conventional specimens produced from wrought Ti-6Al-4V. Crack nucleation sites developed due to near-surface defects such as concentrated pores or lack-of-fusion regions.

The presence of the capillary did not alter the fatigue initiation location. A stress relief did significantly improve the stress level at failure of the specimens produced by PBF indicating that both internal defects and residual stresses had a negative impact on the fatigue performance. These results indicated the importance of the imperfections on the fatigue life of a component produced by PBF and the applicability of structural health monitoring systems. [113].

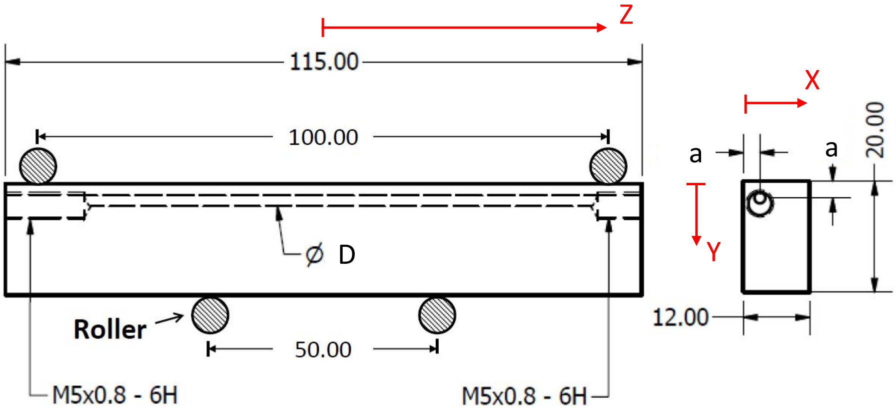

Figure 2.11: Four point bending fatigue test setup and specimen with straight capillary. Dimensions in millimetre.

The closer the capillary is located to the outer surface, the sooner a fatigue crack is detected when growing from the outer surface. However, a trade-off is to be considered since locating the capillary closer to the outer surface may result in fatigue initiation at the capillary surface. The presence of the internal feature may not alter its fatigue performance. The evaluation of different topologies of the integrated capillaries was presented by Strantza et al. [114]. The work presented fatigue test results of as-built (AB) and stress relieved (SR) Ti-6Al-4V specimens produced by laser based DED with straight capillaries. The distance in between the capillary edge and the outer surface of the specimen was varied. This distance is reffered to as 'a' throughout this work and is defined as depicted in Figure 2.11. The stress level at failure was about 200 MPa larger for a capillary positioned at $a = 3\ mm$ than $a = 2\ mm$. Fatigue initiation occured in both cases at the capillary surface. This must have been a result of a rough capillary surface finish. A stress relief action did not alter the fatigue performance and residual stresses therefore will not have affected the test result. A conventional specimen with drilled capillary located at a distance $a = 2\ mm$ from the specimen edge performed much better as the specimens with additive manufactured capillary. It was concluded that the capillary surface roughness was most important and more investigations on the capillary surface roughness and finishing methods should be conducted [114, 115].

A comparative study with other NDT techniques such as Liquid Penetrant (LP), Eddy Current (EC), radiography and Acoustic Emission (AE) have furthermore shown that the different techniques confirmed the existence of the crack, proving the reliability of the innovative SHM system. Those NDT techniques were considered suitable for the evaluation of the structural integrity of AM components and highlight the added value of those NDT techniques in the localization capability of the system. This capability presents an advantage for industrial users who aim to validate the correct functionality of the system with the standard available NDT methodologies [116].

2.3 Additive Manufacturing

Many AM technologies were used throughout this thesis work. Fused Deposition Modelling (FDM) and Stereolithography (SLA) were mainly used as a prototyping technology for proof-of-concept studies related to the eSHM development. Since these technologies produce polymer parts, these components were not used for fatigue related studies. Specimens produced by Directed Energy Deposition (DED) on the contrary, were mainly used to evaluate the fatigue properties of additively manufactured metals and to evaluate the behaviour of the integrated eSHM system within a metal additively manufactured component. Powder Bed Fusion (PBF) was used to manufacture tensile test specimens for the proof-of-concept studies related to the UM principle of the eSHM system. In the following paragraphs, the working principle of each of these AM technologies will be discussed in detail followed by a discussion on the most important material properties listed in the literature.

2.3.1 Fused Deposition Modelling (FDM)

Currently being the most affordable AM technology, FDM is the most widespread AM technology. As many FDM printers are already on the consumer market, many hobbyist can afford one for AM prototyping in polymers. The material that is to be deposited is a thermoplast. The process of FDM printing is depicted in Figure 2.12 a) (Figure adapted from [117]). The material is melted through a heated nozzle. By moving the heated nozzle and feeding material through the nozzle, material is deposited on the buildplate along the trajectory of the nozzle movement. Tracks of semi-molten material are laid next to each other till the layer is completed. The buildplate is lowered and the next layer is deposited on top of the previous layer. This procedure is repeated till the part built has been completed.

Two main material types are currently available for the FDM technology: polylactic acid (PLA) and Acrylonitrile butadiene styrene (ABS). Although PLA is easier to print and therefore more widespread, only ABS was used throughout this thesis work. The main reason is the permeability of the FDM component. Since FDM deposits semi-molten tracks next to each other, adjacent tracks and stacked layers are not molten together. Small air gaps remain present in between the tracks and layers. As the principle of eSHM is based on the evaluation of the pressure inside a 3D printed capillary, air - and watertightness of the capillary is of primary importance for this particular study. Only ABS can be post processed with acetone in order to blend together the layers after deposition and thereby creating an air- and watertight capillary.

2.3.2 Stereolithography (SLA) and Digital Light Processing (DLP)

Back in the 1980s, SLA was developed as the first AM technology. SLA stands for Stereolithography Apparatus and is based on the photopolymerization process. The hardening of a liquid polymer is based on the exposure to laser (UV) light. A schematic representation of the SLA process is depicted in Figure 2.12 b) (Figure adapted from [118]). The laser sents out a beam and the XY mirror controls the position where the beam hits the polymer resin. At this location, the polymer resin hardens. By scanning the pattern defined in the G-code, the laser determines which part of the liquid resin solidifies. After completion of the first layer, the build platform lowers and the sweeper distributes a new layer of resin across the component. The laser will now scan the second layer and so forth till the build has been completed. In recent years, a related AM process based on photopolymers has emerged. One layer is scanned at once using a beamer projecting the layer outline onto the buildplate. The light sent by the beamer solidifies the entire layer at once. This technology is called “Digital Light Processing (DLP)”. Because of the nature of both processes, the solidification of a pure liquid, SLA and DLP produce air-and watertight components without the need of any post treatment.

2.3.3 Directed Energy Deposition (DED)

The Directed Energy Deposition (DED) method, also very well known under the trade names ”Laser Metal Deposition (LMD)”, ”Laser Engineered Net Shaping (LENS)” and ”Laser Cladding”. The DED process is depicted in Figure 2.13 a) (Figure adapted from [119]). A laser is used to locally melt the metallic subtstrate and thus the creation of a melt pool. Metal powder particles are injected into the melt pool by a nozzle. The particles melt inside the meltpool. As the nozzle with laser beam is moving away from the melted region, the melt pool solidifies while another region is heated to its melting point. The added metal particles now form a part of the solidified track that is left behind the nozzle. Since the clad head is continuously moving over the substrate, material can be added on top of the substrate according to the design specified in the CAD design. Upon completion of the layer, the distance between the clad head and the work piece is increased by one layer thickness and the same procedure is repeated. The nozzle head often also exhibits an inert gas shielding, creating an inert environment around the melt pool in order to prevent oxidation during the process.

The nature of the process does not require the substrate to be flat. DED has therefore the major advantage over PBF that material can be added on top of an existing, sometimes complex shaped base part, creating high added value at a little AM cost. The DED process is generally also much faster than its major competitor PBF. On the downside, the geometric accuracy that can be achieved is generally less than with PBF. Also the surface quality is less good with DED. The heat affected zone of the DED is much smaller as compared to the PBF process, leading to smaller thermal stresses in the component.

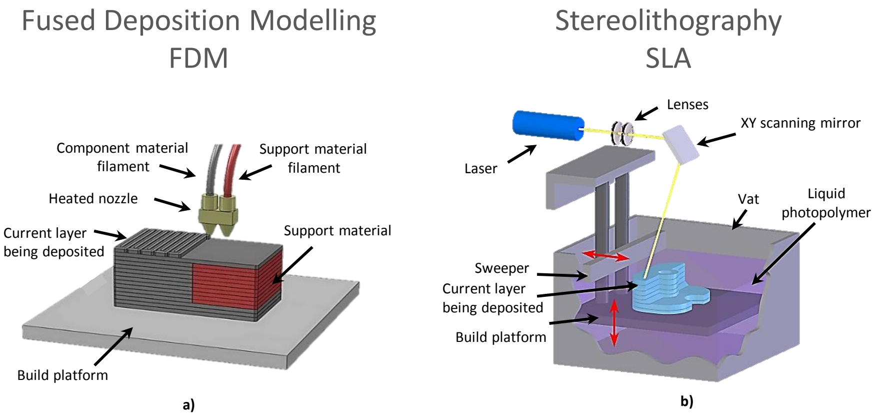

Figure 2.12: Polymer AM technologies. a) Fused Deposition Modeling b) Stereolotihography

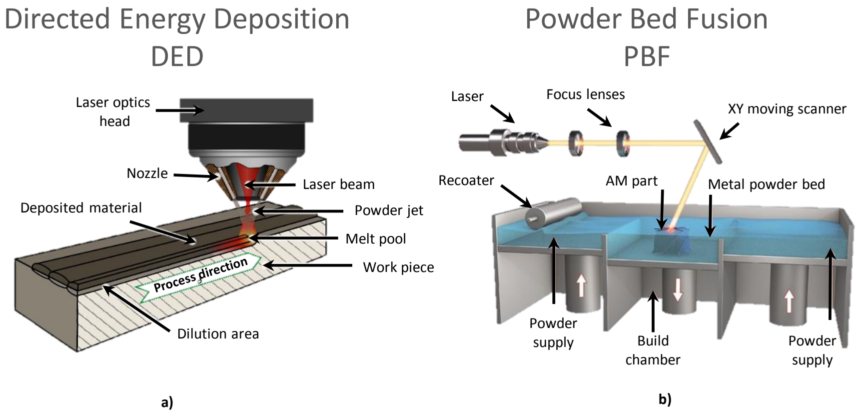

Figure 2.13: Metal AM technologies. a) Directed Energy Deposition b) Powder Bed Fusion

Tensile properties of laser based DED material

The mechanical properties of Ti-6Al-4V produced by laser based DED are commensurate with those of wrought material without the need for post-fabrication heat or pressure treatments. Of particular note is that the ductility values achieved in the present component exceed those previously found in AM Ti6Al4V, with significant ductility achieved in both the longitudinal and transverse directions. The long and thin prior-β grains growing along the build direction result in anisotropic tensile elongation properties, rendering the ductility significantly higher along the transverse direction than the longitudinal direction. [120]. The work of Saboori et al. provides an in-depth review on the microstructure and mechanical properties of Ti-6Al-4V produced by laser based DED [121]. The cooling gradients are determining the microstructure and thus the mechanical properties of the Ti-6Al-4V material. A finer microstructure is obtained closer to the water cooled buildplate, leading to higher strenghts in specimens extracted from the bottom half of the build [120].

Fatigue properties of laser based DED material

The fatigue performance of Ti-6Al-4V produced by laser based DED has also been discussed in the literature. In the work of Sterling et al. [122], fatigue lives of Ti-6Al-4V produced by laser based DED were found to be shorter than wrought Ti-6Al-4V, largely due to pores. The fatigue life of Ti-6Al-4V produced by laser based DED is predominately controlled by the presence of physical defects, in particular the unmelted particles at the surface [123].

2.3.4 Powder Bed Fusion (PBF)

With the principle of SLA in place and the developments in laser technology, metal AM technologies based on laser scanning were developed. Powder Bed Fusion (PBF) is the standard terminology for the process which is also often reffered to as ”Selective Laser Melting” (SLM). The principle is very similar to the SLA process, as can be seen from Figure 2.13 b) (Figure adapted from [124]). A laser is used as heat source to locally melt the metal and join metal powder particles of the powder bed. A thin layer of loose metal particles is in place on the powder bed. The laser sends out a beam, which is redirected by means of a XY mirror. Loose particles are left behind if the laser did not scan the area. The build platform is lowered and the re-coater distributes a new layer of loose metal particles on top of the previous layer. The laser beam now scans the layer pattern of the second layer and thereby joins the metal powder particles with the layer below. The process is repeated till the last layer has been processed. The loose metal particles have to be removed from the component and the created part has to be cut from the baseplate.

Based on the process nature, a PBF build has to start from a flat base plate and powder bed to allow the recoater to evenly distribute a new layer of loose particles. As such, PBF cannot be used to add new features on existing non-flat structures. PBF generally produces components with higher geometrical accuracy and better surface finish as compared to DED, but require a longer build time. A thermal treatment is also often required to reduce thermal stresses and limit warping after base plate removal.

Tensile properties of laser based PBF material

The bulk of the published mechanical properties has been generated on Ti-6Al-4V, an otherwise expensive and difficult to process material that can now optimally be used by means of additive manufacturing. The yield and tensile strength of cast annealed Ti-6Al-4V are respectively 885 MPa and 930 MPa according to the ASM standard [125, 126]. Yu et al. [127] furthermore presented similar results for wrought Ti-6Al-4V and furthermore concluded that almost all yield and ultimate tensile strengths of laser based PBF are higher than those of wrought Ti-6Al-4V. The ductility of wrought Ti-6Al-4V was much better than that of Ti-6Al-4V produced by laser based PBF. Some anisotropy was reported in between horizontally and vertically produced specimens. Horizontally built specimens having a little higher yield and ultimate tensile strength. The only kind of defect in the samples is few small spherical pores with average diameter of several tens of microns, which do not have significant influences on the tensile properties [128] and can be ignored when exploring the causes of the tensile anisotropies. Any influence that the presence of pores would have on the tensile properties seems to be less than the influence of the orientation of the columnar grains with respect to the tensile test direction. The vertically built samples are tested with the columnar grains parallel to the stress axis and the horizontally built samples are tested with the stress axis perpendicular to the length of the columnar grains [128]. Heat treatments [127] and hipping [128] reduce the tensile anisotropies by altering the microstructure, proving the major effect of the columnar structures on the mechanical anisotropies [127]. The hipping procedure improved ductility but caused reduction in strengths leading to comparable tensile properties as thermomechanically processed and annealed samples [128]. High residual stresses (± 300 MPa) were measured in the as-built specimens suggesting that stress relief of the parts might be required to avoid any potential part distortion [129]. Similar results were obtained for stainless steel AISI 316L. The tensile properties of AISI 316L produced by laser based PBF are superior to those of conventionnaly manufactured material, but ductility is reduced by more than 50% [130,131]. The influence of other process parameters has been widely studied, including laser power [132–134], scan strategy [130], hatch spacing [134,135], scan speed [135] and layer thickness [136] have an influence on the tensile properties.

Fatigue properties of laser based PBF material

Whereas there has been extensive research to determine the range of uniaxial tensile properties possible for PBF (EBM, laser) and DED (laser), much less published research is available for the fracture-critical properties (e.g., toughness, fatigue) of Ti-6Al-4V [137]. Fatigue and crack propagation properties of additive manufactured materials are not very well known yet [138], because a lack of process understanding and a lack of *in situ* process monitoring and control, especially in metal AM systems, currently results in unknown porosity levels and distributions [139]. Multiple sources report a reduced fatigue lifetime. In the work of Chan *et al.* [140], fatigue lifetime of titanium Ti-6Al-4V alloys fabricated by means of additive manufacturing were compared to conventionally produced Ti-6Al-4V alloys (rolled or cast). Conventionally rolled Ti-6Al-4V alloys showed approximately twice the fatigue lifetime of the best additive manufactured Ti-6Al-4V alloys. Gong *et al.* [141] stated that as-built surfaces of laser based PBF Ti-6Al-4V samples become crack initiation sites, resulting in a reduced fatigue lifetime when the stress level exceeds 500 MPa. Similar results were also recorded in the paper of Strantza *et al.* [113], where the SLM Ti6Al-4V samples indicated a stress level at failure under fatigue loading of 590 MPa and 570 MPa.

Chastand et al. [142] investigated the fatigue performance of Ti-6Al-4V produced by laser based PBF in both High Cycle Fatigue (HCF) and Low Cycle Fatigue (LCF) conditions. The authors found that the high roughness of as-built specimens involved a high amount of surface defects that were critical for fatigue performance. Process inherent defects have a major influence on the fatigue performance of Ti-6Al-4V produced by laser based PBF [143]. Regardless of the applied load ratio, it was found that all specimens failed due to crack initiation at defects originating from the production process. Defects play a critical role in laser based PBF Ti-6Al-4V fatigue performance. As-built surfaces become crack initiation sites, especially when the maximum tensile stress is higher than 500 MPa, as reported by Gong et al. [141]. Many more works report that fatigue performance of Ti-6Al-4V samples produced by laser based PBF are negatively affected by surface roughness, pores, residual stresses and internal defects [143–145]. The work of Greitemeier et al. [144] compared the fatigue performance of Ti-6Al-4V specimen produced by laser based PBF and electron beam based PBF. The authors concluded that the lower fatigue limits of the specimens produced by electron beam based PBF can be ascribed to the higher surface roughness of the specimens produced by electron beam based PBF as compared to laser based PBF.

Although the high number of process parameters involved in an AM process has led to widespread fatigue performances, most of them report significant reduction of fatigue life due to the presence of voids, unmelted regions and increased surface roughness. Currently, the lack of proper AM process monitoring and control results in unrepeatable material behaviour. Given that Structural Health Monitoring (SHM) is used to provide continuous information about the structural integrity of a component, the implementation of such a system on AM components is helpful to detect early deterioration of the component.

Chapter 3

Fatigue response of specimens with integrated eSHM system

The integration of the capillaries of the eSHM system may not weaken the structure. The effect of the presence of the capillaries on Ti-6Al-4V specimens is discussed in this chapter. A first study discusses the influence of the capillary on the fatigue properties of the specimen. A second part is dedicated to the effect of the capillary surface roughness on the fatigue performance. A third study is devoted to the location of the capillary in wrought specimens. The AM fatigue specimens discussed in this chapter were produced by M. Rombouts and G. Maes at VITO. The stress relief and EDM cut for SEM analysis was performed by B. Vrancken of the KU Leuven. Fatigue testing was conducted on a test setup at the Department of Mechanics of Materials and Constructions (MeMC) of the VUB. The SEM analysis was conducted on the JEOL JSM-IT300 of the Research Group of Electrochemical and Surface Engineering (SURF) of the VUB. This chapter is based on article [146].

3.1 Introduction

The working principle of the eSHM system is based on the pressure monitoring of a three-dimensional (3D) network of capillaries integrated in the component to be monitored. Very often, the first question arising with the presentation of the eSHM system is the influence of the integrated capillaries on the structural performance. Does it weaken the component? It is very important for a Structural Health Monitoring (SHM) system not to weaken the structure, else a majority of the benefits coming along with the integration of the SHM are consumed by its negative effects on the component. One aspect of this PhD research is the analysis of the presence of the capillaries of the eSHM system on the structural performance of the component.

The eSHM system is made possible thanks to the emerging additive manufacturing (AM) technologies such as laser based Directed Energy Deposition (DED) and laser based Powder Bed Fusion (PBF). The capillaries of the eSHM are integrated during the manufacturing of the component. However, the additive manufacturing technologies still have their limitations. Internal stresses and material imperfections such as pores often detrimentally affect fatigue performance of the AM material, showing the importance of a monitoring system inside AM material. For the current study and reproducibility of the results, it is important to decouple the effects of the AM material itself from the presence of the capillary inside the material. Specimens produced using conventional manufacturing techniques show more consistent material properties. By using conventional manufactured specimens as a first step, the material uncertainties of the AM process are decoupled from the actual influence of the presence of a capillary. Deep gun drilling is used to integrate long elongated holes inside four point bending specimens. The capillaries are straight because of the manufacturing limitations imposed by the drilling operation. In this chapter, the fatigue response of Ti-6Al-4V specimens produced by conventional manufacturing techniques are presented. Test results will be presented of specimens with and without integrated capillaries of the eSHM system. The results will allow to determine whether the insertion of a capillary feature affects the fatigue performance. Furthermore, fracture analysis on basis of Scanning Electron Microscopy (SEM) images and Finite Element Modelling (FEM) simulations will substantiate the drawn conclusions.

A second part of this chapter will then consider Ti-6Al-4V specimens produced by laser based DED. The same procedure will be followed to analyse the intrusive character of the AM capillaries inside AM material. For comparison reasons, the AM specimens have a similar layout with long elongated capillaries.

A third part of the analysis will be devoted to the influence of the location of the capillary in conventional specimens. The specimens will be tested for fatigue in a four point bending configuration. The capillary is to be integrated in the tensile stressed region to detect the growing crack as soon as possible. The closer the capillary is located to the specimen edge, the higher the tensile stresses at the capillary surface. Since fatigue initiation preferably occurs on free surfaces, chances increase that fatigue cracks will initiate at the capillary surface. The location of the capillary is therefore another important parameter to consider.

3.2 Materials and processes

Manufacturing of conventional Ti-6Al-4V specimens

Wrought specimens were produced by conventional milling operations from a mill annealed Ti-6Al-4V plate. All specimens were milled from the same plate. The capillaries were added according to the design presented in Figure 3.1, using deep gun drilling with a drill diameter of 2 mm. The capillaries were added at two distances from the specimen edge, at distances $a = 2$ mm and $a = 3$ mm as defined in Figure 3.1. The capillary is not located in the centre of the specimen as to analyse whether the corner with the capillary is favoured for crack nucleation.

Manufacturing of Ti-6Al-4V specimens produced by laser based DED

The additively manufactured specimens were produced by laser based DED using a 7 kW IPG YLS-7000-S2 fibre laser (IPG Photonics, Oxford, MA, USA) with a diameter of 600 µm. The laser beam passed through a focal lens and collimator, which resulted in a laser spot diameter of 1200 µm on the substrate. The process parameters are summarized in Table 3.1.

The specimens were built at a constant laser power of 500 W while the nozzle was moving at a linear scan speed of 1000 $^{\mathrm{mm}}/_{\mathrm{min}}$. The layer thickness

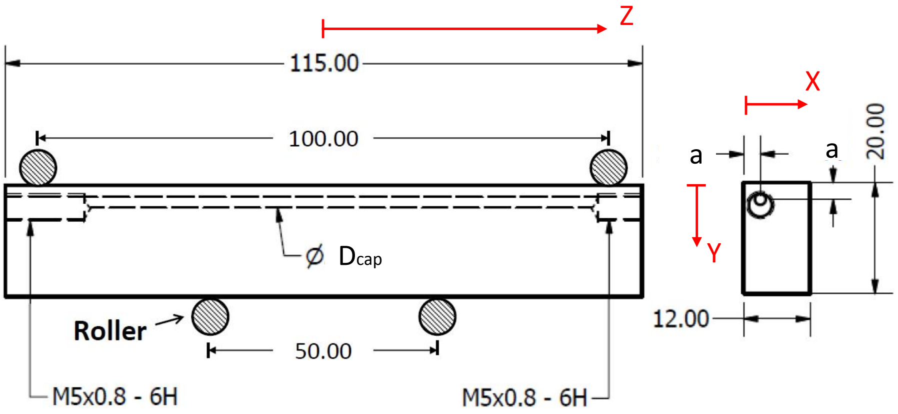

Figure 3.1: Four point bending fatigue test setup and specimen with straight capillary. Dimensions in millimeter.

Table 3.1: Process parameters for the production of Ti-6Al-4V by means of the laser based Directed Energy Deposition (DED) process.

Laser power [W]	Scan speed [mm/min]	Scan spacing [mm]	Layer thickness [mm]	Powder flow [g/min]	Transport gas [l/min]
500	1000	0.3	500	2.96	6-8

was 500 µm. The powder was transported through a continuous coaxial nozzle (Fraunhofer–Institut für Lasertechnik, Munich, Germany) using argon as transport and shielding gas. The transport gas flow rate varied between 6–8 $^{\mathrm{l}}/_{\mathrm{min}}$ blowing 2.96 $^{\mathrm{g}}/_{\mathrm{min}}$ Ti-6Al-4V particles into the melt pool. Specimens were built on Ti-6Al-4V flat plates with a thickness of 18 mm. The build direction was vertical (indicated on Figure 3.2 a) and the scanning direction of successive layers was rotated by an angle of 90°. In one layer, the contours were first scanned before a bidirectional scanning pattern with a scan offset of 0.3 mm was applied. Figure 3.2 a) shows two laser based DED samples in as-built condition. AM processes, such as laser based DED, can introduce high thermal stresses inside the specimen. After the specimens were removed from the base plate, a heat treatment was applied in order to obtain stress relieved conditions. While additively manufactured Specimens 11–13 were subjected to a standard heat treatment often used for conventional Ti-6Al-4V (4 h at 650 °C), Specimens

7–10 were subjected to a heat treatment at lower temperatures in order not to alter the microstructure (2 h at 530 °C). The specimens were then milled to the final dimensions of 115 mm × 20 mm × 12 mm. The corners of the specimens were not rounded. Although the capillaries were designed to have a diameter of 2 mm, the printed capillaries in Specimens 9–13 turned out to have variable diameters varying between 1.4–1.8 mm due to the geometrical inaccuracy of the laser based DED process. In order to improve the capillary surface roughness, the printed capillaries of Specimens 11–13 were drilled through using deep gun drilling with a drill of 2 mm diameter.

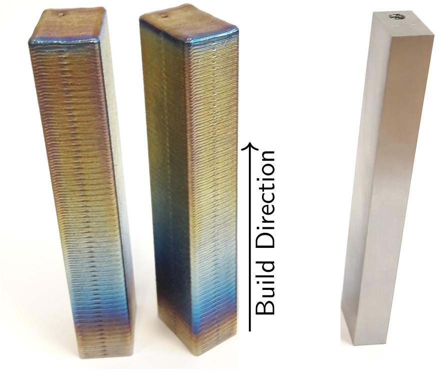

(**a**) (**b**)

*Figure 3.2: Additive manufactured Ti-6Al-4V specimen produced by laser based DED in as-built condition (**a**) before milling and (**b**) after milling*

Installation of the eSHM System

The specimens were equipped with a Kulite XTL-123BEG-190M-1.7 pressure sensor (Kulite Semiconductor Products Inc., Leonia, NJ, USA) at one side and a Clippard MCV-1-M5 check valve (Clippard Instrument Laboratory Inc., Cincinnati, OH, USA) on the other side. In order to properly seal the connections, a Loctite 577 thread sealant (Henkel, Düsseldorf, Germany) was applied to the M5 threads. The anaerobic thread sealant remains liquid until being isolated from oxygen in the presence of the metal ions of the thread. When cured, they form a durable seal by filling up the gaps between the threads. The specimens were then placed in a vacuum oven and the pressure inside the capillary was reduced to approximately 0.4 bara (bara refers to 1 bar of absolute pressure). The check valve prevented the capillary pressure to rise when taken out from the vacuum oven.

In order to prevent occasional leaking through the check valve, an additional Clippard 11755-M5-PKG stop (Clippard Instrument Laboratory Inc., Cincinnati, OH, USA) was screwed onto the check valve end. Figure 3.3 shows the Ti-6Al-4V specimen with the installed eSHM system, just before testing.

Figure 3.3: Fully equipped Ti-6Al-4V specimen with installed pressure sensor at one side and check valve and stop at the other side. The eSHM system is active.

3.3 Experimental Study

3.3.1 Test Procedure

All specimens were subjected to a cyclic fatigue loading in a four-point bending test setup. Figure 3.4 (a) shows the specimen installed in the test bench. In between the two inner rollers, a region of maximum and constant stresses is present in the specimen. The fatigue cracks are expected to nucleate and grow in this region, on the tension side of the specimen. The specimen was placed in the setup with the capillary in the tensional stress area, such that the eSHM system could detect the fatigue cracks as early as possible. The centering brackets held the specimen in place during testing.

As suggested from the literature [36, 147–149], the step-method is considered as a fast methodology to estimate the fatigue strength of a specimen. The experimental observations presented in Nicholas et al. [147] indicate that the step-loading procedure used in their investigation provides a valid method for determining the fatigue limit stress corresponding to a given number of cycles in the high cycle regime. According to the step method, a large number of cycles (considered to be run-out) at constant load level are applied to the specimen. After each completed step, the load level is increased with a fraction of the yield strength while keeping the stress ratio constant. This procedure is generally repeated until failure of the specimen.

In this particular study, each step consisted of 500,000 cycles of a sinusoidal load with a stress ratio (R_i) equal to 0.1 and a testing frequency of 15 Hz. The initial load level must be considered below the expected fatigue strength of the specimen. Therefore, the initial two tested specimens, Specimen 1 and 2, were initially loaded at a load level of 220 MPa. Then, every step, the stress level in the section with maximum stress levels was increased by approximately 76 MPa (i.e. 10% of the yield strength). Given that failure only happened at a load level of 820 MPa, subsequent tests have been started at an increased initial stress level of 589 MPa. However, when a specimen failed in the first step, all subsequent specimens with the same configuration were again started at a lower initial stress level. The different loading steps during the four-point bending tests are depicted in Figure 3.4b. The initial stress levels that were used can be found in the summary table 3.5 on page 78.

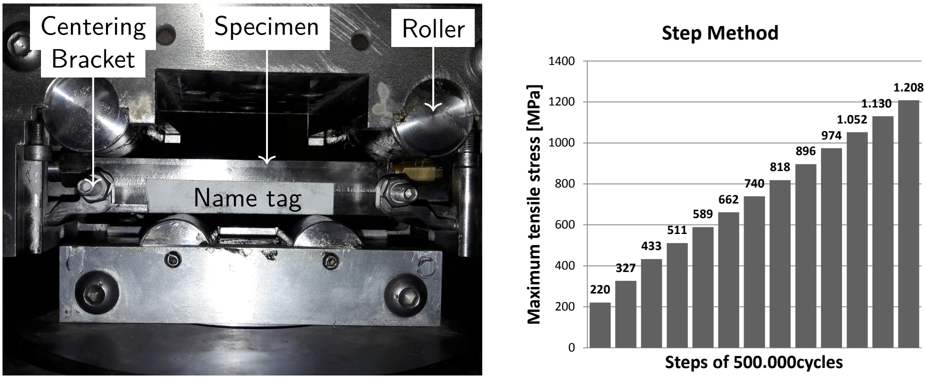

(a) (b)

Figure 3.4: All specimens were subjected to four-point bending fatigue tests according to the step method. (a) specimen installed in the four-point bending test setup and (b) the maximum tensile stress levels in each load step.

3.3.2 Test End Definition

The test procedure described in the previous paragraphs is generally repeated until failure of the specimen. During this investigation, the failure of a specimen was defined differently for specimens with and without embedded eSHM system. Specimens without integrated eSHM system were subjected to the loading until the deformation of the specimen exceeded pre-set limits corresponding to the complete rupture of the specimen.

On the contrary, the test procedure of specimens with integrated eSHM systems was stopped at crack detection by the eSHM system. Figure 3.5 shows the pressure output of the eSHM system during the entire test (left) and a detailed view on the last cycles of the test (right). Initially put under vacuum conditions, the capillary became very sensitive to leaks. During initial testing, no crack was present in the test specimen and the internal capillary pressure remained unchanged and equal to the initial pressure level of approximately 0.4 bara (see Figure 3.5 (left)). However, a fatigue crack initiated at the specimen's outer surface and grew inward towards the capillary. When the crack finally breached the capillary, the crack formed a leak connection between the capillary and the ambient conditions outside the specimen. The resulting leak flow increases the pressure level inside the capillary towards the ambient pressure level. According to Figure 3.5 (right), this happened after about 218,750 cycles or 14,585 s of testing time for Specimen 16. In the following period, the pressure sensor installed at the capillary end registers a rapid pressure increase towards ambient pressure conditions. The test procedure was stopped when the capillary pressure exceeded the pre-set limit of 0.95 bara. Figure 3.5 (right) indicates that, according to this methodology, Specimen 16 failed after 219,377 cycles. All test specimens were successfully stopped by the eSHM system. The specimens still withstood the loading and were not ruptured. In order to be able to inspect the fracture surface, the specimens were loaded further at the load level of the last step until final rupture of the specimen occurred.

3.3.3 Complementary tests

Besides the actual result of the fatigue tests and the fractographic analysis to retrieve the fatigue initiation location, some additional tests were performed to provide more insight in the fatigue test results. As fatigue initiation is strongly depending on the surface finish of the specimens, the surface roughness of the tensile stressed surface of the specimens was determined on a Perthometer PRK (Mahr GmbH, Göttingen, Germany). With a scan length of $l_t = 4.8$ mm and a cut-off wavelength of 0.8 mm, four different scans were performed near the location of the fracture (two on each side of the fracture). The average R_a and R_t values, and their standard deviations, are presented in Table 3.5 on page 78. All specimens had an external

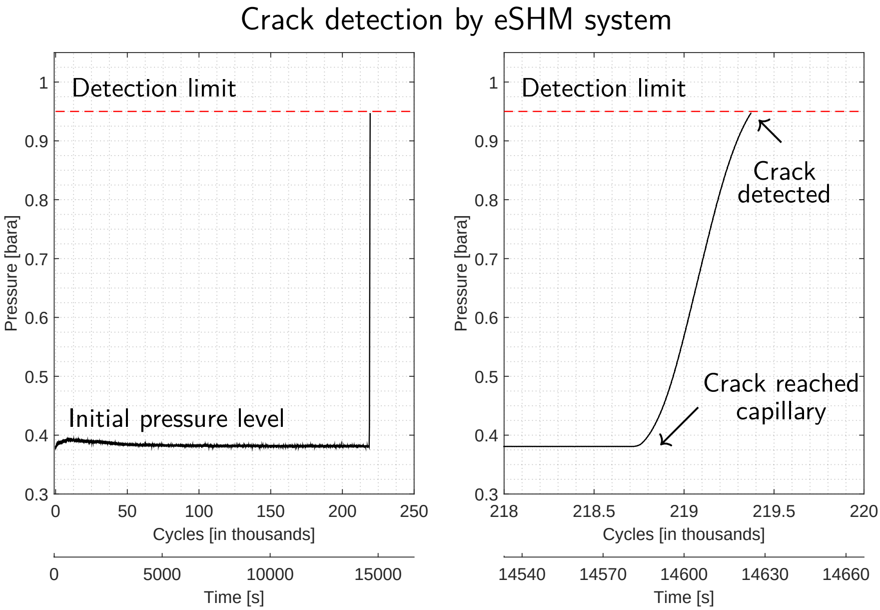

Figure 3.5: Crack detection by eSHM system for Ti-6Al-4V Specimen 16. Capillary pressure output during the entire test (left) and a detailed view on crack detection (right).

surface roughness of 0.24 µm $\leq R_a \leq$ 0.79 µm and 2.59 µm $\leq R_t \leq$ 7.39 µm. Considering that cracks may also have initiated at the internal free surface of the capillary, the capillary surface roughness was also measured. Using Electrical Discharge Machining (EDM), the specimens were longitudinally cut halfway through the capillary. The most tensile stressed half of the capillary was scanned three times using a scan length of $l_t = 15$ mm and cut-off wavelength of 2.5 mm.

Subsequent to the fatigue tests, the hardness of the specimens was measured using Vickers hardness with a Struers Duramin tester (Struers, Ballerup, Denmark). Prior to the hardness measurements, the surface was subsequently polished with a P1200 and P4000 abrasive grinding paper in order to reduce the surface roughness ($R_a \leq 0.1$) as to improve the read-out of the hardness measurements. A 9.807 N load was applied during 10 s for all hardness measurements. Six hardness measurements were performed on each specimen and the average hardness and standard deviation are reported in Table 3.5 on page 78.

3.4 Analysis of the Test Results

A summary of all the specimen's test results can be found in Table 3.5 on page 78, including the fatigue test results as well as the hardness and roughness measurements of the outer surface and capillary surface. The following sections will subsequently discuss the integration of a capillary inside conventional Ti-6Al-4V specimens, the integration of a capillary using laser based AM and finally a study on the location of the capillary.

3.4.1 Integration of an Ideal Capillary

A first analysis is devoted to the effect of the integration of a capillary feature inside Ti-6Al-4V specimens. Six reference specimens were produced using conventional manufacturing techniques without integrated capillary. Three more specimens were produced with an integrated capillary. First the fatigue test results and fractographic analysis will be discussed. Secondly, simulations will be discussed.

Fatigue test results and fractographic analyis

The fatigue test results of the conventional specimens produced from wrought Ti-6Al-4V material are summarized in Table 3.2. The six first specimens without capillary failed between 820 and 896 MPa. The first two specimens were initially loaded at very low stress levels to be sure failure would not occur in the first step. Otherwise, the failure would not provide any information about the fatigue strength of the material. Because of the consistent failure at 820 MPa (maximum stress level inside the specimen), initial stress levels were increased to reduce testing time. Even with significant differences of the initial stress level, and thus the amount of cycles till failure, the actual outcome of the tests is very constant. Five out of the six specimens failed when the maximum stress level inside the specimen was 820 MPa, while a single specimen performed better with failure at 896 MPa. This result is used as benchmark for the following tests and shows that stress cycles at lower stress levels did not significantly influence the fatigue strength as assumed by the step method.

Fractographic analysis was conducted on the fracture surfaces of Specimens 4, 5 and 6. Figure 3.6 presents the SEM micrograph taken from the

Table 3.2: Fatigue test results of wrought Ti-6Al-4V specimens with and without integrated capillary

	a [mm]	Steps till Failure [-]	Stress Level Initial [MPa]	Stress Level Failure [MPa]	Cycles in Last Step [-]
Wrought Ti-6Al-4V Specimen without Capillary					
Specimen 1	-	15	220	820	40,699
Specimen 2	-	8	220	820	300,390
Specimen 3	-	3	665	820	186,599
Specimen 4	-	4	589	820	149,429
Specimen 5	-	4	589	820	77,851
Specimen 6	-	5	589	896	247,865
Wrought Ti-6Al-4V Specimen with Capillary					
Specimen 7	2	6	589	976	384,270
Specimen 8	2	2	589	662	459,360
Specimen 9	2	4	433	662	364,287

fracture surface of Specimen 4. The fatigue crack nucleations are located at the bottom left corner of the specimen. Similarly, Specimen 5 failed due to an internal defect also located in the beam corner. The SEM images of the fracture surface of Specimen 5 are not shown in this text because of the similarity with Specimen 4. Specimen 6 failed due to the presence of an internal defect in the bulk material, as shown in Figure 3.7.

Three other specimens, also produced from wrought Ti-6Al-4V, but with integrated capillaries, showed both better and worse fatigue properties than the specimens without capillaries. Specimen 7 failed only at a load level of 976 MPa, while Specimens 8 and 9 failed at 662 MPa. Specimen 8 did not fail in between the inner rollers of the test set-up, but at the contact point with an outer roller, close to the M5 connection with the pressure sensor. The stress concentration around the roller led to premature failure of the specimen. The actual stress level at failure of the specimen could have been higher than 662 MPa since 459,360 cycles were already survived in this step. In order to overcome the issue of stress concentrations around the rollers, the threaded M5 connections have to be redesigned for future tests in order to maximize the distance between the M5 thread zone and the load insertion by the roller. Fractographic analysis revealed that Spec-

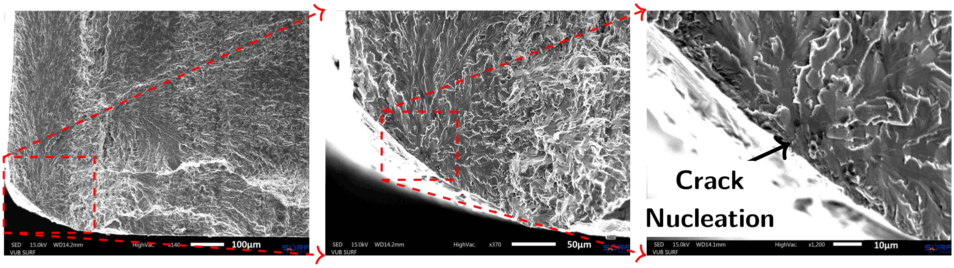

Figure 3.6: SEM images of the fracture surface of Specimen 4 (wrought material without capillaries). The fatigue crack initiated from the bottom left corner of the specimen.

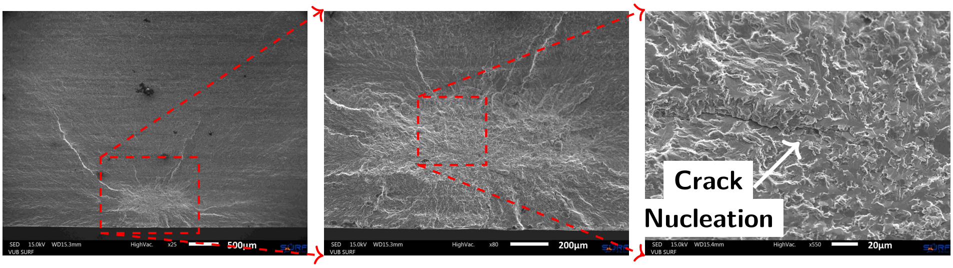

Figure 3.7: SEM images of the fracture surface of Specimen 6 (wrought material without capillaries). The fatigue crack initiated from an internal defect near the bottom of the specimen.

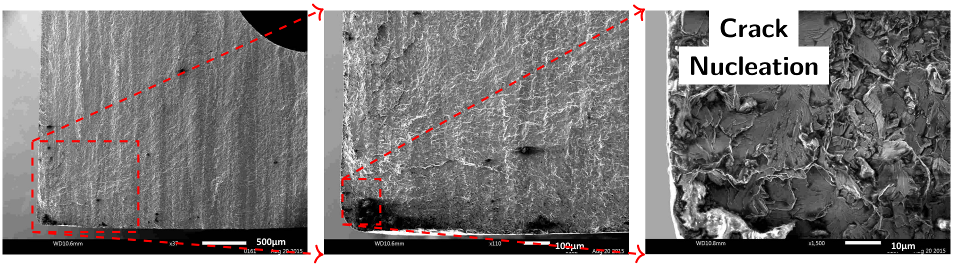

Figure 3.8: SEM images of the fracture surface of Specimen 7 (wrought material with capillary). The fatigue crack initiated from the bottom left corner of the beam.

imens 7 and 9 with integrated capillary failed due to a fatigue crack that initiated from the beam corner that was located closest to the capillary. Figure 3.8 presents the fracture surface of Specimen 7. The fractographic analysis of Specimen 9 is not shown in the current paper since it is very similar to that of Specimen 7. The fatigue crack did not initiate at the capillary surface, likely because of the lower stress levels around the capillary and the low capillary surface roughness (0.55 µm$\leq R_a \leq$0.65 µm). Because of the low capillary surface roughness, the addition of a drilled capillary is modeled without roughness and therefore reffered to as an "ideal" capillary.

FEM Simulations of an Ideal Capillary

The modelling of an "Ideal Capillary" allows analysing the base effect of the addition of a capillary, without its surface finishing complications and resembles quite well the case of a drilled capillary in the conventional Ti-6Al-4V specimens. All simulations were performed using the ABAQUS FEM modelling software (version 6.14, Dassault Systèmes, Vélizy-Villacoublay, France). The load was inserted to the specimen via a surface pressure load of 1 mm width over the full thickness (12 mm) of the specimen and at the location of the inner rollers 50 mm apart. The outer rollers were also simulated through small surfaces of 1 mm width and the full thickness of the specimen (12 mm) to which displacement in the Y-direction and rotations around Y and Z were restricted. The specimens were virtually loaded with a load of $^{37.7}/_{2}$ kN per roller, leading to maximum tensile stress of 589 MPa at the outer surface of the specimen. A tetrahedron mesh was used with a general mesh size of 1 mm and a mesh refinement of 0.25 mm around the capillary. The maximum principal stress levels (in MPa) are plotted along the Z-direction (length direction of the specimen) and the X-direction (from the corner with capillary (x = 0 mm) to the other corner (x = 12mm)). The capillary is located at a distance $a = 2\ mm$ from the outer surfaces of the specimen.

A comparison of the modelling results presented in Figure 3.9 shows the effect of the integration of a capillary. According to Figure 3.9 (left), the addition of the capillary slightly increases (+3%) all stress levels inside the specimen. The stress levels at the capillary remain well below the stress levels found at the bottom of the specimen. It is therefore expected that for materials without defects, fatigue cracks will not initiate at the capillary location. Fractographic analysis of specimens with drilled capillaries in wrought Ti-6Al-4V indeed revealed that the fatigue cracks did not initiate at the capillary surface.

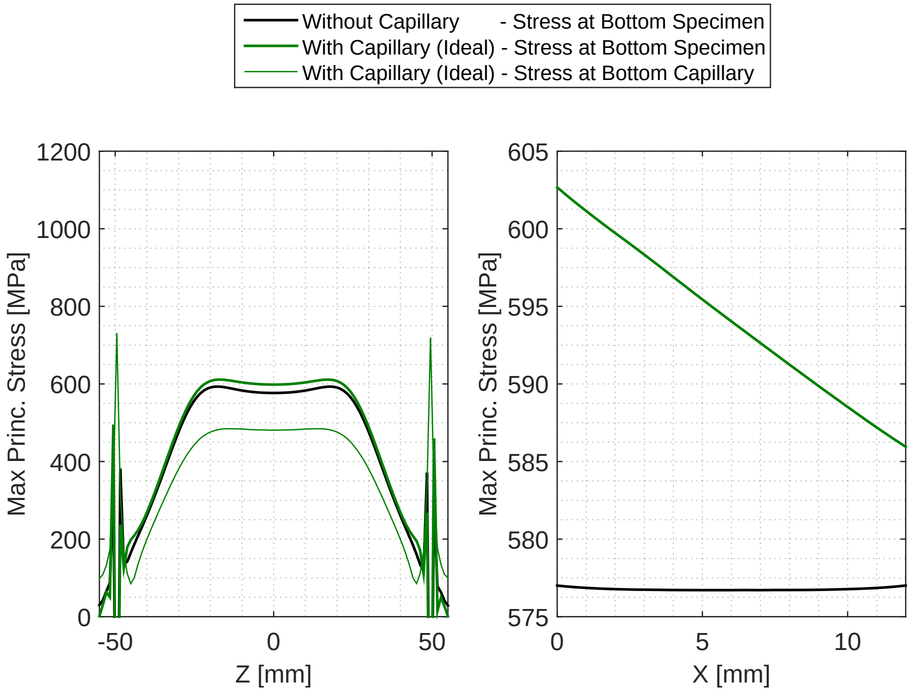

Figure 3.9: The maximum principal stress level plotted in function of the longitudinal Z-direction at the bottom of the specimen and bottom of the capillary (left) and the X-direction at the bottom of the specimen (right). The integration of a capillary slightly increases (+3%) the overall stress level in the specimen. The stress level at the capillary is significantly lower than that at the bottom of the specimen. The stress level increases linearly by 3% from the corner without capillary to the corner with capillary.

When considering the stress pattern along the X-direction in Figure 3.9 (right), the proximity of the capillary near one corner slightly increases the stress level in that corner. Although the difference of the stress level from one corner to the other is limited to only 3%, it is possibly the reason why fatigue cracks seem to prefer this corner as fatigue initiation location as found during the fractographic analysis of Specimens 7 and 9. Further studies are needed to analyse this effect.

3.4.2 Effect of Capillary Surface Roughness

The previous test campaign was extended with Ti-6Al-4V specimens produced by laser based DED. Specimens without capillary (reference) and specimens with capillary were tested. The capillary was added during the AM process by not scanning the area occupied by the capillary. The capillary surface roughness of an AM specimen differed largely from the capillary surface roughness obtained by a drilling operation. The surface finish of the drilled capillaries in wrought Ti-6Al-4V (Specimens 7–9) fell between $0.55\ \mu\text{m} \leq R_a \leq 0.65\ \mu\text{m}$ and $5.86\ \mu\text{m} \leq R_t \leq 10.20\ \mu\text{m}$. The printed capillaries of Specimen 12 and Specimen 13 have a more rough surface, characterized by $13.83\ \mu\text{m} \leq R_a \leq 13.88\ \mu\text{m}$ and $70.40\ \mu\text{m} \leq R_t \leq 72.80\ \mu\text{m}$. As to evaluate the influence of the capillary surface roughness on the fatigue performance of AM specimens, an additional drilling operation was performed on the printed capillaries in Specimens 14–16. As will be shown, the drilling operation has not been succesfull on all specimens. Although the capillary in Specimen 14 obtained a surface finish as good as the drilled capillaries in the wrought Specimens 7–9, some deep notches remained present in Specimens 15 and 16. Simulations were again performed to confirm the effect of the capillary surface roughness on the fatigue test results.

Fatigue test results

In contrast with the predictions from the literature, the stress level at failure of the additively manufactured specimen without capillaries were considerably higher than the reference specimens produced from wrought Ti-6Al-4V. Based on previous testing experience on a Ti-6Al-4V specimen produced by laser based DED (but without stress relief and therefore not included in this study), which failed at a load level of 1293 MPa, it was decided to increase the initial load level to reduce testing time. Starting at initial load levels of 896 and 974 MPa, respectively, Specimen 10 and Specimen 11 only failed in the fourth step at a load level of 1208 MPa. As opposed to Specimen 10, Specimen 11 was subjected to a higher initial load level but with smaller load increments, but both specimens failed at the same load level of 1208 MPa. At these load levels, a considerable part of the specimen is already stressed beyond the yield limit of the material. Since further increasing the stress level would not have led to interpretable results, Specimen 11 that survived 500,000 cycles at 1208 MPa was subjected to the same loading until it finally failed. As compared to the reference

Table 3.3: Fatigue test results of AM Ti-6Al-4V specimens produced by laser based DED with and without integrated capillary

	a	Steps till Failure	Stress Level Initial	Stress Level Failure	Cycles in Last Step
	[mm]	[-]	[MPa]	[MPa]	[-]
AM Ti-6Al-4V Specimen without Capillary					
Specimen 10	-	4	896	1208	308,275
Specimen 11	-	4	974	1208	951,150
AM Ti-6Al-4V Specimen with Printed Capillary					
Specimen 12	2	3	433	589	234,025
Specimen 13	2	3	511	662	262,773
AM Ti-6Al-4V Specimen with Printed/Drilled Capillary					
Specimen 14	2	1	433	433	134,413
Specimen 15	2	1	433	433	236,609
Specimen 16	2	1	589	589	219,377

samples from wrought Ti-6Al-4V (Specimens 1 till 6), the AM specimens resisted more than two million more cycles at increasing load levels beyond the failure level of the wrought Ti-6Al-4V. These observations are in line with the higher hardness (372–403 HV) of the specimens as compared to the wrought Ti-6Al-4V specimens (340–356 HV), expecting higher tensile strength and improved fatigue performance for the harder specimens. Although additively manufactured Specimens 10–13 and Specimens 14–16 were subjected to different heat treatments, no clear differences in hardness could be observed.

Figure 3.10 shows the micrograph of the fracture surface of Specimen 10. The river marks that are present in the micrograph on the right in Figure 3.10 indicate that the crack was nucleated due to a triangular shaped void located in the bulk material. Also the fatigue crack in Specimen 11 initiated at an internal defect. Because of the similarity, the fracture surface of Specimen 11 is not shown in this text.

The capillary surface roughness deteriorated the fatigue performance of Specimen 12 and Specimen 13. Fatigue cracks have initiated at the capillary surface at stress levels (589 MPa and 662 MPa) well below those obtained for the additively manufactured specimens without capillaries. The fracture surface of Specimen 12 is shown in Figure 3.11. The fracture surface of Specimen 13 is not shown in this text since it is very similar to that of Specimen 12. The layerwise addition of contours around the capillary in the vertical build direction has introduced roughness on the capillary surface. The stress concentrations that result thereof lead to premature failure of the specimen. The surface roughness R_a of a capillary produced by laser based DED is found to be more than 20 times higher than that of a drilled capillary.

Because of the latter conclusions from the fractographic analysis, three more specimens (with initial printed capillaries with a diameter of 1.4–1.8 mm) were drilled afterwards with a drill of 2 mm diameter, in an attempt to reduce the capillary surface roughness. Initially loaded at stress levels similar to previous specimens with printed capillaries, the specimens already failed in the initial load step. The specimens failed at low load levels of 433 MPa and 589 MPa, but the fatigue initiation occurred differently in the three specimens. The drilling operation in Specimen 14 was successful and notches were removed from the capillary surface. Fatigue initiation did not occur on the capillary surface, but due to the presence of a severe gas inclusion of approximately 200 µm by 500 µm, as shown in Figure 3.12. As is clear from the fracture surface of Specimen 16 in Figure 3.13 and Figure 3.14 (c), the drilling operation did not remove all traces of the additive building process prior to the drilling operation. Fractographic analysis revealed that the remaining “notches” initiated the fatigue crack. Specimen 15 failed due to the stress concentrations at the roller contact. The M5-thread connection for the pressure sensor is found to be located too close to the rollers. New test specimens will be designed differently such that the M5-thread is located in a stress-less zone.

Figure 3.14 allows comparing the capillary surface finish of a drilled capillary in wrought Ti-6Al-4V material (a), the additively manufactured capillaries using the laser based DED process (b) and the additively manufactured capillaries that were drilled through to reduce the capillary surface roughness (c). Figure 3.14 (b,c) especially deserve some more attention. As is clear from the middle figure in column (b), the tracks are clearly visible as the ridges on the capillary surface. Those ridges are not all exactly parallel to each other. This is because of the lack of proper process control by the use of a constant laser power (500 W) and constant linear scan speed (1000 $^{mm}/_{min}$). With the start of each contour around the capillary, the laser is switched on and the nozzle moves at a constant speed. In the very

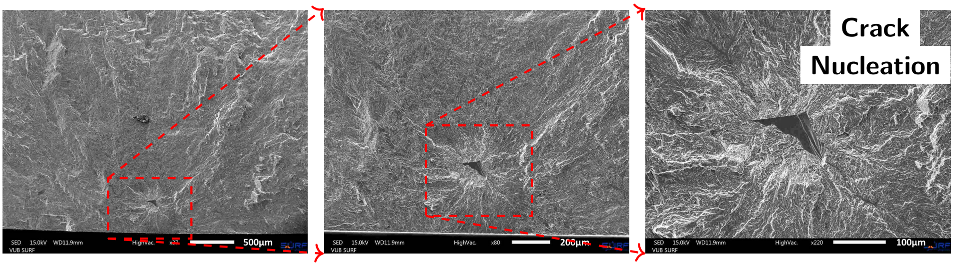

Figure 3.10: SEM images of the fracture surface of Specimen 10 (AM material without capillary). The fatigue crack initiated from an internal defect near the bottom of the sample.

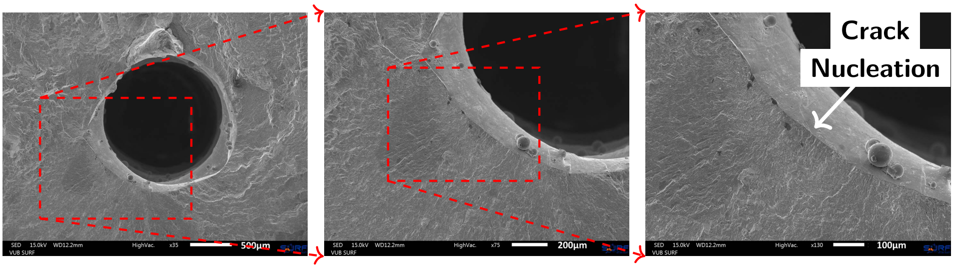

Figure 3.11: SEM images of the fracture surface of Specimen 12 (AM material with printed capillary) reveal that the fatigue crack initiated from a notch formed by the severe surface roughness at the capillary.

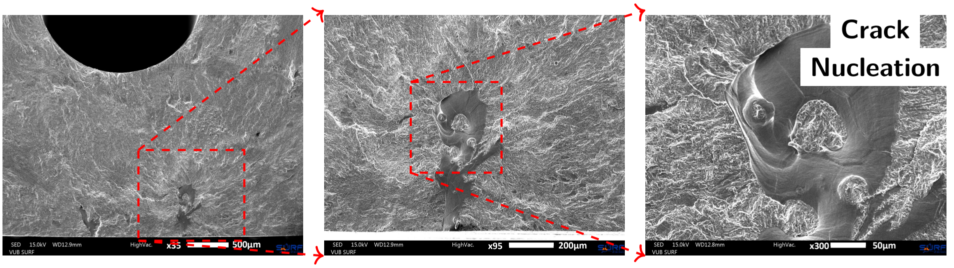

Figure 3.12: SEM images of the fracture surface of Specimen 14 (AM material with drilled capillary). The fatigue crack initiated from a large (sub-) surface defect at the bottom of the sample.

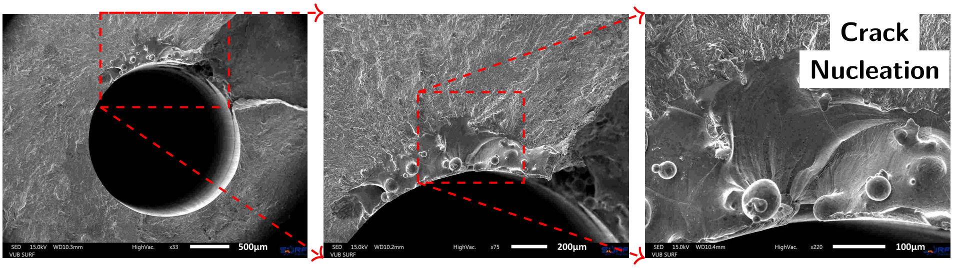

Figure 3.13: SEM images of the fracture surface of Specimen 16 (AM material with printed capillary after drilling operation). The drilling operation did not sufficiently remove the surface roughness of the printed capillaries and therefore did not solve the initiation issue around the capillary.

early beginning of the deposition, the material is not sufficiently heated and the melt pool did not grow to its full size before the nozzle moved away, giving rise to a very small track tip. Gradually heating up the substrate, the melt pool reached its intended size and with it also the track became wider. Each such start location of a track is seen as a narrowed track, as indicated on Figure 3.14 (b). These locations are regions of larger capillary diameters and are thus locations of deeper notches. Even with the drilling operation, some of these deep notches remained present, as depicted in Figure 3.14 (c). A proper closed loop process control system should increase the initial laser power such that the melt pool gains its intended width before moving the nozzle [150, 151].

FEM Simulations of a Capillary with Surface Roughness Modelling

Although the integration of an “Ideal Capillary” did not alter the fatigue initiation location, the roughness of the additively manufactured capillary leads to fatigue initiation at the capillary surface. To confirm this statement, FEM simulations were performed with inclusion of an exact representation of the capillary surface roughness as found on Specimen 12. The specimen was cut halfway through the capillary, such that pictures of the capillary surface could be taken. Through variation of the illumination of the specimen and the development of an edge detection technique, the capillary surface shape of Specimen 12 was determined (see Figure 3.15).

A capillary section of about 9 mm in longitudinal length was reconstructed

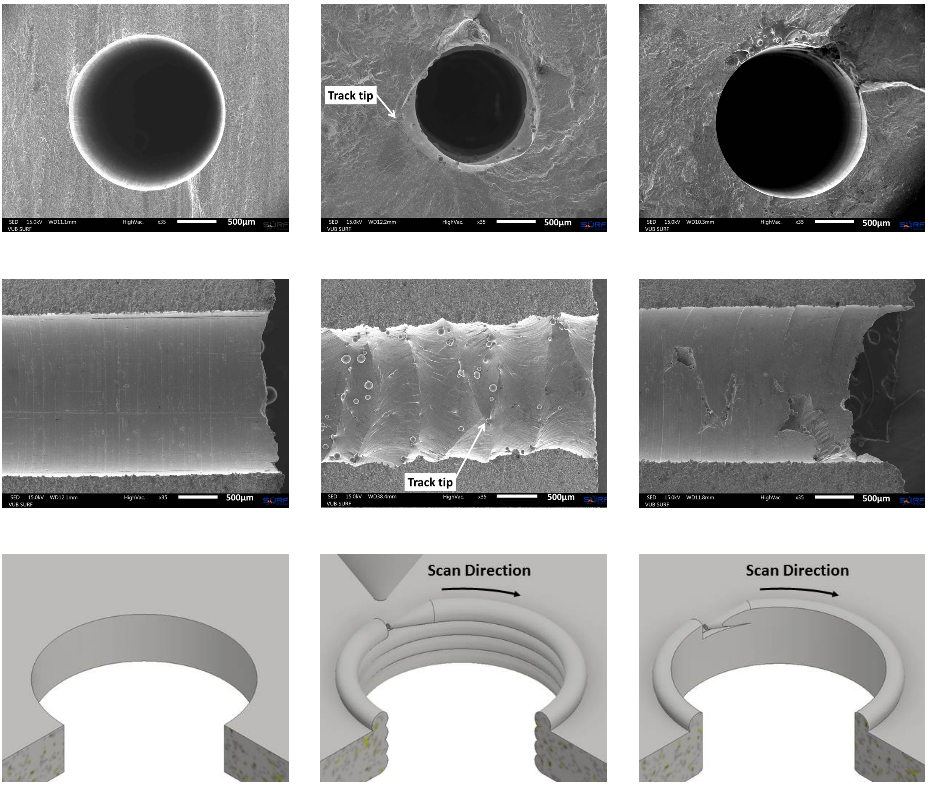

(a) (b) (c)

Figure 3.14: Cross sectional view (top), longitudinal view (middle) and CAD representation of the production process (bottom) of a (a) drilled capillary in wrought Ti-6Al-4V (Specimen 9), (b) vertically built capillary by laser based DED (Specimen 12) and (c) vertically built capillary by laser based DED with additional deep gun drilling (Specimen 16). The fracture surface is on the right for the middle figures.

and modelled in the CAD model of the specimen used for the FEM simulations. Sub-modelling was used to enable the use of a finer mesh at the capillary surface while limiting the computational effort. First a general FEM model of the entire specimen is solved with a coarse tetrahedral mesh with a general mesh size of 1 mm. Secondly, the solution obtained from this first analysis is coupled to a second, smaller, model in which a finer global mesh size is used (0.25 mm) with a further refinement on the rough capillary surface (0.05 mm). The solution of this second FEM analysis

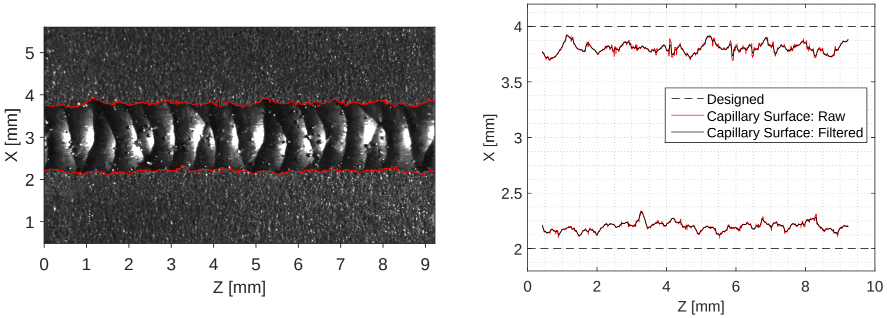

Figure 3.15: Capillary surface edge reconstruction through Matlab image processing of optical images from the capillary surface edge (left) and filtering to remove reconstruction/measurement noise (right).

provides a more accurate determination of the stress levels at the capillary surface. Similarly to the simulations with an “Ideal Capillary”, a load of $^{37.7}/_{2}$ kN per roller, the load level at which Specimen 12 failed, was applied to the specimen.

It is clear from the simulation results presented in Figure 3.16 that the surface roughness of the laser based DED process induced stress concentrations that surpass all stress levels expected in a specimen with an “Ideal Capillary”. The roughness on the capillary makes the capillary surface a preferred location for crack initiation. On top of this capillary roughness, the presence of unmelted particles furthermore increased the capillary surface roughness and can cause crack nucleation.

3.4.3 Topology study of the integrated capillaries

The location of the capillary is crucial in terms of early fatigue crack detection by the eSHM system. A closer location of the capillary near the tensile stressed surface of the specimen allows earlier detection of growing cracks, but increases the chances of crack initiation at the capillary surface. A capillary topology study was performed on wrought Ti-6Al-4V specimens to avoid the effect of material imperfections, residual stresses and capillary surface roughness.

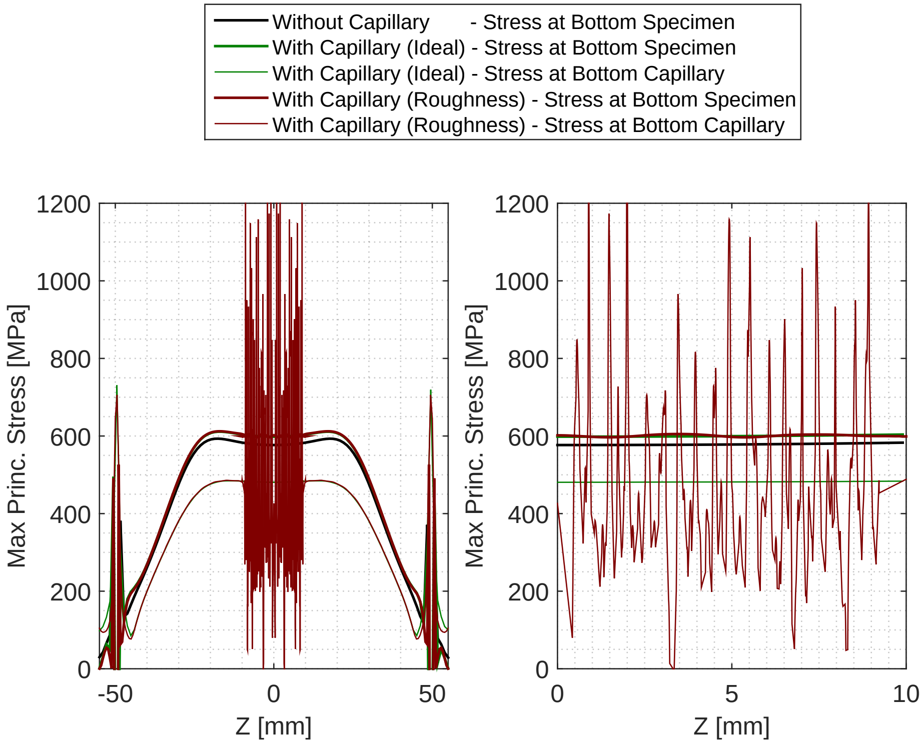

Figure 3.16: The stress level is plotted in a function of the longitudinal Z-direction at the bottom of the specimen and bottom of the capillary. The stress concentration caused by the roughness of the capillary surpasses all stress levels of the specimen with smooth capillaries. The capillary becomes the place were fatigue initiation can be expected.

Fatigue test results and fractographic analysis

Specimens 7,8 and 9 had a capillary located at a distance a=2 mm. The capillary of Specimen 17 was located at a= 3mm and was tested in a similar configuration as Specimens 7 8 and 9. Specimen 17 performed equally well as Specimen 7 with a stress level at failure of 976 MPa and better than Specimens 8 and 9. It has to be noted again that Specimen 8 failed due to a stress concentration at the roller location and almost succeeded the load step at a stress level 662 MPa. It is therefore to be expected that Specimen 8 would have reached the next load step at a stress level of 740 MPa. Fracture analysis has shown that the fatigue crack initiated

Table 3.4: Fatigue test results of wrought Ti-6Al-4V specimens with capillary located at variable distances 'a'.

	a	Steps till Failure	Stress Level Initial	Failure	Cycles in Last Step
	[mm]	[-]	[MPa]	[MPa]	[-]
Wrought Ti-6Al-4V Specimen with Drilled Capillary					
Specimen 7	2	6	589	976	384,270
Specimen 8	2	2	589	662	459,360
Specimen 9	2	4	433	662	364,287
Specimen 17	3	3	820	976	191,196

from the outer surface of Specimen 17. The fracture surface is presented in Figure 3.17 of which the right picture shows the presence of the faceted surfaces at the fatigue initiation location. Fatigue initiation again occurred on the side where the capillary is located. Although more tests are required to confirm this statement, fatigue initiation does not occur at the drilled capillary. The stresses are expected to remain well below those found at the specimen edge (see simulations in section 3.4.1). With increasing distance, the stresses at the capillary edge are even expected to decrease further, decreasing the likelihood of fatigue initiation around the capillary. The experimental test confirmed fatigue initiation at the outer, most tensile stresses, surface. With a failure only at a stress level of 976 MPa, the specimen with integrated capillary of the eSHM outperformed all specimens without capillary.

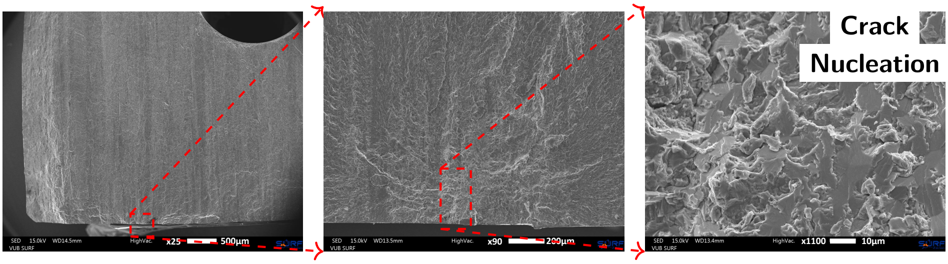

Figure 3.17: SEM images of the fracture surface of Specimen 17 (wrought material with drilled capillary at a distance a = 3 mm). The fatigue crack initiated from the bottom surface of the sample. The faceted surfaces (right) indicate the fatigue initiation location.

3.5 Conclusions

FEM simulations have indicated that the stress levels at the capillary edge remain well below those at the specimen edge. Fatigue crack initiation is therefore expected at the specimen outer surface, as was experimentally confirmed by the fracture analysis of Specimens 7 and 9. The fatigue crack initiated from the corner where the capillary was present. Further tests are required to confirm this effect since FEM simulations indicate that this corner is only favoured by a 3% stress increase in comparison with the other corner.

In contradiction with most literature, the AM Ti-6Al-4V specimens without capillary produced by laser based DED failed only at much larger stress levels as compared to the reference specimens from wrought material. Also their hardness was higher, confirming the same trend. As the AM specimens were heat treated, the effect of residual stresses was omitted from the analysis. The addition of the capillary of the eSHM system lowered the fatigue strength. The geometric inaccuracy of the laser based DED process and the layerwise addition of contours around the capillary in the length direction of the capillary led to the formation of deep notches on the capillary surface. The capillary surface was 20 times rougher as compared to the drilled capillaries inside the wrought specimens. Fatigue initiation occurred due to the stress concentrations induced by the capillary surface roughness and fatigue failure occurred at lower stress levels. A first attempt to reduce the capillary surface roughness only succeeded in Specimen 14. Fatigue initiation did then not occur on the capillary surface but because of the presence of multiple large (sub) surface defects. Because of the large impact of the capillary surface roughness, no interpretations can be made on the use of a different thermal treatment, nor whether the corner closer to the capillary is in favour for crack initiation.

Positioning the capillary further away from the most tensile stressed surface of the specimen (increasing distance ‘a’) decreases the stress levels at the capillary surface. Fatigue initiation is expected not to occur at the capillary edge, as was experimentally confirmed.

From this investigation, it is concluded that the integration of a capillary does not significantly change the fatigue properties of a specimen. The eSHM principle therefore does not jeopardize the structural integrity of the structure. However, the laser based DED process currently lacks a proper process control. The roughness that resulted from the layerwise addition of contours around the capillary limited the fatigue performance of the specimens with printed capillaries. A first attempt to reduce the surface roughness by deep hole drilling through the existing additive manufactured holes did not work out properly since notches remained present after deep gun drilling. In a next test campaign, fatigue properties of Ti-6Al-4V will be investigated for drilled capillaries in a solid block of AM material. Future work will be oriented towards the determination of a suitable post processing step (e.g. chemical etching and abrasive flow machining) to reduce the capillary surface roughness. Surface quality of the integrated capillary is of primary importance not to influence the structural integrity of the component to be monitored.

#	a	Total Steps [–]	Stress Level		Cycles in Last Step [–]	Fatigue Initiation	
			Initial [MPa]	Failure] [MPa]		Location [–]	Cause [–]
Wrought Ti-6Al-4V Specimen without Capillary							
1	-	15	220	820	40,699	-	-
2	-	8	220	820	300,390	-	-
3	-	3	665	820	186,599	-	-
4	-	4	589	820	149,429	Corner	Roughness
5	-	4	589	820	78,851	Corner	Defect
6	-	5	589	896	247,865	Bulk	Defect
Wrought Ti-6Al-4V Specimen with Drilled Capillary							
7	2	6	589	976	384,270	Corner	Roughness
8	2	2	589	662	459,360	Roller	Roller
9	2	4	433	662	364,287	Corner	Roughness
17	3	3	820	976	191,196	Edge	Roughness
AM Ti-6Al-4V Specimen without Capillary							
10	-	4	896	1208	308,275	Bulk	Defect
11	-	4	974	1208	951,150	Bulk	Defect
AM Ti-6Al-4V Specimen with Printed Capillary							
12	2	3	433	589	234,025	Capillary	Roughness
13	2	3	511	662	262,773	Capillary	Roughness
AM Ti-6Al-4V Specimen with Printed/Drilled Capillary							
14	2	1	433	433	134,413	Edge	Defect
15	2	1	433	433	236,609	Roller	Roller
16	2	1	589	589	219,377	Capillary	Roughness

Table 3.5: Summary of Ti-6Al-4V specimens of four-point bending fatigue tests, hardness and roughness measurements. Standard deviation (STD) is given in between round brackets on the right of the average (AVG) value: AVG. (STD.).

Hardness		External Roughness				Capillary Roughness			
Vickers		R_a		R_t		R_a		R_t	
[HV]	[HV]	[µm]	[µm]	[µm]	[µm]	[µm]	[µm]	[µm]	[µm]
Wrought Ti-6Al-4V Specimen without Capillary									
-	-	-	-	-	-	-	-	-	-
-	-	-	-	-	-	-	-	-	-
-	-	-	-	-	-	-	-	-	-
353	(16)	0.51	(0.13)	7.39	(2.28)	-	-	-	-
352	(8)	0.25	(0.05)	2.59	(0.40)	-	-	-	-
352	(9)	0.35	(0.07)	3.90	(0.79)	-	-	-	-
Wrought Ti-6Al-4V Specimen with Drilled Capillary									
356	(20)	0.24	(0.06)	2.66	(0.42)	0.65	(0.17)	10.20	(1.82)
341	(21)	0.40	(0.50)	3.23	(0.42)	0.62	(0.10)	8.35	(1.25)
353	(19)	0.52	(0.10)	5.12	(1.20)	0.55	(0.04)	5.86	(0.66)
-	-	-	-	-	-	-	-	-	-
AM Ti-6Al-4V Specimen without Capillary									
389	(5)	0.36	(0.11)	3.79	(0.59)	-	-	-	-
373	(7)	0.26	(0.12)	3.15	(0.81)	-	-	-	-
AM Ti-6Al-4V Specimen with Printed Capillary									
360	(9)	0.28	(0.18)	4.89	(1.55)	13.88	(0.46)	70.40	(5.21)
377	(3)	0.32	(0.20)	7.18	(2.66)	13.83	(2.20)	72.80	(12.35)
AM Ti-6Al-4V Specimen with Printed/Drilled Capillary									
373	(11)	0.79	(0.11)	5.82	(0.31)	0.60	(0.00)	7.10	(0.25)
383	(5)	0.38	(0.12)	3.55	(0.57)	1.63	(0.06)	57.00	(3.85)
404	(11)	0.43	(0.10)	4.12	(0.71)	7.53	(0.64)	107.30	(17.49)

Chapter 4

Crack size estimation by the eSHM system

Fatigue crack detection by the eSHM system is based on the pressure monitoring of the integrated capillaries. A closer look to the pressure behaviour inside the capillary reveals information about the crack size too. The present chapter will discuss the pressure behaviour inside the capillary. A first model allows retrieving the pressure leakage during the previously described four point bending fatigue tests. A second model predicts the amplitude of Negative Pressure Waves, i.e. the acoustic waves originating from an abrupt leakage. Both models are capable of determining the leak size, closely related to the crack size.

4.1 Introduction

Fatigue crack detection by the eSHM system is based on the pressure variations recorded in the embedded capillaries. The leak flow through the fatigue crack alters the pressure level inside the capillary. This means that the fatigue crack has at least grown to a size that it can create an interconnection between the outside atmosphere and the capillary. The closest distance between the capillary and the surroundings of the specimen is therefore a first measure of the fatigue crack size at detection by the eSHM system. The closer the capillary is located to the outer walls of a component, the smaller the crack can be at detection. However, this measure provides the investigator with a minimal crack size. The actual crack size can be larger since the crack may have initiated at different, further located, locations. This method is therefore not a conservative measure for the fatigue crack size. More elaborated techniques are required to estimate the size of the fatigue crack.

The pressure rise, as shown in Figure 3.5 and repeated in Figure 4.1, is a clear indication of the presence of a leak. A fatigue crack has breached through the capillary. But the pressure measurement reveals more information about the fatigue crack. The mass flow rate through the leak, and thus the pressure rise per unit of time, is closely related to the size of the crack. The size of the leak can be derived from the proposed model and is a measure for the size of the fatigue crack. The proposed model is based on the isentropic flow equations. The model is presented in the following section. The model will be emperically validated on the basis of the three very distinct pressure measurements during the fatigue testing as presented by Strantza et al. [114]. The difference in pressure behaviour was noted in [114], but the actual causes could not be explained. Consequently, important parameters such as crack size and crack closure load will be derived from the comparison with the model.

A second section of this chapter will tackle Negative Pressure Waves (NPWs), acoustic waves that originate from an abrupt density change at the leak location. The pressure waves travel through the capillary and can be used for crack localization purposes (see Chapter 5). Similarly, NPWs are commercially employed as a pipeline inspection technique. The NPWs have been well studied to detect and localize leaks in pipelines. The small amplitude of the NPW is critical for the detection of the NPW. Despite the fact that the amplitude of the NPW contains important information about the leak size, no theoretical amplitude model for the NPWs is present in the literature. The isentropic fluid equations were combined with acoustical equations to derive a theoretical model for the amplitude of the NPW. The model provides insight in the parameters affecting the amplitude of the NPW: leak cross sectional area, pipeline cross sectional area, pressure conditions (vacuum/overpressure, choked/adapted flow) and gas properties. The theoretical model was empirically validated and shown to be a very good fit under all tested configurations. The provided insight allows selecting suitable pressure sensors for the detection of NPWs and estimating the leak size on the basis of the amplitude of the NPW.

4.2 Pressure rise by the leakage flow through a fatigue crack

4.2.1 Model and assumptions

A closer look to the last seconds of the pressure measurement presented in Figure 4.1 reveals the pressure rise is not a continuous pressure increase but shows sinusoidal pressure fluctuations along a line of increasing capillary pressure. A more detailed view on the last seconds of the fatigue test is provided in Figure 4.1

The net increase of the pressure inside the capillary is a result of the leak flow, while the pressure fluctuations are a result of the deformation of the structure. The model calculates the pressure inside the capillary during the four point bending fatigue tests. The crack opening and closure, the deformation of the structure and the flow through the fatigue crack are modelled. Fitting the model to real experiments allows deriving the leak area and thus the fatigue crack opening at the moment of crack detection by the eSHM system. This opening is related to the size of the crack and therefore forms a measure for the fatigue crack size at detection by the eSHM system. The model is based on the following assumptions:

- The fluid medium, air, is considered as an ideal gas
- The flow is assumed to be isentropic. An isentropic process is a process where all types of frictional effects are neglected and no heat transfer takes place. Thus, the process is considered as reversible and adiabatic.

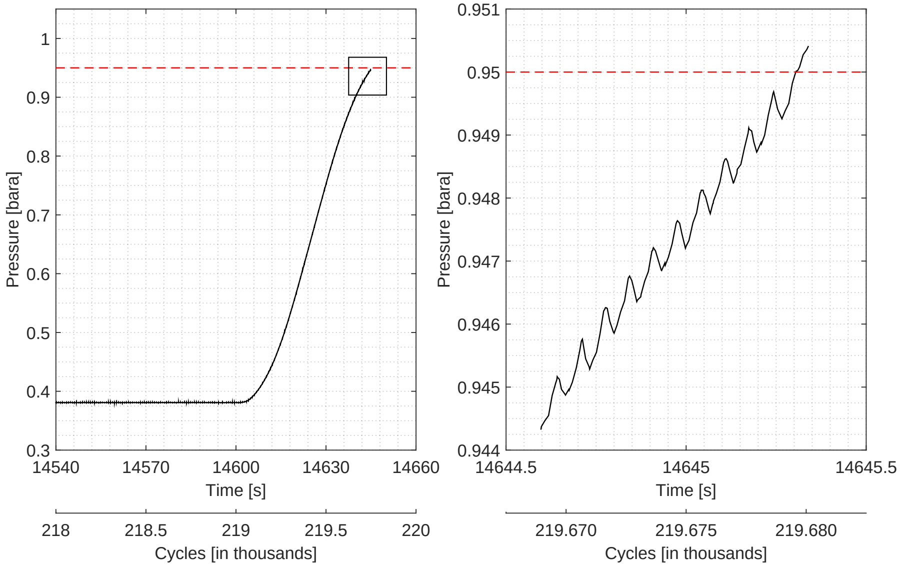

Figure 4.1: Crack detection by eSHM system for Ti-6Al-4V Specimen 16, as discussed in Chapter 3. Fatigue crack is detected by the pressure rise inside the capillary (left). A detailed view on capillary pressure reading during the last second of the test (right) shows pressure pulses on a rising pressure slope.

- The crack is assumed closed below a load limit F_{open} and is considered to open linearly with increasing load levels above the load F_{open}.

Another assumption, but of less importance is that, given that most practical tests were conducted with the capillary of the eSHM under vacuum conditions, also this model is derived for the case that the capillary is initially put under vacuum pressure. The model is also applicable to overpressure cases.

For each consecutive time step Δt, the process chain in Figure 4.2 is completed and the capillary pressure at the end of the time step is computed. The pressure ratio across the leak P_{amb}/P_{cap} determines whether the flow is choked ($M_l = 1$) or adapted ($M_l < 1$). M_l is representing the Mach number. In case of choked flow conditions, the mass flow rate through the leak is limited and flow speed equals the speed of sound in the leak. In case of adapted flow, the leak flow speed is less than the speed of sound. The product of the actual flow speed through the leak, the density of the air in the leak and the leak size (area) allows estimating the mass flow rate through the leak. In one time step, the mass added inside the capillary is limited to $\Delta m = \dot{m}_l \Delta t$. The new pressure inside the capillary is then calculated on the basis of the additional mass inside the capillary. Since the capillary pressure will rise, mass flow rate will decrease as a consequence of the lowering pressure ratio across the leak.

The flow through the crack is restricted by the opening and closing of the crack depending on the load applied to the specimen during the four point bending fatigue tests. A certain load level is to be surpassed to open the crack and induce the leakage flow. This load level is referred to as F_{open}. The crack is then assumed to open linearly with increasing load levels above this load level. Furthermore, the model will include the effect of pressure fluctuations inside the capillary that are caused by the deformation of the specimen under the applied loads.

4.2.2 Equations constituting the model

Assuming that the air flow results in a negligible velocity at infinity (infinite area), the total ambient properties can be equalled to the static ambient properties:

$$P_{t,amb} = P_{amb} \qquad T_{t,amb} = T_{amb} \qquad \rho_{t,amb} = \rho_{amb} \tag{4.1}$$

with P the pressure, T the temperature and ρ the density of the fluid. The addition of subscript ‘t’ is denoting total flow conditions, subscript ‘amb’ refers to ambient conditions. The assumption of isentropic flow (adiabatic and reversible, thus frictionless flow) allows to state that the total properties of the flow remain unchanged during the expansion

$$P_{t,amb} = P_{t,l} \qquad T_{t,amb} = T_{t,l} \qquad \rho_{t,amb} = \rho_{t,l} \tag{4.2}$$

with subscript ‘l’ referring to conditions in the leak. The same assumption of isentropic flow also allows using the isentropic flow equations, which together with equations (4.1) and (4.2) write:

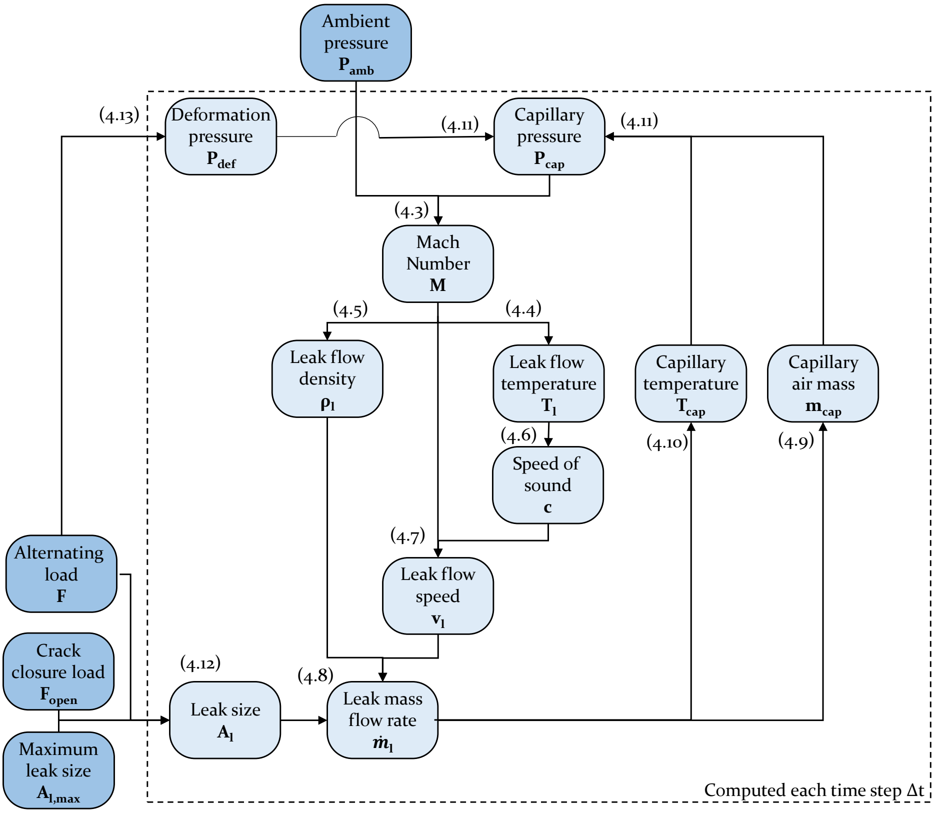

Figure 4.2: Simulation diagram of each computed time step Δt for the reconstruction of the pressure behaviour inside the capillary during the four point bending fatigue tests. The numbers refer to the equations used to solve the problem.

$$\frac{P_{t,l}}{P_l} = \frac{P_{t,amb}}{P_l} = \frac{P_{amb}}{P_l} = \left(1 + \frac{k-1}{2} {M_l}^2\right)^{\frac{k}{k-1}} \tag{4.3}$$

$$\frac{T_{t,l}}{T_l} = \frac{T_{t,amb}}{T_l} = \frac{T_{amb}}{T_l} = \left(1 + \frac{k-1}{2} {M_l}^2\right) \tag{4.4}$$

$$\frac{\rho_{t,l}}{\rho_l} = \frac{\rho_{t,amb}}{\rho_l} = \frac{\rho_{amb}}{\rho_l} = \left(1 + \frac{k-1}{2} {M_l}^2\right)^{\frac{1}{k-1}} \tag{4.5}$$

with '$k = \frac{c_P}{c_V}$' the heat capacity ratio and M_l the Mach number. The pressure inside the leak is equal to the pressure in the capillary $P_l = P_{cap}$. The knowledge of the initial capillary pressure and the ambient pressure then allows computing the Mach number inside the leak (equation (4.3)). Using equations (4.4) and (4.5), the temperature T_l and density ρ_l of the entering air can be computed. The speed of sound is known when the temperature T_l of the entering air is known:

$$c = \sqrt{kR_{air}T_l} \tag{4.6}$$

with k the heat capacity ratio R_{air} the individual gas constant of air. The speed of the entering air v_l can then be found by the multiplication of the Mach number M_l and the speed of sound c:

$$v_l = M_l c \tag{4.7}$$

Knowing the density ρ_l of the entering air, the area of the leak A_l and the flow speed v_l finally allows to compute the mass flow rate through the leak $\dot{m}_l$:

$$\dot{m}_l = \rho_l v_l A_l \tag{4.8}$$

It must be noted here that the area of the leak A_l varies depending on the load applied to the specimen. This effect will be dealt with later (see equation 4.12). The simulation then computes the mass of air that has flown into the capillaries during one time step Δt of the simulation and calculates the mass in the capillary m_{cap} after this time step using a first order Euler Forward Method. The old state is referred to with superscript ‘old’ while the new state is referred to with superscript ‘new’.

$$m_{cap}^{new} = m_{cap}^{old} + \dot{m}_l \Delta t \tag{4.9}$$

The air in the capillary is initially at room temperature. The entering leak flow expands inside the capillary and is therefore colder than the air present in the capillary. As they will mix, the temperature inside the capillary T_{cap} now equals (assuming instantaneous mixing):

$$T_{cap}^{new} = \frac{m_{cap}^{old} T_{cap}^{old} + \dot{m}_l \Delta t T_l}{m_{cap}^{old} + \dot{m}_l \Delta t} \tag{4.10}$$

In order to find the new capillary pressure, it only remains to relate the increase in air mass inside the gallery to an increase in the gallery pressure. This is done using the ideal gas law:

$$P_{cap}^{new} = \frac{m_{cap}^{new} R T_{cap}^{new}}{V_{cap}} (+P_{def}) \tag{4.11}$$

with V_{cap} the capillary volume. The addition of the term P_{def} already included the pressure variations inside the capillary due to the deformation of the structure (see equation 4.13). A new capillary pressure P_{cap} was computed for this time step and can now be used in the computations for the next time step.

The area of the leak depends on the load F acting on the specimen. The crack is assumed closed below a load limit F_{open}. No air flow is then allowed in the model. The crack is furthermore modelled to open linearly when the load exceeds F_{open}:

$$A_l = \frac{F - F_{open}}{F_{max} - F_{open}} A_{l,max} \tag{4.12}$$

The previously described model predicts the airflow through the leak and the capillary pressure rise over time during the fatigue test. The load acting on the specimen deforms the specimen and thus also the integrated capillary, leading to pressure fluctuations inside the capillary. These pressure fluctuations are superimposed on the capillary pressure rise through the leakage flow. The capillary pressure fluctuations are linearly depending on the loads F acting on the specimen:

$$P_{def} = \alpha F \tag{4.13}$$

with α a measure for the sensitivity of the capillary pressure to the load acting on the specimen and, among others, related to the stiffness of the specimen, the capillary static pressure level and Poisson coefficient of the material of the specimen. The sensitivity of the capillary pressure to deformation will further be discussed in Chapter 6. For now, this constant α is found by linearising the pressure variations inside the capillary, during the fatigue testing, but at a moment that the fatigue crack has not yet breached through the capillary (no leak flow).

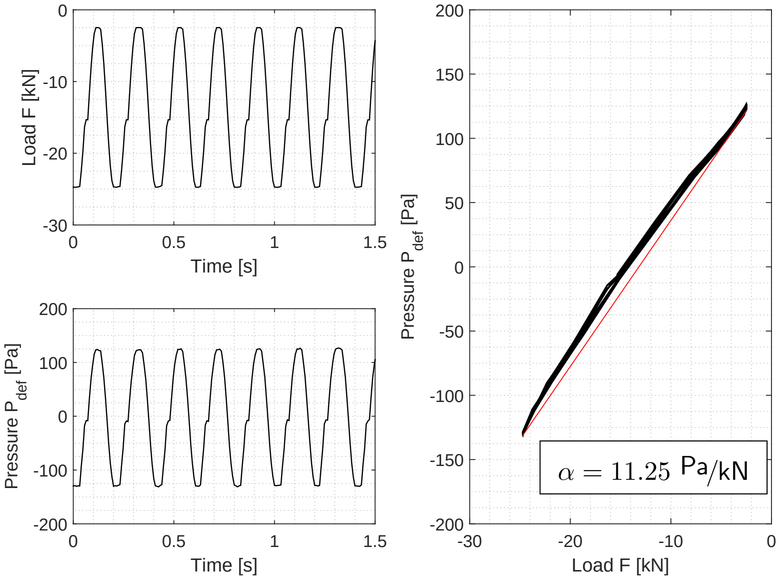

Figure 4.3: Pressure fluctuations caused by alternating load on the specimen. The capillary pressure sensitivity to the load acting on the specimen is derived from the slope on the right: $\alpha = 11.25\ ^{Pa}/_{kN}$.

Validation of the simulation

Strantza et al. [114] presented the pressure measurements at fatigue crack detection by the eSHM system of multiple fatigue tests conducted on stainless steel AISI 316L specimens with an integrated, sinusoidally shaped capillary as depicted in Figure 2.9. The capillaries have a diameter of 3 mm and an overall volume of $V_{cap} = 756\ \text{mm}^3$. The model presented here above will be fitted against these measurements and crack properties will be derived thereof. The common simulation parameters used in the following examples are summarized in Table 4.1. The specific simulation parameters related to the given example are given when the example is discussed.

Loads acting on the specimen during the fatigue testing are recorded during the test campaign and are known. With the initial values fixed by the test campaign, such as initial capillary pressure, initial temperature, etc., the model allows varying three main parameters affecting the pressure behaviour over time. The first being the most important one, the crack size

Table 4.1: Simulation parameters for the reconstruction of the pressure rise by leakage flow through a fatigue crack.

k_{air} [-]	R_{air} [J kg/K]	T_{amb} [K]	$T_{cap,0}$ [K]	P_{amb} [bara]	ρ_{air} [kg/mm^3]	V_{cap} [mm^3]
1.4	287.06	298	298	1	1.02	756

expressed as an area created by the arc between the fatigue crack and the capillary. The width of this area is depending on the opening of the fatigue crack and is therefore a measure of the fatigue crack size. Smaller cracks will not open as much as larger cracks under the same loading conditions. All fatigue cracks are represented by an equivalent flow area, although their shapes may differ. Since the crack opening is depending on the load acting on the specimen, this variable is expressed as the maximum opening the crack will reach during a load cycle ($A_{l,max}$). A second parameter to tweak is (F_{open}), the load at which the crack opens. The third and last parameter (α) is the sensitivity of the capillary pressure to the deformation of the specimen caused by the loads acting on the specimen. The model parameters are varied to find the best fit with the actual measurement.

Since the last model parameter, (α), is not related to the leak phenomena, its value can be derived from earlier pressure measurements during the same test (and same load step) in which no leak phenomenon is involved. The pressure is thus fluctuating around the initial capillary pressure P_0. For the convenience of retrieving α, this pressure level was zeroed in Figure 4.3. The load F and pressure P_{def} are nearly sinusoidal, but the deviations thereof are caused by a too low sampling frequency. This is the primary reason why in a later stage the load is also modelled rather than directly used from the measurement. Modelling the load allows to reduce the time step Δt of the simulation below the sampling interval of the actual measurement, which is required for a good reconstruction of the actual phenomena occurring the crack. Alternatively, the loads can also be interpolated in between the known values. From the analysis in Figure 4.3, α is found to be 11.25 $^{\mathrm{Pa}}/_{\mathrm{kN}}$. The constant is positive since by increasing the compressive loads (more negative F), the region around the capillary becomes more tensile stressed. The capillary is elongated, its volume increases and capillary pressure drops.

The remaining two model parameters, $A_{l,max}$ and F_{open}, were varied till the model predicted a pressure increase similar to the actual measurement.

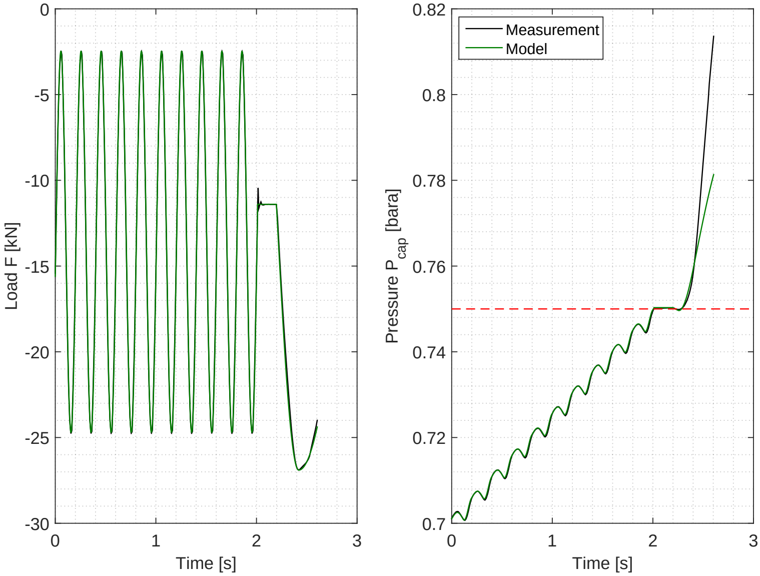

Figure 4.4: Leakage through a fatigue crack during four point bending fatigue test. Model prediction compared with actual measurement. Model parameters: $\alpha = 11.25$ $^{Pa}\!/\!_{kN}$, $F_{open} = -17$ *kN and* $A_{l,max} = 510.4$ μm^2. *The dashed red line indicates the detection limit, the pressure limit at which fatigue testing was stopped (0.75 bara). Simulation parameters:* P_0 = *0.703 bara, dt* $= 2.10^{-4}s$.

Figure 4.4 presents the good comparison of the model with the fatigue test result of Specimen 1 tested in Strantza et al. [114]. Figure 4.5 presents how the pressure behaviour can be understood and is modelled using the simulation model. The comparison with the model allows concluding the following: The fatigue crack was closed for compression loads smaller than 17 kN. Although it follows from a more detailed analysis, one can indeed see from the measurement that at exactly t=2 s, the load was constant at -11.2 kN and no leak flow occurred through the fatigue crack (constant capillary pressure). The maximum opening in the fatigue crack had a size of 510 µm^2. Since the pressure steps between 0 s $< t <$ 2 s are equal in size, it can be concluded that the crack did not grow significantly during the last cycles, as modelled in Figure 4.4. A last interesting comment about this measurement is the stop action. Once the eSHM system has detected the crack (the capillary pressure crosses the pre-set limit of 0.75 bara), a

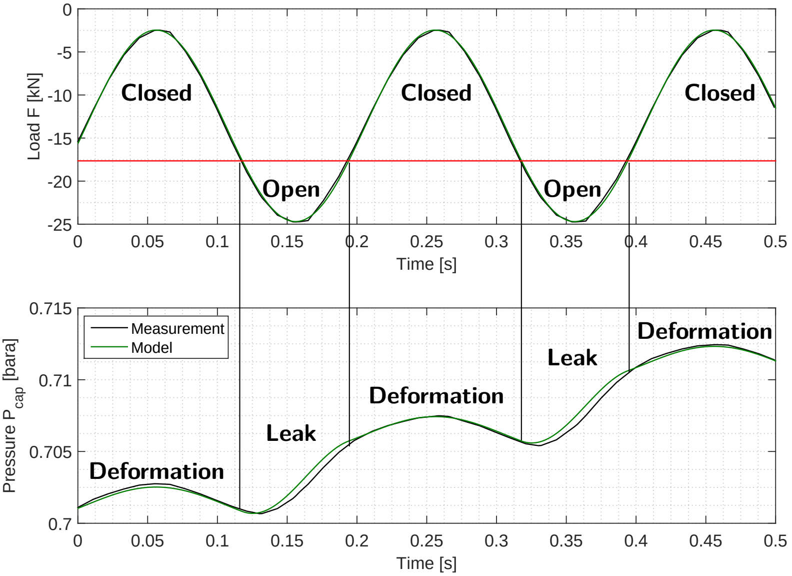

Figure 4.5: The pressure behaviour inside the capillary is a sequence of pressure fluctuations caused by the deformation of the specimen and leakage flow through the opened crack. Leakage flow only occurs when the load exceeds F_{open}. *Even when the crack is opened, the deformation of the specimen leads to an additional pressure variation inside the capillary. Applied to Specimen 1.*

stop action was triggered to the hydraulic test bench. This stop action overloaded the specimen with a single peak load exceeding the highest load level that had acted on the specimen. As a consequence, the crack grew in size during that overload. This can be seen from the pressure increase that is steeper than what the model predicts. In this particular case, the model did not consider that the fatigue crack has grown during the period of evaluation. A single fatigue crack size was fitted to the pressure measurement. With an ideal fit to the first part of the pressure measurement, the model underestimates the pressure change after the overload. It is therefore concluded that the actual leak flow rate (and thus fatigue crack) has grown due to the overload.

The second specimen, Specimen 2 of [114], showed a totally different pressure behaviour. The crack is much larger and pressure rise is much faster.

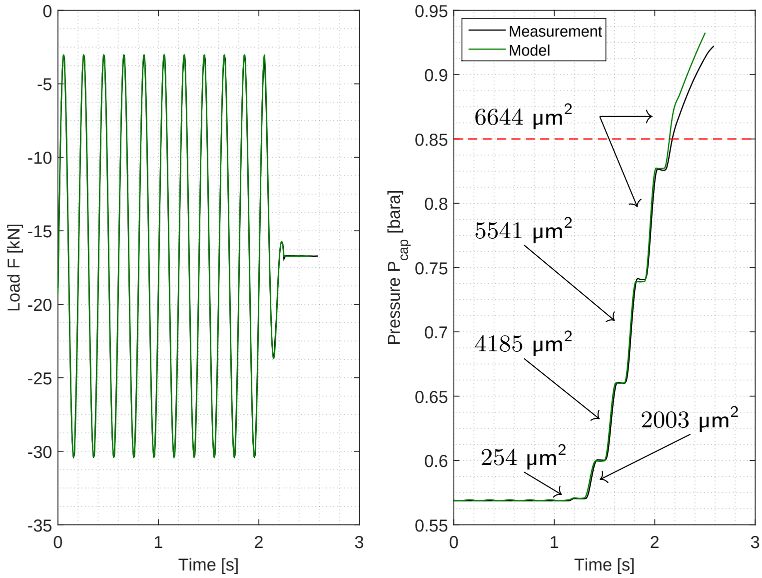

Figure 4.6: Leakage through a fatigue crack during four point bending fatigue test. Model prediction compared with actual measurement. Model parameters: $\alpha = 4\ {}^{Pa}\!/\!_{kN}$*,* $F_{open} = -14$ *kN and variable* $A_{l,max}$*. The crack grows during each fatigue cycle. The dashed red line indicates the detection limit, the pressure limit at which fatigue testing was stopped (0.85 bara). Simulation parameters:* $P_0 = 0.568$ *bara,* $dt = 10^{-4}$*s.*

The pressure steps are increasing in size, which cannot be explained when assuming a constant crack size. The pressure steps are expected to reduce in size since the leak flow will slow down as the pressure differential approaches zero. The crack size must thus have grown in each fatigue cycle, which seems a reasonable assumption since no crack is present at $t < 1.2$ s and in less than one second (five cycles) the crack has reached a size of 6644.24 μm^2, about 13 times larger than the leak size in the previously described test specimen. The size of the crack in each cycle is depicted on Figure 4.6, indicating which pressure step it caused. The specimen was very close to final fracture as could be seen seen from the displacement measurements of the piston. The specimen deformation was increasing in the last five cycles of the test, showing that the crack was growing really fast. The current model assumes that the crack opened at $F_{open} = -14$ kN, but from the comparison with the model, it is probable that the crack opened and

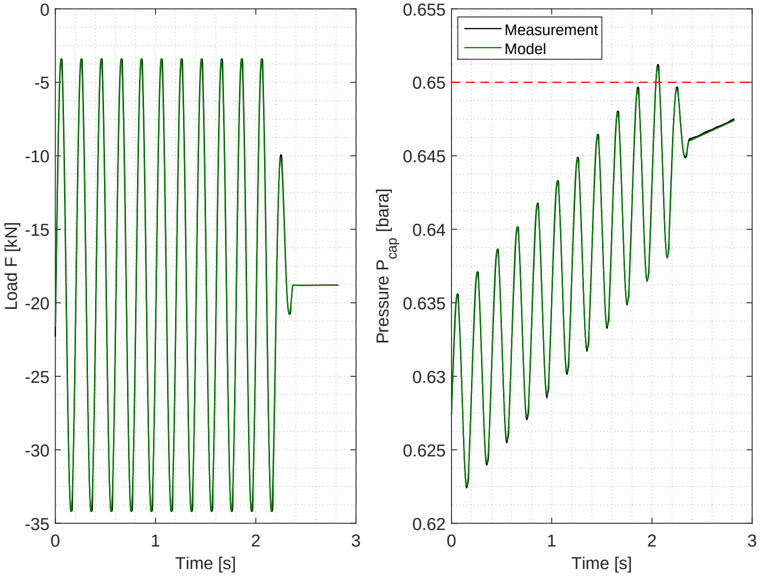

Figure 4.7: Leakage through a fatigue crack during four point bending fatigue test. Model prediction compared with actual measurement. Model parameters: $\alpha = 44.5\ {}^{Pa}\!/\!_{kN}$*,* $F_{open} = -16.3\ kN$ *and* $A_{l,max} = 112.8\ \mu m^2$*. The dashed red line indicates the detection limit, the pressure limit at which fatigue testing was stopped (0.65 bara). Simulation parameters:* $P_0 =$ *0.637 bara,* $dt = 2.10^{-4} s$*.*

closed at different loads. The crack rather seems to open at higher loads ($F_{open} = -$ 22 kN) and to close only at loads below ($F_{close} = -6$ kN).

The discussion of a third specimen, Specimen 3 of [114], will conclude the comparison between the model and the actual measurements. The pressure behaviour is comparable to the first one, except that the pressure fluctuations are more dominant ($\alpha = 44.5\ {}^{\mathrm{Pa}}\!/\!_{\mathrm{kN}}$) and the crack is smaller ($A_{l,max} = 112.8\ \mu\mathrm{m}^2$). The crack seems to open at almost the same load ($F_{open} = -16.3$ kN) as the first specimen discussed. Of particular importance here is the stop procedure. The load is linearly decreasing to the mean value of the sinusoidal load applied before, leaving the crack size intact. It is clear from the pressure behaviour that the crack is still open when a load of -18.5 kN is acting on the specimen. Also after the stop action of the test setup, the model predicts the pressure rise very well, indicating that

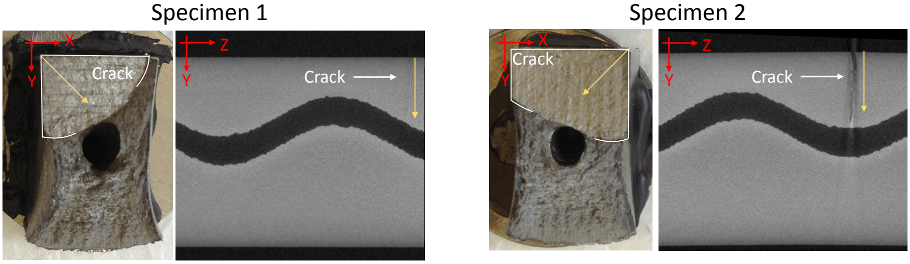

Figure 4.8: Fracture surface and X-ray of Specimen 1 (left) and Specimen 2 (right). The crack is indicated in white while the crack growth direction is indicated in yellow. The cross sectional area taken by the fatigue crack is much larger in Specimen 2.

the fatigue crack did not grow due to the stop action.

Although the actual size of the leak could not be measured during the fatigue testing, fracture surface analysis and X-ray photography of the fatigue test specimen were conducted just after fatigue crack detection by the eSHM system. These pictures, as depicted in Figure 4.8, reveal some information about the crack size. It is clear from this comparison that the fatigue crack in Specimen 2 is much larger than the crack in Specimen 1, as found from the simulation model. The fatigue crack in Specimen 1 is barely visible using X-ray photography since in unloaded condition the crack is closed. The principle of the eSHM system allows characterizing the fatigue crack when loaded and is very sensitive for small cracks that are barely detectable by other NDT techniques, such as the X-ray photography as discussed in this work [116].

4.3 Negative Pressure Waves

Negative Pressure Waves (NPWs) are acoustical waves that arise from the abrupt density change at the leak location. The acoustic waves then propagate away from the leak at the speed of sound and are used as a leak detection and localization methodology for pipelines. Given the hazardous and polluting situations caused by a natural leak and the economic loss thereof, researchers have employed multiple leak detection principles to localize leaks as fast as possible [152, 153]. Also pipeline theft monitoring has been employed for many years in the industry. Among many different strategies, the Negative Pressure Wave (NPW) detection method is one of the most widely adopted to locate a leak [154]. The generation of a NPW is based on the abrupt density change at the leak location in the event of a leak. Considering a pressurized pipeline, the pressure will drop at the leak location, hence the name Negative Pressure Waves. The pressure waves propagate away from the leak towards both ends of the pipeline where they are detected by a pressure sensor. The difference in time-of-arrival at two sensors located on either side of the leak allows deriving the leak location, as will be demonstrated in Chapter 5. Many research efforts focused on the propagation and attenuation properties of the Negative Pressure Waves to improve the localization accuracy [155, 156]. The quality of the pressure data is found to be a critical issue for the success of the methodology [157]. Noise reduction techniques are required to detect the low amplitude NPW [158]. Although critical for the selection of the pressure sensors to be installed, only limited research works are available presenting models for the amplitude of the NPW in liquid media [159] and gaseous media [160, 161]. The most widely used model that Rocha presented for gaseous media is not generally applicable to all pressurization and fluid media types. That formula was empirically derived and focusing on rapid leaks from pressurized pipelines to ambient conditions for the single media methane. The amplitude of the NPW was found to be related to the properties of the gas, the pressure at which the pipeline is operated, the pipeline diameter and most importantly the size of the leak:

Rocha's formula

$$\Delta P = 0.3 P_p \left(\frac{D_l}{D_p} \right)^2 \tag{4.14}$$

with P_p the static pipeline pressure at the leak site, D_l the leak diameter and D_p the pipeline diameter [160, 161]. The constant 0.3 is depending on the fluid properties inside the pipeline.

The model that Rocha presented is well suitable for the prediction of the amplitude of the NPWs for pipelines at high pressures transporting methane gas. As NPWs may also exist inside the capillary of the eSHM system, a new model is required that is valid under a more extensive set of conditions in which the eSHM will be operated for crack detection. The capillary of the eSHM will not be filled with methane and many fatigue tests have already been conducted under vacuum pressure inside the capillary. This new model will be theoretically derived on the basis of the physical understanding of the phenomena causing the generation of the NPW. The isentropic fluid flow equations will be combined with the acoustics equations to derive an optimized model for the amplitude of the NPW under various conditions such as pressurization case, leak sizes, capillary diameters and different gaseous media. Two test setups were build to evaluate the model. A first (large scale) test setup comprised of tubes representing pipeline segments while a second, smaller scale, test setup consisted of capillaries as will be used in the eSHM system. This chapter presents the validation of the theoretically derived formula on the basis of the first, larger scale, test setup. The experimental results will be compared to the theoretical model, allowing to derive conclusions on the feasibility of the model under all tested configurations: pressurization type (vacuum/overpressure, choked/adapted flow), leak diameter, pipeline diameter and fluid medium. It will be demonstrated that the new model can be used under a more broad spectrum of parameters than the current model in place. The following chapter will shortly discuss that the derived formulas are also valid for capillaries (see section 5.3.1).

4.3.1 Theoretical NPW Amplitude Model

Although generally applicable and generalized hereafter, the theoretical model will be derived with the assumption of a capillary under vacuum conditions with a leak to ambient conditions. Considering the fact that air will enter the capillary, we furthermore assume the fluid inside the capillary is air so that we do not have to consider fluid mixing. The event of the leak is considered to be quick, creating an inward flow of ambient air through the leak area, squeezing together the fluid inside the capillary at the leak location. The inward motion of the air entering the capillary can be modelled as a piston pushing air through the leak towards the capillary (see Figure 4.9). The push on the fluid causes the state variables (enthalpy h, pressure P and density ρ) to increase by an infinitesimally small amount (Δh,ΔP and $\Delta\rho$). The propagation of a pressure wave is considered as isentropic ($\Delta s = 0$, with s representing the entropy). The latter assumption implies that the developed model does not include boundary layer attenuation by thermal conduction and viscosity. The smaller the ducts in which the acoustical waves propagate, the more important the effect of the boundary layer and the more important it becomes to model the propagation of acoustic waves as a pseudo-isentropic process [162].

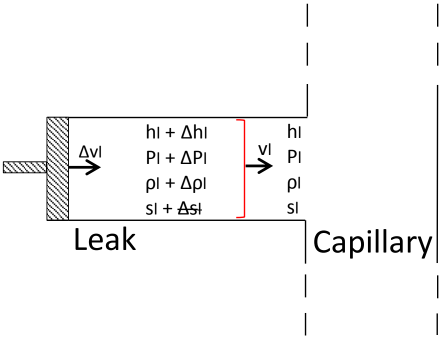

Figure 4.9: Absolute observer

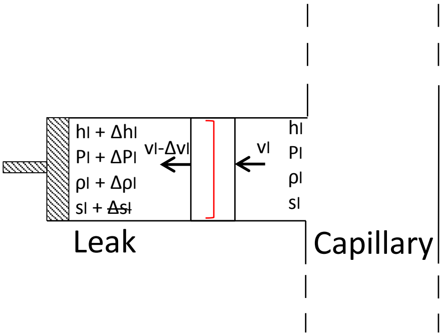

Figure 4.10: Relative observer

Instead of using the perspective of an absolute observer standing still and looking at the wavefront moving to the right in Figure 4.9, we will use the perspective of a relative observer using a control volume that travels together with the wavefront at the speed v_l (see Figure 4.10). The different conservation laws are expressed using the perspective of the relative observer:

Conservation of mass:

$$(\rho_l + \Delta\rho_l).(v_l - \Delta v_l).A_l = \rho_l.v_l.A_l \tag{4.15}$$

Conservation of energy:

$$(h_l + \Delta h_l) + \frac{(v_l - \Delta v_l)^2}{2} = h_l + \frac{v_l^2}{2} \tag{4.16}$$

Isentropic condition:

$$\Delta h_l - \frac{\Delta P_l}{\rho_l} = T_l \Delta s_l = 0 \tag{4.17}$$

and by rearranging and neglecting second order terms:

Conservation of mass:

$$v_l^2 \frac{\Delta\rho_l}{\rho_l} = v_l \Delta v_l \tag{4.18}$$

Conservation of energy:

$$\Delta h_l = v_l \Delta v_l \tag{4.19}$$

Isentropic condition:

$$\Delta h_l = \frac{\Delta P_l}{\rho_l} \tag{4.20}$$

Combining equations (4.19) and (4.20), one finds:

$$\frac{\Delta P_l}{\rho_l} = v_l \Delta v_l \tag{4.21}$$

Together with with equation (4.18), equation (4.21) writes:

$$\frac{\Delta P_l}{\Delta \rho_l} = v_l^2 \tag{4.22}$$

The latter equation is the definition of the speed of sound, thus $v_l = c$. Expressing the speed of the fluid set in motion by the opening of the leak Δv_l in terms of Mach number ($M_l = {}^{\Delta v_l}/_{c}$) and by including the speed of sound of an ideal gas $c = \sqrt{kRT_l}$, equation (4.21), can be rewritten as:

$$\Delta P_l = \rho_l k R T_l M_l \tag{4.23}$$

So far, this formula cannot be used in practice because the speed of the fluid through the leak Δv_l or the Mach number M_l, the density in the leak ρ_l and the temperature in the leak T_l are not known. As ρ_l and T_l are functions of the Mach number, which in term is a function of the applied pressures across the leak, the isentropic flow equations [163, p.644] are expressed as:

$$\frac{P_{t_l}}{P_l} = \left(1 + \frac{k-1}{2} M_l^2\right)^{\frac{k}{k-1}} \tag{4.24}$$

$$\frac{T_{t_l}}{T_l} = \left(1 + \frac{k-1}{2} M_l^2\right) \tag{4.25}$$

$$\frac{\rho_{t_l}}{\rho_l} = \left(1 + \frac{k-1}{2} M_l^2\right)^{\frac{1}{k-1}} \tag{4.26}$$

Assuming that the air flow results in a negligible velocity at infinite distance from the leak (infinite area), the total ambient properties can be equalled to the static ambient properties:

$$P_{t,amb} = P_{amb} \qquad T_{t,amb} = T_{amb} \qquad \rho_{t,amb} = \rho_{amb} \tag{4.27}$$

The assumption of isentropic flow allows to state that the total properties of the flow remain unchanged during the compression

$$P_{t,amb} = P_{t,l} \qquad T_{t,amb} = T_{t,l} \qquad \rho_{t,amb} = \rho_{t,l} \tag{4.28}$$

Under these assumptions, the isentropic flow equations can be written as:

$$M_l = \sqrt{\frac{2}{k-1}\left(\left(\frac{P_{amb}}{P_l}\right)^{\frac{k-1}{k}} - 1\right)} \tag{4.29}$$

$$T_l = \frac{T_{amb}}{\left(\frac{P_{amb}}{P_l}\right)^{\frac{k-1}{k}}} \tag{4.30}$$

$$\rho_l = \frac{\rho_{amb}}{\left(\frac{P_{amb}}{P_l}\right)^{\frac{1}{k}}} \tag{4.31}$$

These expressions for M_l,T_l and ρ_l can now be substituted in equation (4.23):

$$\Delta P_l = \rho_{amb} k R T_{amb} \frac{\sqrt{\frac{2}{k-1}\left(\left(\frac{P_{amb}}{P_l}\right)^{\frac{k-1}{k}} - 1\right)}}{\left(\frac{P_{amb}}{P_l}\right)} \tag{4.32}$$

The pressure wave that originates from the disturbance caused by the leak event will reach the capillary with an amplitude ΔP_l . There, the wave will expand as a circular wavefront and eventually form two pressure waves propagating towards both ends of the capillary. This is shown in Figure 4.11. As the pressure sensors will measure the pressure waves travelling in the capillary, one must find an expression for the amplitude of the NPW in the capillary ΔP_{cap}. The wave energy is distributed into two waves travelling in the capillary section, so that the amplitudes are related by:

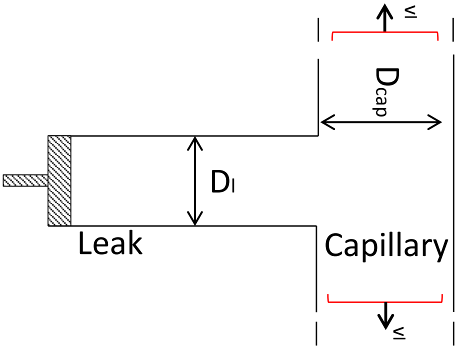

Figure 4.11: When reaching the capillary, the pressure wave will expand and two pressure waves will start propagating towards both ends of the capillary.

$$\begin{aligned} 2\Delta P_{cap} A_{cap} &= \Delta P_l A_l \qquad (4.33)\\ \Delta P_{cap} &= \frac{\Delta P_l}{2}\left(\frac{A_l}{A_{cap}}\right) \qquad (4.34) \end{aligned}$$

The amplitude of the NPW travelling in the pipeline is therefore given by

$$\begin{aligned} \Delta P_{cap} &= \frac{\rho_{amb} k R T_{amb}}{2} \frac{\sqrt{\frac{2}{k-1}\left(\left(\frac{P_{amb}}{P_l}\right)^{\frac{k-1}{k}}-1\right)}}{\left(\frac{P_{amb}}{P_l}\right)} \left(\frac{A_l}{A_{cap}}\right) \qquad (4.35)\\ \Delta P_{cap} &= \dot{m}_l \frac{c}{2\left(\frac{P_{amb}}{P_l}\right) A_{cap}} \qquad (4.36) \end{aligned}$$

The amplitude of the NPW is related to the actual mass flow rate through the leak. As any experimental set-up, or any leak geometry, will not behave like an ideal nozzle, one must consider the discharge coefficient C_D as a manner to evaluate the inefficiency of the nozzle flow ($C_D = \dot{m}_l / \rho_{amb} c M_l A_l$). Therefore, equation (4.36) can be rewritten as

$$\Delta P_{cap} = C_D \frac{\rho_{amb} k R T_{amb}}{2} \frac{\sqrt{\frac{2}{k-1}\left(\left(\frac{P_{amb}}{P_l}\right)^{\frac{k-1}{k}}-1\right)}}{\left(\frac{P_{amb}}{P_l}\right)} \left(\frac{A_l}{A_{cap}}\right) \qquad (4.37)$$

Although the fatigue crack is not circular shaped, the leak used in the test setup will be drilled and is therefore circular. For that purpose, the leak area is expressed in terms of a leak diameter D_l. Considering a circular leak and capillary cross section, the ratio of the cross sectional areas can be expressed as the squared ratio of the diameters. Furthermore, using the ideal gas law ($P_{amb} = \rho_{amb} R T_{amb}$) and since the pressure inside the leak P_l equals the pressure inside the capillary P_{cap} before the leak event:

$$\Delta P_{cap} = C_D P_{amb} k \frac{\sqrt{\frac{2}{k-1}\left(\left(\frac{P_{amb}}{P_{cap}}\right)^{\frac{k-1}{k}} - 1\right)}}{\left(\frac{P_{amb}}{P_{cap}}\right)} \left(\frac{D_l}{D_{cap}}\right)^2 \tag{4.38}$$

The amplitude of the NPW ΔP_{cap} depends on the pressure ratio $\left(\frac{P_{amb}}{P_{cap}}\right)$. In order to complete the derivation, two cases must be considered. In case that the pressure ratio $\left(\frac{P_{amb}}{P_{cap}}\right)$ exceeds the critical value $\left(\frac{P_{amb}}{P_{cap}}\right)^* = \left(\frac{2}{k+1}\right)^{\frac{k}{k-1}}$, the flow in the leak is choked. As a result, the Mach number cannot exceed $M_l = 1$ and the pressure ratio is fixed at $\left(\frac{P_{amb}}{P_{cap}}\right) = \left(\frac{P_{amb}}{P_{cap}}\right)^*$. In case that the pressure ratio $\left(\frac{P_{amb}}{P_{cap}}\right)$ remains below the critical value $\left(\frac{2}{k+1}\right)^{\frac{k}{k-1}}$, the flow in the leak is adapted. The Mach number M_l and the pressure ratio then follow the equations as described here above. One then finally obtains the following equations for the ampltiude of the NPW in a capillary under vacuum conditions:

Choked flow $\left(\frac{P_{amb}}{P_{cap}}\right) > \left(\frac{P_{amb}}{P_{cap}}\right)^*$

$$\Delta P_{cap} = C_D \frac{k}{2\left(\frac{P_{amb}}{P_{cap}}\right)^*} P_{amb} \left(\frac{D_l}{D_{cap}}\right)^2 \tag{4.39}$$

Adapted flow $\left(\frac{P_{amb}}{P_{cap}}\right) < \left(\frac{P_{amb}}{P_{cap}}\right)^*$

$$\Delta P_{cap} = C_D \frac{k}{2} P_{amb} \frac{\sqrt{\frac{2}{k-1}\left(\left(\frac{P_{amb}}{P_{cap}}\right)^{\frac{k-1}{k}} - 1\right)}}{\left(\frac{P_{amb}}{P_{cap}}\right)} \left(\frac{D_l}{D_{cap}}\right)^2 \tag{4.40}$$

The equations predicting the amplitude of the NPW in a capillary under overpressure can be derived similarly and are given by:

Choked flow $\left(\frac{P_{cap}}{P_{amb}}\right) > \left(\frac{P_{cap}}{P_{amb}}\right)^*$

$$\Delta P_{cap} = C_D \frac{k}{2\left(\frac{P_{cap}}{P_{amb}}\right)^*} P_{cap} \left(\frac{D_l}{D_{cap}}\right)^2 \tag{4.41}$$

Adapted flow $\left(\frac{P_{cap}}{P_{amb}}\right) < \left(\frac{P_{cap}}{P_{amb}}\right)^*$

$$\Delta P_{cap} = C_D \frac{k}{2} P_{cap} \frac{\sqrt{\frac{2}{k-1}\left(\left(\frac{P_{cap}}{P_{amb}}\right)^{\frac{k-1}{k}} - 1\right)}}{\left(\frac{P_{cap}}{P_{amb}}\right)} \left(\frac{D_l}{D_{cap}}\right)^2 \tag{4.42}$$

Given the practical use of the NPW for leak localization in pipelines at high pressures (choked condition) and the fact that the empirically found formula (4.14) for the amplitude of the NPW was based on pressurized pipelines resulting in choked conditions in the leak, the empirically found formula is compared to the theoretically developed equation (4.41). Rocha [160] used methane gas (CH_4), for which (P_p now represents the static pipeline pressure):

- k = 1.32
- $\left(\frac{P_p}{P_{amb}}\right)^* = \left(\frac{k+1}{2}\right)^{\frac{k}{k-1}} = 1.845$

and thus:

$$\Delta P_p = 0.357 C_D P_p \left(\frac{D_l}{D_t}\right)^2 \tag{4.43}$$

Although the leak geometry is not known for the work of Rocha, Equation (4.43) is very similar to the equation found by Rocha (see equation

(4.14)). Both equations become identical for a C_D coefficient of 0.84. From the comparison, it is clear that this equation is only valid under conditions of choked flow and pipelines under overpressure for one specific gas (methane). However, for the particular study of pipeline leak detection techniques, the assumption of a pressurized pipeline with $\left(\frac{P_p}{P_{amb}}\right) > \left(\frac{P_p}{P_{amb}}\right)^*$ is mostly valid because pipelines are operated at high pressures.

4.3.2 Validation of the theoretical model in tube segments

The theoretically derived model for the amplitude of the NPW was first empirically validated on a test setup constituting of large tubes instead of capillaries for the ease of assembly and setup modifications. At a later stage, the model was also validated on a setup consisting of capillaries. For the ease of referencing to the capillary properties used in the derivation of the formula's, the same references will be used in this section although those parameters now refer to the tubes of the setup. D_{cap} now refers to the internal diameter of the tubes used in the setup while P_{cap} is the internal pressure inside the tubes of the setup. The set-up allowed to vary all depending parameters affecting the amplitude of the NPW. In order to avoid working with flammable and hazardous fluids, the tests were performed using air and argon. Although air is not an ideal gas, its properties sufficiently approach those of an ideal gas for the purpose of these tests. The test setup is shown in Figure 4.12. Either pressurized air or argon is supplied through tube (1) to a pressure vessel (2). The Topward 6303DS power supply (4) controlling the Linator KPS 3/6-10-236-1-02-10 proportional valve (3) allows regulating the pressure supplied to the set-up, either directly to the tubes (6) or via a Norgren M/58112/09 venturi (5) creating vacuum pressure inside the tubes. During the experiment, the Clippard SLV-2-M5 sleeve valve (7) is closed to stop the pressure supply and reduce the noise on the pressure readings. The Endevco Meggit 8540-200 pressure sensors (8 and 9) record the pressure inside the pipe while the Kulite XTEL-123BEG-190M-1.7 pressure sensor (15) is used to measure the ambient pressure. Sensor (9) is used to measure the absolute pressure level inside the tube, while pressure sensor (8) is used to accurately measure the amplitude of the NPW created by a solenoid fast switching valve (11). In between the solenoid valve and the tube, a leak simulator (10) is fitted with a drilled restriction of known diameter serving as a calibrated leak area through which the NPW passes towards the tubes. A Festo MHE4-MS1H-

3/2G-1/4-K solenoid valve was used for leaks bigger than 1 mm diameter while the Festo MHE2-MS1H-3/2G-M7-K was used for the smaller leaks, because the latter valve limits the flow rate for larger leak sizes, thereby nullifying the calibrated effect of the leak simulator. The Agilent 33210A function generator (13) generates a block pulse that is fed to a mosfet amplifier converting the signal to a power signal which is fed to the valve. The pressure sensors are read out by a LMS Scadas III mobile data acquisition unit (14) and a computer (16) using the LMS Spectral Testing software v15. The data was sampled at the maximum sampling rate of 204.8kHz to accurately determine the amplitude of the NPW. The data was thereafter post processed using Matlab R2014b.

The test setup consists of three tube segments of 0.462 m with tube diameters D_{cap} of 11.6 mm, 16.9 mm and 23.7 mm and leak diameters D_l ranging from 0.4 mm to 2 mm. The ratio of the leak diameter over capillary diameter varies between $0.0169 < {}^{D_l}/_{D_{cap}} < 0.1724$. The pressure inside the tubes can be varied over the pressure range 0.1 bara $< P_{cap} <$ 8 bara (bara refers to 1 bar absolute pressure), comprising both adapted and choked flow conditions in the leak together with the tubes either being at vacuum or overpressure conditions. Most experiments were conducted using air as fluid medium, but to check the influence of the fluid media also pure argon was used in the experiments.

Five tests were conducted for all tested configurations, allowing to evaluate an average amplitude over five independent measurements. One single measurement of pressure sensor (8) in Figure 4.12 is depicted in red in Figure 4.13. The NPW has a steep rising flank after which the pressure settles, before the first reflected wave arrives from the other tube end after 4.5 ms in Fig 4.13. The amplitude of the NPW is therefore found by the difference in pressure between the initial pressure level and the pressure level just before arrival of the reflected pressure wave. In practice, hundreds of datapoints are averaged out (see black in Figure 4.13) to retrieve an approximation of both pressure levels that is not affected by the noise on the measurements. This procedure was repeated for all five tests performed for each configuration, after which the average over the five measurements is evaluated. Since the pressure sensor (8) is installed at the tube end hard wall, the reflected wave is in phase with the incident wave causing the pressure reading of the amplitude of the NPW to be doubled. In addition, the NPW wave that travelled towards pressure sensor (9) reflected at the hard wall and also propagated towards pressure sensor (8) with a little time delay [164]. The

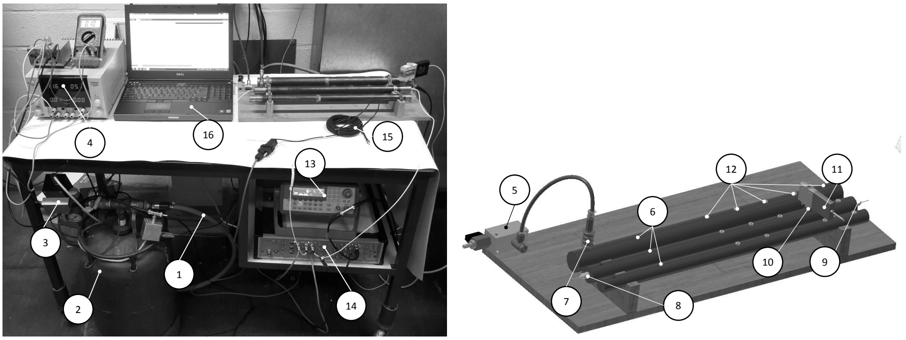

Figure 4.12: Experimental test set-up to verify the theoretical model for the amplitude of the Negative Pressure Waves (NPW). 1) supply tube, 2) pressure vessel, 3) proportional valve, 4) power supply, 5) venturi, 6) testing tube, 7) on-off supply valve, 8) pressure sensor S2, 9) pressure sensor S1, 10) leak simulator, 11) solenoid valve, 12) leak locations L1-L5, 13) function generator, 14) data acquisition, 15) reference ambient pressure sensor, 16) computer.

pressure measurement depicted in Figure 4.13 actually shows the addition of the amplitude of both the direct and reflected NPW and therefore again a doubled pressure reading. In order to compare with the theoretical prediction, the measured amplitude must be divided by a factor four. The amplitude derived from Figure 4.13 is $\Delta P_{cap} = {}^{-8472}/_{4}\text{Pa} = -2118$ Pa and is plotted as the bottom right diamond in Figure 4.14 (top) against the theoretical model predicting the amplitude of the NPW. The use of this particular setup has many advantages. Since the measured amplitude in the test setup is four times larger than the actual amplitude of the NPW, smaller amplitude NPW can be detected using the same sensors, thereby allowing to test smaller leak sizes that would otherwise give rise to non detectable NPW amplitudes. Secondly, the fact that the setup is a closed volume gives rise to pressure plateaus corresponding to the arrival of different NPW, as opposed to one small pressure peak that fades away due to the flow in a pipeline. This allows the easy and accurate determination of the amplitude of the NPW by averaging out multiple data points of one pressure plateau, thereby reducing the impact of noise on the experiment. As a third effect, there is no main flow through the tube at the moment of testing and therefore flow noise is omitted from the experiments.

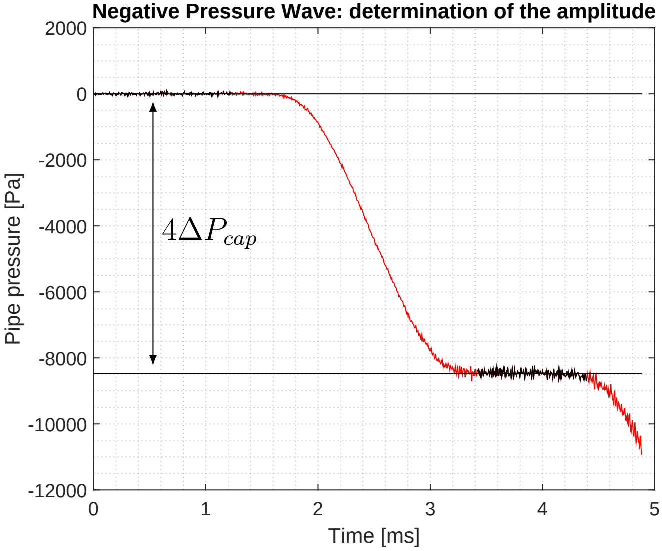

Figure 4.13: Determination of the amplitude of the Negative Pressure Waves (NPW). The NPW is indicated in red, the areas in black are averaged out. The difference in between the black lines equals 4 times the amplitude of the NPW, i.e. $4\Delta P_{cap}$. *Data shown for initial pipeline pressure* P_{cap}*=8 bar, tube diameter* D_{cap}*=23.7 mm, leak diameter* D_l*=2 mm and the fluid is air.*

4.3.3 Results

According to the theoretical model proposed in eqs. (4.39) to (4.42), the parameters affecting the amplitude of the NPWs are the capillary pressure P_{cap}, the leak diameter D_l, the capillary diameter D_{cap} and the fluid medium through the heat capacity ratio k. In the following section, the dependency on these parameters will be analysed and compared with the proposed theoretical model.

Capillary pressure P_{cap}

The variation of the capillary pressure P_{cap} has three main effects on the amplitude of the NPW. At first, the capillary can be pressurized above or below ambient conditions, affecting whether formulas (4.39) and (4.40) (vacuum) or formulas (4.41) and (4.42) (overpressure) should be used. Al-

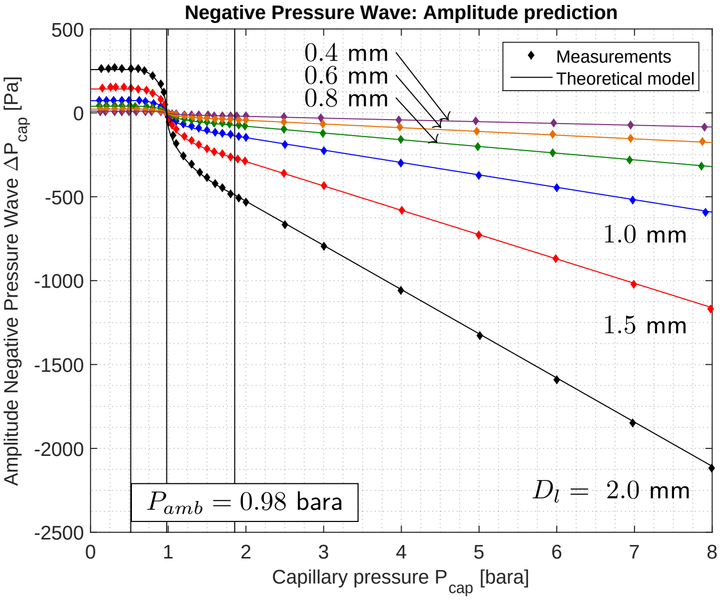

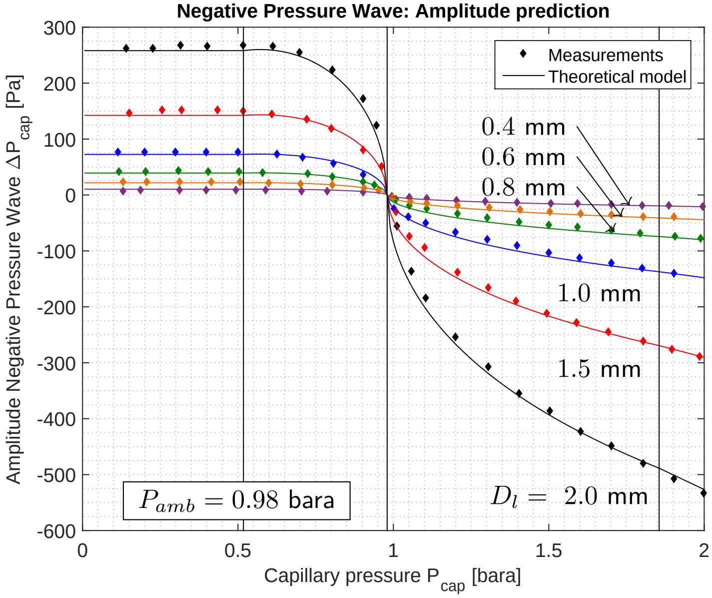

Figure 4.14: Amplitude of the NPW in function of the capillary pressure for different leak diameters and a tube diameter of 23.7 mm. The fluid medium is air. The largest amplitude corresponds to the leak of 2 mm diameter, gradually decreasing to 1.5, 1.0, 0.8, 0.6 and 0.4 mm. The vertical lines highlight the pressure condition where different formula must be used on either side of the line.

though not considered during the theoretical derivation, the pressurization case will alter the sign of the NPW. Commonly referred to as Negative Pressure Waves, because of the initial use in pressurized pipelines, the NPW will actually have a positive sign for vacuum applications. Secondly, the ratio of the capillary pressure P_{cap} over the ambient pressure level P_{amb} determines the flow condition through the leak and determines which of the four formulas eqs. (4.39) to (4.42) should be used. As a third effect, some of these equations are directly dependent on the pipe pressure P_{cap} while others are independent of the pipe pressure P_{cap}.

The measurement results, along with the theoretical predictions, are depicted in Fig 4.14 (top) and a detailed view on 0 bara$<$ $P_{cap} < 2$ bara (bottom). Across the entire spectrum of tested capillary pressures, the derived formulas are all very well able to predict the amplitude of the NPW. Starting from the left in Figure 4.14 (top), absolute vacuum and for all capillary pressures for which $\left(\frac{P_{amb}}{P_{cap}}\right) > \left(\frac{P_{amb}}{P_{cap}}\right)^* = 1.893$ (indicated by the vertical lines), eqn. (4.39) predicts that the amplitude of the NPW is unaffected by the capillary pressure. Increasing the capillary pressure such that the flow through the leak is adapted, eqn. (4.40) becomes a function of the capillary pressure P_{cap}, linearly through the factor P_{cap} and additionally through the Mach number. When the tube is pressurized at pressures above ambient pressures and such that $\left(\frac{P_{cap}}{P_{amb}}\right) < \left(\frac{P_{cap}}{P_{amb}}\right)^* = 1.893$, the amplitude of the NPW is only a function of the pipe pressure through the Mach number. By further increasing the pipe pressure beyond $P_{cap} > 1.893 P_{amb}$, the amplitude of the NPW becomes a linear function of the pipe pressure P_{cap} (see eqn. (4.41)). These findings are also clearly observed in the measurements.

Leak diameter D_l

The amplitude of the NPW is quadratically dependent on the diameter of the leak. The bigger the leak, the larger the amplitude of the NPW. The effect of the size of the leak on the measured amplitudes was evaluated using six different leak sizes ranging from 0.4 mm to 2 mm. Given the quadratic dependence on the leak diameter and the rather large tolerances on the drilled holes, the actual leak dimensions were checked under the microscope to retrieve the exact leak diameters. The micrographs of the calibrated leaks are depicted in Figure 4.15. As depicted in Table 4.2, the size of the leak as measured from the micrographs is always larger than the best fit obtained with the theoretical model. The difference can be acquinted

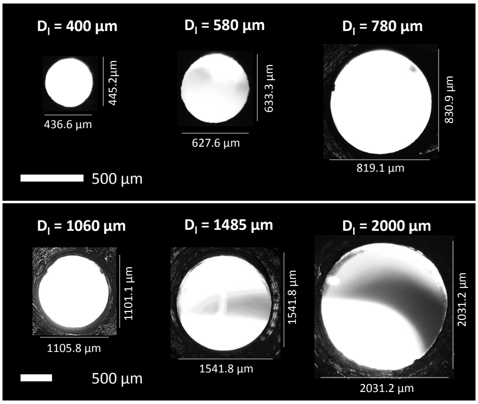

Figure 4.15: Microscopic images of the leaks to measure the exact leak size after drilling. D_l indicating the leak diameter used to fit the formula on the actual measurements.

to the discharge coefficient, ranging from 0.823 for the smallest leak size to 0.970 for the largest leak size. Flow lines do not stay parallel to the leak walls, but converge to a smaller area further down the nozzle, thereby limiting the mass flow rate through the nozzle. The discharge coefficient C_D is the measure of the actual mass flow rate through the nozzle over the theoretical maximum mass flow rate through an ideal nozzle with the same throat size. The discharge coefficient C_D is therefore smaller when flow lines have to bend more around sharp edges. The smaller the difference in flow area before and inside the leak, the more the streamlines stay parallel to the leak wall and the more efficient the nozzle becomes (see Figure 4.16). Larger discharge coefficients are therefore expected for larger leak sizes, as confirmed in Table 4.2 and in accordance with the literature [165].

Capillary diameter D_{cap}

The amplitude of the NPW is inversely proportional to the pipe diameter D_{cap} squared. Similarly as for the experiments conducted with different leak sizes, multiple tubes were selected with internal diameters of D_{cap} 23.7 mm, 16.9 mm and 11.6 mm. All experiments were conducted using a leak with a diameter of 2 mm. Figure 4.18 presents all the experimental results along with the fit with the theoretical model. The vertical lines again indicate the pressure conditions for which on either side of the vertical line different equations should be used.

Table 4.2: Leak diameters D_l [μm]

Drill [μm]	Measured D_l [μm]	Formula fit D_l [μm]	C_D [-]
400	441	400	0.823
600	630	580	0.846
800	825	780	0.894
1000	1103	1060	0.923
1500	1542	1485	0.928
2000	2031	2000	0.970

Fluid medium

The last parameter affecting the amplitude of the NPW is the gaseous medium inside the capillary through the ratio of the specific heats k. As was the case for the capillary pressure P_{cap}, also the ratio of the specific heats influences the amplitude through three effects. First, the value of the specific heat ratio k affects which formula should be used, since the pressure ratios giving rise to choked flow conditions depend on the specific heat ratio. Secondly, for adapted flow conditions, the Mach number depends on the ratio of the specific heats through the power of the applied pressure ratio. As a third effect, and for all pressurization cases, the amplitude of the NPW is linearly dependent on the ratio of the specific heats k. Although its effect is threefold, the variations in specific heat ratio are small and its effect on the amplitude of the NPW remain therefore also limited. Vacuum conditions were not tested using argon since fluid mixing must then be considered.

4.4 Conclusions

The present chapter discussed three principles that are capable of estimating the severity of the damage that is detected by the eSHM system. To be detected by the eSHM system, the fatigue crack must have at least reached a size such that it forms an interconnection between the capillary and the outside atmosphere. The shortest distance between the capillary and an

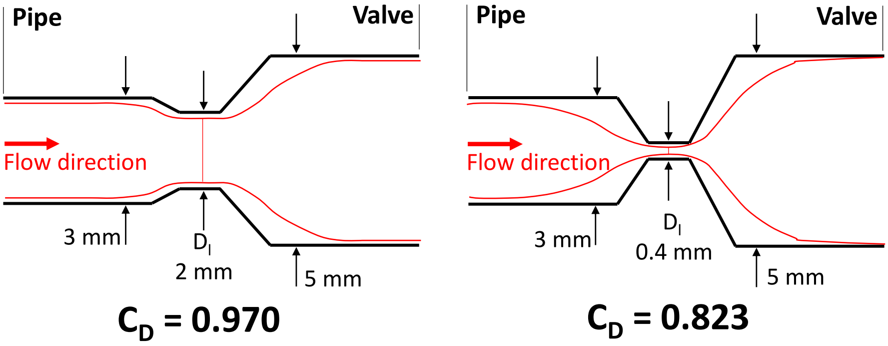

Figure 4.16: Flow lines do not stay parallel to the leak walls, but converge to a smaller area further down the nozzle, thereby limiting the mass flow rate through the nozzle. The discharge coefficient C_D is larger for larger leak sizes. Flow direction as shown for a pressurized pipe.

outer wall of the component therefore forms a first measure of the fatigue crack size.

A second model reconstructed the pressure behaviour inside the capillary. It was concluded that the size of the leak area, as derived from the simulation model, is a measure for the size of the fatigue crack. The larger the fatigue crack, the wider it will open when loaded and the larger the leak flow area will be. A larger fatigue crack will therefore result in a faster pressure rise in time. This conclusion was confirmed by comparison with the actual fatigue crack size visualized by X-ray photography and on the fracture surface. The leak flow through the fatigue crack will typically pass through a section as small as $100 - 10,000$ µm^2. The reconstruction of the pressure behaviour inside the capillary was based on three main parameters: the sensitivity of the capillary pressure to the deformation of the specimen caused by the loads acting upon the specimen (α), the minimal load at which the fatigue crack opens F_{open} and the leak flow area through the fatigue crack at maximum load $A_{l,max}$. These parameters depend all on the knowledge of the loads during the fatigue testing. A good reconstruction of the pressure behaviour inside the capillary, and the derivation of the fatigue crack size, requires the knowledge of the loads acting on the specimen.

Reconstruction of the pressure behaviour inside the capillary will be difficult, or even impossible, when the loads are not known. A third principle,

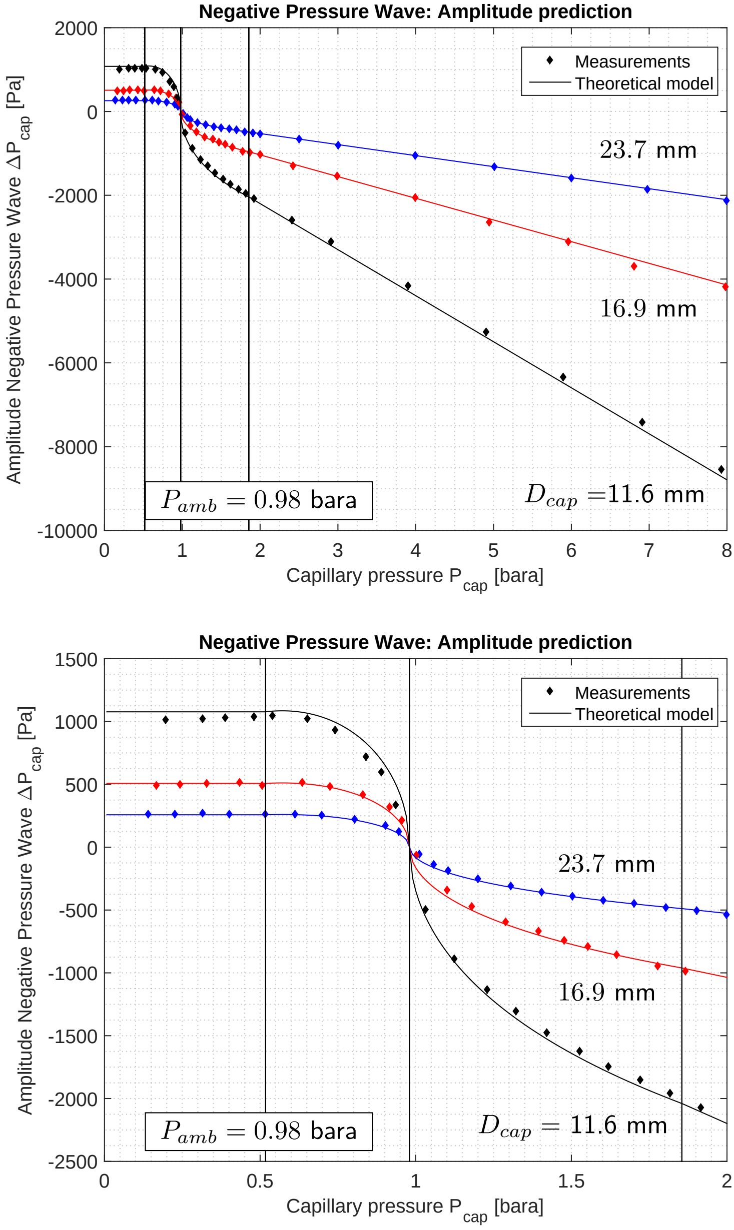

Figure 4.17: Amplitude of the NPW as a function of the pipe pressure for different pipe diameters and a leak diameter of 2 mm. The fluid medium is air. The vertical lines highlight the pressure condition where different formula must be used on either side of the line.

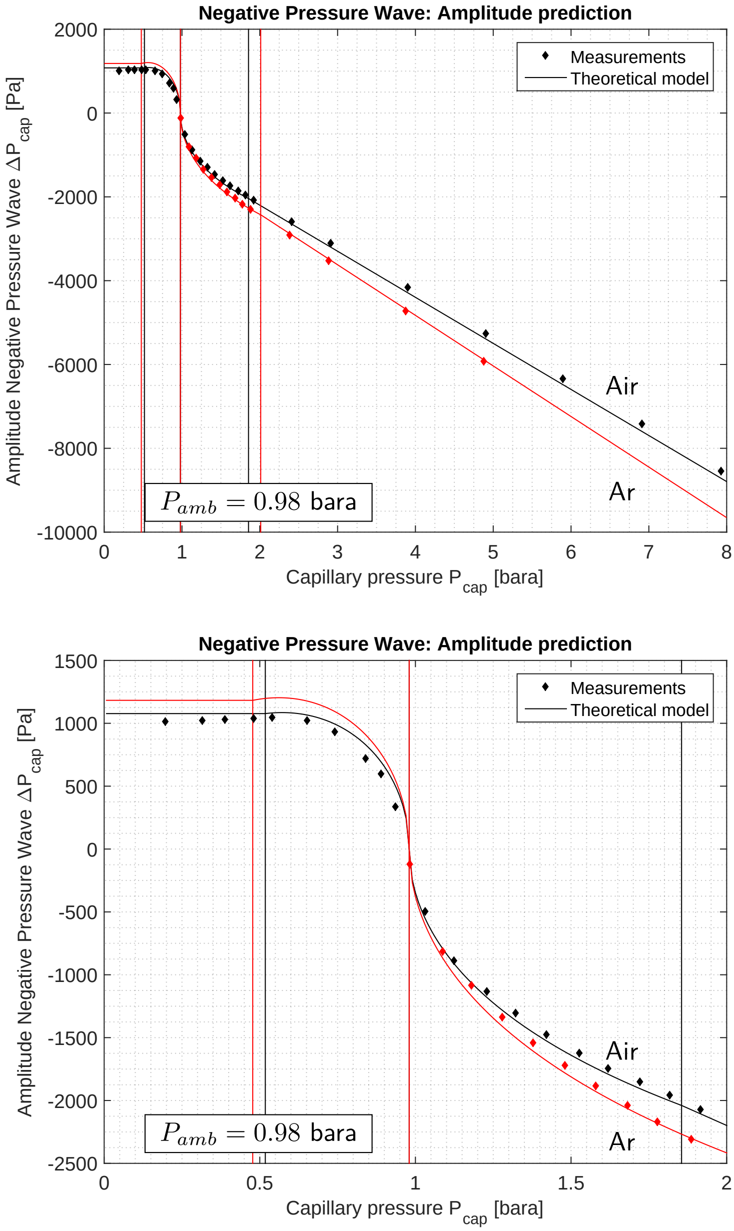

Figure 4.18: Amplitude of the NPW for a leak diameter D_l of 2 mm in a pipe with diameter D_{cap} 11.6 mm filled with air and argon. The vertical lines highlight the pressure condition where different formula must be used on either side of the line.

based on the determination of the amplitude of the NPWs was then presented to derive the leak size through the fatigue crack. Capturing the pressure waves only requires a sufficient high sampling rate and a sensitive pressure sensor, but does not require any information about the loads acting on the structure. The amplitude of the NPWs is closely related to the size of the leak. A new, analytical, model was presented to predict the amplitude of the Negative Pressure Waves. This analytical model was theoretically derived on the basis of the physical understanding of the phenomena causing the generation of the NPW. The isentropic fluid flow equations were combined with the acoustics equations to derive an optimized model for the amplitude of the NPW. The amplitude of the Negative Pressure Waves depend on the pressurization case, the capillary pressure, the leak size, the capillary diameter and the gaseous media present inside the capillary. A test setup was build to evaluate the model. The experimental results validated the model under all tested configurations: pressurization type (vacuum/overpressure, choked/adapted flow), leak diameter, pipeline diameter and fluid medium. The new model can be used under a more broad spectrum of parameters than the current, empirical, model in place. The amplitude of the NPW contains information about the leak, and thus fatigue crack size, at the moment when the fatigue crack opens. This model is more widely applicable than the empirical model currently in place. It is currently unknown whether the opening of a fatigue crack is sufficiently abrupt to generate the NPW.

Considering again the fatigue test measurements. The capillary was put under vacuum conditions inside the capillary such that the flow is choked. With a capillary diameter around 3 mm and measured fatigue crack sizes falling in a range of 100-10,000 µm^2 the amplitude of the NPWs fall in the range $0.60 - 60$ Pa. C_D is considered equal to one since the leak size was derived from an actual mass flow rate measurement which already includes the effect of the discharge coefficient. NPWs were not detected during the actual fatigue tests because of various reasons. The primary reason is the sampling frequency used during the fatigue testing which was around 100 Hz. Sampling frequency must be increased to approximately 10-20 kHz to capture those acoustical waves travelling at the speed of sound. A second very important shortcoming is the current use of absolute pressure sensors which have a limited resolution of 10-20 Pa. Especially in an environment of vibrations generated by the fatigue test machine, the pressure measurements of these absolute pressure sensors are likely not sensitive enough to detect rather small amplitude pressure variations. A third aspect is that the generation of a pressure wave is based on an abrupt pressure change. It is currently unknown whether the opening of a fatigue crack is sufficiently abrupt to generate a pressure wave.

The good fit of the models with the presented experiments shows that the equations used to describe the leak flow through the fatigue crack and leak simulator are valid.

Chapter 5

Crack localization by the eSHM system

The continuous monitoring of the pressure inside the capillaries of the eSHM system has revealed that a crack can be detected and its size can be determined on the basis of the pressure change, i.e. leakage rate. A third aspect that a SHM must be capable of is localizing the defect, thereby enabling localized, more in-depth, non-destructive-testing to evaluate the severity of the damage. The present chapter will discuss the ability of the eSHM system to retreive the damage localization on the basis of the pressure measurements inside the capillary. The discussions starts with a test setup on large scale (based on article [164]), before applying the developed methods to a leak in a capillary.

5.1 Introduction

Negative Pressure Waves (NPWs) serve as a basis for the inspection of pipelines. As explained in the work of Wan *et al.* [166], when a leak happens along the pipeline, the fluid density drops immediately at the leak location. The resulting pressure wave, the NPW, spreads out from the leak point to both ends of the pipeline. The analysis of the time-of-arrival of these wave fronts at known locations at both sides of the leak then allows locating the leak with high accuracy. Silva *et al.* [167] analysed NPWs to locate leaks in pipelines under operation (with flow). The paper reports that the leak in the pipeline could be located with an accuracy comparable to the theoretical uncertainty related to the finite sampling rate that was used.

It must be noted here that one calls the acoustic waves "NPW" as they were first analysed and used in pipeline applications. These pipelines are mostly operated under overpressure to distribute fluids over large distances. A leak lowers the internal pressure, which is the reason why the occurring waves are referred to as "Negative Pressure Waves". In a vacuum application, which we will be using in the eSHM system, the amplitude of the wave will be positive (increasing pressure), so that the name "Positive Pressure Waves" is more opportune. However, this name has never been used in the literature before. We will therefore stick to the name NPW, although the sign of the pressure change depends on the pressurization case.

The location of the leak inside the capillary, and thus the location of the fatigue crack, may also be determined on this basis. Sensors located at each side of the capillary register the arrival of the NPWs. The difference in time-of-arrival of these waves allows locating the leak. This principle is depicted in Figure 5.1. The sensor with name 'S1' will always be referring to the sensor which is closest to the leak (earlier arrival of the pressure wave), while sensor 'S2' will be the sensor located far from the leak (later arrival of the pressure wave).

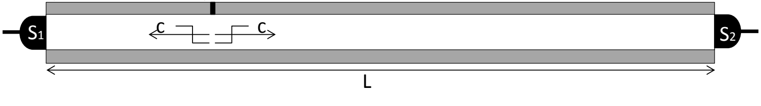

Figure 5.1: The difference in time-of-arrival of the Negative Pressure Waves at the two pressure sensors mounted at both ends of the tube allows locating the crack.

$$\text{Sensor S1} \quad t_1 = \frac{x_1}{c} \tag{5.1}$$

$$\text{Sensor S2} \quad t_2 = \frac{L - x_1}{c} \tag{5.2}$$

Because t_1 and t_2 are only known relatively, only combination of equations (5.1) and (5.2) leads to a localization formula:

$$x_1 = \frac{L - c(t_2 - t_1)}{2} \tag{5.3}$$

The error on the crack location (Δx) is found by adding the errors on the length L, the speed of sound c and the error related to the finite sampling rate, through:

$$\Delta x = \mid \frac{\partial x}{\partial L} \mid \Delta L + \mid \frac{\partial x}{\partial c} \mid \Delta c + \mid \frac{\partial x}{\partial t} \mid \Delta t \tag{5.4}$$

$$= \frac{\Delta L \; + \; \mid t_2 - t_1 \mid \Delta c \; + \; c\Delta t}{2} \tag{5.5}$$

where ΔL, Δc and Δt respectively correspond to the absolute error on the measurements of the length, speed of sound and time. The absolute error on the length of the capillary ΔL is 0.5 mm. The absolute error on the speed of sound Δc is zero as long as the speed of sound is exactly known (e.g. for an ideal gas $c = \sqrt{kRT}$). However, since in a practical application the temperature might not be known, it is interesting to measure the speed of sound (see equation (5.8)). This procedure adds an uncertainty Δc related to the measured speed of sound. Because of the high sonic speed c, it will furthermore be required to use a high sampling rate (lower Δt) to reduce the uncertainty on the estimated location and to deduce the localization feasibility. The sampling rate was set at the maximum of the LMS Mobile III data acquisition system (204.8 kHz), resulting in a theoretical error on the time of 0.00488 ms.

The analysis of NPWs in a closed volume is different than that in a pipeline with continuous flow. On the one hand, the analysis is eased since no flow effects (such as turbulence noise on the pressure measurements) are present. However, on the other hand, the pressure will continuously rise as a consequence of the leak. This pressure change might interfere with the NPW, making the analysis harder to retrieve the leak location. It is therefore part of this analysis to investigate if NPW can also be used to locate a leak in a closed volume (without flow), as will be the case in the embedded capillaries of the eSHM system.

For the ease of practical implementation and to start with a setup similar to the state-of-the-art pipeline inspection techniques, the first measurements will be conducted on a set-up consisting of closed tube segments (a large scale representation of the capillary). The analysis will then be extended to a smaller scale with an actual capillary with a size typical for the current implementation inside Additive Manufactured (AM) components.

For each of the setups, the pressure measurements will be analysed and the localization feasibility will be investigated. The localization accuracy will be improved through signal processing. The analysis will be concluded by investigating the possibility to localize with only a single pressure sensor and derive the effect of the presence of bends in the tube and capillary.

5.2 Large scale test setup

5.2.1 Test setup description

A test set-up was built to investigate the crack localization capability on the basis of the NPW. For the ease of practical implementation, the capillaries are represented by 3/4” tubes (internal diameter of 16.9mm) and with a length of 462 mm. The circular leak had a diameter of 1 mm. The initial pressure level is set at approximately 0.20 bara (bara refers to 1 bar absolute pressure) while the outside environment is at ambient conditions 1.013 bara. The temperatures of the fluid and tubes are expected to be all in equilibrium and at room temperature (293.15 K).

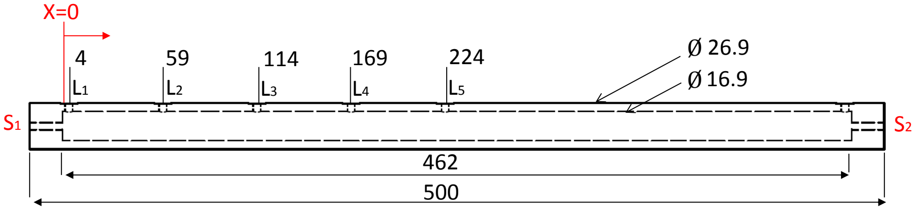

Figure 5.2: Drawing of the 3/4” tube of the test setup (dimensions in mm).

Along the longitudinal direction of the tube, multiple connections are foreseen to simulate different leak positions (called L1 to L5) and to connect the vacuum equipment to the setup. A detailed drawing of the tube can be seen in Figure 5.2. During a test, all but one connection points (L1 till L5) were closed while the remaining hole was connected to a solenoid on/off valve to simulate the opening of the crack. A leak simulator, with a known diameter of 1 mm, is placed in between the valve and the tubes. A step function is sent to the solenoid valve when the valve must be opened and is left open during the test. The last hole, on the right along the length direction of the tube, was used to connect the setup with the vacuum equipment to put the tube at the required initial pressure level before starting the measurement.

The tube was closed at both ends and each side was equipped with a an absolute pressure sensor (Endevco MEGGIT 8540-200), capable of measuring static pressure changes with a high sensitivity (noise level about 10–20 Pa). The sensors were connected to an LMS Scadas III mobile data acquisition system with a maximum sampling rate of 204.8 kHz.

The temperatures are expected to be all in equilibrium and at room temperature (293.15 K). The performed simulations and measurements discussed in the following parts of this manuscript will always be referring to this test setup.

The amplitude of the NPWs can be estimated on the basis of the formula's derived in the previous chapter. Since the capillary is initially set at a pressure below the ambient conditions and since the pressure ratio $\left(\frac{P_{amb}}{P_{cap}}\right) > \left(\frac{P_{amb}}{P_{cap}}\right)^*$, the flow through the leak is choked and equation (4.39) must be used:

$$\Delta P_{cap} = C_D \frac{k}{2\left(\frac{P_{amb}}{P_{cap}}\right)^*} P_{amb} \left(\frac{D_l}{D_{cap}}\right)^2 \tag{5.6}$$

In this equation, the following values must be entered to retreive the expected amplitude of the NPWs:

- The discharge coefficient C_D of the leak. $C_D = 0.923$ (see Table 4.2)
- The ratio of specific heats k of the fluid medium. $k = 1.4$ for air.

- The pressure ratio leading to choked flow condition. $\left(\frac{P_{amb}}{P_{cap}}\right)^* = 1.893$ for air.
- The absolute ambient pressure $P_{amb} = 101300$ Pa.
- The diamater of the capillary (here a setup with tubes: $D_{cap} =$ 16.9 mm)
- The diameter of the leak $D_l = 1$ mm

The amplitude of the NPW will therefore be:

$$\Delta P_{cap} = 121.1 \text{ Pa} \tag{5.7}$$

and may therefore be considered as a large amplitude when comparing to the expected amplitudes from an actual fatigue test 4.4. The expected amplitude range of the NPW was somewhere starting from a 0.6 Pa to over 60 Pa. The detection of smaller amplitude NPWs requires the use of microphones. However, to understand the pressure behaviour inside a leaking closed volume and to derive the leak localization feasibility, it is preferred to use absolute pressure sensors and increase the amplitude of the NPWs such that they are easily detectable by those pressure sensors.

5.2.2 Understanding the pressure behaviour inside a closed volume

Straight tubes

Simulations in “COMSOL Multiphysics” were performed in order to understand the nature of the NPW in more detail. As we are interested in the generation and propagation of the NPW, a time-dependent analysis was chosen. Laminar flow was assumed. The tube with the crack, as described in section 5.1, is represented by a large cylinder (the tube) connected to another smaller cylinder (the crack). Both cylinders contain air that is assumed to be initially at rest. The air is at an absolute pressure of 0.20 bara (vacuum). When the crack is opened, air will enter through the small cylinder (the crack). Therefore, a pressure condition (equal to the ambient pressure) is set to this inlet surface. The no slip condition is applied to all other walls. In order to interpret the development and propagation of

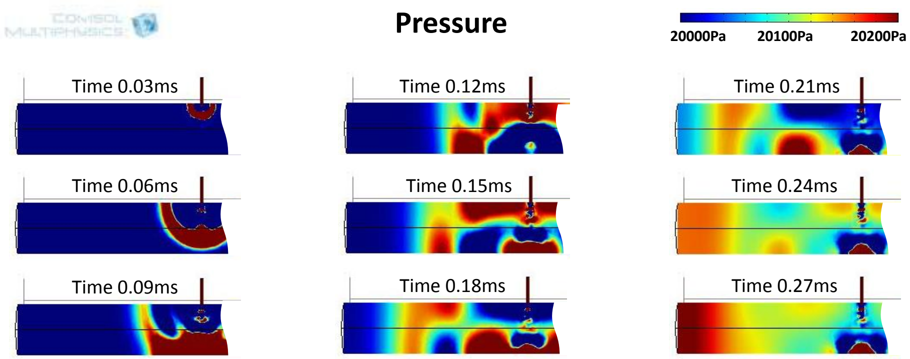

Figure 5.3: Computational fluid dynamics analysis of Negative Pressure Waves (NPWs).

the NPW, the plots only contain the pressure information in the range of 20,000–20,200 Pa (as is expected from equation (5.7)).

Figure 5.3 shows the pressure results of the computational fluid dynamics (CFD) analysis, obtained in a section in the longitudinal direction of the tube. The abrupt opening of the crack results in a discontinuity of the pressure at the crack location. Assuming that the capillary pressure is below the ambient pressure, the low pressure on the inside of the capillary meets the relative higher pressure of the atmosphere. That discontinuity results in a local increase of density and pressure at the crack location. The pressure wave propagates through the crack and expands as a spherical wave front in the tube. Once in the tube, the spherical wave front forms two plane waves that travel in opposite directions at the speed of sound (c) through the tubes.

The last time step in Figure 5.3 clearly indicates that when the NPWs arrive at the end of the tube (acoustically seen as a hard wall reflection), the amplitude of the NPW doubles because the incident wave is in phase with the reflected wave. The reflected wave then travels back to the other side of the tube where it will be detected by the other sensor. The amplitude of the arriving NPW is approximately 100 Pa but is sensed double as strong at the hard wall (see section 4.3.2).

Figure 5.4 presents the pressure measurements for leak location L2 obtained from sensors S1 (black line) and S2 (red line). The plotted signals were filtered The plot is focused at the moment of time-of-arrival of the NPW at the two sensors and is zeroed at the initial pressure level. Vertical line 0 corresponds to the theoretical moment of opening the leak. Vertical lines 1

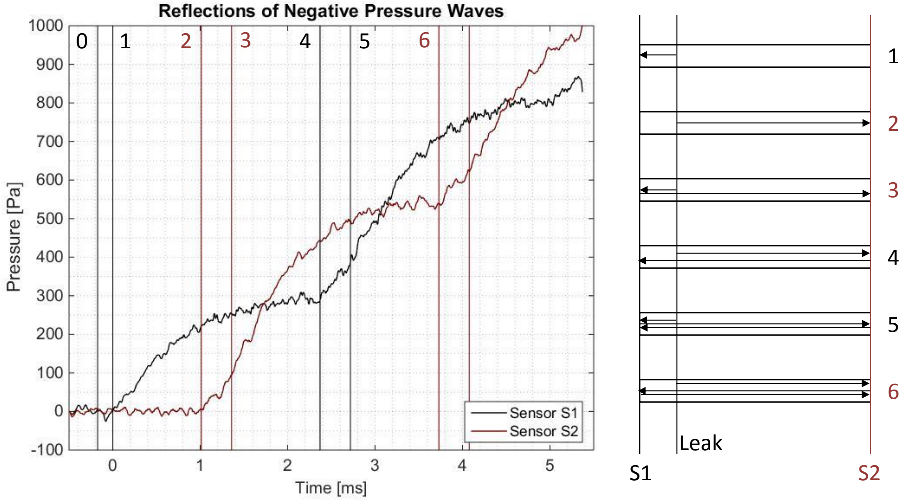

Figure 5.4: Time-of-arrival (TOA) of the (reflections of) Negative Pressure Waves. The measured difference in TOA between vertical lines 1 and 2 is 1.03 ms.

and 2 then correspond to the moment of time-of-arrival at sensors S1 and S2 of which the times are given below the figure.

The difference in time-of-arrival of the pressure waves at sensor S1 and S2 allows locating the leak, as will be explained in the following section. After the initial arrival of the pressure wave, the waves reflect at the hard wall end of the tube and propagate to the other side of the closed volume, with the consecutive arrivals corresponding to the vertical lines 2 till 6 in Figure 5.4.

Several parameters are affecting the pressure behaviour inside the tube, of which the most were already presented before. Starting with those parameters affecting the amplitude of the Negative Pressure Waves, we can refer here to Chapter 4 for a more profound analysis. It was clear from that analysis that the amplitude was mostly determined by the pressure levels inside and outside the tube, the leak and tube cross sectional area and the fluid type inside the tube. All these influences will result in a different amplitude of the Negative Pressure Wave as measured on vertical line 4 of Figure 5.4. The time taken by the Negative Pressure Wave to fully rise to its final value is unaffected by these parameters, except for the fluid type

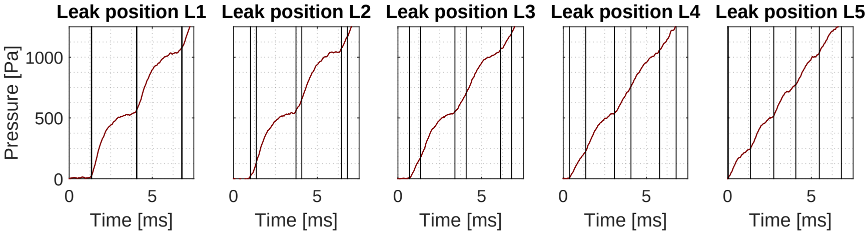

Figure 5.5: The shape of the pressure increase depends on the leak location. The vertical lines correspond to the arrival of the (reflected) Negative Pressure Waves.

affecting the speed of sound inside the tube. This time (e.g. between vertical line 1 and vertical line 4), is characterized by the length of the tube and the speed of sound in the medium inside the tube. Elongating the tube (and keeping the speed of sound constant) will result in longer time periods in between the vertical lines plotted in Figure 5.4. This is directly coupled with a reduced slope of pressure increase, because of the larger volume to be filled with the same leak rate.

The position of vertical lines 3 and 5 relative to the other vertical lines is function of the leak location. These vertical lines represent the arrival of a reflected Negative Pressure Wave at the moment a previous one is still present at this location, leading to a doubled pressure increase. This arrival can be seen as a break point in the pressure rise at the sensor location. The more the leak is positioned near one tube end, the closer the two wave fronts travel behind each other and the more the pressure rise on the other tube end is seen as a continuous pressure with doubled amplitude. This is why, in Chapter 4, the measured amplitude for a leak positioned at L1 was four times the actual amplitude of the pressure wave. On the other hand, the amplitude is doubled because of the incident and reflected wave being in phase at the hard wall tube end. The shape of the Negative Pressure Waves for different leak positions L1-L5 is provided in Figure 5.5.

The pressure signals recorded at both pressure sensor locations are equal because of the continuous reflections occurring at the hard walls of the tubes. The only difference is the delay at which the signal is measured at the sensor locations. This time difference is exactly equal to the time required to propagate from one tube end to the other. Figure 5.6 presents this similarity of the pressure signal recorded at sensor S1 and S2. By

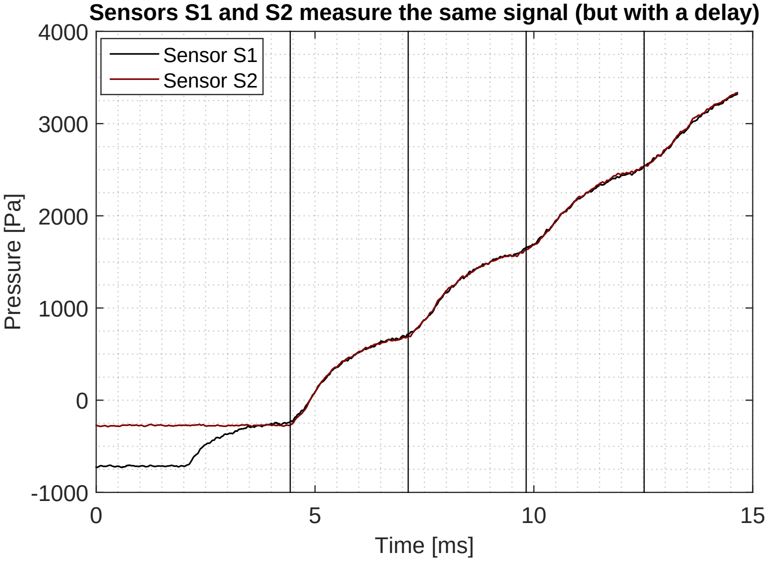

Figure 5.6: Sensors S1 and S2 measure the same signal. Each vertical line corresponds to the time needed for a Negative Pressure Wave to propagate back and fourth inside the tube. The pressure pulses repeat in between the vertical lines, except for some damping and friction effects smearing out the pulse at later time stamps.

delaying the first pressure signal, it is clear that both signals are identical.

Using a least squares analysis, the delay of the complete sensor signal S2 w.r.t. the signal of sensor S1 to become identical is found to be 1.362 ms ($279\Delta T_s$). This comparison between the signals of sensor S1 and S2 can be used to retrieve the speed of sound inside the tube:

$$c = \frac{L}{N\Delta T_s} = \frac{0.462}{0.001362}\frac{\text{m}}{\text{s}} = 339.2 \ \pm\ 1.6 \ {}^{\text{m}}/_{\text{s}}. \tag{5.8}$$

with L the length of the tube, N the optimal shift expressed in datapoints and $\Delta T_s = {}^{1}/_{f_s}$ the sampling time. The error on the speed of sound was calculated by:

$$\begin{aligned}\Delta c &= \mid \frac{\partial c}{\partial L} \mid \Delta L + \mid \frac{\partial c}{\partial N} \mid \Delta N && (5.9)\\ &= \frac{1}{N \Delta T_s} \Delta L + \frac{1}{N^2 \Delta T_s} \Delta N && (5.10)\\ &= 1.6 \ {}^{\mathrm{m}}\!/\!_{\mathrm{s}} && (5.11)\end{aligned}$$

where Δc, ΔL, ΔN respectively represent the errors on the speed of sound, the length of the tube and the number of shifts of the time signal.

Similarly, when considering a single pressure measurement of either sensor S1 or sensor S2, the signal is repeated in between the vertical lines added on Figure 5.6. These vertical lines are equidistant with a time period equal to the time required for the Negative Pressure Waves to travel back and fourth in the tube. A single measurement of one pressure sensor is sufficient for the determination of the exact speed of sound inside the tube because of the reflections at the hard wall end of the tubes. Only the exact length of the tube and a high sampling rate are required to determine the speed of sound with high accuracy.

The Negative Pressure Waves can be seen as pressure pulses on top of a linear rising slope of pressure because of the leakage flow. Because of the continuous reflections occurring at the hard end wall, the pulses remain present in the tube for a longer time. However, their amplitude diminishes as the Negative Pressure Waves are dampened at each reflection and after many reflections only the linear slope remains. The left plot of Figure 5.7 depicts the signal measured by sensor S1 (black) and the linear slope of rising pressure (red) without pressure pulses. The variation of the pressure signal measured by sensor S1 on top of the slope of rising pressure is plotted on the top right of Figure 5.7. The rate at which the amplitude diminishes is related to the area taken by the pressure sensor at this hard wall end of the tube. The sensors absorbs the pressure signal to convert into an electrical signal, limiting the reflected amplitude of the pressure wave after n reflections by:

$$\Delta P_n = \Delta P_0 \left(1 - \left(\frac{D_{sensor}}{D_{tube}} \right)^2 \right)^n \tag{5.12}$$

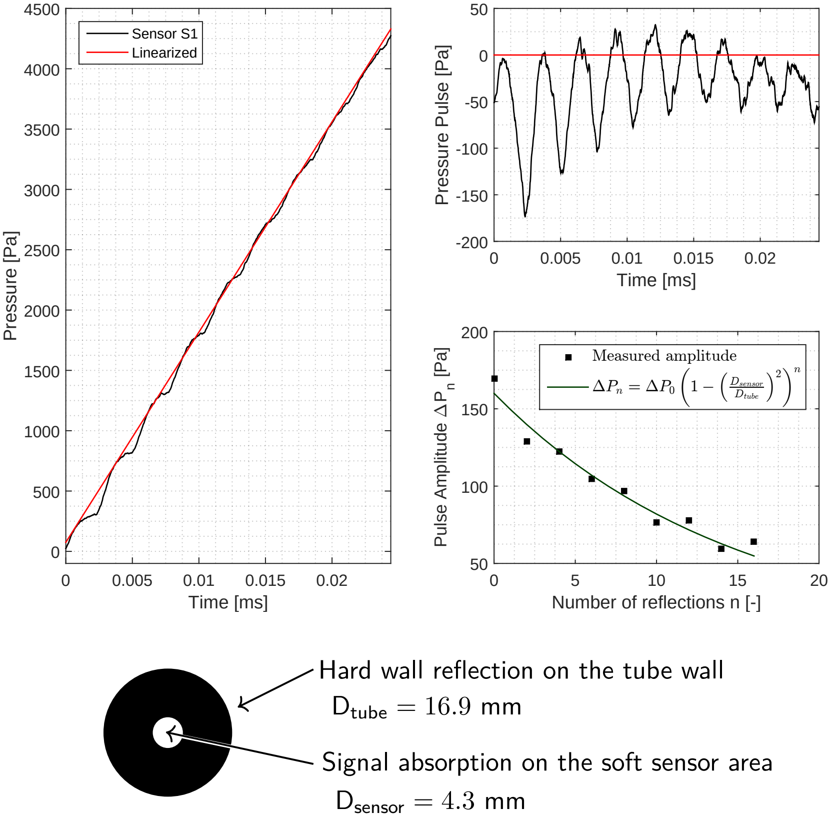

Figure 5.7: The dampening of the Negative Pressure Waves is function of the tube end area taken by the sensor, absorbing a portion of the pressure signal to convert into electrical signal.

with ΔP_0 the initial pulse amplitude w.r.t. linear slope of rising pressure, $1 - \left(\frac{D_{sensor}}{D_{tube}}\right)^2$ the ratio of the tube end section reflecting the pressure wave and n the number of reflections. The larger the area taken by the sensor with respect to the tube or capillary diameter, the stronger this effect and the less reflections will be observed. This will be clear when presenting the pressure measurements inside a capillary.

Bend tube

The design freedom offered by Additive Manufacturing will allow the creation of complex three dimensional objects. The integration of the capillaries to monitor such components will results in bends of the capillary. Such bends may induce additional reflections, making it impossible to localize the leak. Therefore, a set-up was made consisting of two 90°bends. Because of the use of standardized pipe segments, also the tube bends were created using standard elbows screwed on the threaded pipe ends (see Figure 5.8). The measurements revealed that reflections occurred at the fitting ends where the inner diameter of the pipe varies. These reflections made it impossible to localize the leak. This test result made it clear that the internal diameter of the tube and capillaries must be kept constant to reduce undesired reflections. This design constraint was taken into account in the second, small scale, test setup providing successful test results and proving that bends do not disturb the measurements as long as they are smooth and internal capillary diameter are kept constant.

Figure 5.8: Straight tube segments joined together using standard threaded 90°elbows to investigate the effect of bends on the propagation behaviour of Negative Pressure Waves. The internal diameter variations at the elbow interfaces induced undesired reflections of the acoustical waves inside the test setup.

5.2.3 Leak localization on a large scale test setup

Leak localization with two pressure sensors S1 and S2

Point selection Based on the calculated speed of sound inside the tube (see equation (5.8) and given the moments of time-of-arrival of the direct waves (vertical lines 1 and 2 in Figure 5.4), it is possible to estimate the crack location on the basis of equation (5.3). The theoretical error on the localization is calculated on the basis of equation (5.5).

$$x_1 = \frac{0.462 - 339.2 \times 0.00103}{2} \text{ m} = 56.3 \ \pm \ 1.9 \text{ mm.} \tag{5.13}$$

This estimate has to be compared to the real location of the leak, which is 59 mm. We can conclude that the estimation of the leak position is rather good but the localization error is larger than the theoretical error related to measurements. The remaining error is due to noise present on the measurements, which makes it difficult to select the exact moment of arrival of the NPW. Therefore, a sensitivity analysis of the leak localization technique on the basis of the NPW was performed. It is therefore assumed that the moment of time-of-arrival on Sensor S1 and S2 is correct, and we show the theoretical interval of detection of the time-of-arrival on Sensor S2 to have a localization of the leak with an error lower than ±1 cm. The following figure, Figure 5.9, presents the same measurement as Figure 5.4 but is more focused on the moments of time-of-arrival at the sensors. The region corresponding to an inaccuracy of ±1 cm on the localization of the leak was added around the theoretical time-of-arrival at sensor S2.

It must be clear from this measurement that the presence of noise negatively affects the localization accuracy. It is feasible to locate the leak with relative high accuracy, but the uncertainty remains notably larger than the theoretical limit related to the finite sampling rate. Improvement of the test set-up to reduce the noise (e.g. by use pressure sensors with a higher sensitivity) or localization through better processing techniques can solve this issue and increase the localization accuracy.

Least Squares method The best fit in the least-squares sense minimizes the sum of squared residuals between the two pressure signals of sensors S1 and S2. For the leak localization, only the first part of the pressure

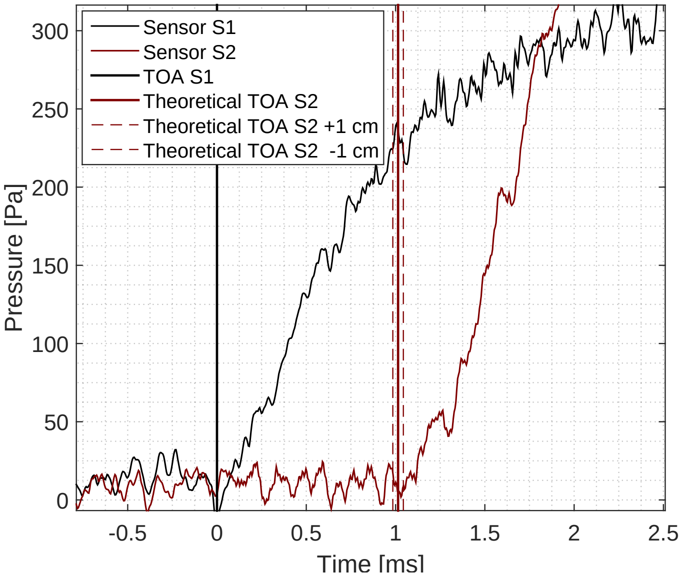

Figure 5.9: Sensitivity analysis for time-of-arrival point selection for crack localization with the leak positioned at L2.

rise is similar at both sensors S1 and S2 and should therefore be considered for this analysis. This part of both sensor measurements is shifted towards each other till the squared residuals are minimized. The optimal shift corresponds to the difference in time-of-arrival of the pressure wave at both sensor locations. This method of determining the delay between the pressure signals is less prone to noise since a larger portion of the measurement is used in this comparison. The plot in the top right corner of Figure 5.10 indicates the part of the signal of Figure 5.4 that will be used for the analysis. The bottom right corner shows that the optimum was found when the signal of sensor S2 was shifted 207 datapoints to the left. The resulting match is plotted on the left of the same figure.

Based on this analysis, we can now estimate the location of the leak. We therefore again use equation (5.3):

$$x_1 = \frac{0.462 - 339.2 \ \times \ \frac{207}{204800}}{2} \text{ m} = 59.6 \pm 1.9 \text{ mm}. \tag{5.14}$$

This location should again be compared to the exact distance, 59 mm. This method clearly reduces the effect of noise on the localization of the leak.

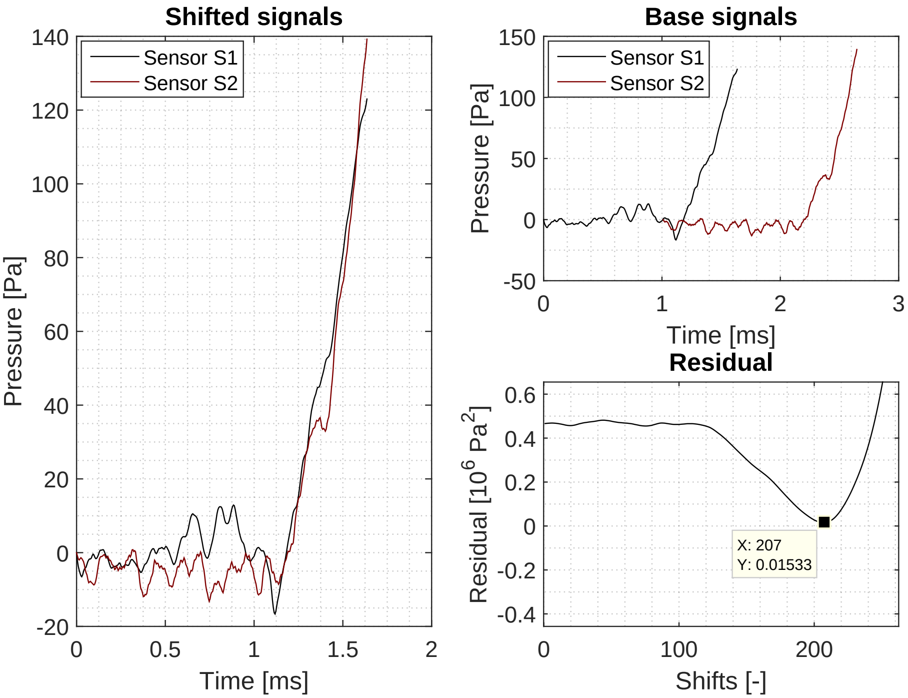

Figure 5.10: Least square analysis on time-of-arrival of Negative Pressure Waves originating from leak position L2.

The leak can be localized within the theoretically expected error margin.

As indicated in Figure 5.2, multiple leak locations (L1–L5) were foreseen on the tube. As to evaluate the leak localization feasibility, it must be possible to distinguish the different leak locations (L1 to L5) from the obtained difference in time-of-arrival of the NPW. Figure 5.11 contains five different measurements for the five different leak locations (L1–L5). The thick vertical line corresponds for all five measurements to the moment of time-of-arrival of the NPW at sensor S1. The figure only shows the data measured at sensor S2. The difference in time-of-arrival between sensor S1 (reference) and S2 (increasing pressure) is compared for the different leak locations.

The more the leak is positioned near the middle of the tube (L5), the smaller the difference in time-of-arrival at the sensor locations because the NPW travelled approximately equal times to both ends of the tube. The NPW that originated from L1, the most extreme leak position, clearly arrived

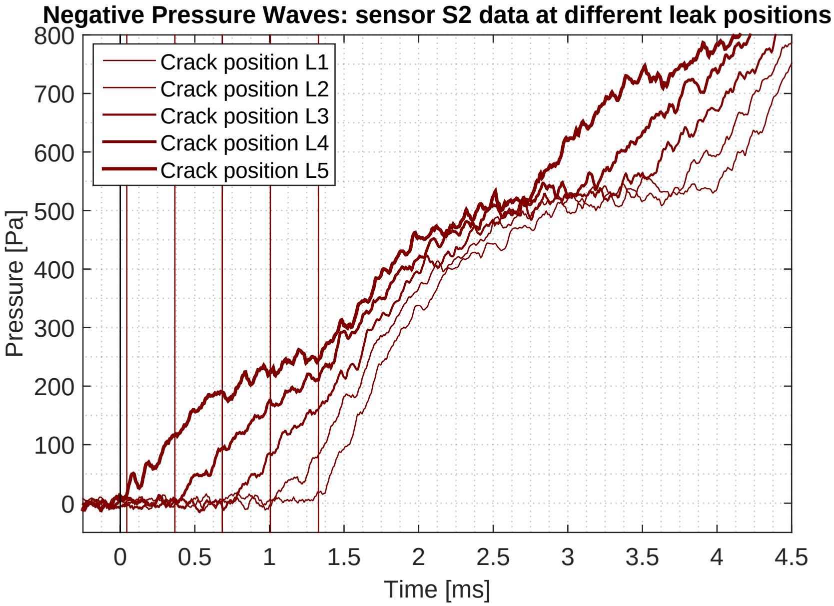

Figure 5.11: Comparison of the difference in time-of-arrival of the Negative Pressure Waves at sensor S2 for different leak positions L1–L5. The origin of the x axis corresponds to the time-of-arrival of the Negative Pressure Waves at sensor S1. The x axis is therefore a representation of the delay between the arrivals of the Negative Pressure Waves at both sensors.

with a large time delay at sensor S2.

The theoretical moments of time-of-arrival corresponding to the different leak locations are highlighted through the thin vertical lines. It is clear from the analysis of Figure 5.11 that the different leak locations can be separated on the basis of the interpretation of the NPW. The following table, Table 5.1, summarizes the localization estimations on the basis of the least squares analysis and the errors on all five measurements (L1–L5).

Although the absolute experimental error does not always fall in the interval defined by the theoretical error, it can be concluded that the leaks can be localized with high accuracy.

Table 5.1: Localization feasibility on basis of difference in time-of-arrival of the Negative Pressure Waves at sensors S1 and S2, using the least squares analysis. (L = 462 mm).

	Exact Location [mm]	Estimated Location [mm]	Absolute Error [mm]	Theoretical Error [mm]
$L1$	4	9.9	5.9	2.1
$L2$	59	59.6	0.6	1.9
$L3$	114	110.9	3.1	1.6
$L4$	169	168.1	0.9	1.4
$L5$	224	222.7	1.3	1.1

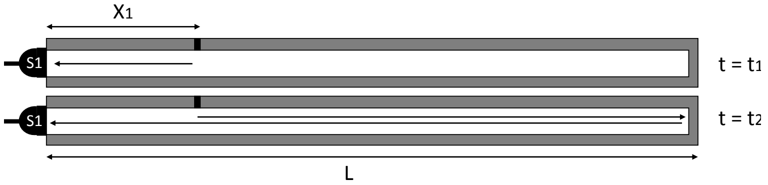

Figure 5.12: The difference in time-of-arrival of the direct and reflected Negative Pressure Waves at one of the sensor locations allows locating the crack.

Leak localization with a single pressure sensor S1

The pressure signals, depicted in Figure 5.5, depend on the leak location. The shape of these pressure pulses is a repetition of the arrival of a direct and reflected Negative Pressure Wave travelling through the tube. The difference in time-of-arrival of an incident and reflected Negative Pressure Wave at the location of one of the sensors, can be used to locate the leak. Figure 5.12 presents the localization principle using only one pressure sensor (sensor S1). This method is only feasible when the Negative Pressure Waves reflect at the hard wall end and the reflected wave can then be observed at the other tube end.

$$\text{Sensor S1} \quad t_1 = \frac{x_1}{c} \tag{5.15}$$

$$\text{Sensor S1} \quad t_2 = \frac{2L - x_1}{c} \tag{5.16}$$

Because t_1 and t_2 are only known relatively, only combination of equations (5.15) and (5.16) leads to a localization formula:

$$x_1 = L - \frac{c(t_2 - t_1)}{2} \tag{5.17}$$

The error on the crack location (Δx) is found by adding the errors on the length L, the speed of sound c and the error related to the finite sampling rate, through:

$$\begin{aligned} \Delta x &= \mid \frac{\partial x}{\partial L} \mid \Delta L + \mid \frac{\partial x}{\partial c} \mid \Delta c + \mid \frac{\partial x}{\partial t} \mid \Delta t & (5.18) \\ &= \Delta L \ + \ \frac{\mid t_2 - t_1 \mid \Delta c \ + \ c\Delta t}{2} & (5.19) \end{aligned}$$

It must be noted that the error on the length ΔL is not divided by two, as was the case in equation (5.5) and therefore becomes twice as important. With the first Negative Pressure Wave arrived, the pressure starts rising in an exponential manner. The breakpoint in the slope of rising pressures corresponds to the arrival of the second Negative Pressure Wave and forms the start of a second exponential pressure rise. Depending on the leak location, this breakpoint occurs sooner or later w.r.t. the arrival of the first wave. The localization principle is therefore based on the determination of this breakpoint. A model of two exponential pressure rise is used to reproduce the measurement signal. A first exponential modelling the pressure rise of the direct Negative Pressure Wave while a second exponential models the arrival of the second Negative Pressure Wave. The analysis then consists in minimizing the residual between the model and the measurement by varying all five parameters affecting the shape of the modelled signal (two amplitudes, two time constants and the breakpoint location). The location of the breakpoint is highlighted in Figures 5.13 and 5.14.

With the arrival of the reflected Negative Pressure Wave at ($t_2 = 2.361$ ms), the location of the leak can be estimated to be:

$$x_1 = 0.462 - \frac{339.2 \ \times \ 0.002361}{2} \ \mathrm{m} = 61.6 \ \pm \ 3.2 \ \mathrm{mm} \tag{5.20}$$

Table 5.2 summarizes the localization estimations and errors of all five measurements (L1–L5).

Except for the determination of the location of leak L4, all errors are relatively small and within the theoretical expected error band. It can be

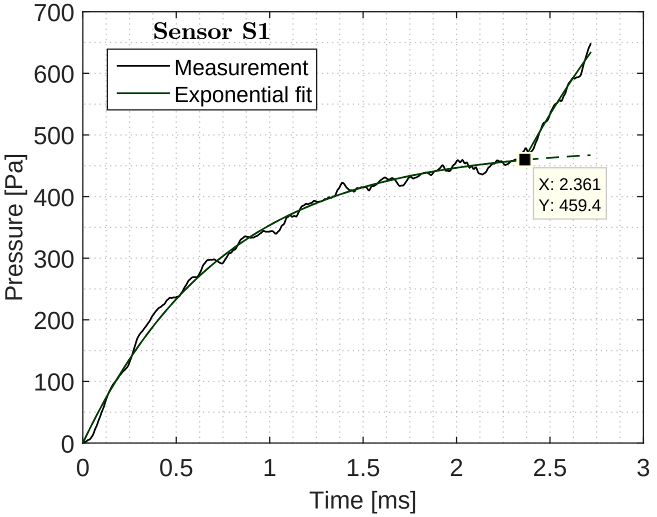

Figure 5.13: The difference in time-of-arrival between the incident (t=0) and the reflected Negative Pressure Wave (t = 2.361 ms) allows locating the leak. The arrival of the reflected wave is seen as a breakpoint in the slope of the rising pressure. The breakpoint location is determined by a double exponential best fit on the measurement.

concluded that the leak can be localized on the basis of a single pressure measurement, as long as Negative Pressure Waves reflect at a hard wall end and propagate back to the other tube end where a pressure sensor is installed.

5.3 Small scale test setup

5.3.1 Test setup description

After the initial investigations on the large scale test setup with tubes, a test setup consisting of capillaries was built. This smaller scale test setup is a closer representation of the actual capillaries that will be integrated inside the AM components. This test setup is depicted in Figure 5.15.

The small scale test setup consisted of two capillary segments (2), joined together at an interface also holding a 3/2 way solenoid valve (3). One

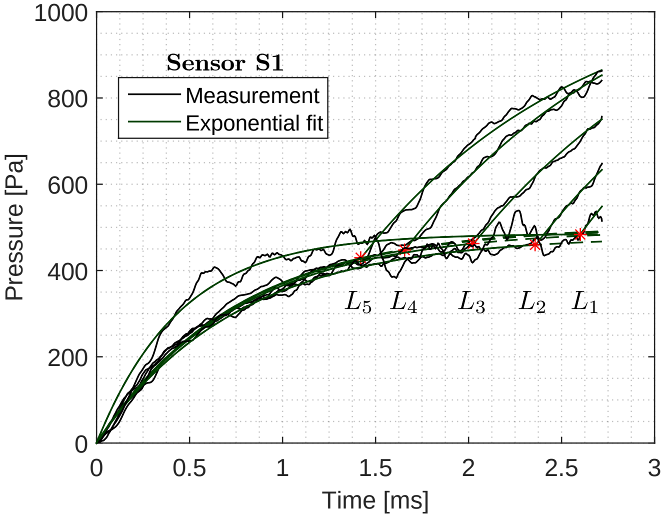

Figure 5.14: The difference in time-of-arrival between the incident (t=0) and the reflected Negative Pressure Wave (t = 2.361 ms) allows localizing the leak. The arrival of the reflected wave is seen as a breakpoint in the slope of the rising pressure. Depending on the leak location, the breakpoint occurs with different delays after the arrival of the direct wave (t = 0s).

inlet of the Festo MHE2-MS1H-3/2G-M7-K solenoid valve is open to the ambient pressure while the second inlet is connected to the venturi (1) for the generation of a vacuum inside the capillary. An Agilent 33210A function generator was used to generate a block pulse that was fed to a mosfet amplifier converting the signal to a power signal to switch the solenoid valve. The (leak) flow is limited by the presence of a leak simulator (4) with a known leak diameter of 1 mm. The leak can be positioned at different locations along the length direction of the capillary by changing the segment lengths of the capillaries. The capillary has an internal diameter of 1.6 mm.

The Endevco MEGGIT 8540-200 pressure sensors (5 and 6) were installed on the free ends of the capillary on either side of the setup. Similarly to the definition on the large scale test setup, we will again define Sensor S1 (5) as the pressure sensor located closest to the leak. Sensor S2 (6) is located at a larger distance from the leak. The pressure sensors were connected to a Scadas III mobile data acquisition unit and data was sampled at the maximum sampling frequency 204.8 kHz. The data was processed through

Table 5.2: Localization feasibility on the basis of difference in time-of-arrival of the direct and reflected Negative Pressure Waves at sensor S1, using the least squares analysis with modelled exponentials. (L = 462 mm).

	Exact Location [mm]	Estimated Location [mm]	Absolute Error [mm]	Theoretical Error [mm]
$L1$	4	2.1	1.9	3.5
$L2$	59	61.8	2.8	3.2
$L3$	114	114.0	0	3.0
$L4$	169	181.0	12.0	2.7
$L5$	224	220.9	3.1	2.5

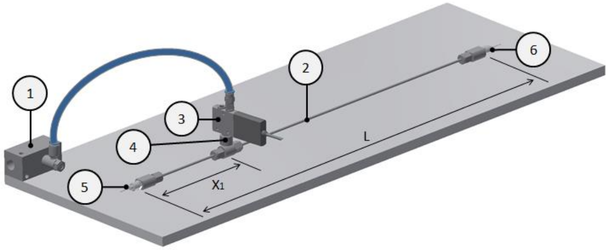

①	Venturi
②	Capillary
③	Shut-off valve
④	Leak size
⑤	Sensor S1
⑥	Sensor S2

Figure 5.15: Experimental test set-up to verify the crack localization feasibility on the basis of Negative Pressure Waves (NPW) inside capillaries

the LMS Spectral Testing software v15 and Matlab R2014b.

Special attention was paid to the design of these interfaces, holding the solenoid valve and the pressure sensors, to reduce the internal reflections. No abrupt variations of the internal diameter may be present and the capillaries were flush mounted against the interfaces. The internal diameter variations must be kept to an absolute minimum in order to reduce undesired reflections. Because of the latter reason, also the connection with the vacuum equipment was designed differently. Instead of having foreseen an extra interface for the vacuum equipment in one of the manifolds, which would have led to an extra disturbance of the internal capillary wall, the vacuum equipment was now installed on the second interface of the 3/2 solenoid valve. The solenoid valve switches between the two inlet ports depending on the voltage signal being high or low. The first inlet is free to the open air for the generation of the leak while the second port is connected to the vacuum equipment. A block pulse is applied to the 3/2 solenoid valve.

First, the pressure inside the capillary is lowered by connecting the vacuum equipment and the capillary through the second port of the solenoid valve. Secondly, by altering the voltage level, the valve interconnects the capillary with the free end of the solenoid valve, generating a leak. With the leak simulator positioned in between the solenoid valve and the capillary, the leak flow is limited by the leak simulator.

The initial pressure level was equal to 0.5 bara while the outside environment was at 1.013 bara. A pressure sensor was installed at both capillary ends (Endevco MEGGIT 8540-200). These sensors were also used throughout the analysis on the large scale test setup. The temperature of the fluid and the capillaries are expected to be all in equilibrium and at room temperature (293.15 K).

The amplitude of the NPWs can be estimated on the basis of the formula's derived in the previous chapter. Since the capillary is initially set at a pressure below the ambient conditions and since the pressure ratio $\left(\frac{P_{amb}}{P_{cap}}\right) > \left(\frac{P_{amb}}{P_{cap}}\right)^*$, the flow through the leak is choked and equation (4.39) must be used:

$$\Delta P_{cap} = C_D \frac{k}{2\left(\frac{P_{amb}}{P_{cap}}\right)^*} P_{amb} \left(\frac{D_l}{D_{cap}}\right)^2 \tag{5.21}$$

In this equation, the following values must be entered to retrieve the expected amplitude of the NPWs:

- The discharge coefficient C_D of the leak. $C_D = 0.923$ (see Table 4.2)
- The ratio of specific heats of the fluid medium. $k = 1.4$ for air.
- The pressure ratio leading to choked flow condition. $\left(\frac{P_{amb}}{P_{cap}}\right)^* = 1.893$ for air.
- The absolute ambient pressure $P_{amb} = 101300$ Pa.
- The diameter of the capillary (here a setup with tubes: $D_{cap} = 1.6$ mm)
- The diameter of the leak $D_l = 1$ mm

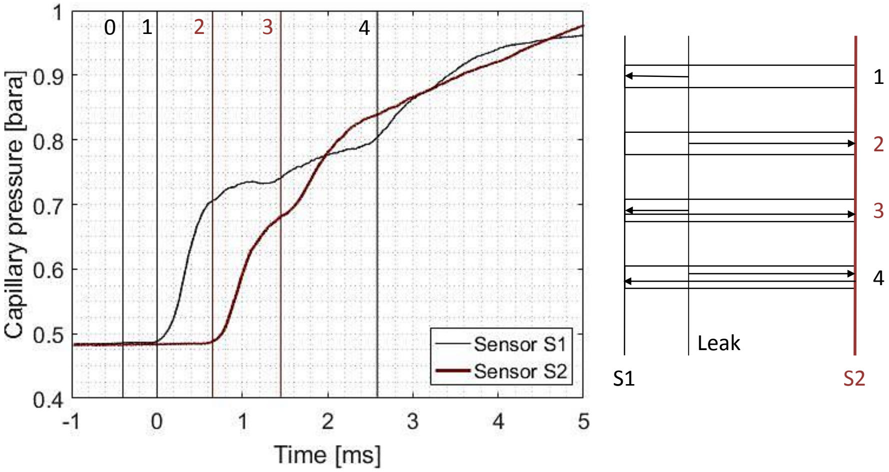

Figure 5.16: Time-of-arrival (TOA) of the (reflections of) Negative Pressure Waves inside a capillary. The measured difference in TOA between vertical lines 1 and 2 is found to be 0.654 ms.

The amplitude of the NPW will therefore be:

$$\Delta P_{cap} = 13510 \text{ Pa} \tag{5.22}$$

5.3.2 Understanding the pressure behaviour inside a capillary

Straight capillary

Figure 5.16 presents the measurement of the pressure inside a capillary. The NPW originates from a leak with a diameter of 1 mm at a location $x_1 = 131$ mm from sensor S1. Sensor S1 and S2 are located at the outermost location, separated by a capillary length of 462 mm and oriented in line with the capillary.

The measurement presents many similarities with the measurements performed on a tube. First, it can be seen that Negative Pressure Waves exist in the capillary. Their amplitude can be predicted using the formulas derived in Chapter 5. For this particular case, the amplitude is expected to be 13510 Pa (see equation (5.22)). At the sensor location, the incident and reflected wave are in phase and the measured amplitude is the double of the actual amplitude of the NPW. The pressure at sensor S1 rises steeply from about 0.483 bara to 0.735 bara, a difference of 25200 Pa, almost the double of the expected 13510 Pa.

At the moment that the leak opens (vertical line 0 as depicted in Figure 5.16), the pressure wave first forms a circular wavefront at the leak location before forming two pressure waves travelling to each side of the capillary. The pressure wave arrives first at the location of the sensor located more closely to the leak location, namely sensor S1 (vertical line 1). With a delay of approximately 0.654 ms, the second NPW arrives at the location of sensor S2 (vertical line 2). In the meantime, the pressure wave that arrived first at sensor S1 has reflected on the capillary end and propagates to the other direction towards sensor S2. This pressure wave arrives at the time corresponding to the vertical line 3. Similarly, the initial wave that reflected at sensor S2 arrives at sensor S1 at the time corresponding to the vertical line 4. On the corresponding measurements of sensors S1 and S2, these events can again be seen as breakpoints on the pressure rise.

Even with initially stronger NPW arriving at the sensors, the arrival of the reflections are less clear as in the case of the tubes. This is a consequence of the presence of the sensor (membranes) recording the pressure signal at the capillary end. A large portion of the amplitude is absorbed to be converted to an electrical signal. In the case of the tubes with a large diameter, only a fraction of the tube end was occupied by the pressure sensor and a large fraction of the tube end reflected the pressure wave.

It is furthermore observed that damping occurs when the Negative Pressure Wave is travelling through the capillary. This was observed when the propagation of the NPW was investigated inside a very long capillary with a diameter of 1.6 mm and a length of $L_{cap} = 3.4$ m. Sensor S1 was located close to the leak location $x_1 = 89$ mm (close to measuring the input signal), while sensor S2 is located at a distance of 3.311 m from the leak. Figure 5.18 presents the pressure measurement inside a capillary with a leak of 1 mm. It is clear from this test result that, although the NPW at the leak location have the same amplitude, the recorded amplitude of the wave travelling to sensor S2 has only half of the amplitude of the wave arriving at the sensor S1. This reduction of the pressure wave amplitude results from (viscous) damping inside the capillary [168].

Many works have reported that the speed of sound inside a capillary v

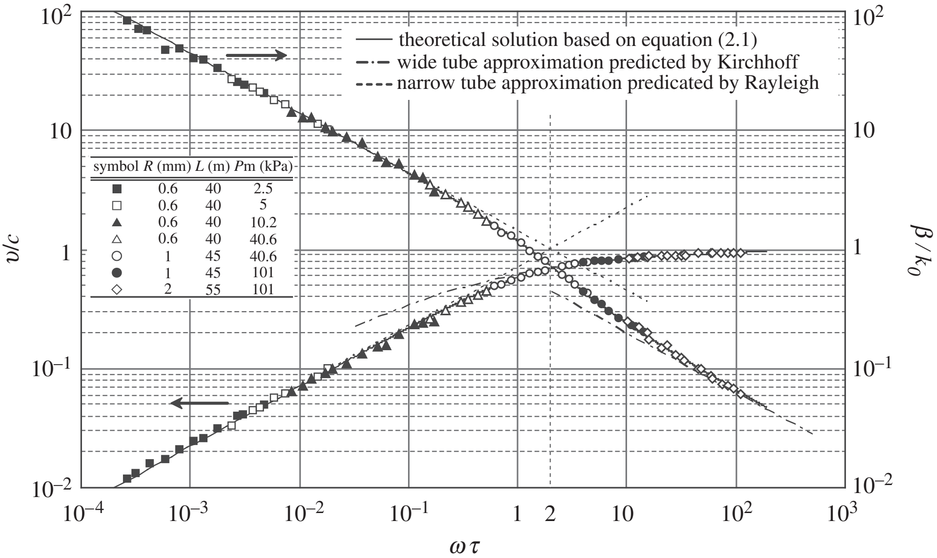

Figure 5.17: Sound wave propagation properties inside a tube. Comparison of experimental propagation constants with various theoretical asymptotic solutions.

is smaller than the speed of sound in open air c [168–171]. The speed of sound inside a capillary or tube is primarly depending on the radius R_{cap} and the pulsation of the sound $\omega = 2\pi f$, with the higher frequencies propagating faster. Figure 5.17 presents the attenuation and propagation speed in function of the frequency and radius of the tube and is entirely taken from the work of Yazaki et al. [168]. The horizontal axis represents the product of the pulsation $\omega = 2\pi f$ and the thermal relaxation time $\tau = \frac{R_{cap}^2}{2\nu_{air}}$. The thermal relaxation time is the time required to establish thermal equilibrium across the section of the flow channel and depends on the radius R_{cap} of the channel and ν_{air} the kinematic viscosity of the air inside the capillary.

For the particular case of the test conduced on the long capillary $L = 3.4$ m with a radius of $R_{cap} = {}^{D_{cap}}\!/_{2} = 0.8$ mm and filled with air of which the kinematic viscosity ($\nu_{air} = 2.18{\times}10^{-5}\text{m}^2/\text{s}$), the thermal relaxation time τ

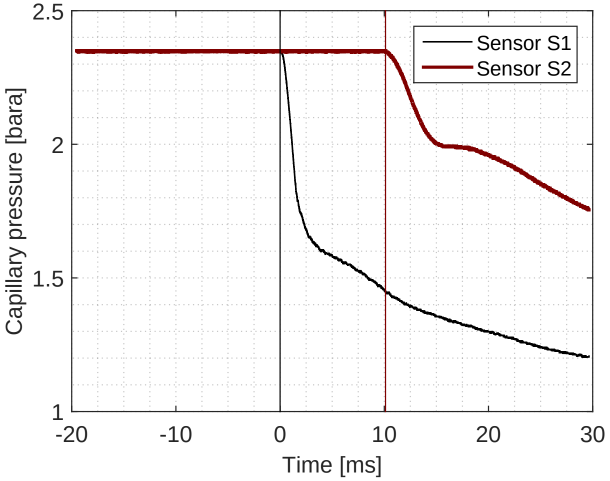

Figure 5.18: Time-of-arrival of the Negative Pressure Waves inside a long capillary (L $= 3.4$ *m) with an internal diameter of 1.6 mm. The measured difference in TOA between vertical lines is found to be 10.117 ms.*

equals:

$$\tau = \frac{R_{cap}^2}{2\nu_{air}} = 0.01467 \text{ s} \tag{5.23}$$

The propagation speed depends on the pulsation an thus the frequency. The signal recorded at the capillary end will therefore be different as compared to the signal recorded more closely to the leak. The higher the frequency of the signal, the higher the product $\omega\tau$ and the higher the propagation speed and the smaller the attenuation when propagating through the capillary. Lower frequencies are more attenuated and propagate slower. Figure 5.18 presents the measurement on the long capillary.

The amplitude of the Negative Pressure Waves measured at sensor S1 and S2 are different. Sensor S1 almost measures the input signal since the distance from the leak is only $x_1 = 89$ mm. The model for the amplitude prediction of the NPW is still valid when considering the signal measured at sensor S1. In a pressurized capillary with a choked leak, equation (4.41)) predicts very well the amplitude recorded on sensor S1 (considering a doubled amplitude because of the reflected and incident wave being in phase):

$$\Delta P_{cap} = \frac{k}{2 * 1.89} P_{cap} \left(\frac{D_l}{D_{cap}} \right)^2 = 34000 \text{ Pa} \tag{5.24}$$

The signal measured at sensor S2, located at a distance of multiple meters from the leak, is clearly distorted when compared to the input signal. The pressure rise is slowed down, the pressure pulse amplitude is weakened (attenuated) and the propagation speed of the NPW was slower as the open air speed of sound. Indeed, the difference in between the time-of-arrival at the sensors is 10.117 ms, which results in an estimated speed of sound:

$$c = \frac{L - 2x_1}{t} = \frac{3.4 - 2{\times}0.089}{0.010117} \frac{\text{m}}{\text{s}} = 318.5 \ \pm \ 0.3 \ \frac{\text{m}}{\text{s}} \tag{5.25}$$

With a measured speed of 318.5 $^{\text{m}}/_{\text{s}}$, the speed of sound inside the capillary is indeed smaller than the speed of sound in open air as considered before. The error on the speed of sound was calculated by:

$$\begin{aligned} \Delta c &= \mid \frac{\partial c}{\partial L} \mid \Delta L + \mid \frac{\partial c}{\partial x_1} \mid \Delta x_1 + \mid \frac{\partial c}{\partial t} \mid \Delta t && (5.26) \\ &= \frac{1}{t} \Delta L + \frac{2}{t} \Delta x_1 + \frac{(L - 2x_1)}{t^2} \Delta t && (5.27) \\ &= 0.3 \ \frac{\text{m}}{\text{s}} && (5.28) \end{aligned}$$

Bend capillary

The design freedom offered by Additive Manufacturing techniques allows the production of complex shaped components. To inspect these with the eSHM system, 3D shaped capillaries will be required. The presence of bends in the capillaries is inevitable. This paragraph analyses the effect of a bend in the capillary on the localization principle based on the Negative Pressure Waves. The test setup consisted of two joint capillary segments, with x_1 being 33 mm and the overall length equal to L = 350 mm. A test, similar to the previously described tests was conducted to retrieve the leak location. Consequently, a first and a second bend with bend radius of 1.5 cm were added to the longest of the two capillary ends. The shortest

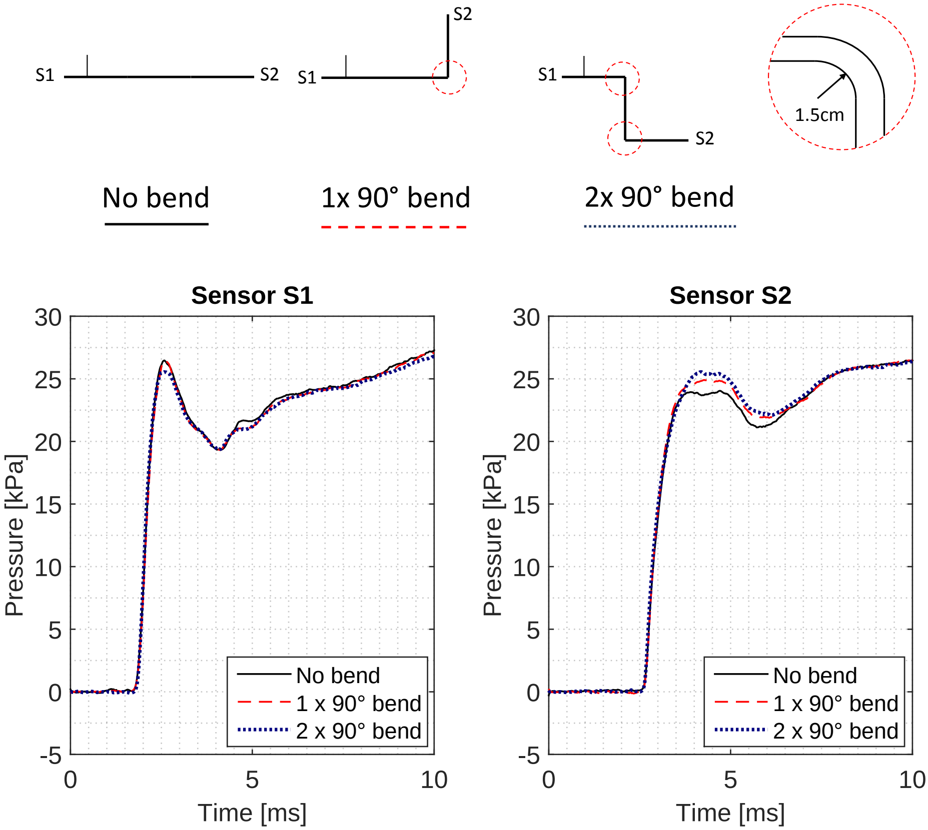

Figure 5.19: The addition of bends to the capillaries does not affect the signal of the Negative Pressure Waves. The shape, amplitude and time-of-arrival of the Negative Pressure Waves remain unaffected.

capillary segment, connected to S1, was not changed. The following Figure, Figure 5.19 depicts the pressure signals recorded by both sensors. Both the x axis of the figure of sensor S1 and S2 have the same time reference $t = 0$ s.

It is clear from this analysis that the pressure signals arrive at both pressure sensors at the same time. The bends do not introduce any delay. Also the shape and amplitude of the pressure signals is not largely influenced by the presence of the bends. The pressure signal received by sensor S1 is not affected since no bends are present. Only small deviations are recorded on the pressure signal of sensor S2. Given this comparison, it is concluded that the addition of bends will not negatively affect the localization feasibility.

No reflections occur on the bends as long as the bends are smooth and no abrupt diameter variations are present (e.g. connections).

5.3.3 Leak localization on a small scale test setup

Leak localization with two pressure sensors S1 and S2

Point selection As a proof for the leak localization feasibility on the basis of NPW inside a capillary, the case of a capillary of $L = 0.462$ m and the leak positioned at $x_1 = 0.131$ m will be considered. The test result is depicted in Figure 5.16. The difference in TOA was determined to be 0.654 ms. The leak position is therefore estimated to be:

$$x_1 = \frac{0.462 - 318.5 \ \times \ 0.000654}{2} \text{ m} = 126.9 \pm 1.1 \text{ mm} \tag{5.29}$$

The error between the real and estimated location is 4.1 mm. This localization error is larger than the error related to the finite sampling rate but remains acceptable. The error is likely related to an additional uncertainty on the speed of sound inside the capillary and possible distortion of signal leading to a different interpretation of the time-of-arrival of the Negative Pressure Wave.

Least Squares A more automated determination of the delay between the arrival of the NPW at sensor S1 and S2 can be on the basis of a least squares analysis. The signal of sensor S2 is shifted forward by a single datapoint each time and the square of the difference in the pressure signals is evaluated. The amount of such shifts required to obtain the lowest value of this squared difference corresponds to the delay in between the arrivals at sensor S1 and S2. Using this method, a larger fraction of the signal is used in the comparison and avoids the influence of noise on the selection of the point of arrival of the waves.

Based on this analysis, we can now estimate the location of the leak:

$$x_1 = \frac{0.462 - 318.5 \ \times \ \frac{138}{204800}}{2} \text{ m} = 123.7 \pm 1.1 \text{ mm}. \tag{5.30}$$

The exact location of the leak is $x_1 = 131$ mm and the estimated location is 123.7 mm. The leak can be located, but the error of 7.3 mm is on the

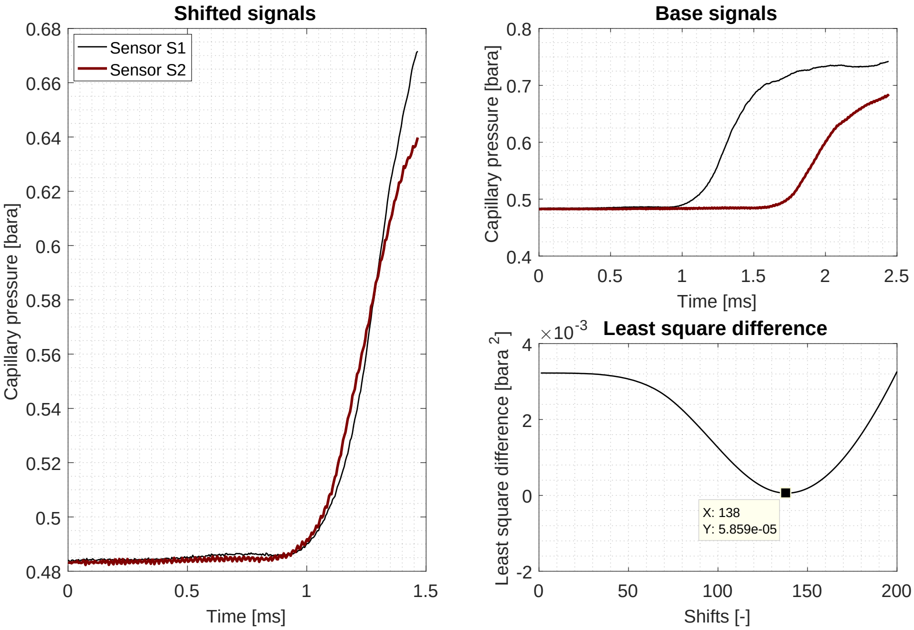

Figure 5.20: Least square analysis on time-of-arrival of Negative Pressure Waves inside a capillary, originating from a leak positioned at $x_1 = 131$ *mm and an overall length of* $L = 462$ *mm.*

large side. This is a consequence of the uncertainty on the speed of sound and the distortion and attenuation of the signal.

5.4 Conclusions

Based on the existing technology of pipeline leak detection and localization on the basis of Negative Pressure Waves, a similar principle was exploited to locate the leak in a closed volume. The continuous and permanent change of the pressure inside the closed volume makes the analysis different from earlier investigations on pipelines with continuous flow. The pressure behaviour and nature of the Negative Pressure Waves was analysed on test setups and the leak localization principle was evaluated on both test setups.

On a larger scale, with a typical tube diameter of above 10 mm, Negative Pressure Waves were clearly present, as well as many reflections occurring at the vertical tube ends on either side. The arrival of the incident NPWs, as well as their reflections, are seen as breakpoints in the pressure rise. The difference in time-of-arrival of these (reflected) waves allows locating the leak. To locate the leak, the exact length of the tube must be known as well as the speed of sound of the fluid inside the tube. The larger the diameter, the more correct the assumption to use the free space speed of sound, which was found to be rather correct for the purposes of these tests. Because of the relatively small amplitude of the NPWs, and the limited resolution of the pressure sensors, the determination of the exact moment of arrival of the NPWs is prone to the presence of noise on the measurement resulting in a larger localization error. By conducting a least squares analysis on a larger fraction of the pressure signal, the error on the leak location could be reduced. Although the general principle makes use of two pressure sensors on either side of the tube, the leak can be located using a single pressure sensor by exploiting the reflections occurring on the tube walls. The leak localization accuracy is however lower.

On a smaller scale, which is considered here as a capillary with an internal diameter of 1.6 mm, the story is different. Keeping all other parameters constant, the amplitude of the NPWs in a capillary is significantly higher than in a tube with a larger diameter. The pressure rise, however, is less instantaneous resulting in a rather gradual increase of pressure making it more difficult to determine the exact moment of arrival of the NPWs. By lengthening the capillary, this effect was enlarged, showing that the signal becomes distorted, pressure rise weakens and speed of sound drops. This test was used to determine the speed of sound inside the capillary which could then be used in the localization formula. The speed of sound inside a capillary lowers with decreasing cross sectional area of the capillary and furthermore depends on the frequency of the sound. The passage through the capillary distorts the pressure signal, leading to larger errors on the localization of the leak. The leak could be localized with an error of approximately 5 mm.

The addition of bends to a capillary did not alter the shape of the pressure signal and will not influence the feasibility to locate the leak. However, the way these bends are introduced on the tube/capillary is important. Internal diameter changes and preferably even connection pieces, must be avoided to limit extra internal reflections on these changes of acoustical impedance.

Leak localization in a closed volume, on the basis of NPWs, is proven to be possible and accurate. The method requires continuous sampling at a very high sampling rate to reduce the theoretical uncertainty related to the sampling frequency. This method will therefore also require online data evaluation to evaluate whether data storage is required or not.

Chapter 6

Usage monitoring

A different approach to condition based maintenance consists in the monitoring of the actual loads that the component has suffered and predicting the remaining useful lifetime of the component. Such a monitoring strategy is called Usage Monitoring. The principle is based on the integration of strain/load sensing elements, especially at fatigue critical areas, to measure the loads at these locations. The integrated capillary of the eSHM system can also be used to measure the deformation, thus strain and loads, acting on a structure. As the structure deforms, so does the integrated capillary which results in pressure fluctuations inside the capillary that can be measured. The present chapter will analyse the feasibility of the eSHM system to function as a Usage Monitoring system. The results presented in this chapter are based on [172].

6.1 Introduction

In-situ load monitoring allows the extraction of usage information of structures, such as counting fatigue cycles, determining whether loads and usage are according to the design and ensure that load limits are not exceeded during operation. This information can then be used to estimate the remaining operational lifetime (RUL) and organize maintenance inspections. The monitoring system must remain operational in changing and possibly hazardous environments with limited (visible) access. Environmental influences, drift over time, disbonding, aggressive fluids and other factors can cause early failure of the monitoring system [50, 173]. For long-term monitoring, the sensors must be robust and give reliable results for a long time. Using glued sensors, like strain gauges, might not be a good solution, since the adhesive can be affected by humidity, temperature, UV light etc. [174]. A robust, integrated and preferably lightweight monitoring system can overcome these issues. One can overcome most of the difficulties of long-term load monitoring by embedding a strain sensor into the component, thereby enabling so-called ‘self-sensing’ components [175–179]. So far, most embedded strain measurements were found in matrix materials such as composites and concrete [180–184]. The sensors are embedded in the matrix material and cured in afterwards.

Additive manufacturing, or 3D printing, now enables such integration of functions inside non-matrix structures such as polymers, metals, ceramics, etc. The layer-wise manner of production allows the inclusion of functionalities inside the component that were not possible by conventional subtractive production techniques. The current work describes a method of integrating a strain sensitive capillary feature inside 3D printed components. The embedded capillary is filled with a fluid and closed by an externally mounted pressure sensor. The elongation (contraction) of the integrated capillary results in a pressure decrease (increase) of the fluid inside the capillary, which is measured by the pressure sensor. As the pressure sensor can be placed at a convenient location, this method of strain sensing is inherently robust and lightweight. The installation cost of the presented system, for structural health monitoring applications, is limited to the installation of an off-the-shelf pressure sensor. The capillary must be incorporated in a strain affected zone but does not induce any additional manufacturing or installation cost.

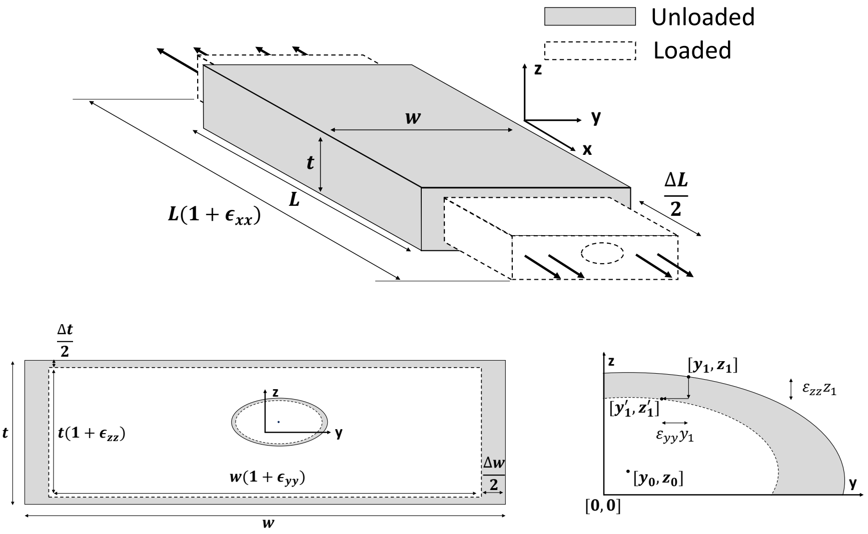

Figure 6.1: Analytical model of a tensile stressed cross section with integrated capillary for usage monitoring.

6.2 Analytical study and simulations

The concept of strain sensing through the integration of capillaries inside the structure that is deforming is first analysed through an analytical study. Such a model will allow the determination of the most important parameters affecting the sensitivity of this strain sensing principle, while it will also reveal what parameters do not affect the sensitivity. The analytical model will predict the pressure change inside a capillary integrated in the cross section of a tensile test specimen with a width w and thickness t, as shown in Figure 6.1. The analytical model will then be validated on the basis of two tensile test campaigns with integrated capillaries.

The following sections will present the derivation of the equations predicting the pressure variation inside the capillary based on a uniform tensile strain applied to the cross section in which the capillary is present. As to avoid stress concentrations around the capillary, sharp edged capillaries will be avoided in the design while capillaries with circular and elliptical shapes are to be preferred. The formula predicting the pressure will be derived for both an elliptical shaped capillary, but remains valid for the special case of a circular capillary.

Figure 6.1 presents a tensile specimen which will be used as a model for the analytical derivation of the pressure variation inside an elliptical capillary expected during a tensile test. Assuming small strains and small displacements, a tensile load acting on the tensile specimen will elongate the specimen in the x-direction:

$$\frac{L_{load}}{L} = (1+\epsilon_{xx}) \tag{6.1}$$

with L_{load} representing the length of the test section after application of the load, L the initial length of the test section and ϵ_{xx} the longitudinal strain. This action is elongating the capillary, thereby increasing the capillary volume. Consequently, the capillary pressure will drop. The Poisson effect limits the capillary volume increase since the cross sectional area of the test specimen, and thus also that of the capillary, will drop. The Poisson coefficient ν of an isotropic material is defined as

$$\epsilon_{yy} = -\nu\epsilon_{xx} \tag{6.2}$$

$$\epsilon_{zz} = -\nu\epsilon_{xx} \tag{6.3}$$

in which ϵ_{yy} and ϵ_{zz} are transversal strains in the y and z direction respectively. With the axis defined as in Figure 6.1, thus with the origin of the axis at the planes of symmetry of the test specimen, any point $[x, y, z]$ of the cross section subjected to an uniform stress ϵ_{xx} will displace to $[x', y', z']$ in the following manner:

$$x' = \epsilon_{xx}x \tag{6.4}$$

$$y' = (1+\epsilon_{yy})\,y = (1-\nu\epsilon_{xx})\,y \tag{6.5}$$

$$z' = (1+\epsilon_{zz})\,z = (1-\nu\epsilon_{xx})\,z \tag{6.6}$$

Considering the case of pure tension, all points that are located on a plane at a given distance x in the unloaded case will remain on a plane and translate to the plane x' when loaded. On any given cross section of the tensile specimen, a point $[x, y_1, z_1]$ located on an ellipse (e.g. the capillary surface) with radius's r_1 and r_2 and the center of the ellipse positioned at $[x, y_0, z_0]$ satisfies the equation:

$$\left(\frac{(y_1 - y_0)}{r_1}\right)^2 + \left(\frac{(z_1 - z_0)}{r_2}\right)^2 = 1 \tag{6.7}$$

With the application of a uniform tensile load and longitudinal strain ϵ_{xx}, all points on the ellipse remain on an ellipse. Indeed, multiplication of the nominator and denominator of equation (6.7) with $(1 - \nu\epsilon_{xx})^2$, leads to the equation:

$$\left(\frac{((1 - \nu\epsilon_{xx})(y_1 - y_0)}{(1 - \nu\epsilon_{xx})\, r_1}\right)^2 + \left(\frac{(1 - \nu\epsilon_{xx})(z_1 - z_0)}{(1 - \nu\epsilon_{xx})\, r_2}\right)^2 = 1 \tag{6.8}$$

$$\left(\frac{(y_1' - y_0')}{r_1'}\right)^2 + \left(\frac{(z_1' - z_0')}{r_2'}\right)^2 = 1 \tag{6.9}$$

which is again an ellipse with radiuses r_1' and r_2' and its center located at $[y_0', z_0']$:

$$r_1' = (1 - \nu\epsilon_{xx})\, r_1 \tag{6.10}$$

$$r_2' = (1 - \nu\epsilon_{xx})\, r_2 \tag{6.11}$$

$$y_0' = (1 - \nu\epsilon_{xx})\, y_0 \tag{6.12}$$

$$z_0' = (1 - \nu\epsilon_{xx})\, z_0 \tag{6.13}$$

After deformation, the new cross sectional area A_{load} of the ellipse equals

$$A_{load} = \pi r_1' r_2' \tag{6.14}$$

$$A_{load} = \pi(1 - \nu\epsilon_{xx})^2 r_1 r_2 \tag{6.15}$$

$$A_{load} = (1 - \nu\epsilon_{xx})^2 A \tag{6.16}$$

where A represents the initial, unloaded, cross sectional area of the capillary. The Poisson effect counteracts the volumetric increase of the capillary volume due to the longitudinal elongation ϵ_{xx} by reducing the cross sectional area of the capillary. The larger the Poisson coefficient, the smaller the cross section of the resulting capillary. To determine the pressure variation ΔP inside the capillary due to a tensile load on the tensile specimen, it suffices to express the definition of the bulk modulus K:

$$\begin{aligned} \Delta P &= -K\frac{\Delta V}{V} && (6.17) \\ \Delta P &= K\left(1-\frac{A_{load}L_{load}}{AL}\right) && (6.18) \end{aligned}$$

in which ΔV represents the capillary volume change and V the capillary volume in unloaded condition. With the inclusion of equations (6.1) and (6.16), the pressure variation inside the capillary becomes:

$$\Delta P = K\Big(1-(1-\nu\epsilon_{xx})^2(1+\epsilon_{xx})\Big) \qquad (6.19)$$

In the special case of the more common circular capillary ($r_1 = r_2 = R_{cap}$), the same derivation can be done and results in the same equation, Equation (6.19). Considering that the strain ϵ_{xx} remains small, one can simplify the equation by neglecting second order terms:

$$\Delta P = K(2\nu-1)\epsilon_{xx} \qquad (6.20)$$

6.2.1 Shape, size and position of the capillary

This analytical development shows that neither the actual shape (ellipse, circle or others), nor the size (the radius) and position of the capillary do influence the sensitivity of the pressure signal inside the capillary when subjected to a longitudinal strain ϵ_{xx}.

6.2.2 Poisson coefficient ν

This development furthermore clearly shows the importance of the Poisson coefficient, naturally limited between $0 < \nu < 0.5$. A Poisson coefficient closer to zero leads to a larger pressure signal for a given elongation while a Poisson coefficient of 0.5 does not induce any pressure variation for a given elongation. The effect of the Poisson coefficient on the pressure signal induces inside the capillary due to the volumetric change of the capillary is depicted in Figure 6.2.

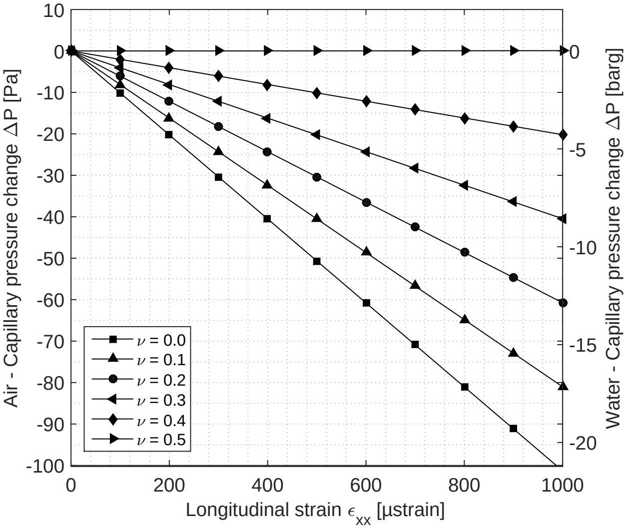

Figure 6.2: The influence of the Poisson coefficient on the sensitivity of the pressure variation inside the capillary based on the analytical model. For air and under constant temperature, the bulk modulus K equals the static pressure level P_0 = 101300 Pa. For water, the bulk modulus equals 2.18 GPa.

The Poisson coefficient cannot be seen as a design parameter. It is a material parameter and the material is most frequently fixed by other design requirements. The Poisson coefficient furthermore has a limited range in which it can be varied, with most materials having a Poisson coefficient ranging between 0.25 to 0.4, although exceptions and new design solutions can result in Poisson coefficients even outside the ‘natural’ limits of $0 < \nu < 0.5$.

6.2.3 Bulk Modulus K

The single design parameter influencing the sensitivity of the usage monitoring system is the bulk modulus K of the fluid inside the capillary. The bulk modulus therefore deserves a litte more attention. The higher the bulk modulus, the larger the pressure variations expected inside the capillary. Figure 6.2 presents the capillary pressure variations for both a compressible (air) and incompressible (water) fluid. Note the large differences in y

Fluid		Bulk modulus [MPa]
Air	K_T	0.1013
Air	K_S	0.142
Water	-	2180

Table 6.1: Bulk modulus of fluids tested (air and water) at P_0=1.013 bara.

scaling because of the significantly higher bulk modulus of water.

Compressible fluid - Air

The isentropic or adiabatic (K_S) and isotherm (K_T) bulk modulus of an ideal gas are given by:

$$K_T = P_0 \tag{6.21}$$

$$K_S = kP_0 \tag{6.22}$$

with $k = {}^{C_P}/_{C_V}$ the heat capacity ratio and P_0 the (initial) static pressure level inside the capillary. Although air is not an ideal gas, these formulas give an approximation of the Bulk modulus of air. The bulk modulus for air is given in Table 6.1. Increasing the static pressure level allows increasing the sensitivity of the system, but requires the selection of a pressure sensor capable of withstanding these higher pressure. With the resolution of a pressure sensor typically limited at a fraction of its range, the increase in sensitivity gained by the higher static pressure level is lost in the resolution of the pressure sensor. As a matter of example, the pressure inside a capillary filled with air at ambient pressure and subjected to a longitudinal strain of 1000 µstrain and inside a material with poisson coefficient of 0.33 will drop by 34.4 Pa. This is a very limited static pressure variation, only measurable with high end pressure sensors.

One can increase the sensitivity of the system by filling the capillary with a fraction of non stressed, incompressible, material (loose solid or a liquid). It must be stressed that the material inside the capillary must remain unloaded since otherwise the same effect (longitudinal strain and poisson effect) will deform this material in a similar fashion and its effect is annihilated. Assuming that a fraction of the capillary is filled with a solid or liquid, and considering that these materials will not deform under the small pressures build up inside the capillary, then the following equation allows predicting the sensitivity of the system:

$$\Delta P = -K\frac{\Delta V}{V - V_{fill}} \tag{6.23}$$

$$\Delta P = -K\frac{\Delta V}{V}\left(\frac{V}{V - V_{fill}}\right) \tag{6.24}$$

which becomes with the inclusion of equation (6.19):

$$\Delta P = K\left(1 - (1 - \nu\epsilon_{xx})^2 (1 + \epsilon_{xx})\right)\left(\frac{1}{1 - \frac{V_{fill}}{V}}\right) \tag{6.25}$$

Figure 6.3 presents the pressure variation inside a capillary subjected to a tensile strain of 1000 µstrain for different Poisson coefficients and filling ratio's V_{fill}/V.

Incompressible fluid - Water

The bulk modulus of a liquid is several orders of magnitude higher than the bulk modulus of a gas. For water, the bulk modulus is typically around 2.2 GPa with only a little difference between the isentropic and isothermal bulk modulus. The bulk modulus of a liquid can be determined on the basis of the determination of the speed of sound in the liquid and the density:

$$c = \sqrt{\frac{K}{\rho}} \tag{6.26}$$

6.3 Prototyping using Fused Deposition Modelling

As a proof-of-concept for the presented strain sensing approach, the capillaries were embedded in tensile test samples produced by Fused Deposition

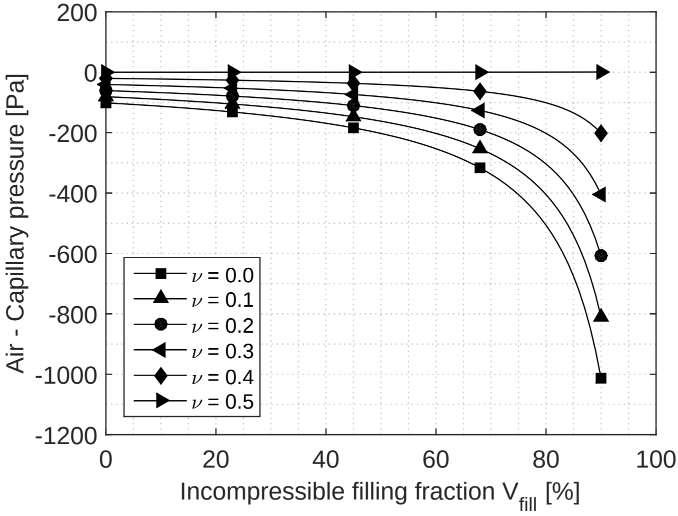

Figure 6.3: The influence of the additional filling with an incompressible medium to increase the sensitivity of the pressure change to a constant tensile strain of 1000 µstrain in a capillary filled with air. The isothermal bulk modulus of air was used (K_T = 101300 Pa).

Modelling (FDM), a typical prototyping Additive Manufacturing technique for the production of polymer parts. The pressure measurements are compared to the state-of-the-art extensometer measurements. The capillaries were filled with air (compressible fluid) and water (incompressible fluid) to investigate the effect of the bulk modulus of the fluid on the sensitivity of the strain sensor. As to compare the measured sensitivity of the system with the theoretically expected values, also the Poisson coefficient of the material was measured on dedicated specimens without capillary.

6.3.1 Design

The tensile test samples were designed in order to compare the state-of-the-art extensometer results with the strain measurements of the proposed monitoring system. To that end, the tensile test samples were designed to accommodate both measurement techniques, in order to investigate the concept of load monitoring using integrated capillaries in 3D printed components. The design is depicted in Figure 6.4.

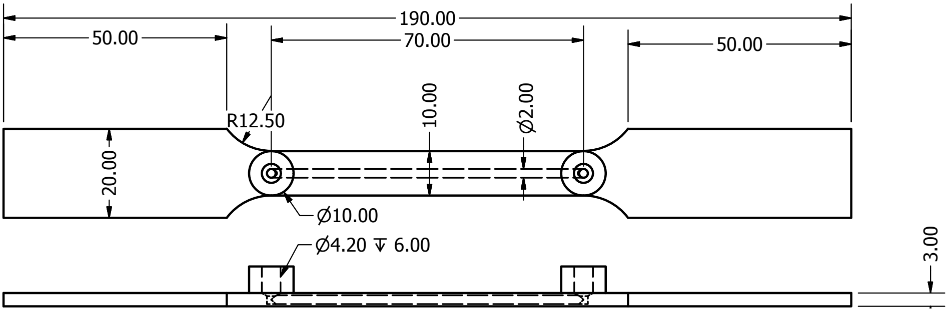

Figure 6.4: Tensile test sample dimensions (in mm).

The proposed strain monitoring system consists of an externally mounted pressure sensor connected to a 2 mm diameter capillary integrated into the test section of the tensile test sample. The extensometer measured the strain in the same test section as the integrated capillary. Alongside this first connection, an additional external connection was added to ease the filling of the capillary, flush the channel, and check that the capillary was not clogged. These connections were threaded using M5 HeliCoil's®. Figure 6.4 gives an overview of the dimensions (in mm) of the tensile test samples and integrated monitoring system. Figure 6.5 shows a tensile test sample with the HeliCoil® threaded connections installed.

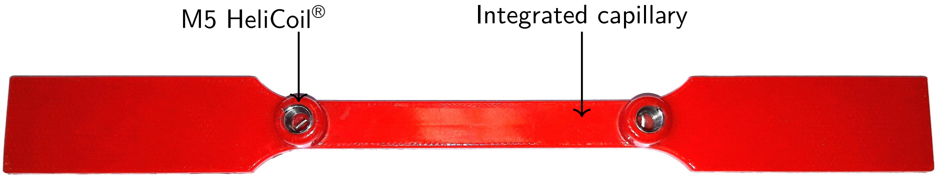

Figure 6.5: 3D printed tensile test sample.

6.3.2 Materials and Production Process

The tensile test sample were produced by an Ultimaker 2+ (Ultimaker, Cambridge, USA), a 3D printer using Fused Deposition Modeling (FDM) technology. FDM, one of the common variants of additive manufacturing techniques, has been widely adopted within the industry for producing complex geometrical parts at a reasonably low cost [185]. The raw material used is in the form of filament that is melted when extruded through a heated nozzle. The material is deposited while the nozzle is moving in a horizontal plane and the material solidifies at the deposited location. The build plate is lowered when the layer is finished and new material added on top of the previous layer until the component is fully completed.

The embedded capillary is filled with air or water and becomes pressurized when deformed during tests. The embedded capillary must therefore be air- and watertight, which largely depends on the choice of material and production process used. Acrylonitrile butadiene styrene (ABS) is a typical material used for the FDM process and can be made water-impermeable. As printed, the ABS material deposited in layers or as strands is incapable of holding water. In particular, for a (micro) fluidic design with imprinted channels and network geometries this issue is critical. The layers do not blend together to create a watertight device, with small gaps and holes in between the deposited material [186]. It is therefore of interest to chemically modify the surface of ABS to become water impermeable.

Water tightness of FDM printed ABS parts is generally ensured by an after-treatment process involving dimethyl ketone (acetone). Immersion or direct contact with acetone may lead to very quick reaction and may damage ABS parts if the dipping time and concentration are not monitored/optimized accurately. Even a short exposure of ABS to hot vapor may lead to non-uniform treated surfaces [187]. Cold vapor treatment was therefore used in the work of Garg et al. [187]. Other works report the use of acetone-water solutions to treat the ABS surfaces [186, 188].

In this manuscript, acetone cold vapour treatment was used in order to melt together the different ABS layers to become water impermeable. A thin layer (5 mm) of liquid acetone was poured on the bottom of a closed container. The samples were held 5 mm above the liquid acetone surface and were turned over every 1.5 h. In order to select a proper duration for the vapour treatment process, the surface roughness and strain sensor performance were compared for as-built, 6 h and 17 h vapor treated tensile test samples. These samples were printed using a layer thickness of 0.250 mm. The optical microscope images, shown in Figure 6.6(a–c), show the bottom side of the tensile test samples (side build plate) in as-built condition, and those that were externally exposed to cold acetone vapour for 6 h and 17 h. It is clear that the cold vapour treatment has modified the surface roughness by blending together adjacent layers. Figure 6.7(a-c) shows Scanning Electron Microscope (SEM) images of the inner surface of the capillary inside the tensile test samples with layer thickness of 0.250

mm for different after-treatment processes.

The strain sensor performance for the different after-treatment processes was evaluated by performing a tensile test and evaluating the sensitivity of the fluid (water) pressure per strain unit. The testing procedure will be discussed in detail in Section 6.3.3. The test results are depicted in Figure 6.8 (bottom). The after-treatment processes also had a major influence on the Young Modulus of the ABS material, as depicted in Figure 6.8 (top). The first three columns of Figure 6.8 show a comparison between the as-built condition of ABS material with a layer thickness of 0.250 mm, and after a 6 h and 17 h cold acetone vapour treatment. It is clear from these results that, although a proper acetone treatment is required to obtain a sealed capillary for the strain measurements, long exposure to cold acetone vapour led to a drastic reduction of the Young Modulus and, as a consequence, poor performance of the strain measurement sensor. It was observed that the capillary walls were sucked inwards, which can be seen as the dark sinusoidal irregularities in the capillary wall depicted in Figure 6.7 (c). The capillary walls could not withstand the internal vacuum pressure levels, as measured with the samples that were treated for 6 h.

Although the surface roughness was greatly improved by long exposure to cold acetone vapor, the bulk material properties of ABS were greatly deteriorated. It was concluded that the duration of the after-treatment process needed to be reduced, such that only the component's surface is affected. In order to improve the surface roughness and better squeeze together different layers, a new batch of samples was printed with a reduced layer thickness of 0.140 mm. This second batch of tensile test samples was externally exposed to cold acetone vapour for a period of 6 h, after which the inner capillary surface was treated by sucking cold acetone vapour through the capillary. The acetone vapour was present in the capillary for 2 h, after which it was flushed again with acetone. The flushing procedure was repeated four times. It can be concluded from Figure 6.6 (d,e) that the surface roughness was indeed ameliorated by the reduced layer thickness. The shape of the capillary was also improved by reducing the layer thickness, as depicted in Figure 6.7. From Figure 6.8 it can be seen that the Young Modulus was less affected by the after treatment procedure and the pressure level inside the integrated capillary became very sensitive to strain.

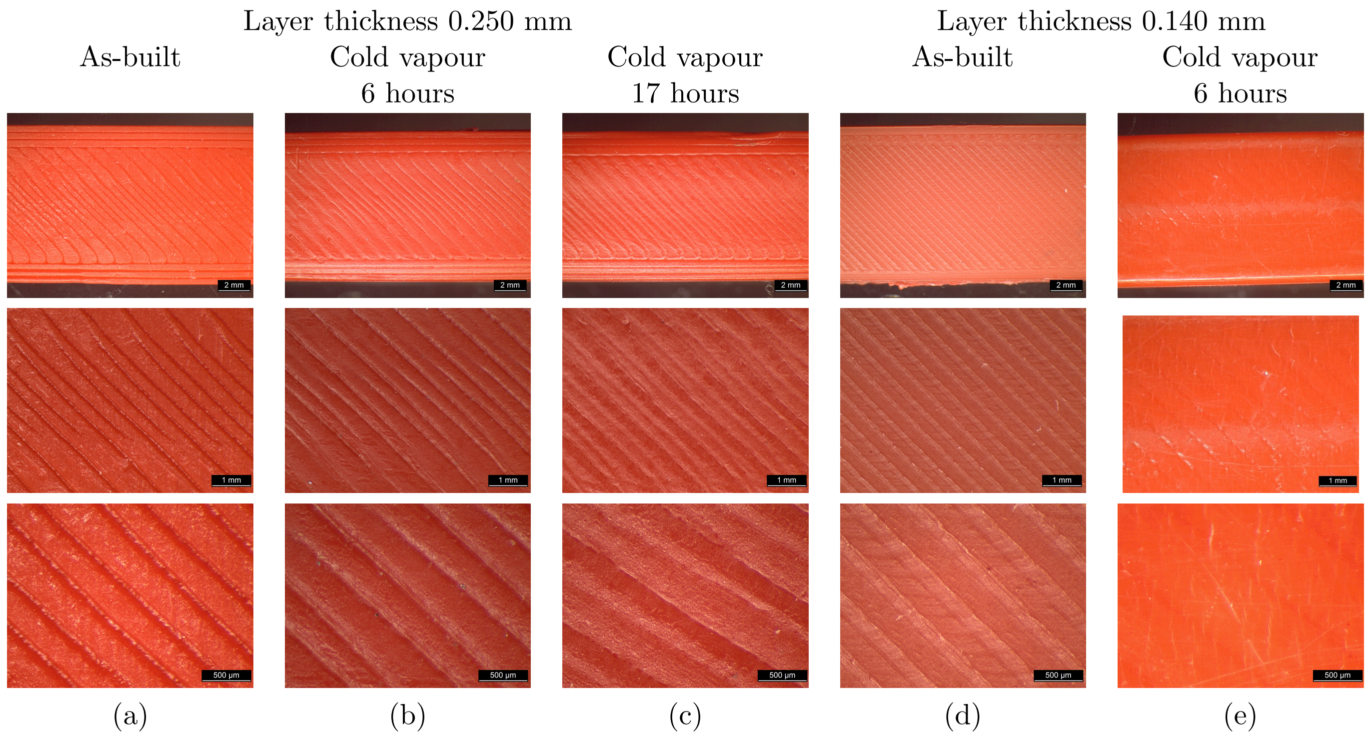

Figure 6.6: Optical microscope images of external surface of acrylonitrile butadiene styrene (ABS) printed tensile test samples with a layer thickness of 0.250 mm for (a) as built condition (b) cold vapour treatment during 6 h (c) cold vapour treatment during 17 h and with layer thickness of 0.140 mm for (d) as-built condition and (e) cold vapour treatment during 6 h.

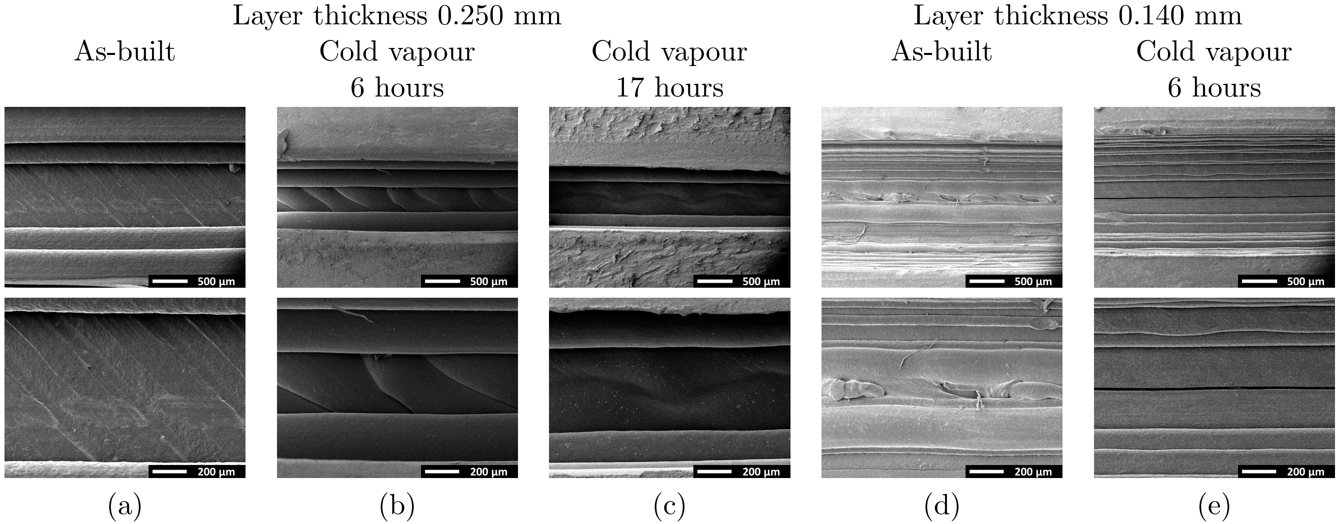

Figure 6.7: Scanning Electron Microscope (SEM) images of capillary surface inside ABS printed tensile test samples with layer thickness of 0.250 mm for (a) as built condition (b) cold vapour treatment during 6 h (c) cold vapour treatment during 17 h and with layer thickness of 0.140 mm for (d) as-built condition and (e) cold vapour treatment during 6 h.

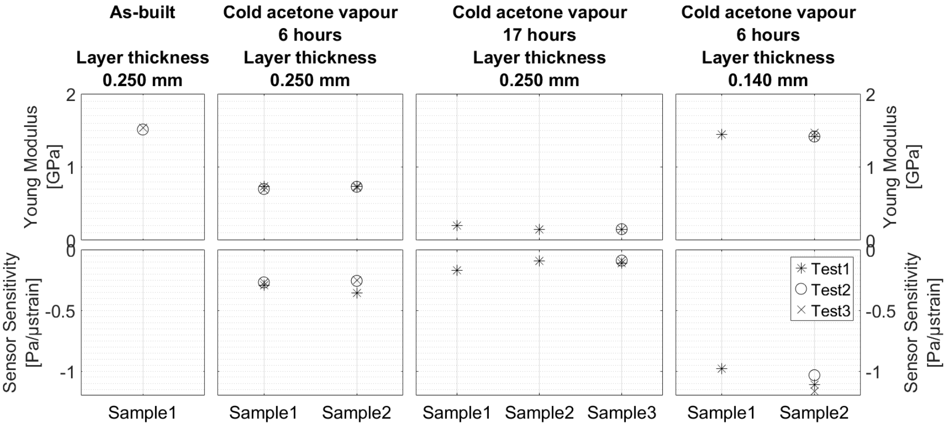

Figure 6.8: Comparison of cold acetone vapour after-treatment processes on Young Modulus (top) and strain measurement system performance (bottom) of ABS printed parts. The capillary is filled with water.

The latter, improved batch of tensile test samples, was further tested in order to explore the possibilities of the newly developed strain monitoring technique. Two test cases were considered: the capillary of the load monitoring system filled with either a compressible fluid (air) or an incompressible fluid (water). For both cases, the pressure sensor was first installed at one side of the capillary. When the capillary was filled with air, the other end was closed without any further treatment. Only when the capillary was entirely filled with water, was the sample left open at the other capillary end and fully immersed in a bottle of water (with the open connection at the top) and placed in a vacuum oven. This process ensured that all air bubbles escaped from the capillary before closing it at the other end. The fully prepared load monitoring system is shown in Figure 6.9.

6.3.3 Testing

The load monitoring system consisted of an integrated capillary filled with a fluid and connected to an externally mounted pressure sensor. The chosen absolute pressure sensor (Kulite XTL-123A-190, Kulite Semiconductor Products, Inc., Leonia, USA) with a limited range from 0–1.7 bar, is compatible with all nonconductive and non-corrosive liquids or gases.

The tensile test samples were placed in an Instron 5885 H (Instron, Norwood, USA) tensile testing machine with Instron 2518-103 load cell (10 kN

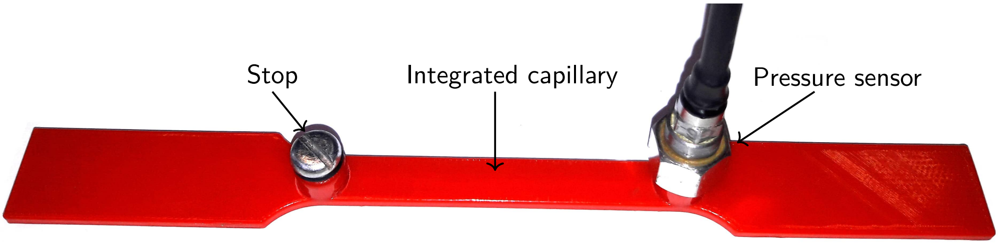

Figure 6.9: The presented load monitoring system for 3D printed structures.

static). An Instron 2630-030 extensometer was furthermore installed on the test section. The pressure sensor, extensometer, load cell and cross head displacement were all recorded using an LMS Scadas III mobile data acquisition system (Siemens, Munich, Germany). All channels were synchronously sampled at a rate of 6.4 kHz. Figure 6.10 shows the entire setup.

6.3.4 Results

The sensitivity of the proposed load monitoring system with a capillary embedded within the 3D printed structure is shown in this section, by comparing the pressure measurements with the strain measurements of the extensometer. Subsequently, both the results from the capillary filled with air and water are described, before being compared to the theoretical predicted values.

Determination of the Poisson coefficient

The Poisson coefficient of the material used must be known to be able to compare the measurement with the theoritical prediction. The Poisson coefficient of the ABS material was determined on the basis of multiple tensile tests by measuring longitudinal and transversal strain with strain gauges. The tensile test specimens used for this analysis had a similar design as depicted in Figure 6.4, except that no capillary and connections were foreseen as to avoid stress concentrations in the test specimen.

Figure 6.11 presents the transversal strain versus the longitudinal strain during multiple tensile tests on tensile test specimens manufactured by

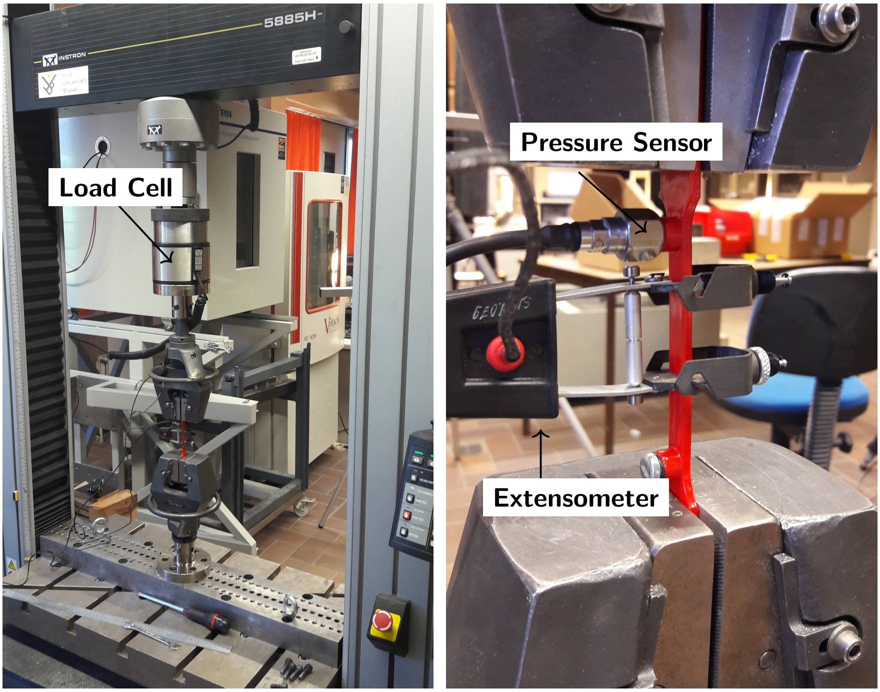

(a) (b)

Figure 6.10: (a) Tensile test setup (b) Detailed view of the two strain measurements: extensometer and pressure sensor connected to the integrated capillary.

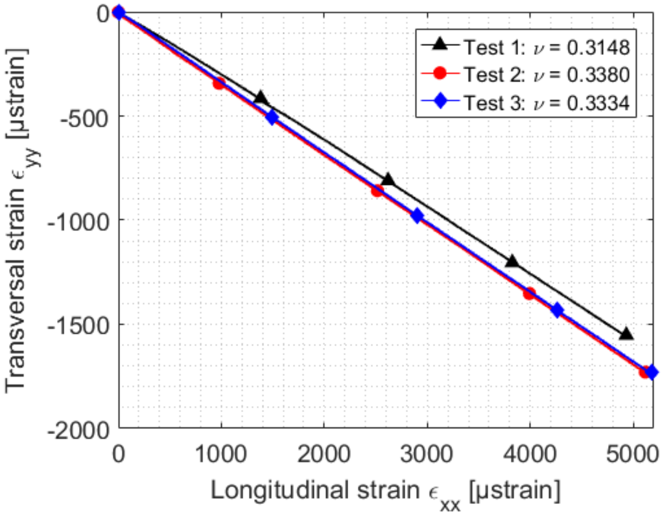

Figure 6.11: Determination of the Poisson coefficient of ABS.

FDM in ABS material. The measured Poisson coefficient corresponds to the slope of the measurement and is given in the legend of the corresponding measurement. The average Poisson coefficient ν of ABS was found to be 0.329.

Capillary Filled with Air

The load monitoring system was first tested using a compressible fluid (air) inside the capillary. When under tension, the capillary is elongated and narrowed due to Poisson effects. The net result of the volumetric change of the capillary is positive and the pressure dropped with tension load. Because of the compressibility of the gas, only limited pressure drops were expected. Figure 6.12 shows all measurement results for the case of compressible fluid in the capillary.

The initial pressure level inside the capillary was equal to the ambient condition ($K_T = P_0 = 98,000$ Pa). The pressure inside the capillary dropped proportionally with the strain measured by the extensometer on the outside of the same test section. The pressure dropped at an averaged rate of -0.0400 Pa/µstrain The theoretically expected sensitivity of a capillary

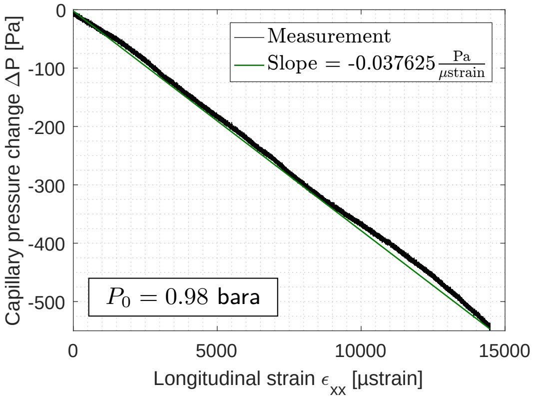

Test	P_0 [bara]	Slope [Pa/µstrain]
1	0.98	-0.0376
2	0.98	-0.0412
3	0.98	-0.0390
4	0.98	-0.0420
Avg.		-0.0400

Figure 6.12: Tensile testing results of a capillary filled with air. The capillary pressure is linear with respect to the longitudinal strain during tensile testing (left). Multiple test results are presented and compared in the table (right).

filled with air (P_0 = 98,000 Pa; k = 1.4) and a Poisson coefficient of 0.329 equals:

$$\text{Isothermal: } \frac{\Delta P}{\epsilon_{xx}} = P_0\,(2\nu - 1) = -0.0335\ \frac{\text{Pa}}{\text{µstrain}} \tag{6.27}$$

$$\text{Adiabatic: } \frac{\Delta P}{\epsilon_{xx}} = kP_0\,(2\nu - 1) = -0.0469\ \frac{\text{Pa}}{\text{µstrain}} \tag{6.28}$$

depending on whether the expansion can be considered as isothermal or adiabatic. The tests were conducted at a displacement rate of 1 mm/min and the complete extension lasted 1.5 min. This is a rather slow test rate, but the polymer ABS might also be a bad thermal conductor leading to a compression that cannot be considered isothermal, nor adiabatic and therefore with a pressure variation in between the extreme values of either isothermal and adiabatic expansion. We can conclude that the experiments are in line with the theoretically expected values.

The standard deviation σ of the noise on the pressure was found to be σ = 1.3 Pa. Given this standard deviation, 99.73% of all errors due to noise remain within a band of 3σ = 3.9 Pa, which leads to an uncertainty of ±101 µstrain.

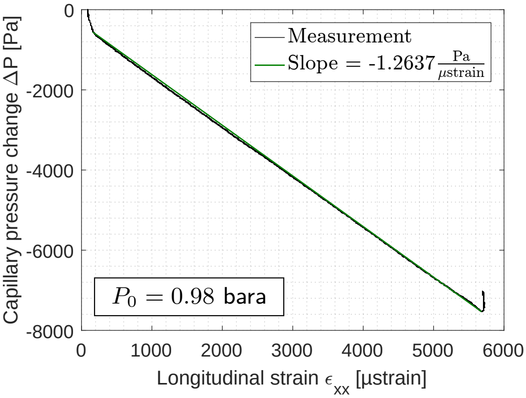

Test	P_0 [bara]	Slope [Pa/µstrain]
1	0.98	-1.2637
2	0.98	-1.3669
3	0.98	-1.1286
4	0.98	-1.0343
Avg.		-1.1984

Figure 6.13: Tensile testing results of a capillary filled with water. The capillary pressure is linear with respect to the longitudinal strain during tensile testing (left). Multiple test results are presented and compared in the table (right).

One way to improve the sensitivity is to install a more precise pressure sensor, but the sensors are already very sensitive. However, the accuracy of the load measurement method is mainly limited by the compressibility of the gas inside the capillary. Incompressible fluids are much more sensitive to volume variations and therefore form a better basis for the proposed strain measurement system using embedded capillaries.

Capillary Filled with Water

The same tests as above were repeated for samples with integrated capillaries filled with water. Starting with water at atmospheric pressure in the closed capillary, any deformation of the volume was expected to immediately give rise to a very high pressure change due to the incompressibility of the liquid (water). Therefore, the system signal-to-noise ratio was expected to increase, as for the same noise level (same pressure sensor) a larger signal was expected compared to the previous case. Figure 6.13 details all measurements of the tensile test and the load monitoring system based on water.

Figure 6.13 (left) shows a linear relationship between the strain measured by the extensometer and the pressure variations measured by the load monitoring system, except for both ends of the tests where non-linear behaviour was observed. As soon as the crosshead started moving, the pressure dropped by approx. 500 Pa, which was recovered when the crosshead stopped moving. In between, the curve fits very well to a linearised curve with slope -1.2637 Pa/µstrain, which is about 32 times more sensitive than the case where the capillary is filled with air.

The water-based load monitoring system was much more sensitive to strain variations than the air-based load monitoring system. Given the standard deviation of the noise on the pressure sensor ($\sigma = 1.3$ Pa), 99.73% of all errors due to noise remain within a band of $3\sigma = 3.9$ Pa, which now gives an equivalent uncertainty of ±3.1 µstrain on the strain measurements, which is about 3 times less sensitive than conventional strain gauges (±1 µstrain). Although much more sensitive than the same test carried out when the capillary was filled with air, the system with a capillary filled with water is not as sensitive as predicted from theory ($K_{H_2O} = 2.2$ GPa,$\nu = 0.329$):

$$\frac{\Delta P}{\epsilon_{xx}} = K_{H_2O}\,(2\nu - 1) = -752.4\,\frac{\text{Pa}}{\mu\text{strain}} \tag{6.29}$$

6.4 Tensile test specimen produced with metal Additive Manufacturing

The production of tensile test specimens using FDM with acetone post treatment is cumbersome. The specimens are also not very robust. The response of the polymer specimens changes after multiple tests and leaks become unavoidable. A tensile test campaign was therefore carried out on metal additive manufactured specimens produced with Selective Laser Melting (SLM). This additive manufacturing technique is currently the most widespread metal additive manufacturing technique. Its high geometrical accuracy allows the production of small tensile specimens with integrated capillaries for the conduction of this tensile test campaign.

6.4.1 Design

The test specimen has a similar design as the tensile test specimens produced using the FDM prototyping technology. Some small modifications

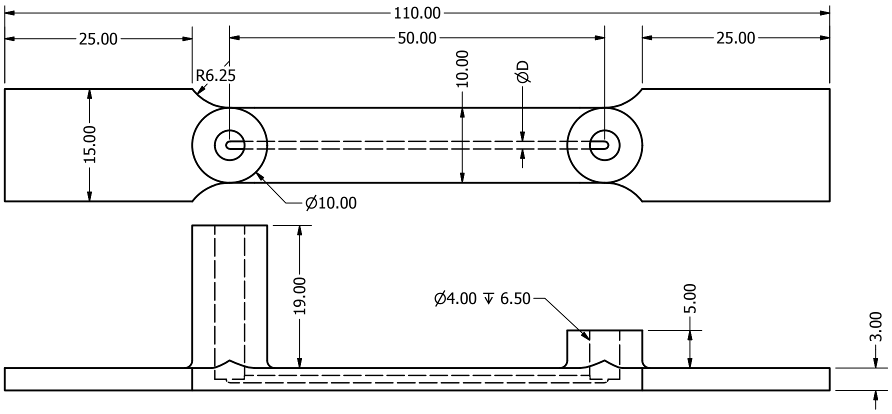

Figure 6.14: Dimensions of the metal additive manufactured tensile test specimen (in mm).

were made. The length of the specimen was shortened to a minimum to reduce the production cost which is directly proportional to the build height. Secondly, one of the fittings foreseen for the pressure sensor was made taller, such that it could accompany another type of pressure sensor that is capable of withstanding larger initial pressure levels. The final design is depicted in Figure 6.14.

6.4.2 Materials and Production Process

The tensile test specimens were produced in stainless steel AISI 316L. The built direction was vertical and support structures were used to create the overhanging part of the specimens shown in Figure 6.15. The contours were first scanned at 500 mm/s with a laser power of 80 W while hatching occurred at 675 mm/s at a laser power of 150 W. The hatch spacing was 80 µm and layer thickness was 20 µm. The powder particles of the powder bed have a particle size distribution between 15-40 mm/s. In order to limit oxidation, the oxygen content inside the built chamber was lowered to 0.1% and shielding gas at a flow speed of 2.5 m/s furthermore prevented oxygen from entering the area of molten metal.

After production, the loose metal particles of the powder bed inside the capillary have to removed using pressurized air. These specimens are automatically waterproof.

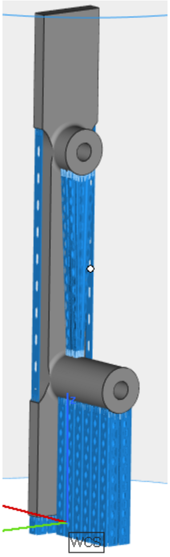

Figure 6.15: Built orientation and support structures for the production of the tensile test specimen using laser based Powder Bed Fusion.

6.4.3 Testing

The load monitoring system consisted of an integrated capillary filled with a fluid and connected to an externally mounted pressure sensor. The chosen absolute pressure sensor (Kulite XTL-123A-190, Kulite Semiconductor Products, Inc., Leonia, USA) with a limited range from 0–1.7 bara, is compatible with all non-conductive and non-corrosive liquids or gases.

The tensile test samples were placed in an Instron 5885 H (Instron, Norwood, USA) tensile testing machine with Instron 2518-103 load cell (10 kN static). An Instron 2630-030 extensometer was furthermore installed on the test section. The pressure sensor, extensometer, load cell and cross head displacement were all recorded using an LMS Scadas III mobile data acquisition system (Siemens, Munich, Germany). All channels were synchronously sampled at a rate of 6.4 kHz. Figure 6.16 shows the entire setup.

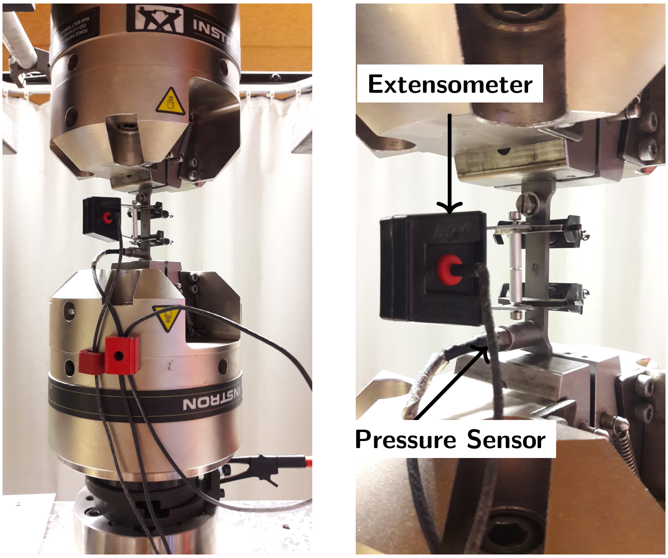

(a) (b)

Figure 6.16: (a) Tensile test setup (b) Detailed view on the strain measurement through the extensometer and the pressure sensor connected to the integrated capillary of the eSHM system.

6.4.4 Results

Before discussing the test results of the tensile test campaign on specimen produced by laser based PBF, the Poisson coefficient of such specimens must be determined. The Poisson coefficient is required to compare the experimental results against the theoretical predictions.

Determination of the Poisson coefficient

The Poisson coefficient was determined during a tensile test on two specimens with a similar design as depicted in Figure 6.14, except that no capillary nor connections were foreseen on the specimen. The test specimens had a dog bone shape with two-element 90° planar rosette strain gauges installed at both sides of the test specimen. Figure 6.17 presents the tensile test specimen in the test setup for the determination of the Poisson coefficient using strain gauges.

Each specimen was tested three times and the Poisson coefficient was de-

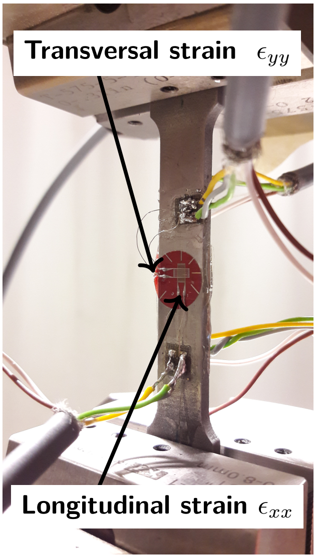

Figure 6.17: Detailed view of the two strain measurements (longitudinal and transversal) through strain gauges for the determination of the Poisson coefficient of the additive manufactured AISI 316L.

termined on the basis of a rosette strain gauge on the front and the back of the specimen, resulting in six measurements that were averaged out to find the Poisson coefficient of that specimen. Figure 6.18 presents the strain gauge measurements for Specimen 1 (top) and Specimen 2 (bottom) and for both the front and back strain gauges.

The average Poisson coefficient of Specimen 1 and Specimen 2 were respectively 0.3275 and 0.3142. The Poisson coefficient considered for the remaining part of this chapter is therefore the average of these two specimens, $\nu = 0.321$.

Capillary filled with air

Multiple tensile tests with a capillary filled with air were conducted. Figure 6.19 presents the test result with an initial capillary pressure of 1.2 bara. In the table, multiple measurement results are presented for initial capillary pressure levels equal to ambient pressure, $P_0 = 0.98$ bara. During all these tests, the expansion occurred over a testing time of 70 s.

The pressure drop due to the tensile strain on the test specimen is larger

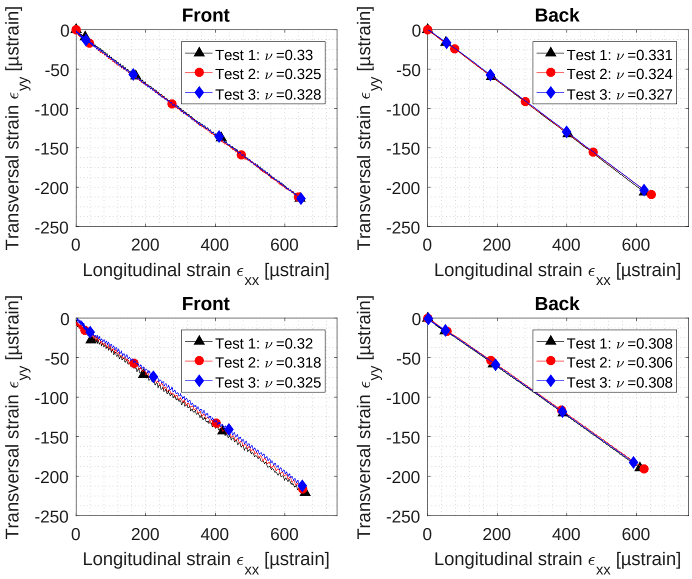

Figure 6.18: Determination of the Poisson coefficient of stainless steel AISI 316L produced with laser based PBF. Each plot presenting three consecutive tests for front (left) and back (right) strain gauges of Specimen 1 (top) and Specimen 2 (bottom).

when the initial pressure level is increased. The bulk modulus is proportional to the pressure inside the capillary and is therefore expected that the capillary pressure becomes more sensitive to the tensile strain. Theoretically, the sensitivity of the system at an initial pressure level $P_0 = 1.2$ bara and a Poisson coefficient $\nu = 0.321$ is expected to be:

$$\text{Isothermal: } \frac{\Delta P}{\epsilon_{xx}} = P_0\,(2\nu - 1) = -0.0430\,\frac{\text{Pa}}{\text{µstrain}} \tag{6.30}$$

$$\text{Adiabatic: } \frac{\Delta P}{\epsilon_{xx}} = kP_0\,(2\nu - 1) = -0.0601\,\frac{\text{Pa}}{\text{µstrain}} \tag{6.31}$$

From this analysis, it can be concluded that the measurement again lies in between the theoretically barriers defined by an isothermal and adiabatic expansion. Since the expansion occurs over a period of 70 s and the steel will conduct heat to compensate for the cooling inside the capillary, it was expected that the experiment would more fit with the assumption of an

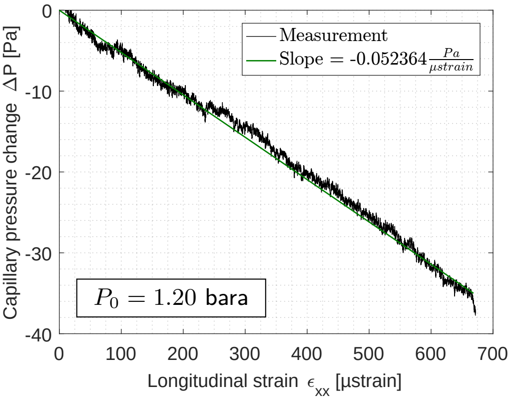

Test	P_0 [bara]	Slope [Pa/µstrain]
1	1.2	-0.0524
2	0.98	-0.0361
3	0.98	-0.0337
4	0.98	-0.0340
Avg.		-0.0346

Figure 6.19: Tensile testing results of a 316L tensile test specimen with an integrated capillary filled with air. The capillary pressure is linear with respect to the longitudinal strain during tensile testing (left). Multiple test results are presented and compared in the table (right).

isothermal expansion. This assumption holds true for the experiments at 0.98 bara:

$$\text{Isothermal: } \frac{\Delta P}{\epsilon_{xx}} = P_0\,(2\nu - 1) = -0.0351\ \frac{\text{Pa}}{\text{µstrain}} \qquad (6.32)$$

It is concluded from this analysis that the theoretical model is well capable of predicting the pressure drop inside the capillary filled with air. The pressure signal is very weak because of the compressibility of the gas inside the capillary.

Capillary filled with water

In order to increase the sensitivity of the strain sensing system, the capillaries of the eSHM system were again filled with water. Figure 6.20 presents an example of the test result while the table presents three measurements conducted on the same test specimen. The test was conducted both under tension and compression and the initial pressure level was increased in order to extent the test range.

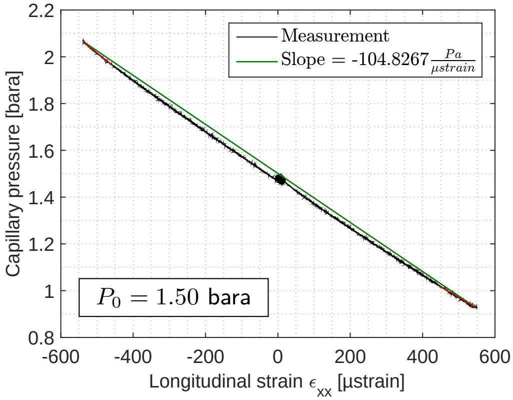

Test	P_0 [bara]	Slope [Pa/µstrain]
1	1.50	-104.83
2	1.25	-107.65
3	1.15	-108.95

Figure 6.20: Tensile and compression test on a stainless steel 316L dog bone test specimen with an integrated capillary filled with water. The capillary pressure is linear with respect to the longitudinal strain, both under tension and compression for the range tested (left). Multiple test results are presented and compared in the table (right).

The pressure variation is nearly linear with the strain on the tensile test specimen. The maximum sensitivity obtained during this test campaign was -108.95 Pa/µstrain. The bulk modulus K corresponding to this measured slope is:

$$K = \frac{\frac{\Delta P}{\epsilon_{xx}}}{(2\nu - 1)} = 292.8 \text{ MPa} \tag{6.33}$$

Given that 99.73% of all errors due to noise on the pressure measurement remain within a band of $3\sigma = 3.9$ Pa, which now gives an equivalent uncertainty of 0.036 µstrain. The eSHM principle can be used to measure strain in a very sensitive way. More test results are summarized on page 186.

6.5 Influence of thermal expansion on the embedded usage monitoring system

The structure with integrated capillary of the eSHM may be exposed to varying temperatures. The thermal expansion of the structure will also induce a pressure variation inside the capillary. This effect will be quantified in a first section and will be measured in a subsequent section.

6.5.1 Analytical study

For the analytical derivation, we assume that a capillary is present inside an isotropic solid material. We furthermore assume that both the solid structure and the fluid inside the capillary have the same temperature and that the temperature is uniform throughout the entire structure with capillary. The structure is free to expand such that no thermal stresses are induced inside the structure. The solid, isotropic, material will equally expand in all directions such that the change in capillary volume with temperature is given by:

$$\Delta V^{solid} = \alpha_V^{solid} V_0 \Delta T \approx 3\alpha_L^{solid} V \Delta T \tag{6.34}$$

with ΔV the volumetric change due to the thermal change ΔT, V_0 the initial volume of the capillary and α_V^{solid} and α_L^{solid} respectively the volumetric and linear thermal expansion coefficient of a solid. When assuming that the fluid inside the capillary would be allowed to expand, the increase in the volume would be quantified as:

$$\Delta V^{fluid} = \alpha_V^{fluid} V_0 \Delta T \tag{6.35}$$

The difference of the volumetric expansion of the structure with integrated capillary and the volumetric expansion of the fluid inside the capillary will induce a pressure change inside the capillary. In order to simplify the derivation, the fluid and solid are assumed to be always in thermal equilibrium. This difference in volumetric expansion then equals:

$$\Delta V^{solid} - \Delta V^{fluid} = \alpha_V^{solid} V_0 \Delta T - \alpha_V^{fluid} V_0 \Delta T \tag{6.36}$$

Assuming that the internal pressure build-up does not deform the structure, we can express that the fluid inside the capillary is not allowed to expand

Table 6.2: Thermal expansion coefficients of various materials at 20° C

Material	Pressure [bara]	α_V [1/K]
SS 316L	–	51.6
Water	–	207
Air	1	3690

equal to an amount as derived in (6.36), which will result in a pressure change:

$$\Delta P_{cap} = -K\frac{\Delta V^{solid} - \Delta V^{fluid}}{V_0} = -K\left(\alpha_V^{solid} - \alpha_V^{fluid}\right)\Delta T \tag{6.37}$$

Table 6.2 summarizes some thermal expansion coefficients α_V that are of practical importance for the conduction of the practical experiments hereafter.

The thermal expansion coefficient of stainless steel AISI 316L is smaller than those of the fluids that were present inside the capillary during the tensile experiments (see Table 6.2). A temperature increase will thus increase the pressure inside the capillary. Given a 316L stainless steel test specimen with an integrated capillary filled with air or water, then the pressure inside the capillary will be:

$$\text{Air: } \frac{\Delta P_{cap}^{thermal}}{\Delta T} = 368.57\ \frac{\text{Pa}}{°\text{C}} \tag{6.38}$$

$$\text{Water: } \frac{\Delta P_{cap}^{thermal}}{\Delta T} = 3.42\ \frac{\text{bar}}{°\text{C}} \tag{6.39}$$

The influence of the temperature on the pressure measurement inside the capillary is very pronounced and more dominant than the pressure change that will result from the tensile strain applied to the specimen. Indeed, the relative sensitivity of the capillary pressure to a temperature change (equation 6.37) and a change in tensile strain (equation 6.20) is given by:

$$\gamma = \frac{\Delta P_{cap}^{thermal}}{\Delta P_{cap}^{strain}} = -\frac{\left(\alpha_V^{solid} - \alpha_V^{fluid}\right)}{(2\nu - 1)} \frac{\Delta T}{\epsilon_{xx}} \tag{6.40}$$

When deploying the pressure measurement of the integrated capillary as a strain sensor, one must minimize γ to limit the thermal effects on the measurement. This can be done by avoiding thermal changes at the measurement location ΔT and by minimizing the difference in the volumetric thermal expansion coefficient of the solid and the fluid inside the capillary. When deploying the pressure measurement as a thermometer, one must maximize γ by installing the capillary in an area where it is not affected by strain ϵ_{xx} or by choosing a solid material with a Poisson coefficient close to $1/2$.

For the practical case of the tensile test experiments conducted here before, the Poisson coefficient of the stainless steel was determined to be $\nu = 0.321$ and the fluids inside the capillary were air and water. Given these conditions, γ has very distinct values for both fluid types:

$$\text{Air: } \gamma = -10163.1 \times 10^{-6} \frac{\Delta_T}{\epsilon_{xx}} \tag{6.41}$$

$$\text{Water: } \gamma = -434.1 \times 10^{-6} \frac{\Delta_T}{\epsilon_{xx}} \tag{6.42}$$

When deploying the pressure measurement inside the capillary as the intended strain measurement technique, the lower γ is to be chosen. Therefore, the practical thermal tests, conducted hereafter, have a capillary filled with water.

6.5.2 Experimental study

From the previous paragraph, it was clear that the temperature will have a large influence on the pressure measurement inside the capillary. The choice of the fluid inside the capillary allows influencing the relative importance of the strain and temperature to the pressure inside the capillary. In order to limit the influence of the temperature on the pressure measurement, and to increase the signal amplitude during the measurement, the chosen capillary fluid was water.

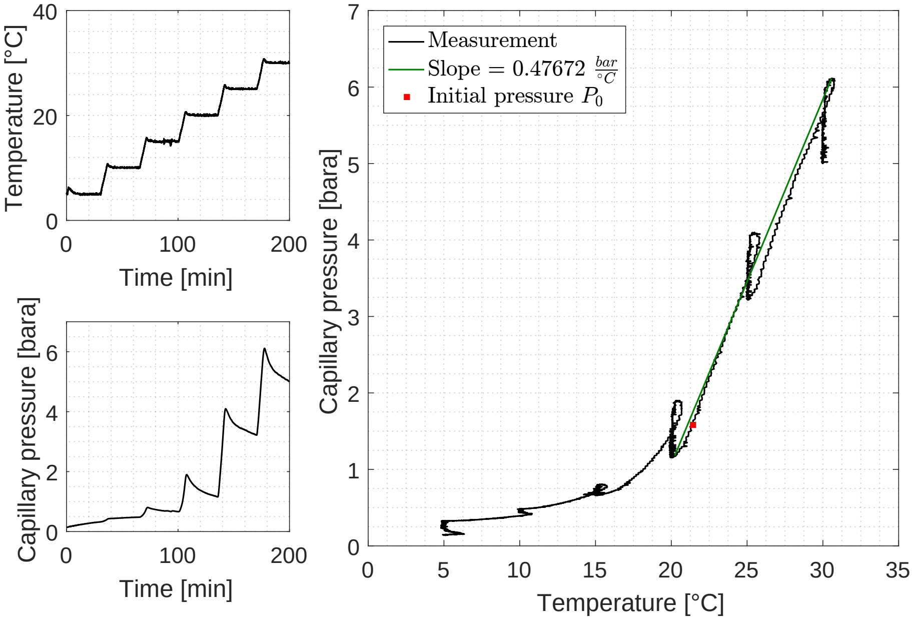

Figure 6.21: Capillary pressure measurement during thermal test on tensile test specimen 2 filled with water. Temperature (top left) and capillary pressure (bottom left) are plotted against time.

The pressure variation inside the capillary due to thermal changes and axial strain are both proportional to the bulk modulus of the water. To investigate the relative importance of the temperature and strain on the capillary pressure, the same specimens were subsequently tested for strain and temperature. After the tensile test campaign, the same test specimen was placed inside a climate chamber for the thermal test.

Results

The thermal measurement on tensile test specimen 2 is presented in Figure 6.21. In the top left corner of Figure 6.21, the temperature as measured inside the climate chamber is plotted against time. The bottom left plot shows the pressure behaviour in function of time, while the right plot shows the effect of temperature on the capillary pressure. The capillary pressure response to an increasing temperature is clearly not linear. The volumetric thermal coefficient of water is not constant with temperature but increases with increasing temperatures. The slope of the pressure measurement therefore increases with increasing temperature. The thermal expansion coefficient is close to zero at 5°C and equals the thermal expansion coefficient of the stainless steel test specimen in that area. The capillary pressure variation with changing temperatures therefore flattens out to the lower temperature side of the thermal test.

At higher capillary pressure, the pressure measurement reveals that a leak is present. After an initial overshoot, due to a temperature overshoot in the climate chamber, the capillary pressure drops. This drop is seen as the vertical variations of the pressure. Notwithstanding this leak, it is clear that the capillary pressure varies almost linearly with the temperature in the second half of the thermal test (T>20°C). The measured sensitivity of the capillary pressure to thermal fluctuations is 0.47672 $^{\mathrm{bar}}/_{^\circ\mathrm{C}}$. From the tensile test campaign, it was derived that bulk modulus during the test equals $K = 292.8$ MPa (see equation 6.33). Given the thermal expansion coefficient of water and stainless steel 316L (see Table 6.2), the theoretically expected sensitivity to thermal changes is:

$$\begin{aligned} \frac{\Delta P_{cap}}{\Delta T} &= -K\left(\alpha_V^{solid} - \alpha_V^{fluid}\right) && (6.43)\\ &= -292.8 \times 10^6 \times (51.6 - 207) \times 10^{-6}\ \frac{\mathrm{Pa}}{^\circ\mathrm{C}} && (6.44)\\ &= 0.4550\ \frac{\mathrm{bar}}{^\circ\mathrm{C}} && (6.45) \end{aligned}$$

The measured sensitivity 0.47672 $^{\mathrm{bar}}/_{^\circ\mathrm{C}}$ is very close to the theoretically expected value, considering the bulk modulus derived form the tensile test and the thermal expansion coefficients of water and steel at 20 °C as known from the literature. More thermal test results are summarized on page 187.

6.6 Conclusions

An analytical model was developed that is capable of predicting the pressure change inside the capillary embedded in the test section of a tensile test specimen when subjected to a tensile load. The model is very well capable of predicting the pressure change to be expected. The capillary pressure change is not influenced by any of the geometrical properties related to the capillary (such as shape, size, location and length). The bulk modulus of the fluid inside the capillary and the Poisson coefficient of the tensile test specimen are the two affecting parameters. When integrating the capillary inside a material with a Poisson coefficient close to 0.5, no volumetric and thus pressure change will result when loaded. The smaller the Poisson coefficient the better the sensitivity of the system. The bulk modulus expresses how a volumetric change results in a pressure change and is higher for an incompressible than a compressible fluid.

First practical tests were conducted on ABS tensile test specimens manufactured using the FDM 3D printing technology. The Poisson coefficient of the ABS material was measured because of its importance for comparison with the theoretical predictions and found to be ($\nu = 0.329$). The theoretical model predicted very well the measured pressure change for the compressible fluid tested (air). The sensitivity of the capillary pressure change to tensile strain increased by using an incompressible fluid inside the capillary, but not to the extent as expected from the theoretical model using the bulk modulus of water.

A second test campaign was launched on stainless steel 316L specimens manufactured using laser based PBF technology. The maximum measured sensitivity of the capillary pressure of the eSHM system to longitudinal strain is 108.95 Pa/µstrain. 99.73% of the measurements will fall within the 3σ interval, corresponding to an uncertainty of 0.036 µstrain on the strain measurement using the eSHM system. The eSHM principle can be considered a sensitive way of measuring strain inside the component.

The capillary pressure was made very sensitive to tensile strain, but also thermal changes affect the capillary pressure. Since the metallic component and the fluid inside the capillary have different volumetric thermal coefficients of expansion, a pressure change inside the capillary is created when temperature is changed. This effect is relatively more important for the case of air, but is still significant for water. The theoretical model predicting the thermal sensitive of the eSHM system has been presented and validated. From a theoretical point of view and applied to the practical case considered here before with the stainless steel 316L tests specimens and water as the fluid inside the capillary, the same pressure builds up in the capillary when subjected to a 1000 µstrain compressive strain or when the specimen is exposed to a thermal change of 2.3 °C. A solution must be developed to decouple the sensitivity to thermal changes and strain.

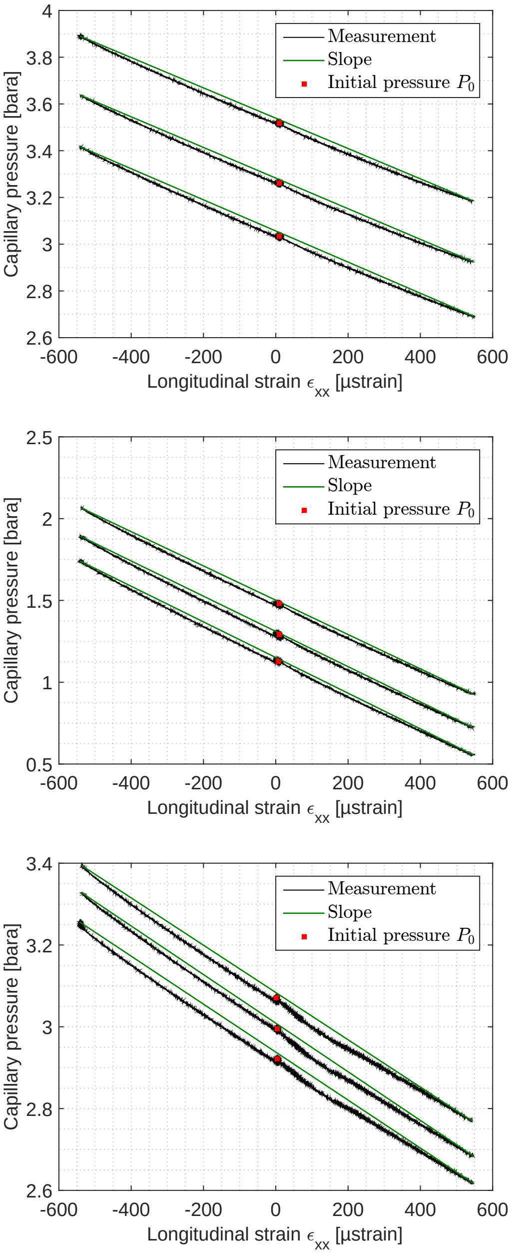

Specimen 1

Test	P_0 [bara]	Slope [Pa/µstrain]
1	3.52	-64.86
2	3.26	-65.53
3	3.03	-66.61

$D_{cap} = 1$ mm

Specimen 2

Test	P_0 [bara]	Slope [Pa/µstrain]
1	1.48	-104.83
2	1.29	-107.66
3	1.13	-108.95

$D_{cap} = 1$ mm

Specimen 3

Test	P_0 [bara]	Slope [Pa/µstrain]
1	3.07	-57.82
2	3.00	-59.41
3	2.92	-58.65

$D_{cap} = 1.5$ mm

Figure 6.22: Tensile and compression test on three tensile test specimens with integrated capillary filled with water. Each plot presents three subsequent tests on a single specimen at varying initial pressure levels. The pressure inside the capillary drops linearly with increasing strain. The slope of the linearised pressure change is shown in the table next to the plot.

Specimen 1

Test	P_0 [bara]	Slope [bar/°C]
1	2.71	0.3252

$D_{cap} = 1$ mm

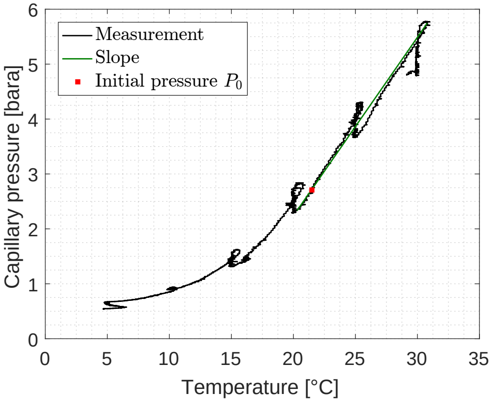

Specimen 2

Test	P_0 [bara]	Slope [bar/°C]
1	1.58	0.4767

$D_{cap} = 1$ mm

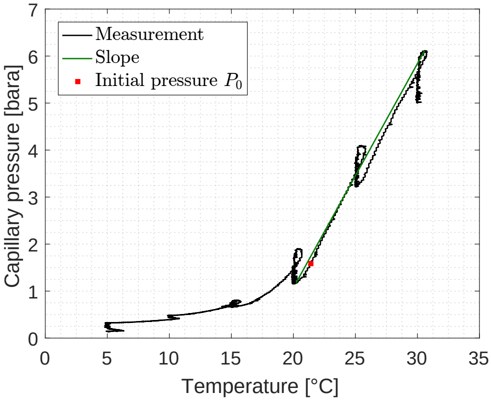

Specimen 3

Test	P_0 [bara]	Slope [bar/°C]
1	3.13	0.1518
2	2.93	0.1346

$D_{cap} = 1.5$ mm

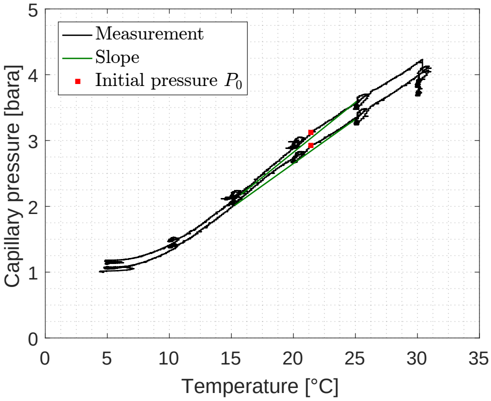

Figure 6.23: Thermal test on three tensile test specimens with integrated capillary filled with water. Each plot presents the thermal tests on a single specimen. The pressure inside the capillary increases with temperature in a fashion related to the thermal expansion coefficient of water (non-linear with temperature). The slope of the linearised pressure change is shown in the table next to the plot.

Chapter 7

Conclusions and future work

The preceding chapters presented a number of new developments of the eSHM system as a Structural Health Monitoring and a Usage Monitoring principle. This chapter summarizes the main conclusions drawn from the presented research and suggest some possible roads for improvements.

7.1 Original contributions to the research topic

The work presented in this thesis contains a number of original contributions to the development of the eSHM system as a SHM and UM technology. The main achievements of this PhD thesis are:

- This work demonstrated that the addition of a capillary itself does not jeopardize the integrity of the structure to be monitored. Rather than the capillary location, the surface roughness/quality of the integrated capillary is of primary importance as to avoid crack initiation at the capillary surface. The deepest notches on the capillary surface are likely those areas where the laser (constant power) started scanning the capillary contour.

- The simulation model presented in Chapter 4 is capable of determining the opening of the crack, the leak flow area, by reconstructing the pressure behaviour inside the capillary during a four point bending fatigue test.

- The amplitude model of the Negative Pressure Waves presented in Chapter 4 is new in the literature. Although a similar, empirical, model has been presented in the literature, the model described in this thesis is based on an analytical derivation, is more complete and incorporates the influence of all affecting parameters. This model has been experimentally verified.

- Leak localization on the basis of Negative Pressure Waves in closed tubes and closed capillaries, as presented in Chapter 5, is new in the literature. Especially the continuous pressure rise, the reflections occurring at the tube ends and the application to capillaries is novel.

- This work presents the proof-of-concept of measuring strains on the basis of the pressure inside the capillary of the novel eSHM system. To the author's best knowledge, the eSHM can be considered as one of the first integrated principles capable of measuring strain in AM components, especially when considering metallic functional AM parts.

7.2 Conclusions

7.2.1 The eSHM system as a SHM system

The eSHM principle consists of the continuous monitoring of pressurized capillaries that are integrated in an AM structure. The eSHM system can be used both as a SHM and UM system. Fatigue cracks are detected when breaching through the capillaries. The resulting leak flow alters the capillary pressure which is detected by the pressure sensor. The idea of the eSHM system arose from the fruitful combination of the design freedom offered by AM and the fatigue crack detection by the embedded SHM system. The resulting SHM system is robust and monitors the AM material that is currently known for its material imperfections.

Many SHM systems are currently being developed but many of them remain in the research phase because of a lack of robustness. Only last year, Comparative Vacuum Monitoring (CVM) became the first SHM principle commercially employed by an aerospace company. CVM has been considered as a very promising SHM methodology and is very comparable in operating principle as the eSHM system. CVM utilizes a polymer patch with pressurized capillaries that sticks to the surface to be monitored. A surface crack breaching multiple capillaries will induce a leak flow that is detected. More and more research is ongoing to integrate the SHM functionality inside the component.

The integration of the SHM system may not weaken the structure to be monitored. The integrated capillaries of the eSHM may not induce fatigue initiation. Four point bending fatigue tests have been conducted to analyse the influence of the capillary of the eSHM on the structural integrity of the structure to be monitored. FEM simulations have indicated that the stress level at the capillary surface of an “Ideal Capillary” (i.e. without capillary surface roughness), located at a distance a = 2 mm, remains about 20% below the maximal stress level found at the tensile stressed outer specimen surface. Fatigue initiation is not expected at the capillary surface, as was experimentally confirmed by several tests. Because of the addition of the capillary, the overall stress level increase remains limited to 3%. In practical applications, this overall stress level increase can be compensated by increasing the structure’s section.

A second test campaign investigated the effect of the addition of a capillary produced by laser based Directed Energy Deposition (DED). New reference specimens, without capillary, but produced using laser based DED were tested and their fatigue performance was better than the conventional specimens. The addition of a capillary, however, weakened the structural performance significantly. The fatigue cracks initiated from the capillary surface because of the capillary surface roughness and the resulting stress concentrations. Inclusion of the exact capillary roughness profile in the FEM simulations revealed that most stress concentrations on the capillary surface surpass the stress levels expected on the most tensile stressed outer surface. Fatigue crack initiation is therefore expected at the capillary surface, as was experimentally discovered. An attempt to reduce the capillary surface by drilling through the already present printed capillaries did not turn out successful as deep notches remained present. Those deeper notches are likely a result of the AM process using a constant laser power and constant speed. The laser must be given the time and power to create a melt pool with its intended size before continuing the contour scan.

The closer the capillary is located to the outer wall where fatigue cracks are expected to grow, the smaller the fatigue cracks will be at detection. This distance is a first measure of the fatigue crack size at detection. However, chances increase that the fatigue initiation occurs on the capillary surface when located closer to the outer surface of a four point bending fatigue test specimen. Experiments have shown that, as long as the capillary surface roughness does not lead to stress concentrations surpassing the stresses expected at the outer surface of the beam, the crack initiation still occurs at the outer surface. The capillary may be located fairly close to the outer surface to detect the fatigue crack earlier.

Chapter 4 tackled the determination of the crack size on the basis of the pressure measurements of the eSHM system. First, the filling of the capillary was analysed to retrieve the leak flow rate and thus leak flow area. This is a measure for the opening of the fatigue crack. The numerical model, derived on the basis of the application of the isentropic flow equations to the leak flow, allowed reconstructing the pressure behaviour inside the capillary on the basis of three independent parameters: the sensitivity of the capillary pressure to deformation α, the load at which the crack opens F_{open} and the crack size at maximum load $A_{l,max}$. The latter parameter is a measure for the severity of the damage since a larger leak area indicates that the crack is wider open and therefore also larger.

A second approach constituted in the analysis of the amplitude of Negative Pressure Waves that originate from the abrupt density change at the leak location. The empirical model known in the literature is not widely applicable for the various pressure conditions in which the eSHM can be operated. The most fundamental contribution of this PhD work is the development of an analytical model that is more widely applicable, as was presented in Chapter 4. The model was derived by combining the isentropic flow equations and the acoustical equations. The model was empirically validated by varying all depending variables. The amplitude of the Negative Pressure Waves depends on the size of the leak D_l, the size of the capillary D_{cap}, the capillary pressure P_{cap} and the heat capacity ratio of the fluid inside the capillary k.

As presented in Chapter 5, the Negative Pressure Waves were successfully used to localize a leak in a closed volume. A first test setup consisted of closed tubes representing the capillaries of the eSHM system. The difference in time-of-arrival of the NPWs at two pressure sensors on either side of the tube allows locating the leak with high accuracy. The reflections occurring at the hard wall of the tube end even allow to localize the leak on the basis of a measurement with a single pressure sensor. The exact speed of sound inside the tube was determined and found to be close to the speed of sound in open air. Since the amplitude of the Negative Pressure Waves were small, the exact moment of arrival could not easily be determined because of the noise on the measurement. The delay estimation on the basis of a least squares method on a larger fraction of the pressure signal allowed to determine the leak position with a higher accuracy.

The use of Negative Pressure Waves as a leak localization method in capillaries was found to be more cumbersome. The pressure signal distorts when travelling through a narrow capillary at a speed depending on the frequency of the sound. The speed of sound was therefore accurately determined on a long capillary. The pressure waves inside a capillary with 1.6 mm diameter travel at a speed of 318.5 $^{m}/_{s}$. Because of the distortion of the pressure signal, leak localization on the basis of the time signals has proven to be less accurate as in the larger tubes.

7.2.2 The eSHM system as a UM system

The pressure inside the capillary depends on the strain acting at the capillary location. Tensile test specimens with integrated capillaries in the test section were produced using various additive manufacturing techniques. An analytical model presenting the capillary pressure sensitivity to longitudinal strain in a tensile test specimen was developed in Chapter 6:

$$\Delta P_{cap} = K\left(1 - (1 - \nu\epsilon_{xx})^2 (1 + \epsilon_{xx})\right)$$

which reads in a more simplified manner:

$$\Delta P_{cap} = K\,(2\nu - 1)\,\epsilon_{xx}$$

with ΔP_{cap} the capillary pressure change, K the bulk modulus, ν the Poisson coefficient and ϵ_{xx} the longitudinal strain.

The bulk modulus K of the fluid inside the capillary and the Poisson coefficient ν have an important impact on the sensitivity of the eSHM system. The larger the bulk modulus and the smaller the Poisson coefficient, the more sensitive the system becomes. The system is insensitive for the geometrical aspects of the capillary, such as its shape, location and even size of the capillary.

Tensile test specimens were produced using the Fused Deposition Modelling (FDM) prototyping technique. As the as-built specimens are not airtight, a cumbersome post treatment involving acetone was required to seal the pores in between adjacent layers and tracks. The Poisson coefficient of the ABS material was measured and equal to 0.329. The tensile tests were conducted using both a compressible (air) and incompressible (water) fluid inside the capillary. The sensitivity of the capillary pressure change when filled with air at ambient pressure was small (-0.0400 Pa/µstrain), but as expected from the theoretical model presented. The use of an incompressible fluid increased the sensitivity of the system to -1.1984 Pa/µstrain. The theoretical model, however, predicted a sensitivity of 752.4 Pa/µstrain when considering that the capillary is filled with pure water. Yet, this test campaign has proven the capabilities of the eSHM system to be utilized as an UM system.

A second bunch of tensile test specimens were manufactured using laser based Powder Bed Fusion. The Poisson coefficient of the stainless steel 316L used for the production of the tensile test specimens was measured to be 0.321. With a capillary filled with air at ambient pressure, the pressure drop inside the capillary was -0.0346 $^{\mathrm{Pa}}/_{\mu\mathrm{strain}}$ as predicted from the theoretical derivation and assuming isothermal expansion. Increasing the capillary pressure increases the sensitivity of the system, as also expected from the theoretical model. The sensitivity of the eSHM system to tensile strain was significantly improved. The maximal sensitivity obtained during the tensile test campaign was -108.95 $^{\mathrm{Pa}}/_{\mu\mathrm{strain}}$. This measurement allows the determination of the average strain level around the capillary with an error equal to $3\sigma = 0.036$ µstrain. The eSHM system can be considered as a very sensitive system to longitudinal strain.

As also presented in Chapter 6, thermal changes affect the pressure inside the capillary. The equation predicting the capillary pressure change for a given temperature change is given by:

$$\Delta P_{cap} = -K \left(\alpha_V^{solid} - \alpha_V^{fluid} \right) \Delta T$$

with ΔP_{cap} the capillary pressure change, K the bulk modulus, α_V^{solid} and α_V^{fluid} the volumtric coefficients of thermal expansion of the solid and the fluid respectively and ΔT the temperature change. The larger the difference in the coefficient of thermal expansion, the more the capillary pressure will be influenced by a thermal change. In practice, for the combination of the stainless steel 316L specimens filled with water, the thermal sensitivity of the eSHM system was measured to be 0.4767 $^{bar}/_{^{\circ}C}$, very close to the theoretically expected value of 0.4395 $^{bar}/_{^{\circ}C}$. The eSHM system is very sensitive to thermal changes as well.

7.3 Future work

The presented research in this thesis has tackled some important questions of the integrated eSHM system, especially in terms of fatigue response and providing an estimation of the severity and location of the damage. This thesis has furthermore proven the concept of measuring strain on the basis of the monitoring of the capillary pressure. The eSHM is still a very new concept and some challenges remain to be tackled. The following section presents some initial guidelines for the continuation of the research activities on the eSHM system.

7.3.1 Fatigue response of specimens with integrated eSHM system

The fatigue test campaigns on specimens produced by laser based Directed Energy Deposition (DED) process have highlighted that, above others, the capillary surface finish is of critical importance. The laser based DED process is known for being geometrically less accurate but for having better fatigue properties. On the short term, the following step would be to drill capillaries in a solid AM component manufactured by laser based DED, such that the capillary surface roughness issue is solved. On the longer term, solutions must be developed to produce capillaries with a good surface finish using the laser based DED process. Post processes such as chemical etching and abrasive flow machining will be considered. Closed loop process control of the laser based DED process will be required to avoid the deeper notches when scanning the capillary contours. A hybrid manufacturing approach, combining additive and subtractive manufacturing techniques, is likely to be the best solution to post process the capillary surface.

7.3.2 Crack size estimation

A measure for the crack size was obtained by reconstructing the pressure change inside the capillary during a four point bending fatigue test. The derived values of the three independent variables must be experimentally verified using separate test campaigns. The obtained leak flow area is an indication, but not yet an exact measure of the crack size. A relationship between the leak flow area and the fatigue crack size is to be developed and will likely be based on the reduction of the bending stiffness of the test specimens.

7.3.3 Crack localization

The method presented to localize the leak is based on the presence and propagation of Negative Pressure Waves inside a capillary. So far, the leak has been simulated on test setups resembling the capillary of the eSHM system. An important milestone would be the detection of Negative Pressure Waves inside the capillary when a fatigue crack breaches the capillary. A question that will arise is if the opening of a fatigue crack is abrupt enough to create Negative Pressure Waves and to what extent it possibly affects the amplitude. During a fatigue test campaign and for the comparison with the numerical model predicting the pressure behaviour over time in the capillary, the crack was assumed to open gradually depending on the load acting on the component. Therefore, a first test to be conducted would be to analyse a specimen in which a crack is present that was detected by the eSHM system. The crack must be closed when unloaded, such that the capillary can still be pressurized to conduct new tests. The test specimen must then be subjected to a fast switching load signal with an amplitude such that the fatigue crack is opened. This test principle was already tried out on a single test specimen without success. Especially the noisy environment of such a fast vibrating test bench made it impossible to detect small amplitude Negative Pressure Waves, if any were present.

The smallest amplitudes of the Negative Pressure Waves detected by the absolute pressure sensors used so far are in the order of 10-20 Pa. Below these values, the electrical noise level of the pressure sensors becomes significant, especially when conducting fatigue testing with vibrating pressure sensors. A second approach that should be followed is the use of microphones for the detection of the Negative Pressure Waves. Microphones are capable of detecting much smaller amplitude signals and are more likely to be capable of detecting the Negative Pressure Waves during the fatigue tests. Special attention must be paid that the venting channel of the microphone, usually on the back of the microphone, is connected with the static pressure level of the capillary at all times. This will likely require the development of a special enclosure around the microphone. Electret microphones are small and cheap examples of microphones that are potentially suitable for this application.

It is furthermore expected that the leak localization accuracy can be further improved by investigating the propagation properties of acoustical waves inside capillaries in more detail. Frequency based delay estimations, such as the transmissibility approach, may allow to estimate the delay in between the arrivals of the distorted pressure signals in a more accurate way than the current time-based approaches.

One of the biggest benefits of the eSHM as a crack detection methodology is the memory function that is inherent to the working principle. Although the pressure sensors must be installed at all times, the eSHM principle does not require the continuous monitoring of the pressure inside the capillary. At any given moment, the pressure inside the capillary can be consulted to inspect if a fatigue crack has breached the capillary so far. With the addition of the crack localization feature on the basis of the Negative Pressure Waves inside the eSHM system, continuous monitoring of the pressure inside the capillary is required at very high sampling rates. An on-board and online data evaluation system must then be developed capable of throwing away the unnecessary data. The localization principle furthermore requires the use of multiple pressure sensors, or even microphones in combination with absolute pressure sensors. The system is therefore likely to become more complex and less attractive for the industry. A different approach to the fatigue crack localization is therefore welcomed, even if it is not directly based on the pressure measurements of the eSHM system.

7.3.4 Usage Monitoring

The eSHM system can also be employed as a Usage Monitoring principle. The sensitivity of the system is depending on the bulk modulus of the fluid that is present in the capillary. For applications that are not prone to thermal variations, increasing the bulk modulus of the fluid inside the capillary will lead to a more sensitive system. From an application point of view, it would furthermore be interesting to select a new fluid type that can be used in a temperature range below the freezing point of water.

Most applications will however operate at various temperatures, affecting the pressure inside the capillaries of the eSHM system. Most applications in which the eSHM can be utilized will therefore require the insensitivity to thermal changes. The capillary pressure changes due to thermal effects must be avoided, or at least decoupled from those pressure variations that are related to the strain that is acting on the component.

Last but not least, the pressure inside capillaries of the eSHM system have shown to be very sensitive for thermal changes. It is therefore very well possible that the eSHM can be utilized as a very accurate temperature sensor as well.

References

[1] Paul Markillie. A third industrial revolution. Online available at http://www.economist.com/node/21553017, April 2012. Accessed on 27-11-2017.

[2] Jeremy Rifkin. The third industrial revolution: How the internet, green electricity, and 3-d printing are ushering in a sustainable era of distributed capitalism, March 2012. Accessed on 27-11-2017.

[3] Gartner. Gartner says consumer 3d printing is more than five years away. Online available at https://www.gartner.com/newsroom/id/2825417, August 2014. Accessed on 27-11-2017.

[4] General Fabb. About that hype cycle. Online available at http://www.fabbaloo.com/blog/2017/8/2/about-that-hype-cycle, August 2017. Accessed on 27-11-2017.

[5] Astm f2792-12a, standard terminology for additive manufacturing technologies. (Withdrawn 2015), 2012.

[6] Scott J Grunewald. New industry report: Metal 3d printing is now the fastest growing segment of the 3d printing industry. Online available at https://3dprint.com/144859/metal-3dp-fastest-growing/, August 2016. Accessed on 27-11-2017.

[7] Royston Jones. Topology optimization joins the mile high club. Online available at http://altairenlighten.com/opinion/topology-optimization-joins-the-mile-high-club/, June 2012. Accessed on 27-11-2017.

[8] Sarah Anderson Goehrke. Frustum's topology optimization comes to siemens' nx software in a partnership bringing design innovation to additive manufacturing. Online available at https://3dprint.com/169099/frustum-siemens-nx/, March 2017. Accessed on 27-11-2017.

[9] 3D Systems (formerly LayerWise).

[10] Marc Albert. Additive manufacturing adds to amerimold. Online available at https://www.additivemanufacturing.media/blog/post/additive-manufacturing-adds-to-amerimold, May 2012. Accessed on 27-11-2017.

[11] Ginger Gardiner. Structural health monitoring: Decades of demonstrations build confidence in local shm. Online available at https://www.compositesworld.com/articles/structural-health-monitoring-decades-of-demonstrations-build-confidence-in-local-shm, July 2015. Accessed on 27-12-2017.

[12] Robert Bond Randall. *Vibration-based Condition Monitoring: Industrial, Aerospace and Automotive Applications.* Wiley, 2011.

[13] Christian Boller, Fu-Kuo Chang, and Yozo Fujino, editors. *Encyclopedia of Structural Health Monitoring.* John Wiley & Sons, Ltd, jan 2009.

[14] C. R. Farrar and N. A. J. Lieven. Damage prognosis: the future of structural health monitoring. *Philosophical Transactions of the Royal Society A: Mathematical, Physical and Engineering Sciences*, 365(1851):623–632, feb 2007.

[15] Olivier Cherrier, Pierre Selva, Valérie Pommier-Budinger, Frédéric Lachaud, and Joseph Morlier. Damage localization map using electromechanical impedance spectrums and inverse distance weighting interpolation: Experimental validation on thin composite structures. *Structural Health Monitoring: An International Journal*, 12(4):311–324, jun 2013.

[16] Maria Strantza. *Additive Manufacturing as a Tool for Structural Health Monitoring of Metallic Structures.* PhD thesis, Vrije Universiteit Brussel, April 2016.

[17] Ali Fatemi Ralph I. Stephens. *Metal Fatigue in Engineering.* JOHN WILEY & SONS INC, 2000.

[18] Md Abdul Maleque and Mohd Sapuan Salit. Mechanical failure of materials. In *Materials Selection and Design*, pages 17–38. Springer Singapore, 2013.

[19] Ludovic Noels. Fracture mechanics online class, September 2015.

[20] Claude Bathias and André Pineau. *Fatigue of Materials and Structures.* John Wiley & Sons Inc, 2010.

[21] Linear elastic fracture mechanics (lefm): Part two. Online available at http://www.totalmateria.com/, December 2010. Accessed on 12/12/2017.

[22] A. Nussbaumer H-P Günther R. Heimerich S. Herion M.H. Kolstein S. Walbridge B. Androic O. Dijkstra Ö. Bucak B. Kühn, M. Lukic. Assessment of existing steel structures: Recommendations for estimation of remaining fatigue life. *JRC Scientific and Technical Reports*, (First edition):1–108, February 2008.

[23] N.E. Cherolis. Facets on fatigue fractures. *Microscopy and Microanalysis*, 19(S2):1838–1839, aug 2013.

[24] Jaap Schijve. *Fatigue of Structures and Materials.* Springer, 2001.

[25] Joris Everaerts. *Fatigue crack initiation and facet formation in Ti-6Al-4V wires.* KU Leuven, 2017.

[26] A.J. McEvily, T. Nakamura, H. Oguma, K. Yamashita, H. Matsunaga, and M. Endo. On the mechanism of very high cycle fatigue in ti–6al–4v. *Scripta Materialia*, 59(11):1207–1209, dec 2008.

[27] M. Janeček, F. Nový, P. Harcuba, J. Stráský, L. Trško, M. Mhaede, and L. Wagner. The very high cycle fatigue behaviour of ti-6al-4v alloy. *Acta Physica Polonica A*, 128(4):497–503, oct 2015.

[28] E. Takeuchi, Y. Furuya, N. Nagashima, and S. Matsuoka. The effect of frequency on the giga-cycle fatigue properties of a ti-6al-4v alloy. *Fatigue & Fracture of Engineering Materials & Structures*, 31(7):599–605, jul 2008.

[29] Q Wang. Effect of inclusion on subsurface crack initiation and gigacycle fatigue strength. *International Journal of Fatigue*, 24(12):1269–1274, dec 2002.

[30] Yoshiyuki Furuya and Etsuo Takeuchi. Gigacycle fatigue properties of ti–6al–4v alloy under tensile mean stress. *Materials Science and Engineering: A*, 598:135–140, mar 2014.

[31] M.A. Miner. Cumulative damage in fatigue. *Journal of Applied Mechanics*, 12:159164, 1945.

[32] S Ishihara and A.J McEvily. A coaxing effect in the small fatigue crack growth regime. *Scripta Materialia*, 40(5):617–622, feb 1999.

[33] Scott M. Thompson, Linkan Bian, Nima Shamsaei, and Aref Yadollahi. An overview of direct laser deposition for additive manufacturing; part i: Transport phenomena, modeling and diagnostics. *Additive Manufacturing*, 8:36–62, oct 2015.

[34] G. M. Sinclair. *An Investigation of the Coaxing Effect in Fatigue of Metals.* Defense Technical Information Center, 1952.

[35] N. Nishitani and S. Nishida. Correlation between the existence of fatigue limit and non-propagating micro-crack. *Trans. Japan Soc. Mech. Engn.*, 39:1385–1394, 1973.

[36] R Bellows. Validation of the step test method for generating haigh diagrams for ti–6al–4v. *International Journal of Fatigue*, 21(7):687–697, aug 1999.

[37] J. Everaerts, B. Verlinden, and M. Wevers. Internal fatigue crack initiation in drawn ti–6al–4v wires. *Materials Science and Technology*, 32(16):1639–1645, jan 2016.

[38] Vydehi Arun Joshi. *Titanium Alloys: An Atlas of Structures and Fracture Features.* CRC Press, 2006.

[39] Donald J. Wulpi. *Understanding How Components Fail.* ASM International, 1999.

[40] G.A. Georgiou. Probability of detection (pod) curves: Derivation, applications and limitations. *Health and Sefety Executive*, pages 1–144, 2006.

[41] G. Barndt and K. McCool. Development efforts and requirements for implementation of navy structural usage monitoring. In *Proceedings of the Americal Helicopter Society 58th Annual Forum*, June 2002.

[42] S. Maley, J. Plets, and N.D. Phan. Us navy roadmap to structural health and usage monitoring - the present and future. In *Proceedings of the American Helicopter Society 63rd Annuals Forum*, May 2007.

[43] J. M. W. Brownjohn. Structural health monitoring of civil infrastructure. *Philosophical Transactions of the Royal Society A: Mathematical, Physical and Engineering Sciences*, 365(1851):589–622, feb 2007.

[44] Fu-Kuo Chang. *Structural Health Monitoring 2000*. CRC Press, 1999.

[45] Fu-Kuo Chang. *Structural Health Monitoring: Current Status and Perspectives*. CRC Press, 1998.

[46] Patent file: Us3667862 a 00000000 dw197225, 1972.

[47] R.J.H. Wanhill. Some notable aircraft service failures investigated by the nlr. Technical Report NLR-TP-2009-001, National Aerospace Laboratory NLR, 2009.

[48] Patent file: Gb359239 a 19311022, 1931.

[49] *State-of-the-Art in Structural Health Monitoring for Aeronautics*, Proc. of Internat. Symposium on NDT in Aerospace, Fraunhofer Inst. for Nondestructive Testing (IZFP), 2008.

[50] Abid Ali Khan, Suhaib Zafar, Nadeem Shafi Khan, and Zahid Mehmood. History, current status and challenges to structural health monitoring system aviation field. *Journal of Space Technology*, 4(1):1–8, July 2014.

[51] Alfredo Güemes. Shm technologies and applications in aircraft structures. In *Proceedings of the 5th International Symposium on NDT in Aerospace*, pages 1–8, 2013.

[52] Nobuo Takeda. Fiber optic sensor-based shm technologies for aerospace applications in japan. In Wolfgang Ecke, Kara J. Peters, and Norbert G. Meyendorf, editors, *Proceedings of the Smart Sensor Phenomena, Technology, Networks and Systems*, volume 6933, pages 1–13. SPIE, 2008.

[53] T.H.T. Chan, L. Yu, H.Y. Tam, Y.Q. Ni, S.Y. Liu, W.H. Chung, and L.K. Cheng. Fiber bragg grating sensors for structural health monitoring of tsing ma bridge: Background and experimental observation. *Engineering Structures*, 28(5):648–659, apr 2006.

[54] Shiyin Wei, Zhaohui Zhang, Shunlong Li, and Hui Li. Strain features and condition assessment of orthotropic steel deck cable-supported bridges subjected to vehicle loads by using dense FBG strain sensors. *Smart Materials and Structures*, 26(10):104007, aug 2017.

[55] G. T. Webb, P. J. Vardanega, N. A. Hoult, P. R. A. Fidler, P. J. Bennett, and C. R. Middleton. Analysis of fiber-optic strain-monitoring data from a prestressed concrete bridge. *Journal of Bridge Engineering*, 22(5):05017002, may 2017.

[56] Dongtao Hu, Yongxing Guo, Xianfeng Chen, and Congrui Zhang. Cable force health monitoring of tongwamen bridge based on fiber bragg grating. *Applied Sciences*, 7(4):384, apr 2017.

[57] Y. Q. Ni, Y. Xia, W. Y. Liao, and J. M. Ko. Technology innovation in developing the structural health monitoring system for guangzhou new TV tower. *Structural Control and Health Monitoring*, 16(1):73–98, feb 2009.

[58] Liang Ren, Chao-Lin Yuan, Hong-Nan Li, and Ting-Hua Yi. Structural health monitoring system developed for dalian stadium. *International Journal of Structural Stability and Dynamics*, 16(04):1640018, may 2016.

[59] Marcus Perry, Jack McAlorum, Grzegorz Fusiek, Pawel Niewczas, Iain McKeeman, and Tim Rubert. Crack monitoring of operational wind turbine foundations. *Sensors*, 17(8):1925, aug 2017.

[60] Alexandros Iliopoulos, Wout Weijtjens, Danny Van Hemelrijck, and Christof Devriendt. Fatigue assessment of offshore wind turbines on monopile foundations using multi-band modal expansion. *Wind Energy*, 20(8):1463–1479, mar 2017.

[61] Wayne Baker, Iain McKenzie, and Rhys Jones. Development of life extension strategies for australian military aircraft, using structural health monitoring of composite repairs and joints. *Composite Structures*, 66(1-4):133–143, oct 2004.

[62] A. Cigada, G. Moschioni, M. Vanali, and A. Caprioli. The measurement network of the san siro meazza stadium in milan: Origin and implementation of a new data acquisition strategy for structural health monitoring. *Experimental Techniques*, 34(1):70–81, jan 2010.

[63] Austin Downey, Simon Laflamme, and Filippo Ubertini. Experimental wind tunnel study of a smart sensing skin for condition evaluation of a wind turbine blade. *Smart Materials and Structures*, 26(12):125005, oct 2017.

[64] Sandro Diord, Filipe Magalhães, Álvaro Cunha, Elsa Caetano, and Nuno Martins. Automated modal tracking in a football stadium suspension roof for detection of structural changes. *Structural Control and Health Monitoring*, 24(11):2006, mar 2017.

[65] Kaoshan Dai, Ying Wang, Yichao Huang, Weidong Zhu, and Yongfeng Xu. Development of a modified stochastic subspace identification method for rapid structural assessment of in-service utility-scale wind turbine towers. *Wind Energy*, 20(10):1687–1710, may 2017.

[66] T. Mickens, M. Schulz, M. Sundaresean, A. Ghoshal, A.S. Naser, and R. Reichmeider. Structural health monitoring of an aircraft joint. *Mechanical Systems and Signal Processing*, 17(2):285–303, mar 2003.

[67] Joel Smithard, Patrick Norman, Steve van der Velden, Ian Powlesland, George Jung, Nik Rajic, and Steve Galea. The acousto ultrasonic structural health monitoring array module for damage detection in structures. *Procedia Engineering*, 188:448–455, 2017.

[68] Andrea Bulletti, Pietro Giannelli, Marco Calzolai, and Lorenzo Capineri. An integrated acousto/ultrasonic structural health monitoring system for composite pressure vessels. *IEEE Transactions on Ultrasonics, Ferroelectrics, and Frequency Control*, 63(6):864–873, jun 2016.

[69] M. Gresil, A. Muller, and C. Scoutis. Acousto-ultrasonics structural health monitoring of aerospace composite materials. In *Proceedings of the 6th Conference on Emerging Technologies in Non-Destructive Testing*, pages 1–7, May 2015.

[70] Richard D. Finlayson, Mark Friesel, Mar Carlos, Phil Cole, and L.C. Lenain. Health monitoring of aerospace structures with acoustic emis-

sion and acousto-ultrasonics. In *Proceedings of the 15th World Conference on Non Destructive Testing*, 2000.

[71] A. Raghavan and C. E. S. Cesnik. Review of guided-wave structural health monitoring. *The Shock and Vibration Digest*, 39(2):91–114, mar 2007.

[72] Wiesław J. Staszewski. Structural health monitoring using guided ultrasonic waves. In *Advances in Smart Technologies in Structural Engineering*, pages 117–162. Springer Berlin Heidelberg, 2004.

[73] Joseph L. Rose. Ultrasonic guided waves in structural health monitoring. *Key Engineering Materials*, 270-273:14–21, 2004.

[74] W.J. Staszewski. Ultrasonic/guided waves for structural health monitoring. *Key Engineering Materials*, 293-294:49–62, 2005.

[75] Jeffrey Steven Crider. Damage detection using lamb waves for structural health monitoring. Master's thesis, Unites States Air Force Institute of Technology, March 2007.

[76] Henry A. Sodano. Development of an automated eddy current structural health monitoring technique with an extended sensing region for corrosion detection. *Structural Health Monitoring: An International Journal*, 6(2):111–119, jun 2007.

[77] Neil J. Goldfine, Vladimir A. Zilberstein, Darrell E. Schlicker, Yanko Sheiretov, Karen Walrath, Andrew P. Washabaugh, and Douglas Van Otterloo. Surface-mounted periodic field eddy current sensors for structural health monitoring. In Tribikram Kundu, editor, *Advanced Nondestructive Evaluation for Structural and Biological Health Monitoring*. SPIE, jul 2001.

[78] Hua Ding, Yu Ting He, and Shen Bo Jiao. Rosette eddy current sensor for structural health monitoring. *Applied Mechanics and Materials*, 330:430–436, jun 2013.

[79] G Wheatley, J Kollgaard, J Register, and M Zaidi. Comparative vacuum monitoring (CVM™) as an alternate means of compliance (AMOC). *Insight - Non-Destructive Testing and Condition Monitoring*, 47(3):153–156, mar 2005.

[80] D. Roach. Real time crack detection using mountable comparative vacuum monitoring sensors. *Smart Structures and Systems*, 2009.

[81] Ginger Gardiner. Structural health monitoring: Ndt-integrated aerostructures enter service. Online available at https://www.compositesworld.com/articles/structural-health-monitoring-ndt-integrated-aerostructures-enter-service, March 2015. Accessed on 19-12-2017.

[82] Edited by: Fu-Kuo Chang and Edited by: Fotis Kopsaftopoulos. *Structural Health Monitoring 2015: System Reliability for Verification and Implementation*. DEStech Publications, Inc, 2015.

[83] Structural health monitoring market: Bridges & dams application segment to remain dominant in terms of market share throughout the forecast period: Global industry analysis (2012 - 2016) and opportunity assessment (2017 - 2027). Technical report, Future Markets Insights, 2017.

[84] Zhen Sun, Zilong Zou, and Yufeng Zhang. Utilization of structural health monitoring in long-span bridges: Case studies. *Structural Control and Health Monitoring*, 24(10):1979, jan 2017.

[85] Junwon Seo, Jong Wan Hu, and Jaeha Lee. Summary review of structural health monitoring applications for highway bridges. *Journal of Performance of Constructed Facilities*, 30(4):04015072, aug 2016.

[86] Zengshun Chen, Xiao Zhou, Xu Wang, Lili Dong, and Yuanhao Qian. Deployment of a smart structural health monitoring system for long-span arch bridges: A review and a case study. *Sensors*, 17(9):2151, sep 2017.

[87] Wei Lu, Jun Teng, Chao Li, and Yan Cui. Reconstruction to sensor measurements based on a correlation model of monitoring data. *Applied Sciences*, 7(3):243, mar 2017.

[88] Jun Teng, Wei Lu, Yan Cui, and Rengui Zhang. Temperature and displacement monitoring to steel roof construction of shenzhen bay stadium. *International Journal of Structural Stability and Dynamics*, 16(04):1640020, may 2016.

[89] Austin Downey, Filippo Ubertini, and Simon Laflamme. Algorithm for damage detection in wind turbine blades using a hybrid dense sensor network with feature level data fusion. *Journal of Wind Engineering and Industrial Aerodynamics*, 168:288–296, sep 2017.

[90] Peyman Poozesh, Kai Aizawa, Christopher Niezrecki, Javad Baqersad, Murat Inalpolat, and Gunnar Heilmann. Structural health monitoring of wind turbine blades using acoustic microphone array. *Structural Health Monitoring: An International Journal*, 16(4):471–485, nov 2016.

[91] I. Herszberg, M.K. Bannister, H.C.H. Li, R.S. Thomson, and C. White. Structural health monitoring for advanced composite structures. In *Proceedings of the 16th International Conference on Composite Materials*, 2007.

[92] A.M. Stefani. Review of air carriers' use of aircraft repair stations. Technical Report FAA report number AV-2003-047, Federal Aviation Authoroty (FAA), 2003.

[93] R.Henrich H. Speckmann. Structural health monitoring (shm) - overview on technologies under development. In *Proceedings of the 16th World Conference on NDT (WCNDT)*, 2004.

[94] Structural Monitoring Systems. Structural monitoring systems executes worlds first commercial supply and marketing agreement with delta air lines, August 2017. Accessed on 19-12-2017.

[95] S. Roy R. Nardari Y-H Li. S-J Kim. F. Kopsaftopoulos. F-K Chang N. Salowitz., Z. Guo. A vision on stretchable bio-inspired networks for intelligent structures. In *Proceedings of the 9th Conference and International Workshop on Structural Health Monitoring (IWSHM)*, pages 1–13, September 2013.

[96] Joseph T. Muth, Daniel M. Vogt, Ryan L. Truby, Yiğit Mengç, David B. Kolesky, Robert J. Wood, and Jennifer A. Lewis. Embedded 3d printing of strain sensors within highly stretchable elastomers. *Advanced Materials*, 26(36):6307–6312, jun 2014.

[97] Shu Minakuchi, Hidehiko Banshoya, Shingo Ii, and Nobuo Takeda. Hierarchical fiber-optic delamination detection system for carbon fiber reinforced plastic structures. *Smart Materials and Structures*, 21(10):105008, aug 2012.

[98] Yong-Lae Park, Carmel Majidi, Rebecca Kramer, Phillipe Bérard, and Robert J Wood. Hyperelastic pressure sensing with a liquid-embedded elastomer. *Journal of Micromechanics and Microengineering*, 20(12):125029, nov 2010.

[99] Sung-Yueh Wu, Chen Yang, Wensyang Hsu, and Liwei Lin. 3d-printed microelectronics for integrated circuitry and passive wireless sensors. *Microsystems & Nanoengineering*, 1:15013, jul 2015.

[100] Hiroki Ota, Sam Emaminejad, Yuji Gao, Allan Zhao, Eric Wu, Samyuktha Challa, Kevin Chen, Hossain M. Fahad, Amit K. Jha, Daisuke Kiriya, Wei Gao, Hiroshi Shiraki, Kazuhito Morioka, Adam R. Ferguson, Kevin E. Healy, Ronald W. Davis, and Ali Javey. Application of 3d printing for smart objects with embedded electronic sensors and systems. *Advanced Materials Technologies*, 1(1):1600013, mar 2016.

[101] Matt Saari, Bryan Cox, Edmond Richer, Paul S. Krueger, and Adam L. Cohen. Fiber encapsulation additive manufacturing: An enabling technology for 3d printing of electromechanical devices and robotic components. *3D Printing and Additive Manufacturing*, 2(1):32–39, mar 2015.

[102] Austin G. Scheyer and Steven R. Anton. Impedance-based structural health monitoring of additive manufactured structures with embedded piezoelectric wafers. In Jerome P. Lynch, editor, *Sensors and Smart Structures Technologies for Civil, Mechanical, and Aerospace Systems 2017*. SPIE, apr 2017.

[103] Nouari Saheb and Samir Mekid. Fiber-embedded metallic materials: From sensing towards nervous behavior. *Materials*, 8(12):7938–7961, nov 2015.

[104] Robert R. J. Maier, William N. MacPherson, James S. Barton, Mark Carne, Mark Swan, John N. Sharma, Simon K. Futter, David A. Knox, Benjamin J. S. Jones, and Scott McCulloch. Embedded fiber optic sensors within additive layer manufactured components. *IEEE Sensors Journal*, 13(3):969–979, mar 2013.

[105] Adriaan Spierings Thomas Bauer Robert R.J. Maier Konrad Wegener Philip Stoll, Jinesh Mathew. Embedding fibre optical sensors into slm parts. In *Proceedings of the 27th Inernational Solid Freeform Fabrication Symposium - An Additive Manufacturing Conference*, 2016.

[106] X. Li and F. Prinz. Embedding of fiber optic sensors in layered manufacturing. In *Proceedings of the Solid Freeform Fabrication Symposium*, 2000.

[107] Xiaochun Li. *Embedded Sensors in Layered Manufacturing.* PhD thesis, Stanford University, 2001.

[108] John J Schomer. Embedding fiber bragg grating sensors through ultrasonic additive manufacturing. Master's thesis, Ohio State University, 2017.

[109] Sensor embedding in additive manufacturing (seam) team. Technical report, DON innovations, 2016.

[110] Dieter De Baere, Maria Strantza, Michaël Hinderdael, Wim Devesse, and Patrick Guillaume. Effective structural health monitoring with additive manufacturing. In Vincent Le Cam, Laurent Mevel, and Franck Schoefs, editors, *Proceedings of the 7th European Workshop on Structural Health Monitoring*, pages 2314–2321, July 2014.

[111] Maria Strantza, Dieter De Baere, Marleen Rombouts, Stijn Clijsters, Isabelle Vandendael, Herman Terryn, Patrick Guillaume, and Danny Van Hemelrijck. 3d printing for intelligent metallic structures. In *Proceedings of the 7th European Workshop on Structural Health Monitoring*, 2014.

[112] Maria Strantza, Dieter De Baere, Marleen Rombouts, Gert Maes, Patrick Guillaume, and Danny Van Hemelrijck. Feasibility study on integrated structural health monitoring system produced by metal three-dimensional printing. *Structural Health Monitoring: An International Journal*, 14(6):622–632, sep 2015.

[113] Maria Strantza, Reza Vafadari, Dieter de Baere, Bey Vrancken, Wim van Paepegem, Isabelle Vandendael, Herman Terryn, Patrick Guillaume, and Danny van Hemelrijck. Fatigue of ti6al4v structural health monitoring systems produced by selective laser melting. *Materials*, 9(2):106, feb 2016.

[114] Maria Strantza, Reza Vafadari, Dieter De Baere, Marleen Rombouts, Isabelle Vandendael, Herman Terryn, Michaël Hinderdael, Ali Rezaei, Wim Van Paepegem, Patrick Guillaume, and Danny Van Hemelrijck. Evaluation of different topologies of integrated capillaries in effective structural health monitoring system produced by 3d printing. In *Proceedings of the 10th International Workshop on Structural Health Monitoring (IWSHM)*, pages 153–160, September 2015.

[115] Maria Strantza, Michaël Hinderdael, Dieter De Baere, Isabelle Vandendael, Herman Terryn, Danny Van Hemelrijck, and Patrick Guillaume. Additive manufacturing for novel structural health monitoring systems. In *Conference proceedings of the 8th European Workshop on Structural Health Monitoring*, pages 1–9, 2016.

[116] Maria Strantza, Dimitrios Aggelis, Dieter de Baere, Patrick Guillaume, and Danny van Hemelrijck. Evaluation of SHM system produced by additive manufacturing via acoustic emission and other NDT methods. *Sensors*, 15(10):26709–26725, oct 2015.

[117] Extruderande tillverkningsmetoder - fused deposition modeling. Online available at http://www.design.lth.se/om-institutionen/forskningslaboratorier/3dprintlab, November 2016. Accessed on 29-11-2017.

[118] Stereolithography. Online available at http://www.custompartnet.com/wu/stereolithography, 2008. Accessed on 29-11-2017.

[119] What is laser cladding? Online available at https://www.fst.nl/about/laser-cladding/. Accessed on 29-11-2017.

[120] Beth E. Carroll, Todd A. Palmer, and Allison M. Beese. Anisotropic tensile behavior of ti–6al–4v components fabricated with directed energy deposition additive manufacturing. *Acta Materialia*, 87:309–320, apr 2015.

[121] Abdollah Saboori, Donato Gallo, Sara Biamino, Paolo Fino, and Mariangela Lombardi. An overview of additive manufacturing of titanium components by directed energy deposition: Microstructure and mechanical properties. *Applied Sciences*, 7(9):883, aug 2017.

[122] Amanda Sterling, Nima Shamsaei, Brian Torries, and Scott M. Thompson. Fatigue behaviour of additively manufactured ti-6al-4v. *Procedia Engineering*, 133:576–589, 2015.

[123] A. W. Prabhu, T. Vincent, A. Chaudhary, W. Zhang, and S. S. Babu. Effect of microstructure and defects on fatigue behaviour of directed energy deposited ti–6al–4v. *Science and Technology of Welding and Joining*, 20(8):659–669, jun 2015.

[124] Christian Leinenbach. Selective laser melting. Online available at https://www.empa.ch/web/coating-competence-center/selective-laser-melting. Accessed on 29-11-2017.

[125] Asm handbook, vol. 1.

[126] H. K. Rafi, N. V. Karthik, Haijun Gong, Thomas L. Starr, and Brent E. Stucker. Microstructures and mechanical properties of ti6al4v parts fabricated by selective laser melting and electron beam melting. *Journal of Materials Engineering and Performance*, 22(12):3872–3883, aug 2013.

[127] Hanchen Yu, Jingjing Yang, Jie Yin, Zemin Wang, and Xiaoyan Zeng. Comparison on mechanical anisotropies of selective laser melted ti-6al-4v alloy and 304 stainless steel. *Materials Science and Engineering: A*, 695:92–100, may 2017.

[128] Chunlei Qiu, Nicholas J.E. Adkins, and Moataz M. Attallah. Microstructure and tensile properties of selectively laser-melted and of HIPed laser-melted ti-6al-4v. *Materials Science and Engineering: A*, 578:230–239, aug 2013.

[129] M. Simonelli, Y.Y. Tse, and C. Tuck. Effect of the build orientation on the mechanical properties and fracture modes of slm ti-6al-4v. *Materials Science and Engineering: A*, 616:1–11, oct 2014.

[130] Jyoti Suryawanshi, K.G. Prashanth, and U. Ramamurty. Mechanical behavior of selective laser melted 316l stainless steel. *Materials Science and Engineering: A*, 696:113–121, jun 2017.

[131] F. Bartolomeu, M. Buciumeanu, E. Pinto, N. Alves, O. Carvalho, F.S. Silva, and G. Miranda. 316l stainless steel mechanical and tribological behavior: A comparison between selective laser melting, hot pressing and conventional casting. *Additive Manufacturing*, 16:81–89, aug 2017.

[132] A.A. Deev, P.A. Kuznetcov, and S.N. Petrov. Anisotropy of mechanical properties and its correlation with the structure of the stainless steel 316l produced by the slm method. *Physics Procedia*, 83:789–796, 2016.

[133] Di Wang, Changhui Song, Yongqiang Yang, and Yuchao Bai. Investigation of crystal growth mechanism during selective laser melting

and mechanical property characterization of 316l stainless steel parts. *Materials & Design*, 100:291–299, jun 2016.

[134] E. Liverani, S. Toschi, L. Ceschini, and A. Fortunato. Effect of selective laser melting (slm) process parameters on microstructure and mechanical properties of 316l austenitic stainless steel. *Journal of Materials Processing Technology*, 249:255–263, nov 2017.

[135] Zhongji Sun, Xipeng Tan, Shu Beng Tor, and Wai Yee Yeong. Selective laser melting of stainless steel 316l with low porosity and high build rates. *Materials & Design*, 104:197–204, aug 2016.

[136] Xuezhi Shi, Shuyuan Ma, Changmeng Liu, Cheng Chen, Qianru Wu, Xianping Chen, and Jiping Lu. Performance of high layer thickness in selective laser melting of ti-6al-4v. *Materials*, 9(12):975, dec 2016.

[137] John J. Lewandowski and Mohsen Seifi. Metal additive manufacturing: A review of mechanical properties (postprint). Technical report, Case Western Reserve University, 2016.

[138] Eric Wycisk, Shafaqat Siddique, Dirk Herzog, Frank Walther, and Claus Emmelmann. Fatigue performance of laser additive manufactured ti–6al–4v in very high cycle fatigue regime up to 109 cycles. *Frontiers in Materials*, 2, dec 2015.

[139] John A. Slotwinski, Edward J. Garboczi, and Keith M. Hebenstreit. Porosity measurements and analysis for metal additive manufacturing process control. *Journal of Research of the National Institute of Standards and Technology*, 119:494, oct 2014.

[140] Kwai S. Chan, Marie Koike, Robert L. Mason, and Toru Okabe. Fatigue life of titanium alloys fabricated by additive layer manufacturing techniques for dental implants. *Metallurgical and Materials Transactions A*, 44(2):1010–1022, oct 2012.

[141] Haijun Gong, Khalid Rafi, Thomas Starr, and Brent Stucker. Effect of defects on fatigue tests of as-built ti-6al-4v parts fabricated by selective laser melting. In *Proceedings of the 23rd Annual International Solid Freeform Fabrication SymposiumAn Additive Manufacturing Conference*, pages 499–506., 2012.

[142] Victor Chastand, Astrid Tezenas, Yannick Cadoret, Philippe Quaegebeur, Wilson Maia, and Eric Charkaluk. Fatigue characterization of

titanium ti-6al-4v samples produced by additive manufacturing. *Procedia Structural Integrity*, 2:3168–3176, 2016.

[143] Eric Wycisk, Claus Emmelmann, Shafaqat Siddique, and Frank Walther. High cycle fatigue (HCF) performance of ti-6al-4v alloy processed by selective laser melting. *Advanced Materials Research*, 816-817:134–139, sep 2013.

[144] D. Greitemeier, V. Holzinger, C. Dalle Donne, J. Eufinger, and T. Melz. Fatigue prediction of additive manufactured ti-6al-4v for aerospace: Effect of defects, surface roughness. In *Proceedings of the 28th ICAF Symposium*, 2015.

[145] P. Edwards and M. Ramulu. Fatigue performance evaluation of selective laser melted ti–6al–4v. *Materials Science and Engineering: A*, 598:327–337, mar 2014.

[146] Michaël Hinderdael, Maria Strantza, Dieter De Baere, Wim Devesse, Iris De Graeve, Herman Terryn, and Patrick Guillaume. Fatigue performance of ti-6al-4v additively manufactured specimens with integrated capillaries of an embedded structural health monitoring system. *Materials*, 10(9)(993):1–19, aug 2017.

[147] T. Nicholas. Step loading for very high cycle fatigue. *Fatigue and Fracture of Engineering Materials and Structures*, 25(8-9):861–869, sep 2002.

[148] Theodore Nicholas. *High Cycle Fatigue: A Mechanics of Materials Perspective*. Elsevier Science, 2006.

[149] R Morrissey and T Nicholas. Staircase testing of a titanium alloy in the gigacycle regime. *International Journal of Fatigue*, 28(11):1577–1582, nov 2006.

[150] Wim Devesse, Dieter De Baere, Michaël Hinderdael, and Patrick Guillaume. Hardware-in-the-loop control of additive manufacturing processes using temperature feedback. *Journal of Laser Applications*, 28(2)(022302):1–8, may 2016.

[151] Wim Devesse, Dieter De Baere, and Patrick Guillaume. Design of a model-based controller with temperature feedback for laser cladding. *Physics Procedia*, 56:211–219, 2014.

[152] Lawrence Boaz, Shubi Kaijage, and Ramadhani Sinde. An overview of pipeline leak detection and location systems. In *Proceedings of the 2nd Pan African International Conference on Science, Computing and Telecommunications (PACT 2014)*. IEEE, jul 2014.

[153] Pal-Stefan Murvay and Ioan Silea. A survey on gas leak detection and localization techniques. *Journal of Loss Prevention in the Process Industries*, 25(6):966–973, nov 2012.

[154] Wei Liang, Lai bin Zhang, and Zhao hui Wang. State of research on negative pressure techniques applied to leak detection in liquid pipelines. In *2004 International Pipeline Conference, Volumes 1, 2, and 3*. ASME, 2004.

[155] Tarek R. Sheltami, Abubakar Bala, and Elhadi M. Shakshuki. Wireless sensor networks for leak detection in pipelines: a survey. *Journal of Ambient Intelligence and Humanized Computing*, 7(3):347–356, mar 2016.

[156] Qingmin Hou, Liang Ren, Wenling Jiao, Pinghua Zou, and Gangbing Song. An improved negative pressure wave method for natural gas pipeline leak location using FBG based strain sensor and wavelet transform. *Mathematical Problems in Engineering*, 2013:1–8, 2013.

[157] Chun Hua Tian, Jun Chi Yan, Jin Huang, Yu Wang, Dong-Sup Kim, and Tongnyoul Yi. Negative pressure wave based pipeline leak detection: Challenges and algorithms. In *Proceedings of 2012 IEEE International Conference on Service Operations and Logistics, and Informatics*. IEEE, jul 2012.

[158] Wenqing Lu, Wei Liang, Laibin Zhang, and Wei Liu. A novel noise reduction method applied in negative pressure wave for pipeline leakage localization. *Process Safety and Environmental Protection*, 104:142–149, nov 2016.

[159] Chuanhu Ge, Guizeng Wang, and Hao Ye. Analysis of the smallest detectable leakage flow rate of negative pressure wave-based leak detection systems for liquid pipelines. *Computers & Chemical Engineering*, 32(8):1669–1680, aug 2008.

[160] Samuel Rocha. Acoustic monitoring of pipeline leaks. Number 89-0333, pages 283–290, 1989.

[161] John Loth, Gary Morris, Richard Guiler, Deepak Mehra, and George Palmer. Technology assessment of on-line acoustic monitoring for leaks/infringements in underground natural gas transmission lines, January 2003.

[162] René Christensen, Peter Juhl, and Vicente Cutanda Henriquez. Practical modeling of acoustic losses in air due to heat conduction and viscosity. *The Journal of the Acoustical Society of America*, 123(5):3420–3420, may 2008.

[163] Yunus A Cengel and John M Cimbala. *Fluid Mechanics: Fundamentals and Applications*. McGraw-Hill, 2nd edition, 2010.

[164] Michaël Hinderdael, Dieter De Baere, and Patrick Guillaume. Proof of concept of crack localization using negative pressure waves in closed tubes for later application in effective SHM system for additive manufactured components. *Applied Sciences*, 6(2)(33):1–12, jan 2016.

[165] R. Biswas M.M. Rahman and W.I. Mahfuz. Effects of beta ratio and reynold's number on coefficient of discharge of orifice meter. *J Agrid Rural Dev*, 7(1&2):151–156, June 2009.

[166] Jiangwen Wan, Yang Yu, Yinfeng Wu, Renjian Feng, and Ning Yu. Hierarchical leak detection and localization method in natural gas pipeline monitoring sensor networks. *Sensors*, 12(12):189–214, dec 2011.

[167] Reinaldo A. Silva, Claudio M. Buiatti, Sandra L. Cruz, and João A.F.R. Pereira. Pressure wave behaviour and leak detection in pipelines. *Computers & Chemical Engineering*, 20:S491–S496, jan 1996.

[168] T. Yazaki, Y. Tashiro, and T. Biwa. Measurements of sound propagation in narrow tubes. *Proceedings of the Royal Society A: Mathematical, Physical and Engineering Sciences*, 463(2087):2855–2862, aug 2007.

[169] Michael R. Stinson. The propagation of plane sound waves in narrow and wide circular tubes, and generalization to uniform tubes of arbitrary cross-sectional shape. *The Journal of the Acoustical Society of America*, 89(2):550–558, feb 1991.

[170] J.-G. Ih, C.-M. Park, and H.-J. Kim. A model for sound propagation in capillary ducts with mean flow. *Journal of Sound and Vibration*, 190(2):163–175, feb 1996.

[171] A. Cummings. Sound propagaton in narrow tubes of arbitrary cross-section. *Journal of Sound and Vibration*, 162(1):27–42, mar 1993.

[172] Michaël Hinderdael, Zoé Jardon, Margot Lison, Dieter De Baere, Wim Devesse, Maria Strantza, and Patrick Guillaume. Proof of concept of integrated load measurement in 3d printed structures. *Sensors*, 17(2)(328):1–12, feb 2017.

[173] W.J. Stazewski, C. Boller, and G.R. Tomlinson. *Health Monitoring of Aerospace Structures: Smart Sensor Technologies and Signal Processing*. Wiley, 2004.

[174] Arvid Hejll. *Civil Structural Health Monitoring: Stregies, Methods and Applications*. PhD thesis, Lulea University of Technology, 2007.

[175] Dylan K. Hardy, Matthew F. Fadden, Mohammad Jamal Khattak, and Ahmed Khattab. Development and characterization of self-sensing CNF HPFRCC. *Materials and Structures*, 49(12):5327–5342, apr 2016.

[176] Maria S. Konsta-Gdoutos and Chrysoula A. Aza. Self sensing carbon nanotube (CNT) and nanofiber (CNF) cementitious composites for real time damage assessment in smart structures. *Cement and Concrete Composites*, 53:162–169, oct 2014.

[177] Baoguo Han, Xun Yu, and Jinping Ou. *Self-Sensing Concrete in Smart Structures*. Butterworth-Heinemann, 2014.

[178] C. Boller. Next generation structural health monitoring and its integration into aircraft design. *International Journal of Systems Science*, 31(11):1333–1349, jan 2000.

[179] Fu-Kuo Chang. *Structural Health Monitoring 2013, a Roadmap to Intelligent Structures: Proceedings of the Ninth International Workshop, September 10-13, 2013, Stanford University*. DEStech Publications, Inc, 2013.

[180] Baoguo Han and Jinping Ou. Embedded piezoresistive cement-based stress/strain sensor. *Sensors and Actuators A: Physical*, 138(2):294–298, aug 2007.

[181] Timo Schotzko and Walter Lang. Embedded strain gauges for condition monitoring of silicone gaskets. *Sensors*, 14(12):12387–12398, jul 2014.

[182] S. F. Masri, M. S. Agbabian, A. M. Abdel-Ghaffar, M. Higazy, R. O. Claus, and M. J. de Vries. Experimental study of embedded fiber-optic strain gauges in concrete structures. *Journal of Engineering Mechanics*, 120(8):1696–1717, aug 1994.

[183] S. Aloisi, U. Galietti, and C. Pappalettere. Strain measurement in composite materials using embedded strain gauges. *Key Engineering Materials*, 144:251–260, 1998.

[184] Hang yin Ling, Kin tak Lau, Li Cheng, and Wei Jin. Viability of using an embedded FBG sensor in a composite structure for dynamic strain measurement. *Measurement*, 39(4):328–334, may 2006.

[185] Pavan Kumar Gurrala and Srinivasa Prakash Regalla. Part strength evolution with bonding between filaments in fused deposition modelling. *Virtual and Physical Prototyping*, 9(3):141–149, may 2014.

[186] Eric J. McCullough and Vamsi K. Yadavalli. Surface modification of fused deposition modeling ABS to enable rapid prototyping of biomedical microdevices. *Journal of Materials Processing Technology*, 213(6):947–954, jun 2013.

[187] Ashu Garg, Anirban Bhattacharya, and Ajay Batish. Chemical vapor treatment of ABS parts built by FDM: Analysis of surface finish and mechanical strength. *The International Journal of Advanced Manufacturing Technology*, 89(5-8):2175–2191, aug 2016.

[188] L.M. Galantucci, F. Lavecchia, and G. Percoco. Quantitative analysis of a chemical treatment to reduce roughness of parts fabricated using fused deposition modeling. *CIRP Annals*, 59(1):247–250, 2010.